Design and Application of Surfaces with Tunable Adhesion to Liquids and Solids

by

Kevin B. Golovin

A dissertation submitted in partial fulfillment
of the requirements for the degree of
Doctor of Philosophy
(Materials Science & Engineering)
in the University of Michigan
2017

Doctoral Committee:

Associate Professor Anish Tuteja, Chair
Professor Jinsang Kim
Associate Professor Pramod Reddy
Professor Michael Thouless

kegolo@umich.edu
ORCiD: 0000-0001-8309-7458

2017

To Randy and Father

ACKNOWLEDGMENTS

I would first and foremost like to thank my advisor, Anish Tuteja. Anish has taught me so much in what feels like such a short burst of time. Almost like an elementary school teacher, Anish has taught me how to read, how to write, and how to think. He's always pushed me when no one else would, and he's never accepted anything but my very best. We've achieved some amazing things together, and looking back it's sometimes hard to figure out where his idea stopped and mine began, and vice versa. Anish has given me the confidence and skills to be successful, and graduating does not mean I no longer need Anish as an advisor.

I would also like to thank my lab members for shaping me into the researcher that I am today. Arun Kota taught me how to critically read and think about each and every sentence of a paper. Duck Hyun Lee spent so much time in the cleanroom for me, often before he knew what I was planning to do with whatever I asked him to make for me. Gibum Kwon and Sai Pradeep Reddy Kobaku, we had some great times together both in lab, at conferences, and late at night with Raghu. I look forward to bumping into both of you in the future. Mathew Boban, so many of my successes came down to your careful work and dedication when you could have been helping yourself. Catherine, your baked goods and MATLAB problems kept me awake throughout the long afternoons. Dhyani, the ice project could not be in better hands than yours. And Jimmy Gose, the drag reduction project would not exist without you and your expertise.

I would be remiss to not thank my committee members. Dr. Kim, I will always remember your Advanced Functional Polymers class. You stated that discovering a property was good, but designing the property was what set great research apart. I took this to heart and still remember it to this day. Dr. Reddy, you always asked the most probing questions whenever we met, and they always lead to new insight. And Dr. Thouless: our countless meetings crammed into your office have been some of the most enlightening times of my doctoral years. My only regret is that we didn't meet years earlier. Thank you all so much.

My doctoral work was sponsored by the Department of Defense through a National Defense Science & Engineering Graduate (NDSEG) fellowship. I thank the DoD for this.

And finally, I would like to thank those closest to me. My parents have always supported me, even when they didn't want to. My siblings have always looked up to me, and I've always looked up to them. I try to set the bar high so they can set it even higher. And of course, last but never least, my beautiful wife Alice Long. We've been through this whole journey together and nothing needs to be said that hasn't already. I love you all. This thesis is for all of you.

TABLE OF CONTENTS

Chapter

LIST OF FIGURES

LIST OF TABLES

ABSTRACT

Fouling affects a wide range of industries around the globe. The two main categories of fouling are the unwanted adhesion of solids, and the unwanted adsorption of liquids. The purpose of this thesis is to understand and design new mechanisms to mitigate fouling. As fouling always occurs at the interface between a surface and the foulant, the main strategy employed in this work is the fabrication of designer coatings that can be applied to any surface, such that the foulant is repelled.

In the first half of this dissertation I discuss new methods for reducing the adhesion of ice to surfaces. Ice adhesion routinely hinders many industries world-wide, and to-date there have been few long-term strategies to mitigate ice adhesion. We first design elastomeric coatings exhibiting the lowest ice adhesion strengths ever reported, and formulate a predictive model for the phenomenon of interfacial slippage, such that the ice adhesion strength of any surface can be rationally designed. We then utilize fracture mechanics to design surfaces exhibiting low interfacial toughness with ice, such that the force to remove the accreted ice becomes independent of the iced area. These results contradict the last 70 years of ice-adhesion analysis.

One of our new techniques for repelling ice, and solid foulants in general, is the fabrication of liquid-like, covalently grafted monolayers. We show that surfaces treated with these monolayers also exhibit extreme liquid repellency, including the first-ever reported fluorophobic surfaces (*i.e.* surfaces that repel extremely low surface tension, fluorinated liquids). The second half of this thesis discusses various new ways of repelling a wide variety of different fouling liquids. We fabricate optically transparent surfaces capable of repelling a wide variety of low surface tension liquids. We also design extremely mechanically robust superhydrophobic surfaces that can self-heal after physical and chemical damage. Finally, we utilize some of these water-repellent systems to effectively reduce friction drag in turbulent flow.

CHAPTER 1

Introduction

1.1 Introductory remarks

In 2006, two primitive stone tools covered in birch-bark-tar were found in Central Italy[21]. Carbon dating of the site indicated that the tools were from the Middle Pleistocene, roughly 200,000 years ago. Primitive humans most likely utilized the birch-bark-tar to bind the stone implements to a wooden shaft (*i.e.* a primitive axe). Understanding the adhesion between objects has been important for the human race (and pre-human hominins) for at least two thousand millenia.

Over this vast stretch of time, humans have mastered how to adhere objects together, with adhesives exhibiting a large range of adhesive strengths (ranging from temporary gums that adhere posters to walls, to powerful epoxies that can be sanded and drilled). The purpose of this dissertation, however, is to solve the opposite problem. Whereas increasing adhesion dates back hundreds of thousands of years, reducing the adhesion between everyday objects still plagues many common industries today. In the first half of this thesis I will discuss how the adhesion of ice to surfaces can be reduced. We will then turn our attention to reducing liquid adhesion, with a focus on the repulsion of liquids that spread on all natural surfaces.

Along the way, we will always try to keep durability in mind. Altering the adhesive properties of an interface is only useful so long as the properties remain altered. Therefore, in all of the following work, we design systems where durability is characterized by a material's ability to maintain its low adhesive property. This definition of durability is in stark contrast to traditional durability characterization methods, but is necessary for next-generation designer interfaces, such as those fabricated in this body of work.

1.2 Bonding

The fundamental study of adhesion should always begin with a discussion on bonding. Bonds can either be chemical or physical, with the strength of hydrogen bonds lying between these two

Table 1.1: The strengths of the three relevant kinds of bonds discussed in this work[17].

Type	Bond Energy (kJ/mol)	Examples
Chemical	$10^2 - 10^3$	Urethanes, epoxides, cyanoacylates
Hydrogen	$10^1 - 10^2$	H_2O, HF, NH_3, dihalides
Physical	$10^0 - 10^1$	noble gases, friction, cohesion of non-polar liquids

extremes[17]. Chemical bonds involve the sharing or transfer of electrons, and rupturing such bonds requires a large amount of energy. Conversely, physical bonds mainly arise from weak van der Waals interactions, and breaking physical bonds requires much less energy than breaking chemical bonds. Hydrogen bonding is an extreme example of polar interactions, and the strength of hydrogen bonds approaches the strength of weak chemical bonds[22]. Typical bond energies are shown in Table 1.1. Interfacial engineering, at its heart, involves controlling bonds at interfaces. For reduced adhesion, bonds should always be limited to van der Waals interactions. In contrast, chemical bonding is the main strategy employed by permanent glues and adhesives.

In a homogeneous solid material, the bonds within the bulk are always at a lower energy state than the bonds at the surface[23]. This discrepancy arises because the material always prefers to be in contact with itself rather than the surrounding environment. The energy of such a free surface is termed surface energy, γ_{SV}, where SV denotes a solid-vapor interface (typically air), and conventionally the units are given in J/m^2 for solids (*i.e.* an energy per unit area of surface). When two solid surfaces come into contact, the overall free energy of the system can be reduced by creating an interface. Although the interaction between the two solids may not be highly favorable, joining eliminates an entire free surface. Initially the energy of the system is given by,

$$\mathscr{F} = \gamma_1 A + \gamma_2 A = (\gamma_1 + \gamma_2) A \tag{1.1}$$

where $\mathscr{F}$ is the Helmholtz free energy (at constant temperature, pressure, and number of chemical species), and the surface energies of the two surfaces i are denoted γ_i. When joined,

$$\mathscr{F} = \gamma_{12} A \tag{1.2}$$

where γ_{12} is the interfacial energy between the two solids. When $\gamma_{12} < \gamma_1 + \gamma_2$, the formation of the interface is favorable.

One may recall from an introductory physics course that static friction involves the impedance to motion between two objects separated by an interface. The potential energy required to bring a stationary object impeded by static friction out of rest is often orders of magnitude less than γ_{12}, *i.e.* the energy to separate the interfacial area[24]. This difference arises because the surfaces are not ideally smooth, and the heterogeneity prevents intimate contact between the two solids. However, when a liquid contacts a solid surface, typically all the surface area of the solid becomes wet by the liquid, meaning perfect interfacial contact[1]. It is perhaps no surprise then, that the wettability of interfaces plays a large role in their adhesion properties.

1.3 Fundamentals of wettability

Similar to the atoms within solid surfaces mentioned above, liquid molecules also prefer to remain in the bulk, rather than at an interface. Although the units are the same as surface energy, the energy of a liquid surface is typically given in N/m and is thought of as a tension, *i.e.* surface tension (γ_{LV}, where LV denotes liquid-vapor). The surface tension of several liquids (many used in Chapter 5 and 6) is given in Table 1.2.

Table 1.2: The surface tension of the various liquids used in this work. Values are taken from [18, 19].

Liquid	γ_{LV} (mN/m)
Water	72.1
Diidomethane	67.0
Formamide	57.0
Propylene glycol	45.6
Hexadecane	27.5
Decane	23.8
Ethanol	22.1
Polydimethyl siloxane	19.9
Hexane	18.4
Krytox 100	16.0
Methoxyperfluorobutane	13.0

1.3.1 Young's idealization

When a liquid droplet comes into contact with a rigid, solid surface, the angle the droplet adopts at the three-phase (liquid, solid, vapor) contact line is given by a balance of surface forces acting in the plane of the surface (Fig. 1.1). Young first formalized this relation as[25],

$$\cos\theta_Y = \frac{\gamma_{SV} - \gamma_{SL}}{\gamma_{LV}} \tag{1.3}$$

where θ_Y is referred to as the intrinsic contact angle that the liquid, of surface tension γ_{LV}, makes on the solid surface, of surface energy γ_{SV}. γ_{SL} is the solid-liquid interfacial tension. Typically the surface tension of the liquid, and the surface energy of the solid, are known or can be measured, whereas γ_{SL} depends on the exact interactions between the solid and the liquid, necessitating the measurement of θ_Y. Surfaces are termed hydrophilic when $\theta_Y < 90^\circ$ with water, and hydrophobic when $\theta_Y > 90°$ with water. For a smooth surface, the maximum intrinsic contact angle with water is $\theta_Y \approx 120°$, which occurs on a perfluorinated monolayer ($\gamma_{SV} \approx 6$ J/m^2)[11]. For low-γ_{LV} liquids, there are no known materials that exhibit $\theta_Y > 90°$[26].

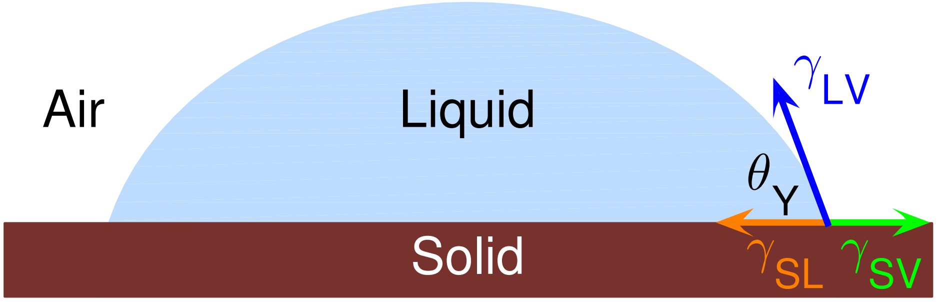

Figure 1.1: A liquid droplet sitting on a smooth, chemically homogeneous surface. The intrinsic contact angle that is adopted, θ_Y, is determined by the balance of the surface forces.

1.3.2 Contact angle hysteresis

θ_Y is an ideal contact angle that is rarely witnessed in practice. Surface roughness, chemical heterogeneity, interactions with the surrounding vapor, viscosity effects, and the composition of the liquid all contribute to what is termed contact angle hysteresis[23]. Contact angle hysteresis is defined as,

$$\Delta\theta = \theta_{adv} - \theta_{rec}. \tag{1.4}$$

θ_{adv} is the maximum possible angle that the liquid adopts on the surface before it advances, *i.e.* before the contact line moves and wets additional area. In contrast, θ_{rec} is the minimum possible angle the droplet assumes before it recedes from the wetted solid. When a droplet is placed on a surface, it will always assume some angle $\theta_{rec} \leq \theta_s \leq \theta_{adv}$, where θ_s is the static contact angle. Although θ_s for small droplets has been shown to approach θ_{adv}[27], it's also been shown that θ_s depends heavily on how the droplet is deposited[28]. Moreover, by definition, θ_s can adopt any value in between θ_{rec} and θ_{adv}. As $\Delta\theta$ can be quite large, proper characterization of a surface should *always* include measurement of both the advancing and receding contact angles. In Chapter 5 we discuss the fabrication and various applications of smooth surfaces exhibiting $\Delta\theta \approx 0°$.

1.3.3 Wenzel's approximation

The effect of roughness on wettability was shown back in the early 1900s to follow what is now referred to as the Wenzel equation[1]:

$$\cos\theta^{*} = r\cos\theta_{Y}, \tag{1.5}$$

where θ^{*} is the apparent contact angle (the macroscopic contact angle observed), and r is the ratio of the actual solid/liquid interfacial area to its projected area (Fig. 1.2a). The Wenzel roughness, r, always assumes a value $r \geq 1.0$.

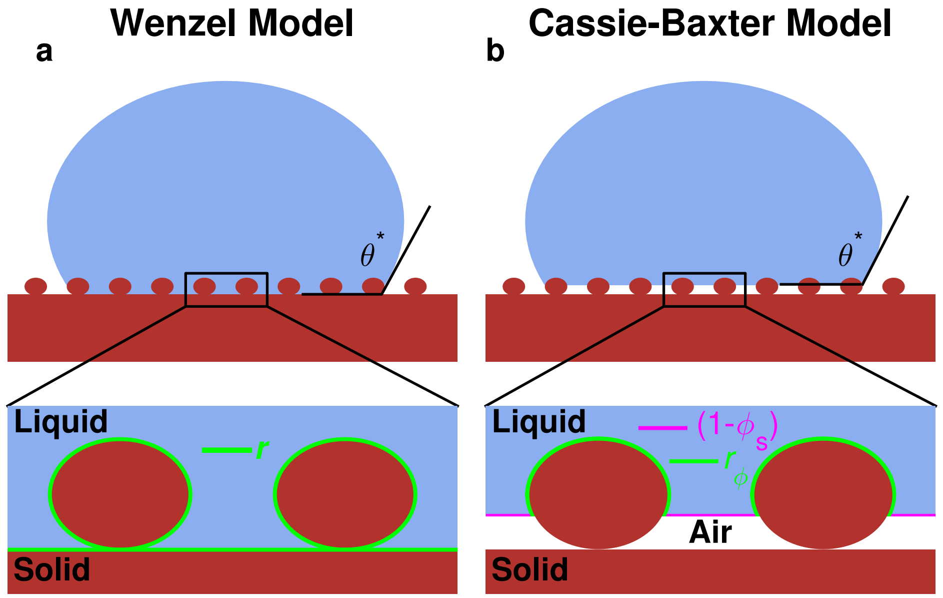

Figure 1.2: The two possible wetting states for a liquid droplet in contact with a solid surface. a, the Wenzel model[1], where the Wenzel roughness, r, is highlighted. b, the composite interface, or the Cassie-Baxter model[2]. Both the fraction of vapor, $(1 - \phi_s)$, and the roughness of the wetted solid, r_ϕ, are highlighted.

Because r is always greater than unity, roughness has the unique property of always enhancing the intrinsic wettability of a given surface. Hydrophilic surfaces become more wettable ($\theta^{*} < \theta_Y$), and hydrophobic surfaces become more hydrophobic ($\theta^{*} > \theta_Y$). However, it should be noted that roughness only alters θ^{*} by increasing $\Delta\theta$, which may not always be favorable. For example, roughening a hydrophobic surface will increase θ^{*} by increasing θ_{adv}, but the additional roughness may decrease θ_{rec}. Static droplets may show higher contact angles, but removing those droplets will be more difficult[29]. Moreover, the Wenzel equation is somewhat limited. For hydrophilic surfaces, combinations of $r\cos\theta_Y \geq 1.0$ yield imaginary contact angles, which are not measurable using the traditional sessile drop method (although other techniques have shown promise[30]). For hydrophobic surfaces exhibiting $r\cos\theta_Y < -1.0$, the Wenzel equation always predicts $\theta^{*} = 180°$.

For such surfaces, though, a different wetting state may be more energetically favorable.

1.3.4 Composite interfaces

Wenzel assumed perfect contact between the liquid droplet and all the surface area of the solid[1]. However, another possible configuration is that pockets of vapor are trapped in between the droplet and the solid surface. Cassie and Baxter were the first to study how such a composite interface affects the apparent contact angle[2]. They proposed,

$$\cos\theta^* = r_\phi \phi_s \cos\theta_Y + (1 - \phi_s)\cos 180^\circ \tag{1.6}$$

where r_ϕ is now strictly the Wenzel roughness of only the fraction of solid in contact with the liquid, ϕ_s (Fig. 1.2b). Liquid droplets assume perfect spheres when free falling (ignoring gravitational effects), and thus the contact angle of air is 180°. Thus, this situation is a special case of the generic formulation for the contact angle of a heterogeneous surface comprised of i distinct patches, with intrinsic contact angles θ_i, Wenzel roughness r_i, and surface fraction ϕ_i[31],

$$\cos\theta^* = \sum r_i \phi_i \cos\theta_i. \tag{1.7}$$

Eq. 1.6 is called the Cassie-Baxter equation and droplets exhibiting such a composite interface are said to be in the Cassie-Baxter state[2]. Dissimilar to the Wenzel state, the Cassie-Baxter state always increases θ^* because it essentially averages an apparent contact angle with the contact angle of air, 180°. However, the pockets of air may be displaced due to pressure[32], and often the Wenzel state is the energetically favorable configuration[33]. Further, even if the Cassie-Baxter state is the global energy minimum, typically some form of energy input is needed to transition the surface from the wetted state to the non-wetted state[34]. But for many applications, high values of θ^*, or pockets of entrapped air, are favorable. As such, maintaining the Cassie-Baxter state over the Wenzel state remains an active area of research.

Contact angle hysteresis for droplets in the Cassie-Baxter state is somewhat different than on fully wetted surfaces. Because pockets of air separate the texture elements of the surface, the liquid advances over the air pockets at $\theta^*_{adv} = 180^\circ$[35], although current goniometric methods make measuring $\theta^*_{adv} > 170^\circ$ difficult[36]. Here I denote the apparent advancing angle of the surface in the non-wetted state with a superscript asterisk (θ^*_{adv}). On an individual texture element that is fully wetted, the liquid still advances at θ_{adv} and locally tries to adopt θ_Y to satisfy Young's relation (Eq. 1.3). Similarly, although locally the liquid dewets from the texture elements at θ_{rec}, macroscopically the angle θ^*_{rec} is observed[27].

The apparent contact angle hysteresis, $\Delta\theta^*$, can be as high as 180° for surfaces in the Cassie-

Baxter state. However, ultra-low values of θ^*_{rec} typically indicate wetting (a transition from the Cassie-Baxter to the Wenzel state locally), and often some areas will become wetted while others remain non-wetted. Researchers have termed this configuration the partially wetted, or impaled state[37]. θ^*_{rec} can also adopt very high values, especially if ϕ_s is low (the droplet mostly contacts air). Increasing θ^*_{rec} while assuming $\theta^*_{adv} \approx 180^\circ$ has the benefit of significantly lowering $\Delta\theta^*$. Many researchers have fabricated surfaces displaying both θ^*_{adv} and $\theta^*_{rec} > 150^\circ$, and $\Delta\theta^* \approx 0^\circ$, with water. Such surfaces are termed superhydrophobic, and exhibit many exciting properties that will be discussed in detail in Chapters 6-8.

1.3.5 Low surface tension liquids

Low-γ_{LV} liquids notoriously spread on all natural surfaces, and are therefore a major source of fouling[26]. Surfaces that can repel such liquids have proven challenging to develop[38]. For smooth surfaces, a liquid will not dewet the surface if $\theta_{rec} = 0^\circ$, which is the case for most solid/low-γ_{LV} liquid combinations. In Chapter 5 we develop omniphobic surfaces, *i.e.* material systems that display non-zero θ_{rec} values and $\Delta\theta \approx 0^\circ$, even for low-$\gamma_{LV}$ liquids. Note that, because smooth surfaces never exhibit $\theta_Y > 90^\circ$ with low-γ_{LV} liquids, the interfacial science community has labeled surfaces with that minimize $\Delta\theta$, rather than maximize θ^*, as omniphobic[19, 39].

Above we stated that a liquid will try to locally maintain θ_Y along the contact line, even if on the macroscale, θ^* is observed. For low-γ_{LV} liquids, however, $\theta_Y < 90^\circ$ always. This means that the liquid will continue to spread on a texture element until θ_Y is achieved along the three-phase contact line (or, at best, until the local contact angle is less than θ_{adv}). If we let ψ be the angle of a texture element, the liquid will always wet the texture if $\psi \geq \theta_Y$[26]. Surfaces exhibiting $\psi \leq 90^\circ$ are termed re-entrant, and have the unique ability of being able to support the Cassie-Baxter state even for low-γ_{LV} liquids. Although a standard value have not been set in the literature, such surfaces are called superoleophobic if they exhibit roughly $\theta^* > 150^\circ$ with oils (typically hexadecane), and moderately low $\Delta\theta^*$. Similarly, surfaces are termed superomniphobic if they exhibit $\theta^* > 150^\circ$ and low $\Delta\theta^*$ with essentially all known liquids. The various terminologies for wettability are summarized in Table 1.3.

We end this section on wettability by noting that, because the surface tension of water (72.1 mN/m) is much greater than low-γ_{LV} liquids (typically 15 - 30 mN/m, Table 1.2), omniphobic and superomniphobic surfaces are typically also hydrophobic and superhydrophobic, respectively. However, many interesting properties have been achieved by counter intuitive surfaces where this is not the case[43, 44].

Table 1.3: The various designations for liquid repellency discussed in this work.

Designation	Repels	θ (°)	$\Delta\theta$ (°)	Examples
Hydrophobic	Water	$\theta_Y > 90°$	-	Polyethylene, Teflon, silicones[23]
Superhydrophobic	Water	$\theta^* > 150°$	$\Delta\theta^* \approx 0°$	Lotus, lucinato kale, and savoy cabbage leaves[40]
Oleophobic	Oils	$\theta^* > 90°$	-	Roughened teflon, perfluorinated lubricant-infused systems[32]
Superoleophobic	Oils	$\theta^* > 150°$	$\Delta\theta^* < 10°^\dagger$	Micro-hoodoos, electrospun systems[41]
Omniphobic	All	-	$\Delta\theta^* \approx 0°$	Liquid-like monolayers, smooth, perfluorinated films[39]
Superomniphobic	All	$\theta^* > 150°$	$\Delta\theta^* < 10°^\dagger$	Hierarchcial perfluorinated re-entrant texture[42]

†A placeholder as no standard value has been formalized by the interfacial science community.

1.3.6 Interfacial slippage

At the solid/liquid interface, the usual boundary condition assumed is that the velocity of the solid matches the velocity of the liquid during flow[45]. As the solid is stationary relative to the flow, this dictates that the fluid is at rest at the solid/liquid interface. This assumption is referred to as the no-slip boundary condition, and is found everywhere from polymer melts[46, 47], to chemical plant design[48], to flows over naval vessels[49]. However, this is not the only possible boundary condition. A non-zero velocity can arise in certain solids, especially those with liquid-like properties[50]. In this work we refer to such a phenomenon as interfacial slippage, and we investigate its usage in a wide range of engineering applications. In Chapters 2 and 3 we discuss how interfacial slippage can be used to reduce ice adhesion. In Chapter 5 we utilize it to fabricate omniphobic surfaces exhibiting extremely low $\Delta\theta$. And we reduce drag in turbulent flow by engendering interfacial slippage in Chapter 8 using superhydrophobic surfaces.

1.4 Adhesion mechanics

In the previous section we discussed the adhesion of liquids to solids. We now move the discussion to solid/solid adhesion, remembering that intimate interfacial contact is typically only achieved using liquids in some way: soldering[51], glue[52], bio-fouling attachment[53], water freezing on a car windshield[54], licking shut an envelope[55], etc. The interfacial adhesion between two solids may be characterized by the shear force, F, that it takes to break the bond of interfacial area (length by width) $L \times w$ (Fig. 1.3),

$$\tau = F/(Lw). \tag{1.8}$$

Here we have characterized the strength of the interface as τ, a shear stress, but the fracture of

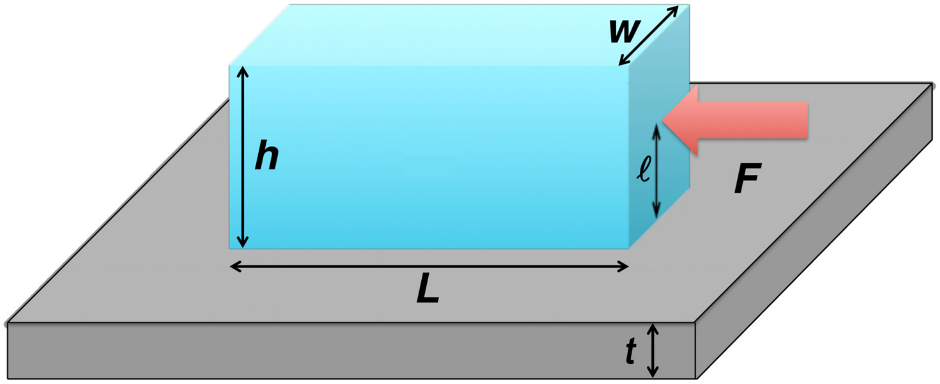

Figure 1.3: A schematic of the various geometric lengths relevant to our discussion on solid/solid adhesion. A force F impacts a solid adhered to a surface of thickness t a height ℓ above the interfacial plane. The solid measures $(L \times w \times h)$ length by width by height.

interfaces is typically a mixed mode problem (normal and shear contributions)[10]. For the purposes of the work described herein, we will first only consider the shear strength of interfaces, and note that the one of the main problems we address in Chapters 2-4, the fracture of adhered ice, is a process dominated by shear. Also note that the above case assumes any initial de-bond of the interface, a, is such that $a \ll L$. It is recognized that interfaces may also be characterized by their toughness, Γ, but we save this discussion for Chapter 4, where we explore the interfacial toughness between ice and a host of different surfaces in more detail.

1.4.1 The work of adhesion

The work of adhesion, W_a, required to dewet a liquid from a solid surface is found by integrating over all receding events occurring at the contact line[23]. It is given by,

$$W_a = \gamma_{LV}(1 + cos\theta_{rec}). \tag{1.9}$$

For many solid/solid interfaces, such as those formed by capillary bridges, the work of adhesion is proportional to the adhesion strength, *i.e.* $\tau \propto W_a$[56]. The main example we will address in Chapters 2-4 is ice adhesion, but many other examples exist, including clathrate hydrate formation[57], pressure sensitive adhesives[55], solder strength[51], barnacle attachment[58], fiber pull-out in fiber-reinforced composites[59], and the drying of paints[60]. Perhaps ironically, much of this work was first formulated to understand why adhesion failed, and how to increase the adhesion strength. In contrast, much of this current work utilizes the same fundamentals, but to reduce unwanted adhesion.

1.4.2 Interfacial cavitation

Interfaces need not fail solely by adhesive strength. Often buckling of the interface can occur from a modulus mismatch between the two surfaces[61]. Consider a rigid block adhered to a soft film. A buckling instability causes the interface to cavitate at a shear stress that goes as[62],

$$\tau = B(W_a G/t)^{1/2}, \tag{1.10}$$

where G is the shear modulus of the film of thickness t, and $B = 1.3(L/\ell)$, where L and ℓ are defined in Fig. 1.3. When the force, F, contacts the rigid block at a plane ℓ above the interfacial plane, a torque is generated that causes hydrostatic tension at the edge of contact, and hydrostatic compression at the opposite end. Whereas the interface could fail by pure shear (Mode-II), the tension generated makes the problem mixed-mode, and now the interface can fail due to normal forces (Mode-I) as well. If an elastic instability develops from the Mode-I component, the interface may cavitate, and the rigid block may be detached at a shear stress much lower than the work of adhesion[62].

1.5 Outline of this thesis

In the following chapter we examine the above scenario, where soft surfaces cavitate, for the case of ice adhesion. We discuss how durable, low ice adhesion materials may be systematically fabricated. We also explore modifying the ice/solid interface through the addition of mobile chains, either covalently attached or un-bonded, to enable interfacial slippage. In Chapter 3 we build a model for interfacial slippage in order to predict and design the ice adhesion strength of any polymeric surface. Chapter 4 explores how interfacial toughness plays a role in controlling ice adhesion. There we show how common materials like engineering plastics can display any possible ice adhesion strength. In Chapter 5 we utilize surfaces exhibiting interfacial slippage to reduce the adhesion of solids other than ice. We also show that these surfaces can display omniphobicity, and we begin our discussion of liquid-repellent surfaces there.

Chapter 6 investigates fabricating some of the first superomniphobic surfaces that are also optically transparent. We then tackle the issue of the mechanical durability of superhydrophobic surfaces in Chapter 7. We present new design parameters that will allow researchers to fabricate extremely mechanically robust superhydrophobic surfaces from a wide range of starting components. Finally, we utilize some of these mechanically superior superhydrophobic surfaces to reduce the friction drag experienced during turbulent flow. The discussion comes full circle, as the underlying mechanism allowing for the drag reduction turns out to be interfacial slippage, the very same slippage causing the low ice adhesion observed in Chapter 2.

CHAPTER 2

Designing Durable Icephobic Surfaces

2.1 Introduction

Ice accretion and its subsequent removal is a safety hazard for aircraft, power lines, motor vehicles, marine structures, communication towers, and wind turbines[8]. The most common methods for ice removal are extremely energy intensive[56], and there exists a strong need to develop methods where ice is passively removed from a surface (*i.e.* no external energy input)[63].

Previously, there have been numerous publications related to developing icephobic' surfaces[56, 63, 64, 65, 66, 67, 3, 68, 69, 70, 71, 72]. Such surfaces utilize different approaches including, delaying droplet freezing time[65, 72, 73, 74], preventing frost formation[66, 3, 71] and lowering the ice adhesion strength, τ_{ice}[56, 64, 66, 67, 3, 68, 69, 70, 72, 75]. Icephobic surfaces can be defined by an ice adhesion strength $\tau_{ice} < 100$ kPa[72]. In comparison, structural materials like aluminum or steel have extremely high τ_{ice}, around 1600 and 1400 kPa, respectively[63]. However, to passively remove ice with no external energy input, such as on airplane wings, power lines, or boat hulls, extremely low values of τ_{ice} are required. For example, Dou *et al.* found that a strong breeze detached ice when $\tau_{ice} \leq 27 \pm 6$ kPa[75].

Previous work has shown that on many different high modulus solids,

$$\tau_{ice} = B\gamma_{LV}(1 + \cos\theta_{rec}), \tag{2.1}$$

where B is an experimental constant, γ_{LV} is the surface tension of water and θ_{rec} is the receding water contact angle[56]. Effectively, $\tau_{ice} \propto W_a$ (Eq. 1.9), and B accounts for the geometry of the setup. For non-textured surfaces, this provides a theoretical lower limit of $\tau_{ice} \approx 150$ kPa (as the maximum $\theta_{rec}^{max} \approx 120°$)[11]. Superhydrophobic surfaces display an ultra-high θ_{rec}^{*} through the incorporation of texture, and have been shown to possess τ_{ice} as low as 50 kPa. However, an increasing body of work suggests that even these moderately low ice adhesion values cannot be maintained due to condensation and frost formation[65, 66, 72, 74, 73, 76]. To date, the lowest ice adhesion values have only been reported using lubricants ($\tau_{ice} = 16$ kPa) or gels ($\tau_{ice} =$

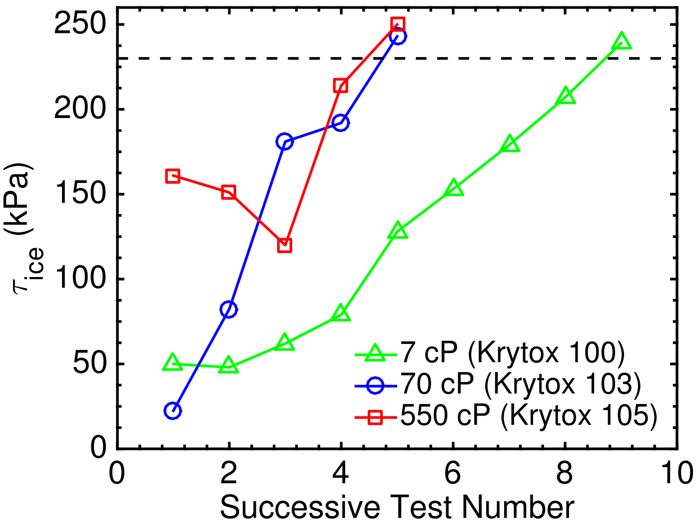

Figure 2.1: Variation of τ_{ice} with the number of icing / deicing cycles for SLIPS-based[3] icephobic surfaces. The dotted line represents τ_{ice} for the surface without oil.

0.4 kPa) [3, 19, 77, 78]. Lubricated surfaces purportedly achieve low ice adhesion by minimizing $\Delta\theta$ through the formation of a low surface energy (typically highly fluorinated) lubricating free-oil layer. But again, the icephobicity for such surfaces can be short-lived, once the oil has been displaced and removed by water droplets[67], frost[71] or during accreted ice removal (Fig. 2.1). Overall, there are no reports of durable icephobic surfaces that maintain or even exhibit $\tau_{ice} < 15$ kPa.

In this work we study the ice adhesion of elastomers. Elastomers are viscoelastic, *i.e.* they can demonstrate both solid-like and liquid-like properties. We control the viscoelastic nature of our elastomers in two ways. First, we modify the crosslink density, ρ^{CL}, of our elastomers to alter their physical stiffness ($G = RT\rho^{CL}$ assuming isotropy, where G is the shear modulus, T is the temperature, and R is the universal gas constant). Recall Eq. 1.10 from Sec. 1.4.2, where $\tau \propto G^{1/2}$. This is a macroscopic relationship that predicts the shear stress required to cleave two surfaces apart, a process that occurs through interfacial cavitation[62, 79].

Second, we alter the no-slip boundary condition[52] at the ice-elastomer interface through the addition of uncrosslinked, polymeric chains. In solid-solid contact, conservation of momentum usually dictates that the velocity at the interface is zero, or equivalently that there is no slip. However, if the polymeric chains within the elastomer are sufficiently mobile, slippage (*i.e.* a non-zero slip velocity) can occur at the solid-solid interface, as has been observed previously for polymer melts[79, 46], adhesives[52] and rubbers[79]. When a hard surface slides over a soft elastomer,

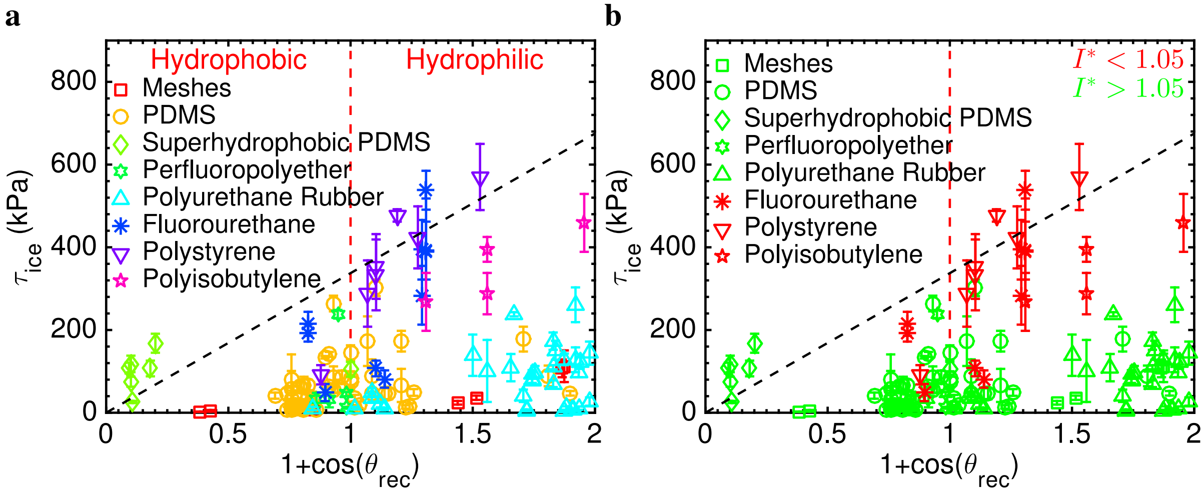

Figure 2.2: Surface chemistry independence. a, The various icephobic surfaces fabricated in this work. It is clear that most of the fabricated surfaces do not follow the theoretical $\tau_{ice} \propto 1 + \cos\theta_{rec}$ trend. For example, for coating AY (Table 2.1), $\tau_{ice} = 27 \pm 10$ kPa, although $\theta_{rec} = 12°$. b, When recolored using the developed I^* parameter (with a cutoff of $I^* = 1.05$, discussed later), it is apparent that the linear trend between ice adhesion and surface energy only applies for high modulus ($I^* < 1.05$) elastomers without interfacial slippage.

such as during interfacial slippage, the shear stress to slip at the interface is given by,

$$\tau = Gfa/kT \qquad \text{or} \qquad \tau \propto G^1. \tag{2.2}$$

Here f is the force required to detach a single chain of segmental length a, and k is Boltzmann's constant[6, 50]. By tailoring ρ^{CL} for different elastomeric coatings, and by additionally embedding miscible, polymeric chains to enable interfacial slippage, here we show that it is possible to systematically design icephobic coatings with extremely low ice adhesion ($\tau_{ice} < 0.2$ kPa). Overall, we've designed a comprehensive library of over 100 icephobic surfaces that can be rough, smooth, hydrophobic, or hydrophilic, as shown in Fig. 2.2 (also see Table 2.1). It is clear from Fig. 2.2 that the variations in τ_{ice} for the different icephobic coatings developed in this work cannot be explained by variations in the parameter $(1 + \cos\theta_{rec})$. For soft surfaces, this is because the interface either cavitates or slips at a force lower than that required by the work of adhesion[62].

Table 2.1: A library of icephobic surfaces. The coating fabrication methodology, resulting ice adhesion strengths, cross-link densities, and water contact angles for all the samples fabricated in this work. SG, Sylgard; SO, silicone oil; PS, polystyrene; PIB, polyisobutylene; PFPE, perfluoropolyether; FPU, fluorinated polyurethane polyol; PMPS, poly-methylphenyl siloxane; RT, room temperature; NS, no slippage (no oil was added to the coating); IS, interfacial slippage (miscible oil was added but no lubricating liquid layer formed) [confirmed by atomic force microscopy (AFM), optical microscopy, and the shape of the force versus time curves]; L, lubricated [excess oil (either intentionally or otherwise) was added to the coating, which formed a thick lubricating layer] (confirmed using the same methods as for interfacial slippage).

	Polymer base	Nonreactive oil	wt %	Reactive oil	wt %	Cure (°C/hour)	ρ^{CL} (mol/m^3)	τ_{ice} av. (kPa)	τ_{ice} min. (kPa)	τ_{ice} max. (kPa)	Type	$\theta_{adv}/\theta_{rec}$ (°)
A	SG 184 10:1	-	-	-	-	150/24	307 ± 8	264	245	340	NS	120/94
B	SG 184 10:1	-	-	-	-	80/2	333 ± 45	47	36	57	IS	131/26
C	SG 184 20:1	-	-	-	-	80/2	112 ± 1	178	147	251	NS	129/45
D	SG 184 4:1	-	-	-	-	80/2	33 ± 45	89	42	165	IS	127/36
E	SG 184 3:1	-	-	-	-	80/2	268 ± 2	15	6	29	L	122/76
F	SG 184 2:1	-	-	-	-	80/2	222 ± 9	14	6	23	L	118/77
G	SG 184 5:2	-	-	-	-	80/2	267 ± 21	16	8	26	L	112/100
H	SG 184 1:1	-	-	-	-	80/2	162 ± 5	14	6	29	L	112/89
I	SG 184 10:1	100cP SO	25	-	-	80/2	219 ± 13	35	26	56	IS	123/89
J	SG 184 10:1	100cP SO	50	-	-	80/2	72 ± 11	87	40	120	IS	114/94
K	SG 184 10:1	100cP SO	75	-	-	80/2	-	55	30	71	IS	114/94
L	SG 184 10:1	-	-	PMHS	25	80/2	215 ± 10	10	1	31	L	105/103
M	SG 184 10:1	-	-	PMHS	50	80/2	75 ± 13	67	31	121	IS	118/101
N	SG 184 10:1	-	-	PMHS	75	80/2	-	17	5	39	L	121/102
O	SG 184 1:1	100cP SO	25	-	-	80/2	32 ± 2	173	58	237	IS	124/86
P	SG 184 1:1	100cP SO	50	-	-	80/2	13 ± 2	46	17	74	IS	124/8S
Q	SG 184 1:1	100cP SO	75	-	-	80/2	-	18	0.15	47	IS	104/103
R	SG 184 1:1	-	-	PMHS	25	80/2	102 ± 5	17	1	40	L	125/104
S	SG 184 1:1	-	-	PMHS	50	80/2	14 ± 4	6	1	30	L	106/105
T	SG 184 1:1	-	-	PMHS	75	80/2	-	9	0.4	31	L	105/103
U	SG 184 10:1	100cP SO	25	PMHS	25	150/24	536 ± 97	64	50	78	IS	119/95
V	SG 184 10:1	100cP SO	15	PMHS	15	80/2	-	31	1	137	L	108/104
W	SG 184 10:1	100cP SO	10	PMHS	10	150/24	459 ± 9	74	40	116	IS	123/90
X	SG 184 10:1	-	-	PMHS	10	80/2	283 ± 9	37	4	71	IS	114/100
Y	SG 184 10:1	-	-	PMHS	10	150/24	284 ± 41	173	122	234	NS	121/78
Z	SG 184 10:1	-	-	PMHS	20	80/2	197 ± 4	45	19	82	IS	109/105
AA	SG 184 10:1	-	-	PMHS	20	150/24	348 ± 28	64	34	92	IS	118/93
BB	SG 184 10:1	-	-	PMHS	25	150/24	452 ± 9	302	275	346	NS	103/84
CC	SG 184 10:1	100cP SO	25	PMHS	15	150/24	405 ± 27	58	41	73	IS	112/104
DD	SG 184 10:1	100cP SO	20	PMHS	20	80/2	107 ± 2	37	9	67	IS	109/100
EE	SG 184 10:1	100cP SO	25	PMHS	25	80/2	150 ± 8	35	5	77	IS	116/99
FF	SG 184 10:1	100cP SO	25	PMHS	10	150/24	290 ± 25	41	24	55	IS	121/90
GG	SG 184 10:1	5cP SO	25	-	-	80/2	181 ± 5	145	109	178	IS	121/90
HH	SG 184 10:1	1000cP SO	25	-	-	80/2	153 ± 7	45	33	53	IS	100/85
II	SG 184 10:1	10000cP SO	25	-	-	80/2	67 ± 2	81	13	226	L	120/104
JJ	SG 184 10:1	SO AP 1000	25	-	-	80/2	216 ± 3	66	12	171	L	113/78
KK	SG 527	-	-	-	-	150/24	0.68	14	8	25	NS	130/89
LL	1:9 SG 527:184	100cP SO	25	-	-	150/24	182 ± 11	14	7	18	IS	112/103
MM	1:3 SG 527:184	100cP SO	25	-	-	150/24	123 ± 2	10	6	17	IS	111/104
NN	1:1 SG 527:184	100cP SO	25	-	-	150/24	76 ± 1	9	6	12	IS	112/102
OO	3:1 SG 527:184	100cP SO	25	-	-	150/24	46 ± 2	6	4	8	IS	114/101
PP	3:1 SG 527:184	-	-	-	-	150/24	50 ± 2	10	4	49	IS	123/100
QQ	1:3 SG 527:184	-	-	-	-	150/24	104 ± 4	141	130	154	NS	122/95
RR	1:1 SG 527:184	-	-	-	-	150/24	110 ± 5	19	7	37	IS	117/88

	Polymer base	Nonreactive oil	wt %	Reactive oil	wt %	Cure (°C/hour)	ρ^{CL} (mol/m^3)	τ_{ice} av. (kPa)	τ_{ice} min. (kPa)	τ_{ice} max. (kPa)	Type	$\theta_{adv}/\theta_{rec}$ (°)
SS	9:1 SG 527:184	100cP SO	25	-	-	150/24	8.0 ± 0.8	6	4	7	IS	121/98
TT	9:1 SG 527:184	-	-	-	-	150/24	9.1 ± 0.9	134	132	139	NS	121/96
UU	PFPE	-	-	-	-	0.1	160 ± 35	238	200	281	NS	115/93
VV	PFPE	Krytox 100	25	-	-	0.1	96 ± 24	31	17	53	IS	115/95
WW	PFPE	Krytox 105	25	-	-	0.1	124 ± 33	31	16	55	IS	104/98
XX	PFPE	Krytox 103	25	-	-	0.1	-	12	10	13	IS	114/91
YY	PFPE	-	-	CN4002	10	0.1	-	45	33	51	L	117/91
ZZ	FPU	-	-	-	-	80/72	1098 ± 98	538	257	627	NS	103/72
AB	FPU	-	-	-	-	80/72	475 ± 14	394	334	479	NS	105/73
AC	FPU	-	-	-	-	80/72	316 ± 17	284	204	399	NS	101/73
AD	FPU	Krytox 100	25	-	-	80/72	1142 ± 158	595	538	713	IS	101/72
AE	FPU	Krytox 105	25	-	-	80/72	1112 ± 77	392	283	520	IS	105/72
AF	FPU	-	-	NCO C50	75	150/24	1332 ± 48	246	194	320	IS	108/84
AG	FPU	100cP SO	5	NCO C50	75	80/72	-	82	61	100	IS	109/82
AH	FPU	100cP SO	10	NCO C50	75	80/72	-	49	22	66	IS	106/96
AI	PS	-	-	-	-	RT/24	447,000	336	189	370	NS	97/86
AJ	PS	200 M_w PS	25	-	-	RT/24	-	424	271	569	IS	103/74
AK	PS	200 M_w PS	50	-	-	RT/24	-	570	378	642	IS	109/58
AL	PS	540 M_w PS	25	-	-	RT/24	-	477	454	510	IS	100/79
AM	PS	SO AP 1000	25	-	-	RT/24	-	92	59	112	L	103/97
AN	PS	PMPS	10	-	-	RT/24	-	354	218	491	IS	98/84
AO	PS	PMPS	5	-	-	RT/24	-	333	217	498	IS	99/84
AP	PIB	-	-	-	-	RT/24	8,000	395	335	453	NS	125/56
AQ	PIB	Polybutene	25	-	-	RT/24	-	288	220	419	IS	128/56
AR	PIB	Polybutene	50	-	-	RT/24	-	459	341	620	IS	130/71
AS	PIB	Polybutene	75	-	-	RT/24	-	268	176	442	IS	128/72
AT	Vytaflex 10	-	-	-	-	RT/24	26 ± 7	144	84	254	NS	52/12
AU	Vytaflex 40	-	-	-	-	RT/24	95 ± 14	151	118	192	NS	80/26
AV	Vytaflex 60	-	-	-	-	RT/24	290 ± 17	261	157	360	NS	82/23
AW	Vytaflex 40	Vegetable	20	-	-	RT/24	53 ± 4	11	5	22	L	68/21
AX	Vytaflex 40	Cod liver	15	-	-	RT/24	29 ± 2	27	9	51	IS	75/12
AY	Vytaflex 40	100cP SO	10	-	-	RT/24	-	41	18	83	L	82/45
AZ	Vytaflex 40	-	-	NCO Di-50	1	RT/24	47 ± 3	109	51	179	IS	96/49
BA	Vytaflex 40	-	-	NCO Di-50	5	RT/24	52 ± 2	101	42	232	IS	110/56
BB	Vytaflex 40	-	-	NCO Di-50	10	RT/24	34 ± 7	139	49	243	IS	113/60
BC	Vytaflex 40	100cP SO	10	NCO Di-100	50	RT/24	21 ± 1	11	6	15	IS	97/89
BD	Vytaflex 40	-	-	NCO Di-50	50	RT/24	42 ± 0.4	44	25	55	IS	106/81
BE	Vytaflex 40	100cP SO	5	NCO Di-50	50	RT/24	-	36	18	57	IS	100/85
BF	Vytaflex 40	100cP SO	10	NCO Di-50	50	RT/24	-	11	6	17	IS	95/86
BG	Vytaflex 40	-	-	NCO Di-50	75	RT/24	171 ± 4	49	38	65	IS	102/85
GH	Vytaflex 40	100cP SO	10	NCO Di-50	75	RT/24	-	9	3	12	IS	91/82
BI	Vytaflex 40	1000cP SO	10	NCO Di-50	75	RT/24	-	10	5	14	IS	99/90
BJ	Vytaflex 40	5cP SO	10	NCO Di-50	75	RT/24	-	18	12	24	IS	102/83
BK	Vytaflex 40	10000cP SO	10	NCO Di-50	75	RT/24	-	19	14	31	IS	102/92
BL	Vytaflex 40	100cP SO	5	-	-	RT/24	-	77	70	90	L	70/42
BM	Vytaflex 40	100cP SO	10	-	-	RT/24	-	80	58	91	L	68/42
BN	Vytaflex 40	100cP SO	15	-	-	RT/24	-	98	68	128	L	65/41
BO	Vytaflex 40	100cP SO	20	-	-	RT/24	-	93	76	107	L	67/42
BP	Vytaflex 40	Vegetable	5	-	-	RT/24	62 ± 2	128	77	200	IS	79/23
BQ	Vytaflex 40	Vegetable	10	-	-	RT/24	62 ± 4	238	233	247	IS	89/48
BR	Vytaflex 40	Vegetable	15	-	-	RT/24	49 ± 2	121	91	151	IS	32/20
BS	Vytaflex 40	Vegetable	20	-	-	RT/24	53 ± 4	173	141	227	IS	43/34
BT	Vytaflex 40	Cod liver	5	-	-	RT/24	-	129	107	166	IS	67/29

	Polymer base	Nonreactive oil	wt %	Reactive oil	wt %	Cure (°C/hour)	ρ^{CL} (mol/m^3)	τ_{ice} av. (kPa)	τ_{ice} min. (kPa)	τ_{ice} max. (kPa)	Type	$\theta_{adv}/\theta_{rec}$ (°)
BU	Vytaflex 40	Cod liver	10	-	-	RT/24	-	70	56	85	IS	59/34
BV	Vytaflex 40	Cod liver	15	-	-	RT/24	-	110	100	120	IS	46/34
BW	Vytaflex 40	Cod liver	15	-	-	RT/24	29 ± 2	4	2	9	IS	43/25
BX	Vytaflex 40	Cod liver	20	-	-	RT/24	52 ± 1	11	3	15	IS	88/44
BY	Vytaflex 40	Safflower	2.5	-	-	RT/24	63 ± 0.5	30	20	43	IS	100/32
BZ	Vytaflex 40	Safflower	5	-	-	RT/24	50 ± 0.5	11	9	16	IS	82/28
CA	Vytaflex 40	Safflower	10	-	-	RT/24	45 ± 5	6	4	12	IS	72/24
CB	Vytaflex 40	Safflower	15	-	-	RT/24	33 ± 1	4	1	7	IS	67/29
CC	Vytaflex 40	Safflower	20	-	-	RT/24	32 ± 0.4	6	3	11	L	56/44
CD	Vytaflex 40	Safflower	25	-	-	RT/24	45 ± 2	4	2	6	L	52/43
CE	Vytaflex 40	Cod liver	20	-	-	RT/24	-	97	76	114	L	34/21

Coatings AB - AH, AX - AZ, BD - BJ, and BW - CD were dropcast (500 mg/mL). All others are spin-cast at 1500 rpm for 60 s (200 mg/mL). The ρ^{CL} of coatings AI and AP were approximated from the elastic modulus. Coatings UU - YY are UV cured.

2.2 Materials and methods

2.2.1 Experimental design

The objective of this study was to understand the ice adhesion of elastomers, both with and without interfacial slippage. The materials were chosen to span a wide range of chemistries and mechanical properties. The evaluation of these materials involved characterizing their ice adhesion strengths, their mechanical properties, and their resultant durability. The ice adhesion measurements were designed such that an increase in ice adhesion due to repeated icing/de-icing cycles could be observed. The durability characterizations were designed such as to provide a wide range of potentially damaging exposures. By evaluating durability always with respect to ice adhesion, the potential for misrepresenting icephobic durability was avoided.

2.2.2 Synthesis

Polydimethyl siloxane (Sylgard 184 or Sylgard 527, Dow Corning), silicone oil (5 cP - 10,000 cP, Sigma Aldrich) and polymethylhydrosiloxane (PMHS, Sigma Aldrich) were used as received. Sylgard 184 is crosslinked in a 10:1 base:crosslinker ratio, and Sylgard 527 in a 1:1 ratio, per supplier instructions. The crosslinker for both of these products contains a copolymer of PDMS and PMHS, effectively controlling the crosslink density, ρ^{CL}. Previous work has shown how mixing these two formulations can alter ρ^{CL} without deviating from stoichiometry[80]. To increase ρ^{CL}, PMHS can be added along with a high temperature (150 °C) cure. Curing at 80 °C results in PMHS not effectively crosslinking within the PDMS elastomer, acting as a lubricant. To differentiate this effect, samples were either cured at 80°C for a minimum of 2h, or 150 °C for 24h. To create PDMS filled with 25 wt% silicone oil while maintaining the same modulus as Sylgard 184, 10 wt% PMHS was required. To create a low ρ^{CL} PDMS with every chain chemically crosslinked, we used solvent extraction with toluene over a two week period in order to fully remove any uncrosslinked chains. Excess toluene was changed out daily. Without such an arduous step, PDMS contains ≈4% uncrosslinked chains which act as lubricants[81] (Fig. 2.1). To spin-coat these surfaces, solutions at a polymer concentration of 200 mg/mL were formed in hexane. Silicon wafers were rinsed with acetone and were then spincast with the different solutions at 1500 rpm for 60 s, followed by curing. For the dip-coated meshes, the substrates were submerged in the same 200 mg/mL solutions for 45 min and blown dry to avoid pore clogging, followed by the same curing recipe as above.

Perfluoropolyether (PFPE, Sartomer 4002) was crosslinked using 354 nm ultraviolet light under nitrogen with 1% 2-hydroxy-2-methyl propiophenone (Sigma Aldrich) as the photoinitiator. SLIPS surfaces were recreated using published methods[3]. Fluorinated polyurethane (FPU, Fluonova) was crosslinked using 8 wt% 1,6-hexamethylene diisocyanate per manufacturer instructions. Krytox 100, 103, and 105 were purchased from Dupont and up to 25 wt% was added to the different polymers. The FPU was also crosslinked using an isocyanate functionalized PDMS (Silmer NCO Di-100, Siltech) at a crosslinker ratio of 75/25 wt%. To this was added 100 cP silicone oil. Solutions were mixed in Vertel-XF or chloroform at a concentration of 200 mg/mL. Vertrel XF is a non-ozone depleting fluoro-solvent that has replaced Asahiklin 225. Si wafers were rinsed with acetone and the solutions were spincast at 1500 rpm for 60 s, followed by curing at 80 °C overnight.

The polyurethane rubber samples with known modulus (Smooth-On Inc.) were mixed at a 1:1 base:crosslinker ratio per instructions. For lubricated samples, the oil (vegetable oil-Kroger, cod liver oil-Fisher, 100 cP silicone oil-Sigma Aldrich, safflower oil-Jewards International, or isocyanate-functionalized silicone oil-Silmer NCO Di-50) was added at levels of 1, 5, 10, 15, or 20 wt%. The rubber was cured at room temperature overnight. This rubber was altered using a 50/50 wt% ratio of the rubber crosslinker and an isocyanate functionalized PDMS (Silmer NCO Di-100, Siltech) in order to improve silicone oil miscibility. The ρ^{CL} of the urethanes was altered by varying either the type of isocyanate crosslinker, the urethane index and/or through the addition of oil. Films were produced by either spin coating or dip coating glass slides in chloroform solutions at a solute concentration of 200 mg/mL, or spray-coating (500 mg/mL) or drop-casting without dilution.

Polystyrene (PS, $M_w = 190,000$, Scientific Polymer) was dissolved in toluene at a concentration of 200 mg/mL and to it was added silicone oil (AP 1000, Sigma Aldrich), polymethylphenyl siloxane (PMPS, Sigma Aldrich), or low molecular weight PS ($M_w = 200$ or 540 g/mol, Scientific Polymer). Polyisobutylene (PIB, $M_w = 400,000$ g/mol, Scientific Polymer) was dissolved in heptane at a concentration of 200 mg/mL and to it was added polybutene ($M_n \approx 920$ g/mol, Sigma Aldrich). Both PIB and PS samples were spin-cast using the same recipe as above, and then cured at room temperature for 24 h. See Table 2.1 for a complete list of fabrication recipes and resulting

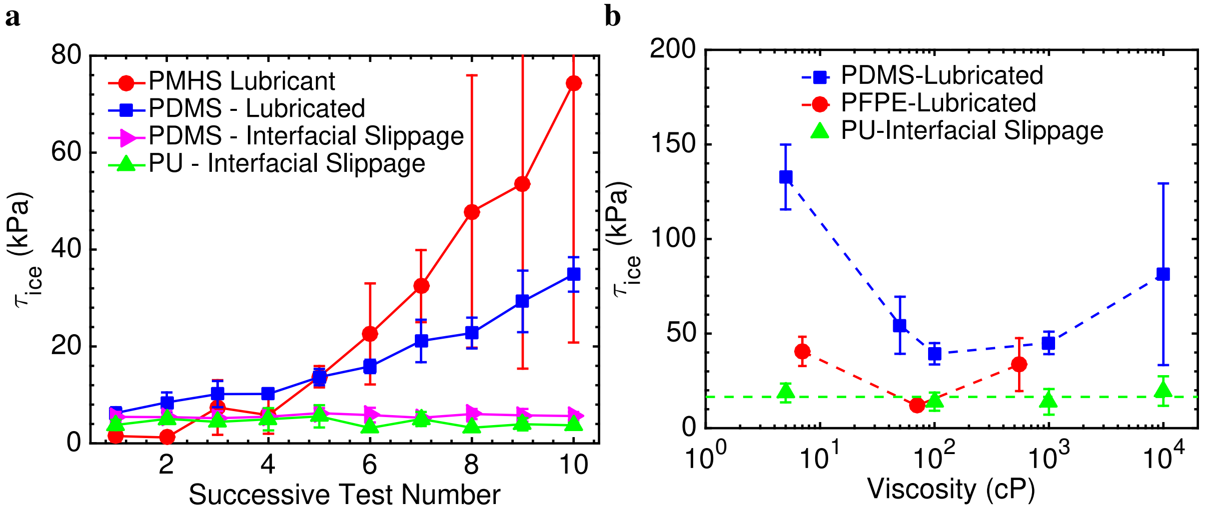

Figure 2.3: Comparison between interfacial slippage and lubrication. a, Variation of τ_{ice} with the number of icing/deicing cycles. The values of τ_{ice} for both the lubricant and the lubricated systems increase with an increasing number of icing/deicing cycles. In comparison, there is no change in τ_{ice} values for the surfaces with interfacial slippage over multiple icing/deicing cycles. b, Variation in τ_{ice} with oil viscosity. Values of τ_{ice} for lubricated surfaces strongly depend on the oil viscosity and follow a typical Stribeck relationship[4]. In comparison, the values of τ_{ice} for surfaces with interfacial slippage are markedly independent of viscosity (coatings BH, BI, BJ, and BK in Table 2.1).

surface properties.

To fabricate the surfaces for determining I^*, elastomers were made with and without oil, modifying one of the two surface such that the crosslink densities matched to within 5% error. For example, the FPU with oil displayed a lower ρ^{CL} than the FPU without oil. As such, we varied the ratio of different hexamethylene diisocyanate crosslinking agents until the desired crosslink density was achieved. Similar methods were used for PDMS (explained above) and PU samples.

For Fig. 2.3a, the lubricant surface is fabricated by spin-casting PMHS onto a Si wafer at 1500 rpm from a 200 mg/mL solution in toluene. The lubricated surface is PDMS with a free layer of silicone oil (50 wt%, 100 cP) on the surface. The oil is added post-cure to ensure a thick, liquid layer remains present on the surface. For Fig. 2.3b this same methodology is used with oils of varying viscosity, 5 cP - 10,000 cP for silicone oils in PDMS, and 7 cP - 550 cP Krytox oils in PFPE.

To fabricate a hard, hydrophobic layer, the FPU was spincast with 20 wt% fluorodecyl-POSS, creating a smooth, low surface energy film. Whereas pure, spincast fluorodecyl-POSS results in a relatively rough surface (due to crystallization), a 20 wt% film within the FPU is smooth and exhibits a surface energy of 11 mN/m, close to the surface energy of pure fluorodecyl-POSS[26]. The model superhydrophobic surface was the commercial product NeverWet (Rustoleum Inc.) and was sprayed on glass slides per instructions. The 2-part commercial icephobic coating R-2180

(Nusil Inc.) was dipped out of a hexane solution (1:1 ratio) at a concentration of 1000 mg/mL. The two silanized surfaces were Si wafers treated with either 1H,1H,2H,2H heptadecafluorodecyl-trichlorosilane (Gelest Inc.) or K13, a chlorine-terminated PDMS ($M_w = 2,000 - 4,000$, Gelest Inc.).

2.2.3 Photolithography

A 3 μm thick layer of photoresist (SPR 220-3.0, Shipley) was spin-coated on a silicon wafer and baked for 90 s at 115 °C. The lateral layouts of the micropattern were defined by 365 nm UV exposure (Karl Suss MA6 mask aligner) and developing in AZ300 MIF. Inductively coupled plasma reactive-ion etching (ICP-RIE, STS Pegasus) formed ≈ 30 μm and 75 μm deep micropore arrays in the exposed regions, and the photoresist was stripped (Baker PRS 2000). To construct pillars of a precise thickness, two methods were adopted. For thick substrates, the uncured PDMS was poured onto the Si mold, degassed, and cured. For thin substrates, the uncured PDMS was spincast on the Si mold at 5,000 rpm, for 60 s with a ramp rate of 5 s. Glass slides were then placed atop the spin-cast layer. The PDMS was degassed to remove air bubbles between the glass slide and mold, and finally the whole system was cured.

2.2.4 Ice adhesion evaluation

The ice adhesion strength, τ_{ice}, was measured using a custom setup described previously[56]. Briefly, a force gauge was mounted to a movable stage. The gauge pushes the ice adhered to a substrate on top of a Peltier plate. The thickness of ice is 5-8 mm whereas the gauge contacts the surface < 1 mm from the surface. Testing was done at -10 °C except for a temperature study done between -5 °C and -35 °C. 0.5 mL of water was used for all testing. Surfaces are allowed sufficient time to fully freeze before testing. For smooth coatings, τ_{ice} was found to be independent of the time between the water freezing completely, and the ice being sheared off. τ_{ice} is the maximum force required to shear off a given area of ice. Force vs. time curves were acquired for surfaces with $\tau_{ice} < 250$ kPa by a Mark-10 force gauge which has a minimum resolution of .0005 N. With this gauge, a τ_{ice} as low as 1.0 kPa can be measured with an accuracy of $\pm.05$ kPa. An Imada force gauge was used for surfaces with $\tau_{ice} < 250$ kPa, which has a resolution of 0.1 N.

2.2.5 Outdoor testing and evaluation at the U.S. Army's CRREL

We coated the right half of a license plate with our icephobic PDMS ($\rho^{CL} = 102 \pm 5$ mol/m^3, 25 wt% PMHS), and placed it outside during February 2013. Freezing rain occurred on the night of the 26th, and the plate was imaged the following morning. The uncoated side showed significant

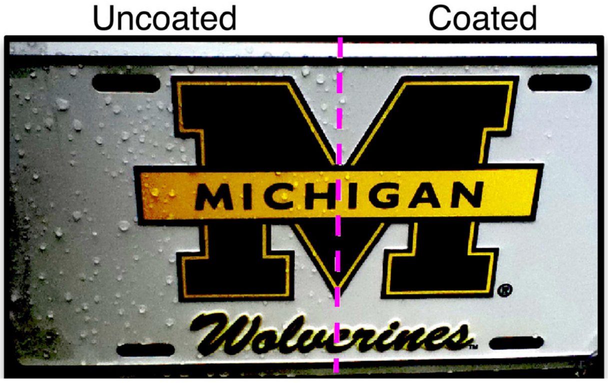

Figure 2.4: A half-coated license plate during outdoor winter 2013 testing, with ice only accreted on the uncoated side.

ice accretion, whereas all accreted ice on the coated side sheared off during the ice storm (Fig. 2.4). Between December and March 2014, two glass panels (1 ft^2) were placed outdoors, one of them coated with our icephobic PDMS ($\rho^{CL} = 76 \pm 1$ mol/m^3, 25 wt% silicone oil).

CRREL samples included a low ρ^{CL} PDMS coating ($\rho^{CL} = 110 \pm 5$ mol/m^3), a low ρ^{CL} PDMS coating containing 25 wt% silicone oil ($\rho^{CL} = 76 \pm 1$ mol/m^3), our polyurethane containing 15 wt% safflower oil ($\rho^{CL} = 52 \pm 1$ mol/m^3), and our PDMS-modified polyurethane containing 10 wt% silicone oil ($\rho^{CL} = 21 \pm 1$ mol/m^3). The CRREL ice adhesion setup involves aluminum tabs with an area of ice ≈ 10 cm^2[9]. Ice is grown from starter crystals under precisely controlled environmental conditions. A starter crack is formed at the base of the specimen and then the ice is pulled in a direction normal to the surface plane. In this way, Mode-I type fracture is evaluated.

2.2.6 Degree of crosslinking determination

Swelling studies were performed using toluene and acetone as the probe solvents. Substrates were submerged in excess solvent until a constant mass was achieved. Fully swollen substrates were patted dry prior to measurement to minimize any errors due to evaporation. Large enough substrates were used so that the error associated with evaporated toluene vapor was $< 2\%$. Swollen samples were placed in an 80 °C oven under vacuum to remove the toluene until the mass remained constant. In this manner the extractable and permanent mass content could be discerned[82]. Flory-Huggins interaction parameters for the FPU, PFPE, and PU were estimated by determination of their solubility parameter by swelling in a large number of solvents, as explained elsewhere[5] (Fig. 2.5).

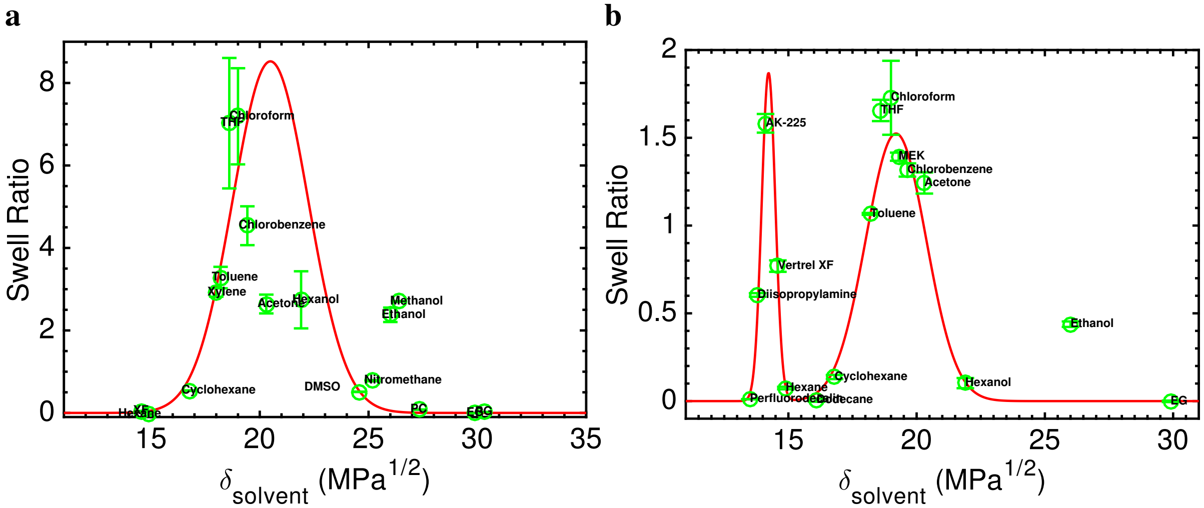

Figure 2.5: Elastomer solubility parameter determination. a, Equilibrium swell ratios for the PU as a function of the probe solvent's solubility parameter, $\delta_{solvent}$. The data is fitted to a Gaussian. b, Equilibrium swell ratios for the FPU as a function of $\delta_{solvent}$. The data is fitted to a bi-modal Gaussian, accounting for the swelling of the fluorinated and urethane components independently. The peak around 19 MPa$^{1/2}$ is characteristic of the urethane bond[5]

2.2.7 Mechanical characterization

To make dog-bone specimens, the uncured material (PDMS, FPU or PU) was poured on fluorosilanized glass panels 1 ft × 1 ft in area. For PDMS and PU, no solvent was added as the viscosity was low enough to produce smooth puddles of the liquid polymer. To the FPU was added 1 mL n-butyl acetate (Sigma Aldrich) per 5 g FPU polyol and crosslinker. Once cured, dog-bone samples with dimensions outlined in ASTM D412, Die D were stamped out[83]. Tensile testing was done on a MTS Insight 10 using a 10 kN load cell and a 56 mm gauge length (Fig. 2.6). The crosshead was controlled at 10 mm/min.

Mechanical abrasion was performed using a Linear Taber Abrasion machine with a CS-10 resilient abrader and a total weight of 1100 g. The abrader is refaced before each set of abrasion cycles using sand paper (from Taber). Refacing is done at 25 cycles/min for 25 cycles. For abrasion, samples are clamped down and abraded for up to 5,000 cycles at 60 cycles/min and a stroke length of 25.4 mm. For PDMS samples (Sylgard 184) the coating was completely removed after < 50 cycles. Abrasion samples were drop-cast onto glass slides without dilution, giving a final coating thickness of ≈ 2 mm.

2.2.8 Additional durability testing

Thermal cycling was performed by leaving a coated glass slide on a 70 °C hotplate. After 24 hours, the ice adhesion at -10 °C was measured and this process was repeated 10 times. Probing the low

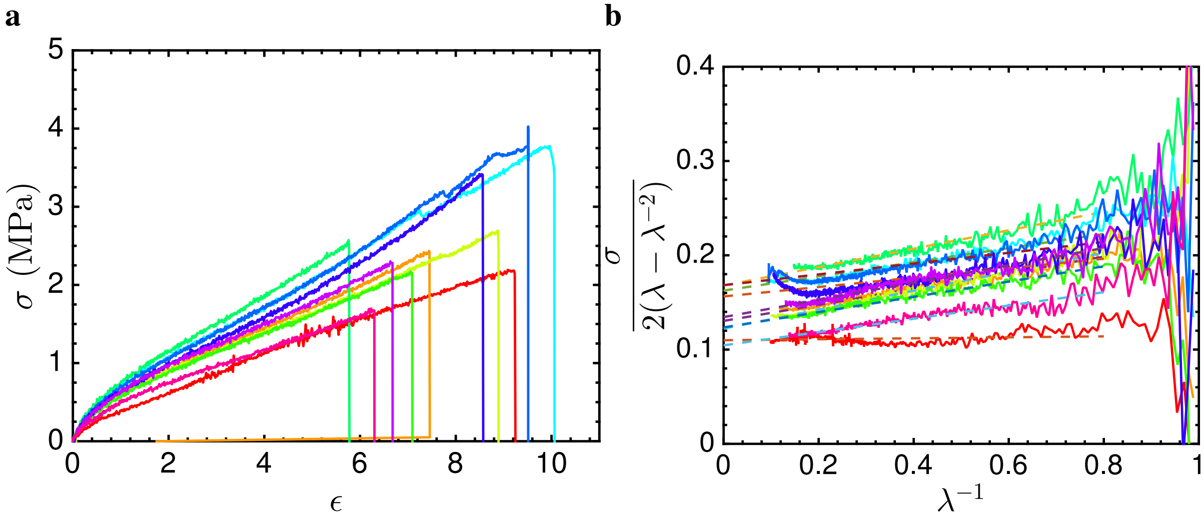

Figure 2.6: Tensile test data. a, Stress-strain results for our icephobic polyurethane rubber (VytaFlex 40, 15 wt% safflower oil). Note that the elongations at break are in excess of 1,000%. b, Re-plotting the data using Mooney-Rivlin axes allows ρ^{CL} to be computed (intercept of the y-axis at infinite elongation). Due to inaccuracies of the test machine at very small strains, linear regressions for the stress-strain data were fit when $\lambda^{-1} \leq 0.8$, where λ is the extension ratio. For all the materials tested, error between swelling studies and tensile test data was typically $<\ 5\%$. The error between measured samples was usually much larger than the test method discrepancy, *i.e.* the two test methods gave statistically equivalent crosslink densities, with an overall uncertainty of around 10%.

temperature characteristics of the coatings was done by adjusting the Peltier plate from -5 °C down to -35 °C.

Corrosion testing was done in accordance to ASTM B117[84]. Briefly, steel tabs measuring 25 mm × 75 mm were spray-coated at 500 mg/mL. The coated pieces are hung in a salt-spray fog chamber (Bemco Inc.) kept at 35 °C for 200 hours. A 25 mm scratch is made along the length of the coating so that the steel underneath is exposed. After the accelerated corrosion, the ice adhesion is measured.

A major concern for most hydrophobic polymers is their adhesion to substrates. We conducted standard peel tests in accordance with ASTM D3359[85]. A standard tape (Elcometer 99) is pressed on coated substrates using a rubber eraser. Substrates tested were steel, copper, aluminum and glass. An elongated ×' pattern is cut into the coating before the tape is applied. After pulling the tape off quickly and at an angle of 180°, the coating is evaluated for removal from the substrate. On all substrates tested, our coating showed no sign of removal. We then repeated this process 10 times, followed by ice adhesion measurement.

Chemical stability was evaluated by submerging glass slides dropcast with out icephobic PU (with silicone, safflower or vegetable oil) in 1.5 M HCl and NaOH solutions. The coated pieces were submerged for 5 minutes and then rinsed with copious amounts of deionized water. After drying, the ice adhesion was measured.

2.2.9 Microscopy and contact angle analysis

Optical images were taken using a VistaVision VWR optical microscope with a $5\times$ objective. Tapping-mode atomic force microscopy (AFM) was conducted using a Veeco Innova instrument. Veeco TESPA tips and Hi Res C probes were used for imaging. Contact angles were measured using a Ramé-Hart 200-F1 goniometer. Measurements were made by advancing and receding a single droplet of liquid (≈ 10 μL) from a 2 mL micrometer syringe (Gilmont). Averages from at least three independent measurements are reported.

2.2.10 Statistical analysis

Ice adhesion measurements are performed a minimum of 10 times successively on three different samples. Reported ice adhesion values are the average of these 30 measurements. Errorbars on all plots are one standard deviation. Crosslink density determination is performed on four separate samples and then averaged. The error in crosslink density is propagated through the Flory-Rhener analysis. Best fits are found through the method proposed by York *et al.*[7] to account for error in both dependent and independent variables. The ice adhesion measurements taken post-durability characterization are the average of three successive measurements on three different samples. Contact angles are the average of three independent measurements on each sample.

2.3 Results and discussion

2.3.1 Mechanisms for low ice adhesion

We first attempted to understand the effects of interfacial slippage and ρ^{CL} on τ_{ice}, using a shear-based (Mode-II) ice adhesion test, conducted at -10 °C[56]. To do so, we tested four representative polydimethylsiloxane (PDMS) samples: high ρ^{CL} PDMS ($\rho^{CL} = 307 \pm 8$ mol/m^3), low ρ^{CL} PDMS ($\rho^{CL} = 50 \pm 2$ mol/m^3), high ρ^{CL} PDMS with oil ($\rho^{CL} = 290 \pm 25$ mol/m^3, 25 wt% silicone oil) and low ρ^{CL} PDMS with oil ($\rho^{CL} = 46 \pm 2$ mol/m^3, 25 wt% silicone oil) (Fig. 2.7). For high ρ^{CL} PDMS (unaltered Sylgard 184), $\tau_{ice} = 264 \pm 19$ kPa, which matches reported literature values of 200-300 kPa[56, 69].

To achieve a surface with interfacial slippage and the same ρ^{CL} as Sylgard 184, we added both silicone oil (which lowers ρ^{CL}) and polymethylhydrosiloxane (which raises ρ^{CL}) until the equivalent ρ^{CL} was achieved. Such a surface exhibited $\tau_{ice} = 58 \pm 5$ kPa, a 5-fold reduction over unaltered Sylgard 184, highlighting the effect of interfacial slippage provided by the miscible

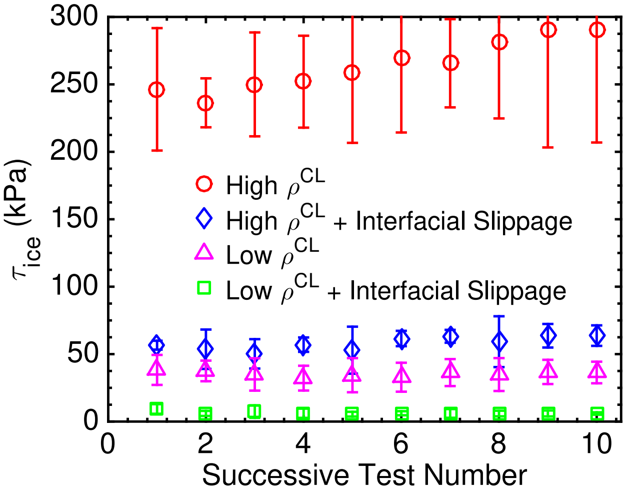

Figure 2.7: PDMS-based coatings having low or high ρ^{CL}, with or without interfacial slippage.

chains. Note that by maximizing the miscibility between the elastomeric network and the chains causing interfacial slippage, we avoid the formation of a liquid layer on top of the substrate than can be easily abraded (discussed later)[66, 67, 71]. For PDMS with a lower ρ^{CL} and devoid of any uncrosslinked chains, we found $\tau_{ice} = 33 \pm 2$ kPa. This is $5\times$ lower than the theoretical minimum of $\tau_{ice} = 150$ kPa, without the use of lubricating layers, fluorination, or texture. Indeed, coatings with values of $\tau_{ice} < 10$ kPa can be fabricated without oil, solely by lowering ρ^{CL} significantly (see coatings KK, PP, and RR in Table 2.1). Similarly, chemically grafted chains that can induce interfacial slippage can lower the ice adhesion as low as $\tau_{ice} = 11 \pm 4$ kPa (Fig. 2.8). Interestingly, both mechanisms can be used independently to fabricate surfaces with lower ice adhesion than anything previously reported. Indeed, when both mechanisms are used in concert, these effects are amplified. Accordingly, for low ρ^{CL} PDMS with interfacial slippage, we measured $\tau_{ice} = 6{\pm}1$ kPa.

We fabricated a series of different icephobic coatings from PDMS, polyurethane rubbers (PU), fluorinated polyurethane polyols (FPU), and perfluoropolyethers (PFPE), with ρ^{CL} varying from 0.68 mol/m^3 to 1203 mol/m^3, as measured by solvent swelling using Flory-Huggins theory[86], and confirmed by Mooney-Rivlin analysis[87] (Fig. 2.6). To enable interfacial slippage, we embedded the elastomers with either silicone, Krytox, vegetable oil, cod liver oil, or safflower oil. Earlier we stated that $\tau_{ice} \propto G^{1/2}$ for elastomeric surfaces in the absence of interfacial slippage. When we measured τ_{ice} for surfaces devoid of any uncrosslinked chains (*i.e.* no added oil), we observed this dependence precisely (Fig. 2.9a).

In order to check if the two mechanisms of interfacial cavitation and interfacial slippage were indeed occurring, we plotted our data in logarithmic coordinates (Fig. 2.10). Because we do not know the other terms in Eq. 1.10 (cavitation) or Eq. 2.2 (slippage), we needed to verify

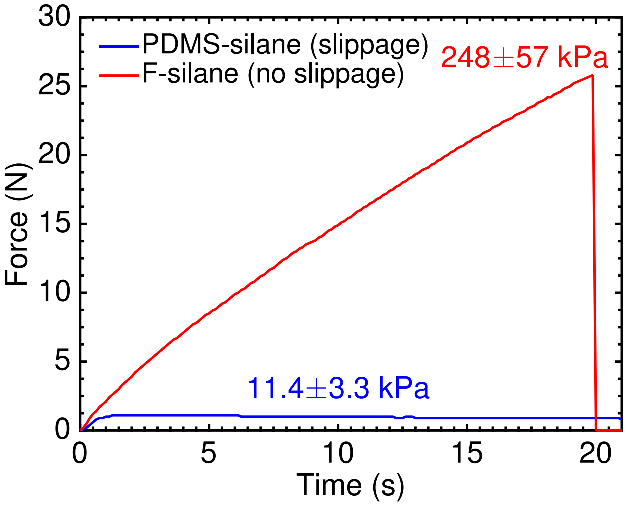

Figure 2.8: When treated with a PDMS-silane, surfaces exhibited interfacial slippage and consequently low ice adhesion. Fluoro-silanes, known to not exhibit interfacial slippage[6], showed relatively high ice adhesion, in spite of their low solid surface energy.

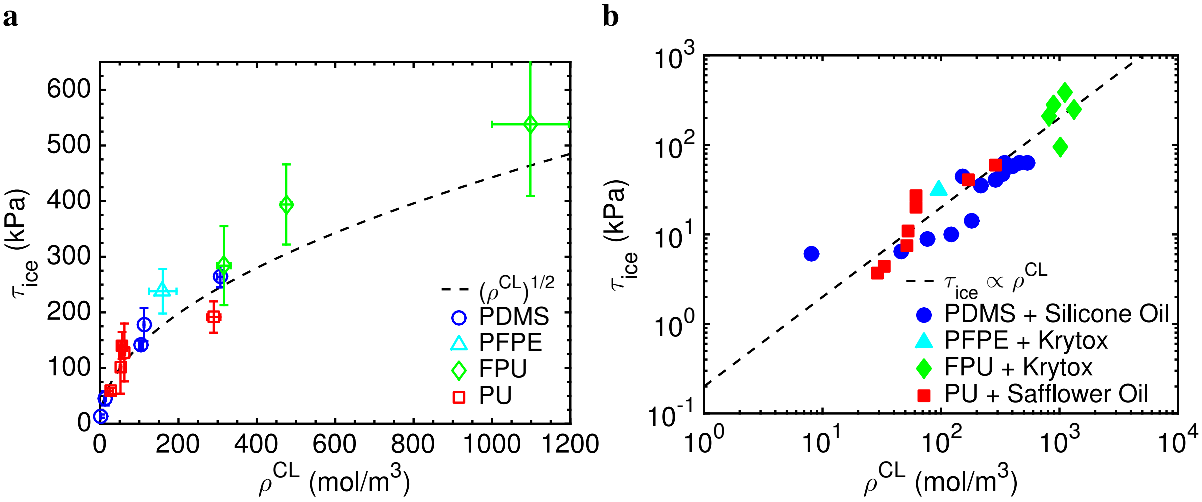

Figure 2.9: Mechanisms responsible for low ice adhesion. a, Relationship between ρ^{CL} and τ_{ice} for coatings without interfacial slippage. Error bars are 1 standard deviation. Notice the surface chemistry independence for these materials. b, Variation of τ_{ice} with ρ^{CL} for coatings with interfacial slippage enabled. The data is plotted on logarithmic axes and the error in the data is shown in Fig. 2.10b.

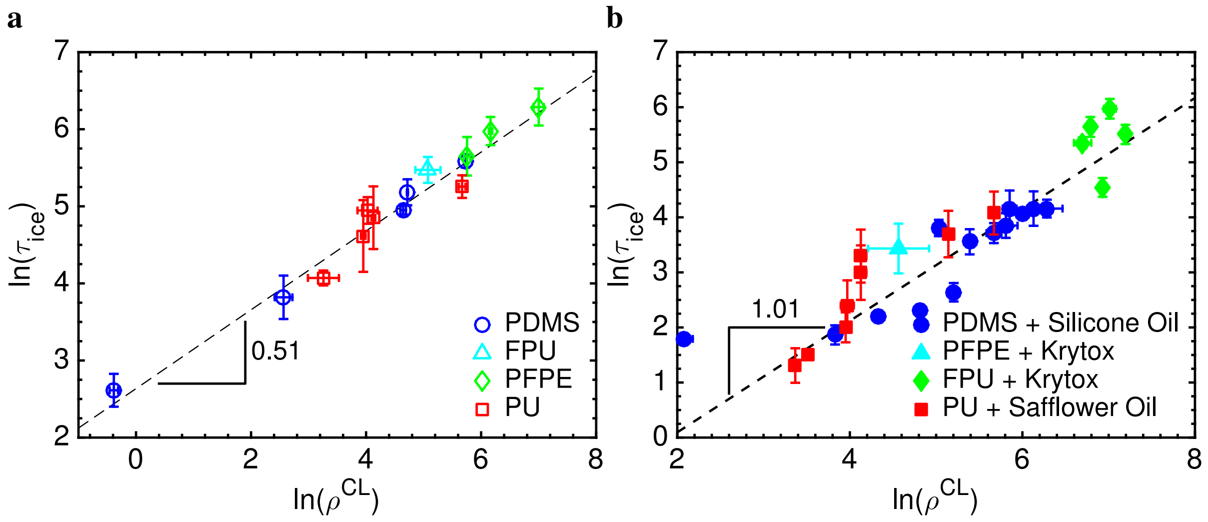

Figure 2.10: Mechanisms responsible for low ice adhesion. a, Relationship between ρ^{CL} and τ_{ice} for coatings without interfacial slippage. Error bars are 1 standard deviation, and the best fit is found using the method proposed by York *et al.*[7]. The slope is 0.51 ± 0.04. b, Variation of τ_{ice} with ρ^{CL} for coatings with interfacial slippage. The best-fit slope is 1.01 ± 0.03.

the dependence of τ_{ice} on ρ^{CL} in both cases. The best-fit slope for the various rubbers without interfacial slippage was 0.51 ± 0.04, and when interfacial slippage was enabled, the best-fit slope was 1.01 ± 0.03. We are therefore confident that these two mechanisms are indeed responsible for the observed reduction in ice adhesion.

Due to interfacial cavitation, the ice abruptly detached from these coatings (Fig. 2.11b). Interestingly, for the different elastomers tested here, we found no significant impact of elastomer chemistry or surface energy on τ_{ice}. The variation in ice adhesion strength was dominated by the changes in ρ^{CL}.

When interfacial slippage is enabled, $\tau_{ice} \propto G^1$, assuming perfect molecular contact between the ice and the coated substrate[6]. As we started with liquid water that was subsequently frozen, this assumption should hold. We confirmed this linear relationship for a number of different icephobic systems, as shown in Fig. 2.10b.

Due to the interfacial slippage, the frictional force persisted long after the ice had un-adhered from its original location (see Fig. 2.11e,f). Thus, we can differentiate elastomers with and without interfacial slippage either by the dependence of τ_{ice} on ρ^{CL}, or by comparing the shape of their force vs. time curves over multiple icing/de-icing cycles. In order to predict the ice adhesion strength reducing potential of interfacial slippage for different elastomers, we developed the dimensionless parameter I^*. I^* is the ratio between τ_{ice} for an elastomer without interfacial slippage ($\tau_{ice}^{no-slip}$), and with interfacial slippage (τ_{ice}^{slip}). Both elastomers must have the same ρ^{CL}. In logarithmic space, we subtract the ice adhesion strength from the surface exhibiting interfacial slippage

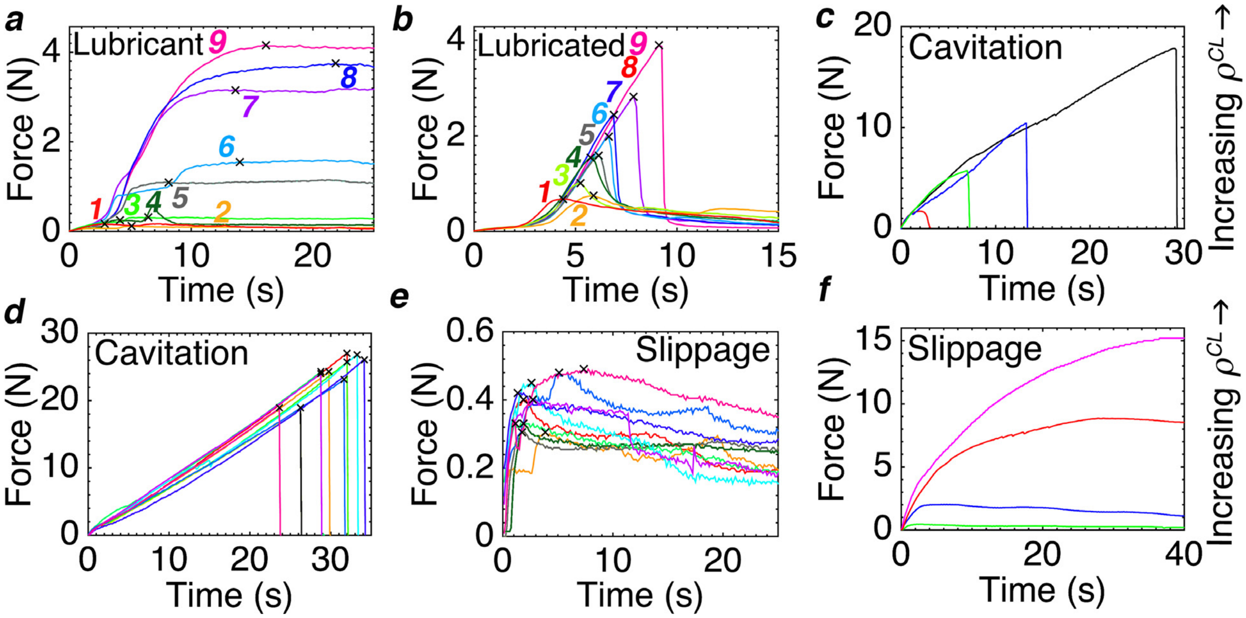

Figure 2.11: Force versus time curve analysis. (a and b) Force versus time curves for a lubricant (PMHS oil) and a lubricated (coating R) surface. The number next to each curve is the order in which the testing was performed. (c) Representative surfaces from Fig. 2.10b, where the ice un-adhered by interfacial cavitation. Note the abrupt drop in force once the ice had detached. Depending on the cross-link density, the ice adhesion can be low or high, but the mechanism for detachment remained the same. (d) The FPU (coating ZZ), which had no uncross-linked chains, caused ice to detach by interfacial cavitation, which resulted in high but consistent ice adhesion values. (e) In contrast, the PU coating ($\rho^{CL} = 33 \pm 1$ mol/m^3, 15 wt% safflower oil) showed interfacial slippage. Note the persistence of a nonzero sliding force long after the ice had moved from its original location. Comparing (a) to (e), it is apparent that lubricated surfaces lose their oily layer quite rapidly, transitioning to high ice adhesion surfaces. (f) In contrast, varying the cross-link density on surfaces exhibiting interfacial slippage, the τ_{ice} values can also be low or high, but the mechanism for detachment remains the same.

from the dry surface as,

$$log(\tau_{ice}^{no-slip}) - log(\tau_{ice}^{slip}) = \frac{1}{2}log(\rho^{CL}) - log(\rho^{CL}) + C \tag{2.3}$$

I^* follows from simplifying the natural logarithms.

$$I^* = \frac{\tau_{ice}^{no-slip}}{\tau_{ice}^{slip}} = \frac{C}{\sqrt{\rho^{CL}}} \tag{2.4}$$

where C is a constant. For 14 different elastomeric surfaces, we precisely made samples with equivalent ρ^{CL}, both with and without interfacial slippage. Our measured I^* values match the trend predicted by (2.4) quite well (Fig. 2.12).

The two important points to note here are that (1) a low ρ^{CL} can help achieve extremely low

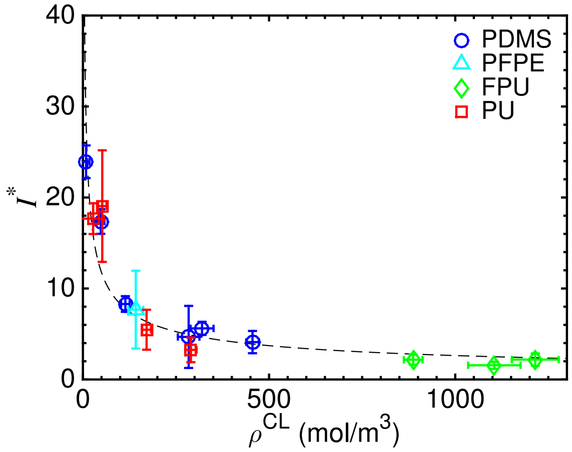

Figure 2.12: The ice-reducing potential I^* as a function of ρ^{CL}. Error bars are 1 standard deviation, and for the best-fit curve shown, $R^2 = 0.89$.

values of τ_{ice}, and (2) interfacial slippage is most effective in lowering τ_{ice} for surfaces possessing a low ρ^{CL}. For example, enabling interfacial slippage for the FPU ($\rho^{CL} = 1098$ mol/m^3) only gives $I^* = 1.6$, whereas for soft PDMS ($\rho^{CL} = 8.5$ mol/m^3), $I^* = 24$. Moreover, by fitting the data shown in Fig. 2.12, we find, $C \approx 83$ mol$^{1/2}$ m$^{-3/2}$. This has the physical interpretation that, for $\rho^{CL} > 7000$ mol/m^3, the addition of oil (or enabling interfacial slippage) will have no effect on τ_{ice} (see Fig. 2.2b). The crosslinked network with such a high ρ^{CL} is too stiff to allow for significant chain mobility. I^* predictions from Eq. (2.4) work well even for systems that only possess physical entanglements. For example, adding 25, 50, or 75 wt% liquid polybutene to polybutadiene ($\rho^{CL} \approx 8,000$ mol/m^3)[88] resulted in statistically equivalent τ_{ice} values as compared to polybutadiene with no embedded polybutene, *i.e.* $I^* = 1.0$. The same was found for polystyrene ($\rho^{CL} \approx 450,000$ mol/m^3)[88] embedded with liquid, low molecular weight polystyrene (Table 2.1).

When designing surfaces with interfacial slippage, a thick, lubricating layer can form if the added oil / polymeric chains start to phase separate from the elastomer. We performed a number of experiments to differentiate lubricated surfaces from surfaces with interfacial slippage. The easiest way to check for a lubricating layer is touching the surface by hand. The layer can also be detected through controlled abrasion, or by repeatedly measuring τ_{ice} over multiple icing/de-icing cycles (Fig. 2.3a). This free liquid layer is also readily viewable in optical micrographs or AFM phase images (Fig. 2.13).

Lubricated systems are also mechanistically different from surfaces with interfacial slippage because they rely on extremely low contact angle hysteresis to achieve their properties[3]. Further, the friction on lubricated surfaces is independent of ρ^{CL}, but heavily reliant on the oil viscosity[4]. In contrast, our icephobic surfaces utilizing interfacial slippage can have high $\Delta\theta$ (Table 2.1),

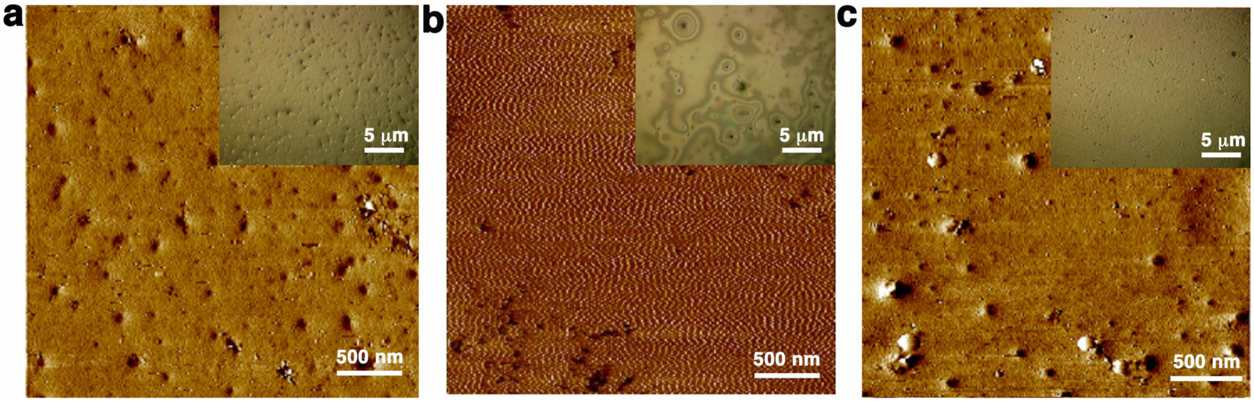

Figure 2.13: AFM phase images and optical micrographs of the PU coating with 15 wt% safflower oil, the PU coating with 10 wt% silicone oil, or the PU coating with no oil, are shown in a, b, and c, respectively. Whereas (a) and (c) appear dry, the lubricating layer is quite visible in (b).

survive harsh mechanical abrasion that should remove any lubricating surface layer (discussed below), display τ_{ice} values that depend strongly on ρ^{CL} (Fig. 2.10), and are independent of oil viscosity (Fig. 2.3b).

Initially we stated that superhydrophobic surfaces may not be icephobic due to wetting of their porous texture by condensing water droplets or frost. However, if the icephobicity arises from low ρ^{CL} and interfacial slippage, superhydrophobic surfaces can be icephobic, even when fully wetted. Using a silicon mold with a square array of holes, we fabricated icephobic, PDMS-based micro-pillars ($\tau_{ice} = 26 \pm 3$ kPa). Droplets of water placed on such a surface display superhydrophobicity, with $\theta^*_{adv}/\theta^*_{rec} = 165°/161°$ with water, and a low roll-off angle of 3° (Fig. 2.14). Such surfaces effectively repel water (above 0 °C) through minimizing the solid-liquid contact area, and solid ice (below 0 °C) through low ρ^{CL} and interfacial slippage. The differing mechanisms allow for a superhydrophobic surface to remain icephobic even when the surface is fully frosted.

2.3.2 Icephobicity of metal meshes

The PDMS-based coatings can also be used to imbue icephobicity to other textured surfaces, such as different wire-meshes, yielding values as low as $\tau_{ice} = 2.4 \pm 0.5$ kPa (Fig. 2.15). Metal meshes were coated with PDMS + silicone oil mixtures to elucidate the effects of porosity on τ_{ice}, in spite of condensation. Each mesh, when tested, was suspended on glass slides $\approx$ 1 mm thick with the area directly below the column of water open to air (inset, Fig. 2.15g). In this way, condensation occurred on the Peltier plate beneath the mesh, but did not reach the column of water during testing. At a Peltier plate temperature of -10 °C, for a suspension height of 1 mm, we found the mesh surface temperature to be around -8 °C. Other experiments indicate that there is

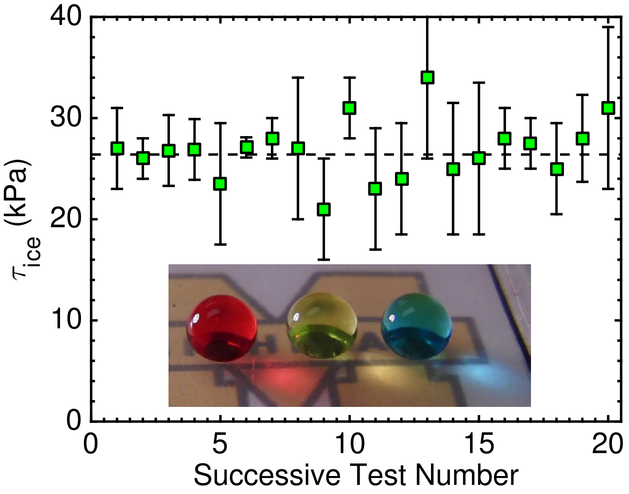

Figure 2.14: Superhydrophobic and icephobic surfaces. Droplets of water placed on icephobic PDMS pillars (coating I in Table 2.1) display superhydrophobicity, with $\theta^*_{adv}/\theta^*_{rec} = 165°/161°$ with water, and a low roll-off angle of 3°. For 20 successive icing/deicing cycles on such surfaces, we measured $\tau_{ice} = 26 \pm 3$ kPa. These surfaces effectively repel liquid water through minimizing the solid-liquid contact area, and solid ice through low ρ^{CL} and interfacial slippage. The differing mechanisms allowed the surface to remain icephobic even after the surface was fully frosted.

a negligible difference in τ_{ice} measured at -8 °C and -10 °C. Wetted fractions, % open area, and surface roughness could all be considered constant for any given mesh. To find the exact surface area in contact with water during testing, we first derive the surface area of a single metal wire with diameter D.

Water comes in contact with the top of each wire until locally Young's relation (Eq. 1.3 has been achieved[25], *i.e.* the angle made at the three-phase contact line is the equilibrium contact angle θ_Y. From geometry, $\frac{\pi}{2} = (\pi - \theta_Y) + (\frac{\pi}{2} - \alpha)$, where α is defined in the inset of Fig. 2.15e. From this we find,

$$\frac{\alpha}{2\pi} = \frac{SA_{wire}}{2\pi D} \tag{2.5}$$

as we have only considered one half of the wire. Therefore,

$$SA_{wire} = D(\pi - \theta_Y). \tag{2.6}$$

For a given mesh, the mesh number M is defined linearly as the number of cells per inch. Thus there are $2M$ wires in any in^2. We must be careful to not double count the surface area from the overlap of wires within the weave. There are M^2 total of these overlaps. We then write,

$$SA_{mesh} = 2MD(\pi - \theta_Y) - DM^2D(\pi - \theta_Y) \tag{2.7}$$

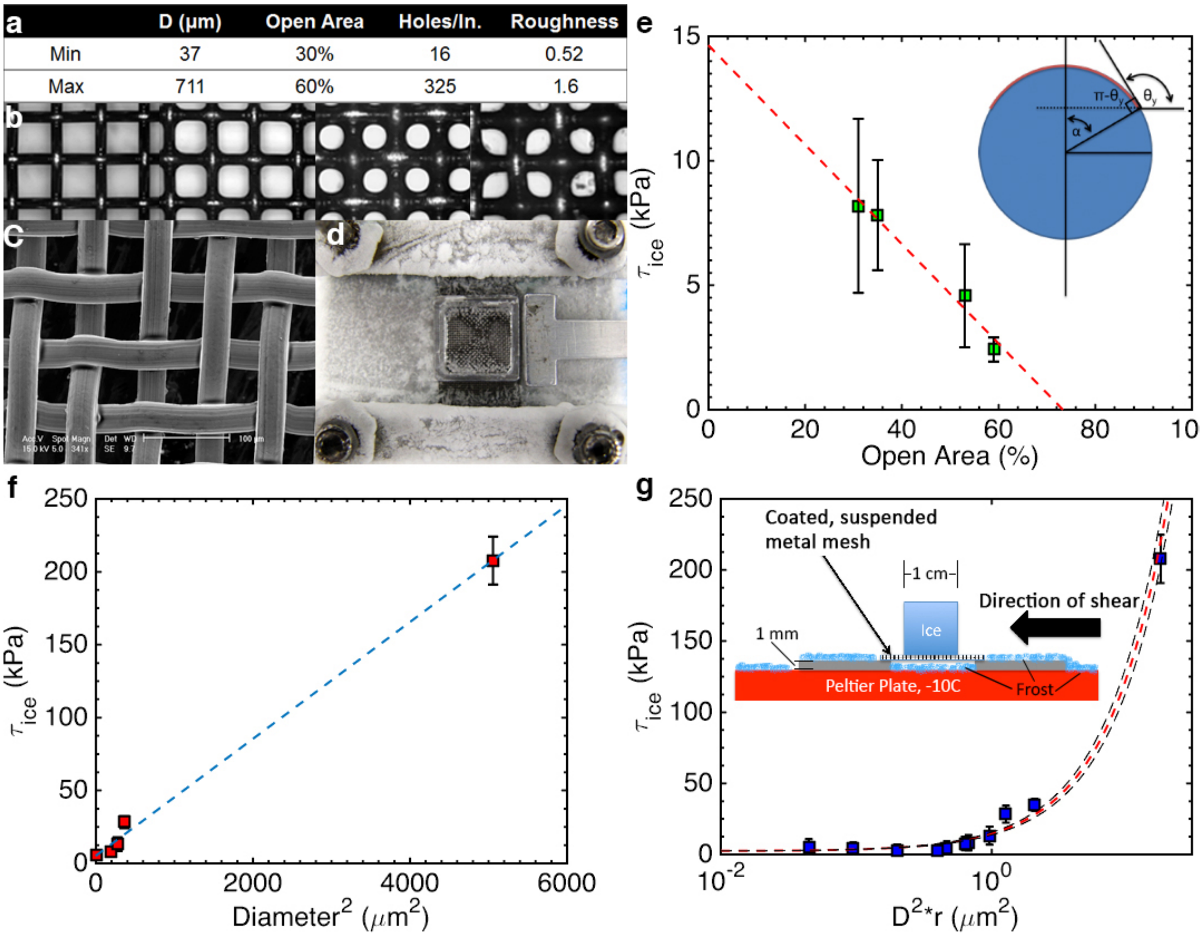

a	D (µm)	Open Area	Holes/In.	Roughness
Min	37	30%	16	0.52
Max	711	60%	325	1.6

Figure 2.15: Icephobicity of coated meshes. a, The parameter space of mesh properties evaluated. b, The effect of dip coat solution concentration on % open area. c, SEM micrograph of a PDMS coated, mesh 500. d, Frost all around our ice testing setup, including underneath the suspended mesh. e, τ_{ice} versus the % open area of meshes with $D = 140\ \mu$m. f, τ_{ice} versus D^2 for meshes with an open area of 30%. g, τ_{ice} for a coated mesh correlated well with the predictor $D^2 r$, where r was the Wenzel roughness and D was the wire diameter. The low interfacial area between ice and the substrate can significantly lower τ_{ice} . A PDMS-coated ($\rho^{CL} = 219 \pm 13$ mol/m^3, 25 wt% 100 cP silicone oil) mesh with a wire diameter of 140 μm and an open area of 59% displayed $\tau_{ice}^{mesh} = 2.4 \pm 0.5$ kPa, whereas $\tau_{ice}^{smooth} = 35 \pm 5$ kPa. The inset shows the experimental setup for suspended metal mesh ice adhesion testing.

$$SA_{mesh} = DM(\pi - \theta_Y)(2 - DM) \tag{2.8}$$

If we consider a unit cell of a mesh, the area contains one cell of the mesh, along with two wires, with an overlapping area of D^2. The side length of this unit cell is simply M^{-1}, whereas the side length of the open area is $M^{-1} - D$. The open area OA is then,

$$OA = \frac{(M^{-1} - D)^2}{(M^{-1})^2}, \tag{2.9}$$

which simplifies to,

$$OA = 1 - DM(2 - DM) \tag{2.10}$$

The total parameter space of metal meshes studied can be seen in Fig. 2.15a. When coating the meshes we used solutions with a polymer concentration of 200 mg/mL in hexane. Coating thickness could alter the above calculations, and thus we experimented to find a coating thickness that minimally altered the dimensions of the mesh while still providing complete surface coverage (Fig. 2.15b,c). The optical image of the test setup shown in Fig. 2.15d highlights how frosting is a major concern for textured surfaces in the Cassie-Baxter state[2]. Underneath the freezing column of water frost is prominently visible, but it did not affect our measurements.

We tested four meshes of differing diameter but constant 30% OA (Fig. 2.15f) and five meshes with constant diameter (140 μm) and differing OA (Fig. 2.15e). We found a linear relationship with τ_{ice} between both OA and D^2. Moreover, we found that D^2r correlated best with τ_{ice} for all the meshes we tested (Fig. 2.15g). Here r is the Wenzel roughness[1], which is the non-dimensional form of SA_{mesh} (which is defined per in^2).

2.3.3 Durability of icephobic coatings

To initially characterize the durability of our icephobic coatings, we evaluated force vs. time curves, and thereby τ_{ice}, for our surfaces over repeated icing/de-icing cycles. For surfaces damaged during the icing/de-icing process, the shape of the force vs time curves changed, and τ_{ice} increased, with increasing icing/de-icing cycles. Both lubricated surfaces, as well as surfaces too soft to prevent physical damage, displayed such behavior within 10 icing/de-icing cycles (Fig. 2.11a,b and 2.3a). However, these soft surfaces often displayed almost immeasurably low τ_{ice} values. We measured $\tau_{ice} = 0.15 \pm 0.05$ kPa for our most icephobic surface (Fig. 2.16). This is one of the lowest τ_{ice} reported thus far, and over five orders of magnitude below τ_{ice} for aluminum. Ice slides off such surfaces solely under its own weight. However, additional icing/de-icing cycles begin to degrade the surface, raising τ_{ice} (Fig. 2.16). Durable surfaces with interfacial slippage, typically possessing higher ρ^{CL}, maintain their low ice adhesion values ($\tau_{ice} = 3.6 \pm 1.0$ kPa) over repeated icing/ de-icing cycles (Fig. 2.3a), and show self-similar force vs. time curves (Fig. 2.11e).

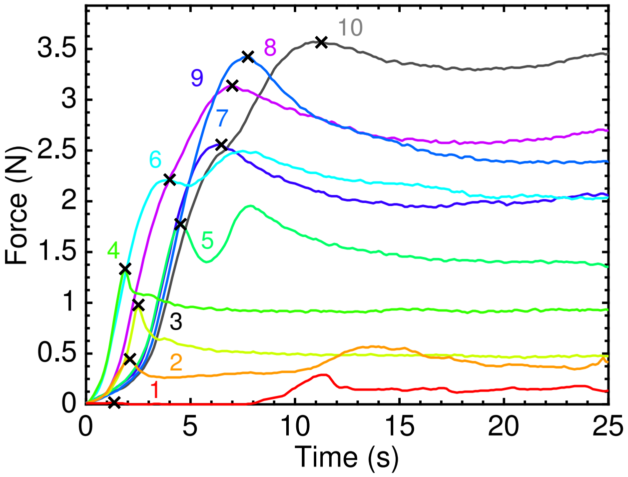

Figure 2.16: The force vs. time curves for coating Q, comprised of Sylgard 184 PDMS and 75 wt% silicone oil (Table 2.1), which displayed an initial ice adhesion strength of $\tau_{ice} = 0.15 \pm 0.05$ kPa. The ×' symbol denotes the time when ice first un-adhered from the coating.

To illustrate the significant advantage of coatings that repel ice through low ρ^{CL} in conjunction with interfacial slippage, we conducted two simple tests for durability: repeated icing/de-icing and relatively mild abrasion (Fig. 2.17). We compare our coatings' performance to other state-of-the-art icephobic coatings, such as commercial superhydrophobic surfaces (NeverWet©), lubricant-infused surfaces[3], extremely low surface energy fluorodecyl POSS coatings[56], and commercially available icephobic coatings (Nusil R-2180). As fabricated, our PU coating (coating CB; $\rho^{CL} = 33$ mol/m^3, 15 wt% safflower oil, $\theta_{adv}/\theta_{rec} = 67°/29°$, $\Delta\theta = 38°$), shows an order of magnitude reduction in τ_{ice} over the other state-of-the-art coatings considered here. Further, after just 10 icing/de-icing cycles, all other coatings, except those fabricated here, exhibit $\tau_{ice} > 200$ kPa (with the exception of the commercial coating Nusil R-2180, which is a low ρ^{CL} PDMS). Additionally, after mild abrasion, only our PU coating remains icephobic, with an ice adhesion strength 2,500% lower than any other coating relying on lubrication or low surface energy.

We additionally tested our PDMS-based coating (coating OO), which can be repeatedly iced but is mechanically very poor, and a PU-based coating, where we intentionally added excess safflower oil (20 wt%) to form a lubricating, free-oil layer (coating CC). There is statistically no difference in τ_{ice} values between the lubricated and interfacial slippage PU-based coatings initially, or after 10 icing/de-icing cycles (see Table 2.1, Fig. 2.18b, Fig. 2.17). However, the lubricated PU coating easily delaminates from essentially all coated substrates (left inset, Fig. 2.18a) due to the presence of the free-oil layer. Similarly, SLIPS-based surfaces utilizing costly, fluorinated lubricants suffer a 10-fold increase in ice adhesion after just a few icing/de-icing cycles (Fig. 2.1). Thus, there is a marked advantage to producing interfacial-slippage-based icephobic coatings. Finally, note

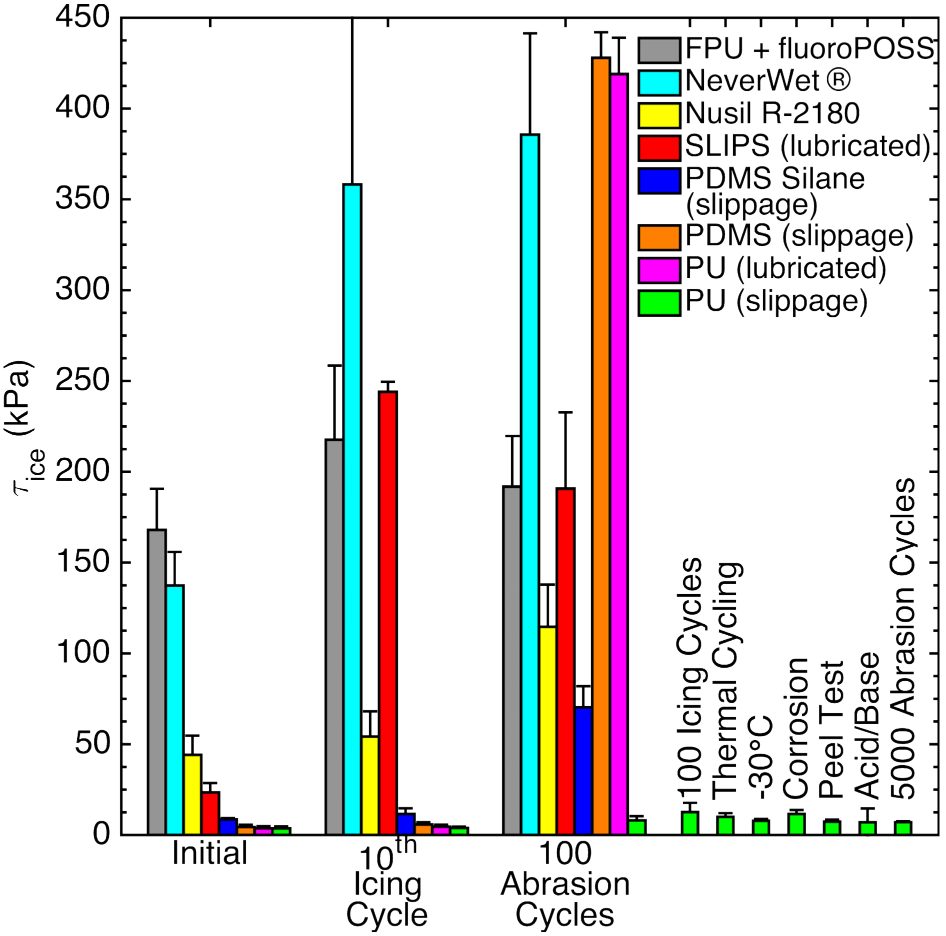

Figure 2.17: Comparison of coatings in this work with other state-of-the-art icephobic surfaces. Also, additional durability characterizations are presented for the PU coating with interfacial slippage (coating CB in Table 2.1). For details on each coating and test configuration, see Sec. 2.2.

that a silicon wafer treated with a PDMS-silane, a surface exhibiting interfacial slippage[52] due to pendent chains[89], also exhibited very low ice adhesion ($\tau_{ice} = 11 \pm 4$ kPa, see Fig. 2.8, Fig. 2.17). In comparison, a Si wafer coated with a low surface energy fluorinated silane exhibits relative high ice adhesion ($\tau_{ice} = 248 \pm 57$ kPa, Fig. 2.8). However, these thin silane coatings can be abraded away relatively easily (Fig. 2.17).

To demonstrate the real-world potential of our durable icephobic surfaces, we conducted outdoor testing during the winter months of 2013 and 2014 in Ann Arbor, Michigan. Over the four months of exposure, both snow and ice accreted severely on an uncoated glass panel. The coated panel often had snow settle on it, but all ice that formed was quickly sheared off even from mild winds[75] (Fig. 2.19). After four months of exposure, the contact angles and τ_{ice} for the coated surface were the same as before testing, highlighting the coating's durability.

Finally, we conducted extensive durability testing (Fig. 2.18a, 2.17) on our icephobic polyurethane

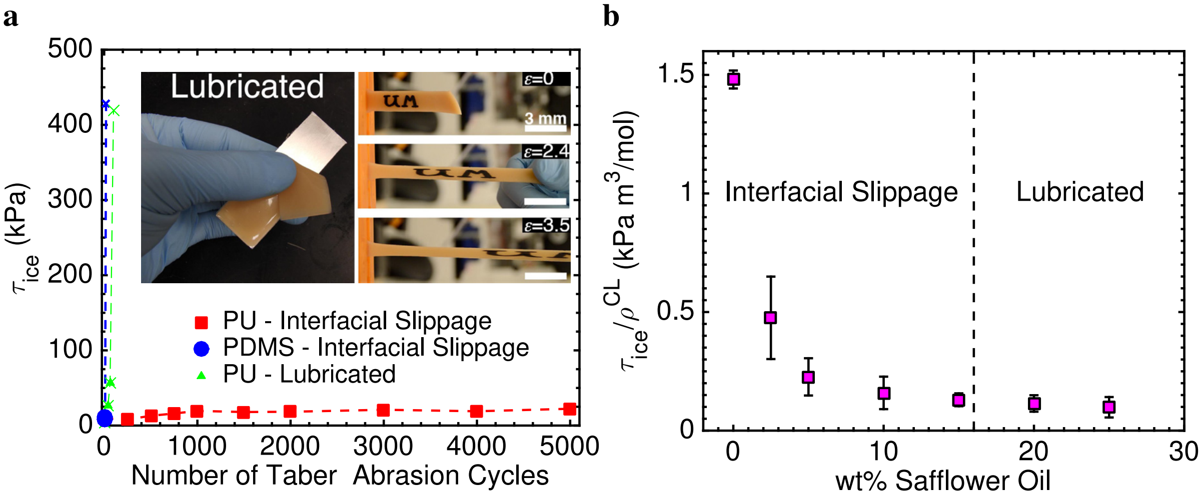

Figure 2.18: a, Mechanical abrasion of three different icephobic coatings. The PDMS (coating NN) and lubricated PU (coating CC) were easily damaged or delaminated within 20 abrasion cycles, whereas the PU with interfacial slippage (coating CB) survived over 5,000 cycles while maintaining low ice adhesion. b, The effect of oil content in our PU on τ_{ice} after normalizing by ρ^{CL}. The miscibility limit of safflower oil is $\approx$ 16 wt%. It was clear that once the oil started to phase separate from the PU elastomer, the mechanism for reduced ice adhesion transitioned from interfacial slippage to lubrication.

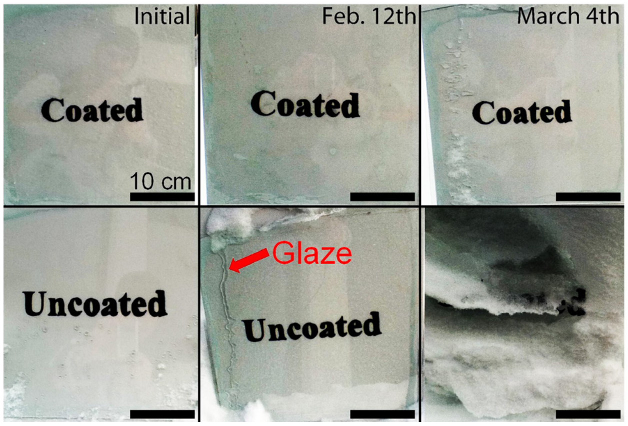

Figure 2.19: Outdoor testing of a PDMS-based coating (coating NN; see Table 2.1) for 4 months during winter 2014. On Februar 12, the un-coated panel was covered with a $\approx$ 7 mm layer of glaze, the type of ice with the strongest adhesion[8]. No ice had accreted on the coated panel. On March 4, 2014, snow followed a night of freezing rain, which completely covered the un-coated panel. The coated panel only had a small amount of accreted ice remaining.

(coating CB) including Taber abrasion (ASTM D4060), acid/base exposure, accelerated corrosion (ASTM B117), thermal cycling, and peel testing (ASTM D3359). We also measured τ_{ice} over 100 icing/de-icing cycles, and evaluated the coating in a temperature range from -5 °C to -35 °C (Fig. 2.20b). After 5,000 abrasion cycles, causing over 600 μm of thickness loss, the coating remains icephobic because icephobicity is an inherent property of the coating. PDMS-based coatings (coating NN) or lubricated PU-based coatings (coating CC), though equally icephobic initially, are completely abraded away (and/or delaminated) after < 20 cycles (Fig. 2.18a). The use of high surface energy elastomers, and the lack of a free oil layer, allows us to create coatings that adhere very well to any underlying substrate. We observed no increase in τ_{ice} even after 10 successive peel tests on steel, copper, aluminum, and glass, or after thermal cycling between -10 °C and 70 °C. The average ice adhesion strength for this coating after all durability testing is $\tau_{ice} = 9 \pm 2$ kPa. We additionally subjected our icephobic polyurethane to a tensile stress of 2.5 MPa, causing the elastomer to elongate by 350% without breaking or losing its icephobic properties (Fig. 2.18a, right inset). Additional tensile testing showed strains in excess of 1,000% (Fig. 2.6). The developed, extremely durable coatings can be spun, dipped, sprayed, or painted onto essentially any underlying substrate, of any size. Finally, we had the extremely low ice-adhesion strengths for multiple surfaces independently verified by Mode-I type (peel test) and Mode-II (zero-degree-cone) adhesion testing at the US Army's Cold Regions Research and Engineering Laboratory[9] (see Fig. 2.20a).

2.4 Conclusions

In this work we discussed two universal attributes, crosslink density and interfacial slippage, that can be used to systematically tailor ice adhesion for elastomeric surfaces, irrespective of material chemistry. It was found that interfacial slippage makes the biggest impact on the ice-adhesion strength of low crosslink density elastomers. Using this understanding, we fabricated a range of different, mechanically durable, long lasting icephobic surfaces, from a wide range of material systems. We foresee such extremely durable icephobic coatings having immediate, worldwide applications across various industrial sectors, academic disciplines, and engineering endeavors. In the next chapter we further explore the addition of oil to polymeric materials. We formulate a new model that accurately predicts the reduction in ice adhesion strength of essentially any material, through the addition of oils or plasticizing agents.

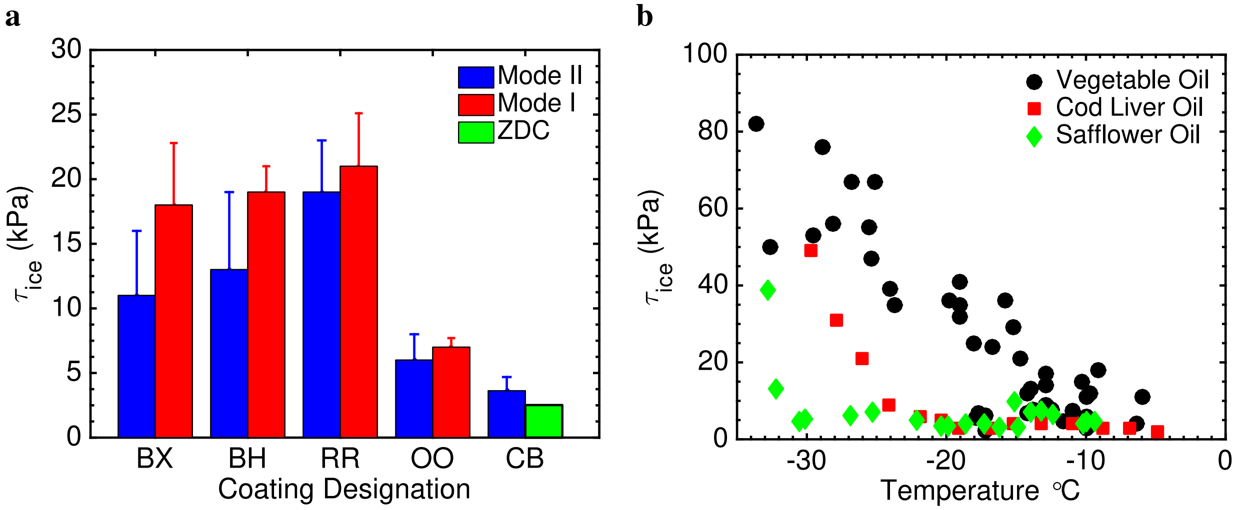

Figure 2.20: Interfacial slippage mechanism additional data. a, Comparison of five samples (BX: PU + 15 wt% vegetable oil, BH: PDMS-modified PU + 10 wt% silicone oil, RR: low ρ^{CL} PDMS without oil, OO: low ρ^{CL} PDMS + 25 wt% silicone oil, CB: PU + 15 wt% safflower oil, see Table 2.1) sent to CRREL compared to data taken in-house. Note that CRREL data points (Mode-I) were the average of two different samples tested once, whereas the in-house data points (Mode-II) were the average of at least 10 subsequent measurements. Mode-I is defined by tensile loading at the ice-substrate interface, whereas Mode-II is defined by shear loading at the ice-substrate interface[9]. The zero-degree-cone test (ZDC) is an alternate method of evaluating Mode-II ice adhesion. b, Low temperature studies for the polyurethane filled with 15 wt% vegetable, cod liver, or safflower oil. The increase in ice adhesion indicated the loss of interfacial slippage, caused by the freezing of the fatty acid chains. The polyunsaturated fatty acid content increases from vegetable to cod liver to safflower oil.

CHAPTER 3

A Predictive Model for Icephobicity

3.1 Introduction

The removal of accreted ice remains a costly, hazardous hindrance, both residentially and industrially across the globe[63, 8]. Coatings that significantly reduce the adhesion between ice and a given surface can be called icephobic[72]. However, very few coatings have been fabricated that facilitate the complete removal of ice without the input of additional energy, *i.e.* surfaces where ice may be removed by its own weight[54, 90, 77, 3, 78, 91, 75, 70]. Typically, these extremely icephobic surfaces have relied on sacrificial lubricants, where the icephobic properties may diminish as the lubricant becomes depleted. There are no methods of predicting the resultant ice adhesion once the lubricant has been removed. This inability to predict the ice adhesion is not limited to initially lubricated surfaces. Although it would be highly desirable, there is currently not a single reported method for predicting and therefore designing the icephobicity of a given surface.

Materials like glass, steel and aluminum display ice adhesion strengths $\tau_{ice} > 1,000$ kPa[54, 56]. The ice adhesion strength of polymeric systems typically ranges from $150 \leq \tau_{ice} \leq 500$ kPa[56, 68]. However, for ice to be removed by wind shear or solely by its own weight, significantly lower τ_{ice} values are necessary. For example, ice accumulation notoriously lowers the efficiency of wind turbines during the winter months[92]. A typical offshore wind turbine blade is 85 m long and rotates at a minimum of 10 rpm[93]. At the blade tip, the centripetal force experienced by a square meter slab of ice that is 1 cm thick is around 12 kN. For this ice to detach, $\tau_{ice} \leq 12$ kPa is necessary. This order-of-magnitude disparity highlights the inherent difficulty in fabricating practically useful icephobic surfaces.

In Chapter 2 we showed that low crosslink density elastomers are intrinsically icephobic[54]. When ice adhered to a low-ρ^{CL} elastomer experiences a shear stress, the ice-elastomer interface can cavitate, causing the ice to detach at low applied loads[62]. Ice adhesion strengths as low as $\tau_{ice} \approx 10$ kPa were reported for dry elastomers solely utilizing interfacial cavitation. However, these extremely soft surfaces are not mechanically robust. Therefore, interfacial cavitation alone offers limited improvement, in terms of durability towards repeated icing/de-icing, over lubricated systems that initially display equally low ice adhesion strengths[77, 78, 91]. Fortunately, engendering slip at the ice interface can further reduce the adhesion of ice to elastomers.

3.2 The model

The purpose of this work is to understand how the ice adhesion of elastomers changes when the elastomer is filled with a water-immiscible liquid. We will refer to this liquid as oil', although any liquid sufficiently immiscible with water will suffice. To predict the ice adhesion of an oil-filled elastomer, we will show that only two properties need be known:

τ_{ice}^{no-oil}, the ice adhesion strength of the unfilled (dry) elastomer.

ϕ_{oil}^{max}, the maximum amount of oil that can swell the dry elastomer.

Based off Chernyak's model for the friction of rubber[50], we previously showed that when interfacial slippage was enabled (recall Fig. 2.9b),

$$\frac{\tau_{ice}^{oil}}{\tau_{ice}^{no-oil}} \propto \frac{\rho_{filled}^{CL}}{\rho_{unfilled}^{CL}}. \tag{3.1}$$

The reduction in ice adhesion of an oil-filled elastomer was shown to be directly proportional to the reduction in crosslink density of the elastomer. It is well known that filling an elastomer with a liquid lowers its effective crosslink density[86]. To predict the reduction in ice adhesion caused by filling the elastomer with oil, a relation between ρ^{CL} and oil content, ϕ_{oil}, is needed. Below we derive such a relation.

If interfacial slippage occurs, the reduction in ice adhesion has been shown to strongly depend on the ρ^{CL}. For example, a 24-fold reduction in τ_{ice} was observed for a soft polyurethane rubber (Fig. 2.12), and essentially no change in τ_{ice} for rigid plastics like polystyrene[54]. However, modification of the base material was necessary to achieve identical ρ^{CL} values for when comparing surfaces that did, and did not, exhibit interfacial slippage. In this work we discuss the more general case, and investigate how τ_{ice} changes when both the crosslink density and interfacial slippage are varied for each elastomer/oil combination. Essentially, we answer the question: for surfaces exhibiting interfacial slippage, how does τ_{ice} depend on ϕ_{oil}?

In our proposed model for interfacial slippage, we assume that the ice adhesion of pure oil is negligible. After all, liquids may be defined by their inability to support shear stresses[23]. Highly lubricated systems have approached this idealization, initially displaying $\tau_{ice} = 1.7$ kPa[78], $\tau_{ice} = 0.4$ kPa[77], and $\tau_{ice} = 0.15$ kPa[54]. At the ice-elastomer interface, we let ϕ_s be the fraction of solid elastomer in contact with ice. The remaining $(1 - \phi_s)$ of the surface is comprised of oil, and we define a lubricated surface such that $\phi_s = 0$. We propose that the ice adhesion strength of an oil-filled elastomer is given by,

$$\tau_{ice}^{oil} = \frac{\rho_{filled}^{CL}}{\rho_{unfilled}^{CL}} \tau_{ice}^{no-oil} \phi_s. \tag{3.2}$$

Eq. (3.2) combines the reduction in crosslink density through the addition of oil, or relation (3.1), with the reduction in adhesion sites at the surface of the oil-filled elastomer. The linear scaling with ϕ_s has the advantage of bounding the ice adhesion of the oil-filled elastomer between $\tau_{ice} = \tau_{ice}^{no-oil}$, when $\phi_{oil} = 0$, and $\tau_{ice} = 0$, when the surface is fully lubricated. To measure ϕ_s we use the theory of hemi-wicking first proposed by Quéré for rough, partially wetted surfaces[33].

3.3 Theoretical underpinning

The Flory-Rehner equation has been successfully used since 1943 to describe how elastomers swell in the presence of liquids[86]. Often it is written as,

$$\rho^{CL} = \frac{\log(1 - \nu_2) + \nu_2 + \chi \nu_2^2}{\nu_1(\nu_2^{1/3} - 0.5\nu_2)} \tag{3.3}$$

where ν_2 is the volume fraction of polymer in a swollen gel and χ is the Flory-Huggins interaction parameter between the polymer and the probe solvent, with molecular volume V_1. Equilibrium swelling occurs when the enthalpic gain from solvating the polymer is balanced by the entropic penalty of stretching the polymer. Flory and Rehner originally derived this equation for natural rubber vulcanates, which are often filled with carbon black. Twenty years later, Kraus extended the Flory-Rehner equation to account for such rigid fillers within the elastic network that would not undergo deformation in the presence of a solvent[94]. If S is the apparent swell ratio of a filled rubber, and S_o is the swell ratio of the unfilled rubber, Kraus proposed that $S = (S_o - \phi)/(1 - \phi)$, where ϕ is the volume fraction of filler. This relation suggests that only the volume of rubber, $(1 - \phi)$, can be swollen by the solvent. For our purposes, this can be rewritten as,

$$\nu_2^{oil} = \nu_2(1 - \phi)/(1 - \nu_2\phi). \tag{3.4}$$

where ν_2^{oil} is the apparent volume fraction of polymer (that had been filled with oil) in a swollen gel, and ν_2 is the volume fraction of polymer (that was initially unfilled) in the gel. Note that $\nu_2 = S_o^{-1}$ and similarly $\nu_2^{oil} = S^{-1}$. For particulate fillers, Kraus showed that the filler-rubber bond strength limited the final swell ratio by some swelling deficiency, $\Delta\nu$. Here the filler is an oil, which may be displaced by the solvent upon swelling, making elastomers pre-filled with oil an idealized case where $\Delta\nu = 0$. When we swelled seven different oil-filled elastomers (Fig. 3.1), good agreement was observed between our experimental swell ratios and Eq. (3.4). We normalize

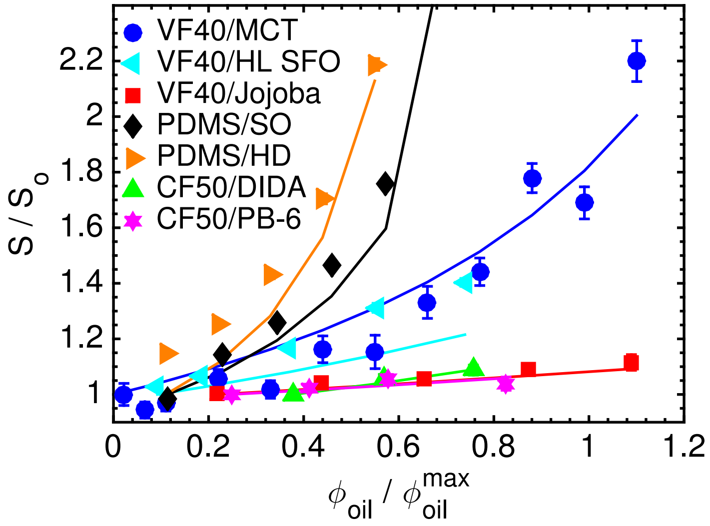

Figure 3.1: The crosslink density reduction of oil-filled elastomers. a, the ratio of the apparent swell ratio to the unfilled swell ratio (no oil) for seven different elastomer/oil combinations, versus the oil content. The oil content has been normalized by the maximum oil solubility within the elastomer for readability purposes only. The solid lines represent Eq. (3.4). b, the crosslink density reduction for the same seven elastomer/oil combinations. VF40: Vytaflex 40. MCT: medium chain triglyceride oil. HL SFO: high-linoleic safflower oil. SO: silicone oil. HD: hexadecane. CF50: Clearflex 50. DIDA: diisodecyl adipate. PB-6: polybutene lubricant. See Sec. 3.4 for details.

ϕ_{oil} by its maximum value, ϕ_{oil}^{max}, for readability purposes only in Fig. 3.1.

Recalling relation (3.1) from above, the reduction in ρ^{CL} of an elastomer, due to swelling by an oil, is proportional to the reduction in ice adhesion. The crosslink density of an oil-filled elastomer can be found by substituting Eq. (3.4) into the Flory-Rehner relation. Dividing the relation for the filled crosslink density by its unfilled counterpart yields,

$$\frac{\rho_{filled}^{CL}}{\rho_{unfilled}^{CL}} = \frac{[\log(\frac{\nu_2(1-\phi)}{(1-\nu_2\phi)}) + \chi(\frac{\nu_2(1-\phi)}{(1-\nu_2\phi)})^2 + \frac{\nu_2(1-\phi)}{(1-\nu_2\phi)}](\nu_2^{1/3} - 0.5\nu_2)}{(\log(1-\nu_2) + \nu_2 + \chi\nu_2^2)[(\frac{\nu_2(1-\phi)}{(1-\nu_2\phi)})^{1/3} - \frac{\nu_2(1-\phi)}{2(1-\nu_2\phi)}]}. \tag{3.5}$$

For large swell ratios (small ν_2), this reduces to,

$$\frac{\rho_{filled}^{CL}}{\rho_{unfilled}^{CL}} = (1-\phi)^{5/3}. \tag{3.6}$$

Because ρ^{CL} is a property of the elastomer, and does not depend on the solvent used to measure it, an appropriate choice of solvent can always be made such that ν_2 is sufficiently small, meaning Eq. (3.6) is not an approximation. Eq. (3.6) makes intuitive sense because all the solvent-specific properties used to measure ρ^{CL}, namely ν_2, V_1 and χ, have dropped out. The degree by which ρ^{CL}

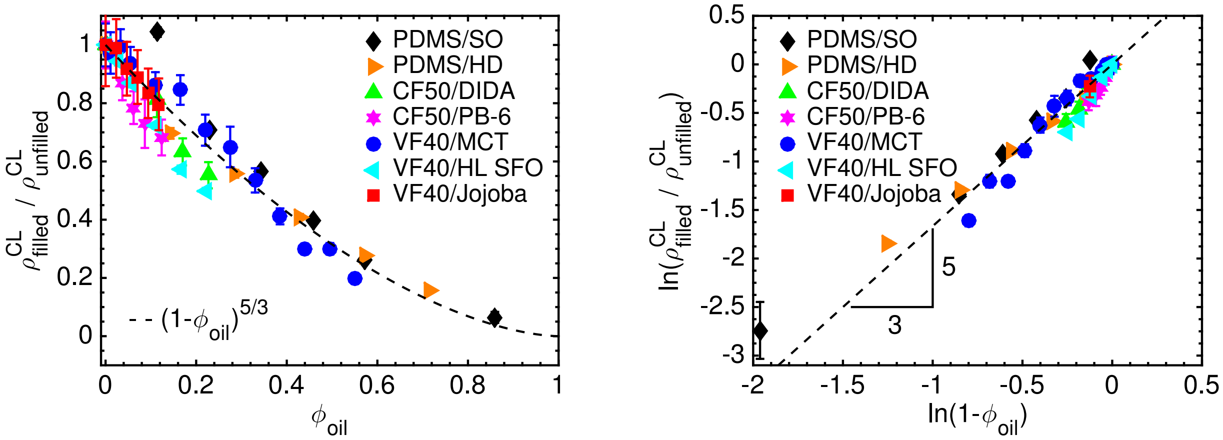

Figure 3.2: (left) The measured reduction in crosslink density for three different elastomers swollen in seven different oils, plotted against the amount of oil within the rubber. (right) the same data plotted in logarithmic coordinates, along with a line of slope 5/3. See the caption of Fig. 3.1 for abbreviation meanings.

is reduced when filled with oil solely depends on ϕ. Note that Flory and Rehner also observed an exponential dependence of 5/3 between ρ^{CL} and ν_2 when they neglected the heat of dilution and assumed ν_2 was small in their original work (equation (19') in their seminal 1943 paper)[86]. In Fig. 3.2, we show excellent agreement between Eq. (3.6) and three different elastomers filled with seven different oils. Thus, Eq. (3.6) accurately predicts how a certain amount of oil will reduce the crosslink density of an elastomer, up to ϕ_{oil}^{max}.

In a binary mixture, the lower surface energy species preferentially migrates to the interface until the gain in surface energy equilibrates with the loss in translational entropy in the bulk[23, 95]. According to the theory of hemi-wicking, the apparent contact angle (θ^*) of a liquid on a film comprised of the same liquid is $\theta^* = 0°$; the liquid perfectly spread on itself[33]. Contrastingly, the equilibrium contact angle of the liquid on an elastomer is given by some (usually) non-zero value, θ_Y. Hence, the apparent contact angle of an oil on an elastomer with some fraction of the *same oil* on its surface may be found using[23, 33],

$$\cos\theta^* = (1-\phi_s)\cos 0° + \phi_s \cos\theta_Y \tag{3.7}$$

where we recall that ϕ_s is the solid fraction of elastomer on the surface. The embedded oil within the elastomer can therefore be used as a probe liquid when measuring contact angles, in order to find the fraction of oil on the surface, $(1-\phi_s)$. If the elastomer is covered by a film of oil, $\theta^* = 0°$. In Fig. 3.3a we show the measured surface fraction of a polyurethane rubber, filled with various amounts of six different oils (described in Sec. 3.4 below).

Because the solubility of an oil in an elastomer depends on its chemical composition[96], full surface coverage ($\phi_s = 0$) was reached at different ϕ_{oil} values for different oils. For example, oil

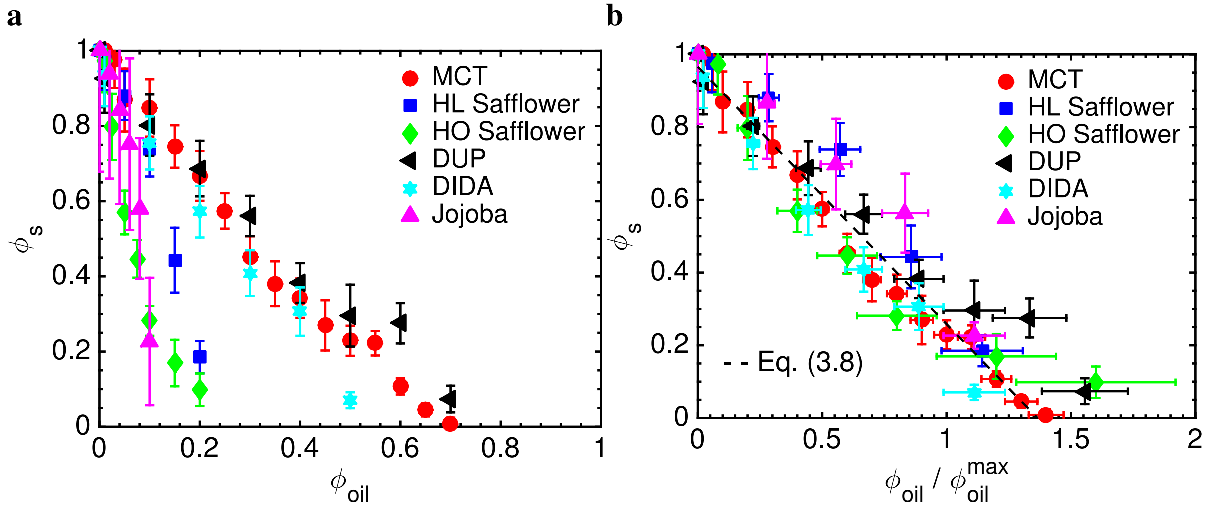

Figure 3.3: The surface fraction of oil-filled elastomers. a, the solid fraction of an oil-filled elastomer versus the oil content within the elastomer. b, this data collapses when the oil content is normalized by its maximum solubility within the elastomer. HO = high oleic. DUP = diundecyl phthalate.

derived from the seeds of the *simmondsia chinensis* plant (jojoba oil) fully covered the surface of a polyurethane rubber around $\phi_{oil} \approx 0.1$. Fractionated coconut oil (also called medium-chain triglyceride or MCT oil) did not reach full surface coverage until $\phi_{oil} \approx 0.7$. By swelling pieces of dry rubber in each oil, ϕ_{oil}^{max} may be measured once a constant mass has been achieved (Table 3.1)[81]. Normalizing the fraction of oil within the rubber by ϕ_{oil}^{max} collapsed all our ϕ_s measurements (Fig. 3.3b). The slope of the best-fit line was $\alpha = 0.7114$, and the solid fraction at $\phi_{oil} = 0$ was set to $\phi_s = 1.0$. This yielded,

$$\phi_s = 1 - \alpha \phi_{oil} / \phi_{oil}^{max}. \tag{3.8}$$

This linear relationship is a quantitative relation between the amount of oil within the bulk of an elastomer, and the amount of oil on the surface of the elastomer. Note that α exceeding unity represents the lack of formation of a free oil film on the surface of the elastomer when $\phi_{oil} = \phi_{oil}^{max}$. We always observed that additional oil was required before $\theta^* = 0°$, and consequently $\tau_{ice} \approx 0$.

Substituting Eq. (3.6) and (3.8) into Eq. (3.2) yielded Eq. (3.9).

$$\frac{\tau_{ice}^{oil}}{\tau_{ice}^{no-oil}} = (1 - \phi_{oil})^{5/3} (1 - \alpha \phi_{oil} / \phi_{oil}^{max}) \tag{3.9}$$

Here the left hand side indicates the reduction in the ice adhesion of the elastomer through the addition of oil. The right hand side is comprised of two terms. The first term gives the reduction in the ice adhesion strength due to a decrease in the crosslink density of the elastomer, and the second term represents the amount of elastomer on the surface capable of forming an adhesive bond to ice. Again, we assume no adhesive bond forms on the fraction of oil partially covering the surface of the elastomer, $(1-\phi_s)$. We now discuss the validity of Eq. (3.9) for a wide range of material systems.

3.4 Materials and methods

3.4.1 Materials

Vytaflex 40, Vytaflex 20 and Clearflex 50 (Smooth-On Inc.) or Sylgard 184 (Dow Corning) were mixed per manufacturer instructions. PB-6 (Soltex Solvents), MCT, eucalyptus (EuO), jojoba, HL SFO, HO SFO, and squalane oil (Jedwards International) or DIDA, DUP, SO (100 cP), and n-hexadecane (Sigma Aldrich) were added to the liquid pre-polymer and the solution was vortexed until homogeneous. The mixtures were then poured onto glass slides and allowed to cure at room temperature (Vytaflex) or at 80°C (Clearflex and PDMS) overnight. For the CF50VF20 coating in Table 3.2, equal parts of the two elastomers were combined.

Polyvinyl chloride (PVC) (M_w = 120,000, Scientific Polymer) was dissolved in a 60/40 vol% mixture of acetone and n-methyl pyrrolidone (Sigma Aldrich). First, a stock solution at a concentration of 100 mg/mL of PVC in this solvent mixture was formed. Once fully dissolved, MCT or DIDA was added to the solution and the system was homogenized using a vortexer at room temperature. The solution was poured onto glass slides and the solvent was allowed to evaporate on a 40°C hotplate overnight. Polystyrene (PS) (M_w = 190,000, Scientific Polymer) or chlorinated natural rubber (CNR) (Covestro) were dissolved in toluene (Sigma Aldrich) at a concentration of 500 mg/mL. Either MCT or DIDA was added, and the solution was homogenized using a vortexer. The solution was poured onto glass slides and the toluene was allowed to evaporate on a 50°C hotplate overnight. Ethyl cellulose (EC) (Scientific Polymer #142) was dissolved in toluene at a concentration of 100 mg/mL. MCT was added, and the solution was homogenized using a vortexer. The solution was poured onto glass slides and the toluene was allowed to evaporate on a 50°C hotplate overnight.

3.4.2 Swelling and ice adhesion measurement

τ_{ice} was measured following the same procedure as outlined in our previous work[54]. The method is described in detail in Section 2.2.4 above. Crosslink densities were measured by swelling 50-200 mg pieces of the various oil-filled elastomers in excess toluene. After 24 hours the toluene was exchanged to remove any oil extracted from the swollen rubber samples. The weight was recorded daily. Once a constant mass was achieved, the samples were placed in a 120 °C oven under

Table 3.1: ϕ_{oil}^{max} for four elastomers and ten different oils.

Oil	VF40	VF20	CF50	VF20CF50
MCT	.51	.62	.065	.36
DIDA	.50	.60	.041	.34
DUP	.50	.62	.047	.34
Jojoba	.11	.11	.051	.11
Squalane	.08	.09	.035	.11
HL SFO	.29	.39	.059	.15
HO SFO	.17	.24	.027	.09
Silicone	.09	.13	.046	.12
PB-6	.24	.29	.060	.15
EuO	.80	.88	.43	.66

vacuum to remove the toluene. The final mass was recorded after the toluene was completely removed. The swell ratio was defined as the ratio of the swollen mass to the final mass, after the solvent and oil were completely extracted. To determine the maximum solubility of an oil in an elastomer, pieces of the elastomer were placed in vials of excess oil. A similar procedure as above was followed. Note, the higher molecular weight of the oils used in this work necessitated large diffusion times before equilibrium swelling was achieved (up to 8 weeks in some cases). The maximum oil solubilities of 10 different oils within four different rubbers, VF40, VF20, CF50, and a 1:1 w/w% mixture of VF20 and CF50 (denoted VF20CF50), are shown in Table 3.1

3.4.3 Surface fraction determination

The fraction of oil on the surface of the oil-filled elastomers was determined through the method of hemi-wicking using a Ramé-Hart 200-F1 goniometer. A drop of oil was advanced on the surface of an elastomer filled with the same oil. The advancing contact angle was used in place of θ_Y. Use of the advancing contact angle largely avoided any temporal effects (for example swelling of the elastomer during contact angle measurement). The values used to determine ϕ_s were the average of at least 5 measurements and typical error in the measurements was $\pm 2°$. Note that samples containing $\phi_{oil} > \phi_{oil}^{max}$ were necessary to achieve $\phi_s \approx 0$. This occurred partly because we chose to use the advancing contact angle for our measurements, and partly because, at $\phi_{oil} = \phi_{oil}^{max}$, additional oil was required to form a thick film on the surface of the elastomer.

3.4.4 Transparency analysis

Optical transparency of the PVC sample was measured using a Varian Cary 50 Bio UVVis Spectrometer. A scan range of 200-800 nm was probed using a scan rate of 600 nm/s. Glass was used as a baseline.

3.5 Results and discussion

3.5.1 Icephobic elastomers

For an oil that is highly miscible with an elastomer, the $(1-\phi_{oil})^{5/3}$ term dominates Eq. (3.9). As such, even relatively large amounts of oil within the elastomer will not drastically reduce the ice adhesion strength. When no oil is present on the elastomer surface, the decrease will solely depend on the reduction in crosslink density. In this case, Eq. (3.9) would reduce to,

$$\frac{\tau_{ice}^{oil}}{\tau_{ice}^{no-oil}} = (1-\phi_{oil})^{5/3}. \tag{3.10}$$

MCT oil displayed high ($\phi_{oil}^{max} \approx 0.5$) miscibility in the polyurethane rubber Vytaflex 40 (VF40). As Fig. 3.4a clearly shows, Eq. (3.9) was a very good approximation to the ice adhesion strength of VF40 filled with MCT oil, especially for $\phi_{oil} \geq 0.2$. Moreover, although the MCT oil was highly miscible with the rubber, clearly Eq. (3.10) did not fully capture the observed reduction in τ_{ice}. The reduced ice adhesion strength depended on both the crosslink density decrease and the presence of oil on the surface. To contrast this, we also filled a fluorinated polyurethane (FPU) with high-linoleic safflower oil. For this system, the surface energy of the fluorinated network was lower than the surface tension of the plasticizer. As such, the observed ice adhesion strength followed Eq. 3.10 (see Fig. 3.6c below). Note that when the actual surface fraction and crosslink density of the oil-filled elastomers were measured (square symbols in Fig. 3.4, also see Sec. 3.4), our model, or Eq. (3.2), predicted the exact ice adhesion strength of the oil-filled elastomer, within experimental error.

Eq. (3.9) also predicted the ice adhesion strength for elastomer/oil combinations with poor miscibility. In contrast to the highly miscible MCT oil, high-linoleic safflower oil (HL SFO) showed limited solubility within the Vytaflex 40 rubber (a complete oil film formed around $\phi_{oil} \approx 0.2$). However, good agreement was still observed for the VF40/HL SFO system (Fig. 3.4b). We found Eq. (3.9) universally applied to many different elastomer/oil combinations, including PDMS filled with silicone oil (Fig. 3.4c) and the polyurethane rubber Clearflex 50 (CF50) swollen with diisodecyl adipate (DIDA, Fig. 3.4d). Note that in the case of CF50, the ice adhesion strength of the dry elastomer was quite high ($\tau_{ice} > 300$ kPa). Therefore, icephobic elastomers may be fabricated from highly non-icephobic base materials through the addition of a miscible oil, and the effect of the oil is well captured by Eq. (3.9).

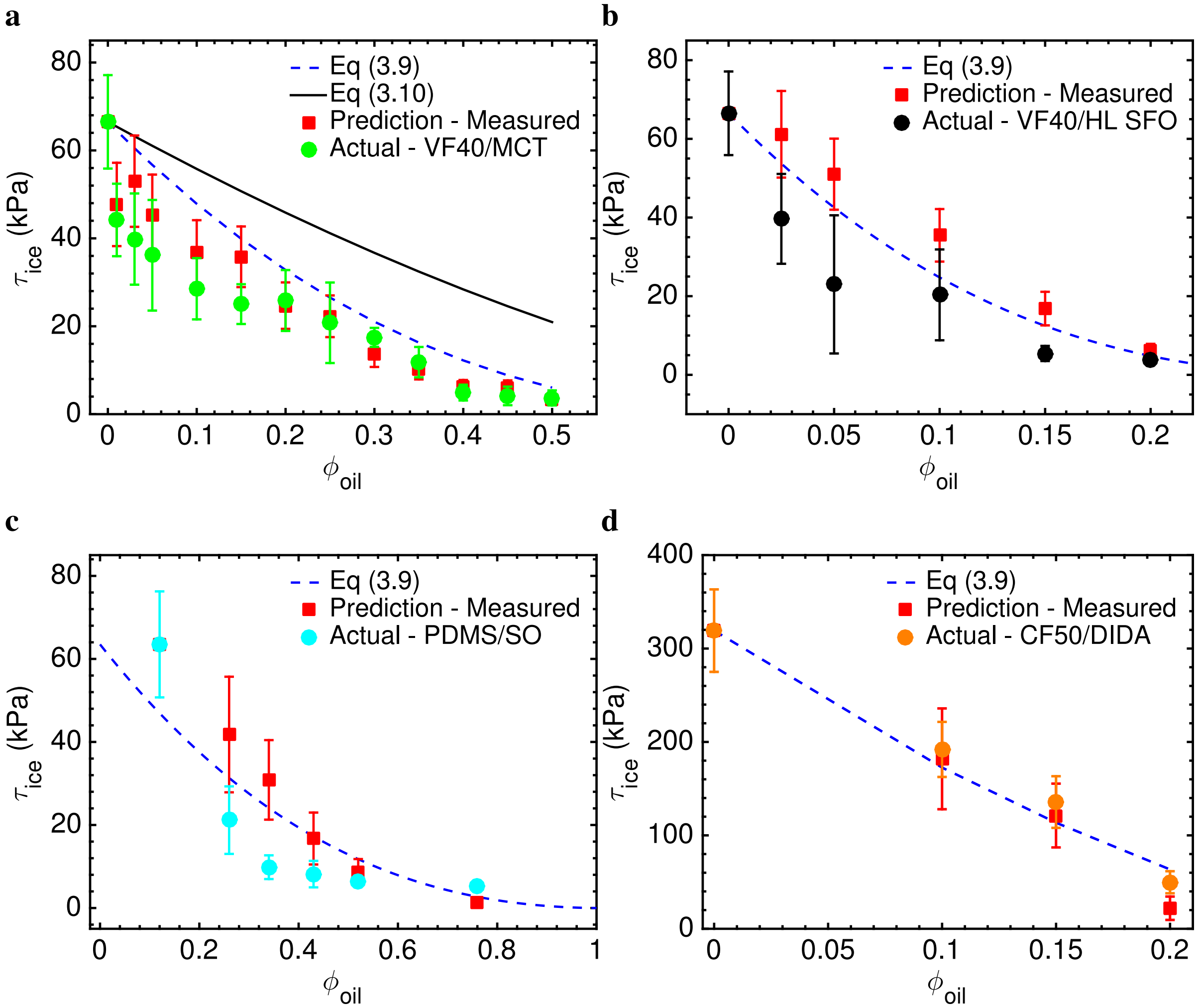

Figure 3.4: Icephobic elastomers. The ice adhesion strength *versus* oil content is shown for four elastomer/oil combinations. a, Vytaflex 40 filled with MCT oil. b, Vytaflex 40 filled with high-linoleic safflower oil. c, PDMS filled with silicone oil. d, ClearFlex 50 filled with DIDA. For all these surfaces, the inputs to Eq. (3.2) can be found by experimentally measuring ρ^{CL} and ϕ_s. The measured predictions using Eq. (3.2) are shown as red squares in a-d.

3.5.2 Icephobic linear polymers

The four systems discussed above were all based on chemically crosslinked rubbers filled with various oils. Quite surprisingly, the applicability of Eq. (3.9) also extended to linear polymers. Linear polymers owe their mechanical properties to crystallinity and the physical entanglement of chains; there are no chemical crosslinks[88]. The mechanical properties can be highly affected by plasticizing agents[97]. We studied the ice adhesion of two common, linear polymers, polyvinyl chloride (PVC) and polystyrene (PS), plasticized with MCT oil or DIDA. Besides the lack of chemical crosslinks, the key difference between the elastomeric rubbers studied above, and the linear polymers studied here, was ϕ_{oil}^{max}. Both MCT oil and DIDA dissolve PS and PVC, meaning $\phi_{oil}^{max} \approx \infty$ for these two plasticizing agents.

When we evaluated the ice adhesion strength of PVC, plasticized with either MCT oil or DIDA, good agreement was still observed with Eq. (3.9) (Fig. 3.5a). Even under the assumption that both oils were infinitely soluble in PVC, making Eq. (3.10) valid, decent agreement was still found between our model and the measured ice adhesion strengths (although Eq. (3.9) was still a better predictor). Allowing ϕ_{oil}^{max} to vary as a free parameter, the best fit to Eq. (3.9) for PVC was $\phi_{oil}^{max} \approx 0.9$ for both plasticizers. Accordingly, PVC plasticized with 85 wt% MCT oil displayed an ice adhesion strength of $\tau_{ice} = 5.2 \pm 2.7$ kPa, although there was no observable free oil layer on the surface of the coating, and the ice adhesion strength did not decrease over 10 icing/de-icing cycles. The PVC/MCT system is particularly promising because, when $0.6 \leq \phi_{oil} \leq 0.9$, the coating is predominantly composed of non-toxic, bio-renewable materials, the material is $> 99\%$ transparent (Fig. 3.5b), the mechanical properties are highly tunable, and the observed ice adhesion strength was always $\tau_{ice} \leq 25$ kPa.

Dissimilar to PVC, PS's mechanical properties were greatly altered by small amounts of plasticizing agents. A mixture of PS + 25 wt% MCT oil or DIDA was a viscous liquid at room temperature ($\tau_{ice} \approx 0$). In contrast, the ice adhesion strength for PVC + 50 wt% MCT oil was $\tau_{ice} > 100$ kPa, because the surface was a semi-rigid plastic. In spite of this difference, Eq. (3.9) still accurately predicted the ice adhesion strength of plasticized PS (Fig. 3.5c), along with other linear polymers like ethyl cellulose and chlorinated natural rubber (Fig. 3.5d).

By normalizing the plasticizer content by ϕ_{oil}^{max}, a few trends became apparent. First, systems with limited oil solubility followed nearly linear reductions in ice adhesion. At low values of ϕ_{oil}, the crosslink density term in Eq. (3.9) is insignificant, and the reduction in τ_{ice} will be dominated by the linear reduction in ϕ_s with increasing ϕ_{oil}. This was observed for the CF50/DIDA, PS/MCT, PS/DIDA and VF40/jojoba combinations. All such systems displayed $\phi_{oil}^{max} \leq 0.2$. Second, because the reduction in τ_{ice} is highly predictable using Eq. (3.9), equally icephobic systems can be designed such that ϕ_{oil} is intentionally very small or very large. A small ϕ_{oil} would require minimal operational changes from the production of the base material. A coating with a large ϕ_{oil} could be environmentally friendly and easily processed, because a majority of the icephobic material could be fabricated from low viscosity, natural oils.

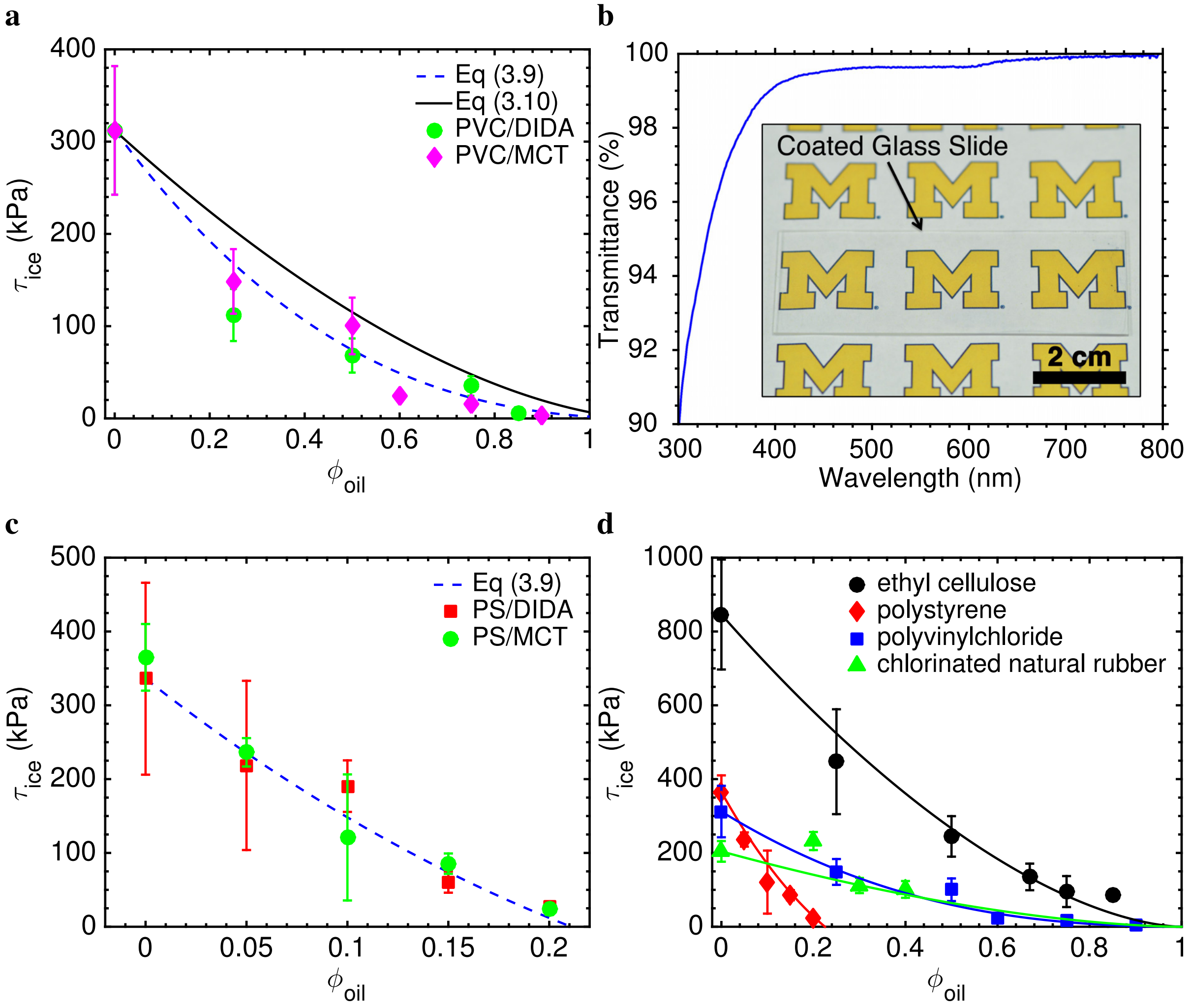

Figure 3.5: Icephobic linear polymers. a, PVC plasticized with MCT oil or DIDA showed good agreement with Eq. (3.9), and excellent icephobicity after $\phi_{oil} \geq 0.5$. b, all the icephobic, linear polymers discussed in this work were $> 98\%$ transparent. Here we show the transmittance *versus* wavelength for PVC plasticized with 50 wt% MCT oil. The inset shows an optical image of the same coating. c, PS became icephobic at very low concentrations of plasticizer, but still fit the proposed theory extremely well. **d,** Excellent agreement was observed between Eq. (3.9) and four polymers plasticized with MCT oil. The solid lines are Eq. (3.9).

3.5.3 Design principles for icephobicity

Designing icephobic elastomers requires knowledge of the inherent ice adhesion strength of the dry elastomer (τ_{ice}^{no-oil}), and the maximum oil content that the elastomer can uptake (ϕ_{oil}^{max}). In Fig. 3.6a we construct a phase diagram for icephobic elastomers. An upper bound to the ice adhesion strength reduction occurs when the oil is infinitely soluble within the elastomer. In this case, Eq. (3.10) describes the minimal possible reduction in τ_{ice} for the elastomer filled with oil. The red region of our phase diagram (Fig. 3.6a) encompasses ice adhesion strengths higher than our model allows. Because the oil can only exist within the bulk of the elastomer, or on its surface, ice adhesion strengths within this regime should never be observed, unless the adhesion of ice to the oil is non-zero. In our previous work[54] we fabricated one such exceptional system: PS filled with liquid, low molecular weight PS ($M_w = 200$ g/mol, coatings AJ and AK in Table 2.1). Upon evaluation of a pure film of this liquid ($\phi_{oil} = 1.0$), we observed $\tau_{ice} \gg 0$. In all of our other systems we have never observed values of τ_{ice}^{oil} in the red region of our icephobicity phase diagram.

If $\phi_{oil} > \phi_{oil}^{max}$, the elastomer's oil capacity has been exceeded, and the surface is necessarily lubricated. Any lubricated system should exhibit an ice adhesion strength less than,

$$\frac{\tau_{ice}^{oil}}{\tau_{ice}^{no-oil}} = (1 - \phi_{oil}^{max})^{5/3}(1 - \alpha). \tag{3.11}$$

This lower bound separates the interfacial slippage regime (green region) from the lubrication regime (blue region) in our phase diagram (Fig. 3.6a). Recall, however, that the ice adhesion strength of lubricated surfaces increases over time[54, 78], making Eq. (3.11) a predictor for the ice adhesion strength that lubricated elastomers will exhibit once their lubricating layer has been removed. Lubricated elastomers may therefore prove advantageous over lubricant-infused surfaces[67, 3]. Lubricant-infused surfaces are based on textured solids for which $\phi_{oil}^{max} \approx 0$, and therefore τ_{ice}^{no-oil} is very high[66, 98]. To illustrate this point, we fabricated lubricated elastomers by over-filling ($\phi_{oil} \gg \phi_{oil}^{max}$) the Vytaflex 40 rubber with four oils of varying miscibility ($\phi_{oil}^{max} =$ 0.07, 0.17, 0.29, or 0.51, for squalane oil, HO SFO, HL SFO, and MCT oil, respectively). All the initial τ_{ice} values were within the predicted lubrication regime (open symbols, Fig. 3.6b). Upon wiping the free oil layer from the surface of the lubricated elastomer, simulating a complete loss of lubricant, we observed exceptional agreement with Eq. (3.11) and the subsequently measured τ_{ice} values of these four elastomer/oil combinations (closed symbols, Fig. 3.6b).

The ice adhesion strength of polymeric systems exhibiting interfacial slippage will always be bounded by Eq. (3.10) and Eq. (3.11). Good agreement was found between these two limiting equations and the ten different systems presented in this study (Fig. 3.6c). The ice adhesion strengths of ten different icephobic formulations, ranging in base material, ϕ_{oil}, and fabrication technique (see Sec. 3.4), are presented in Table 3.2.

As an example highlighting the usefulness of Fig. 3.6, consider some extremely durable elastomer or polymer with $\tau_{ice} = 300$ kPa. This material is not icephobic. For some applications, $\tau_{ice} \leq 30$ kPa is necessary[54, 98, 75]. What oil, and how much oil, should be incorporated for the icephobic coating to achieve this desired ice adhesion strength? According to Fig. 3.6, a reduction in ice adhesion strength to 0.1 necessitates that the coating is at least 47% oil. A coating

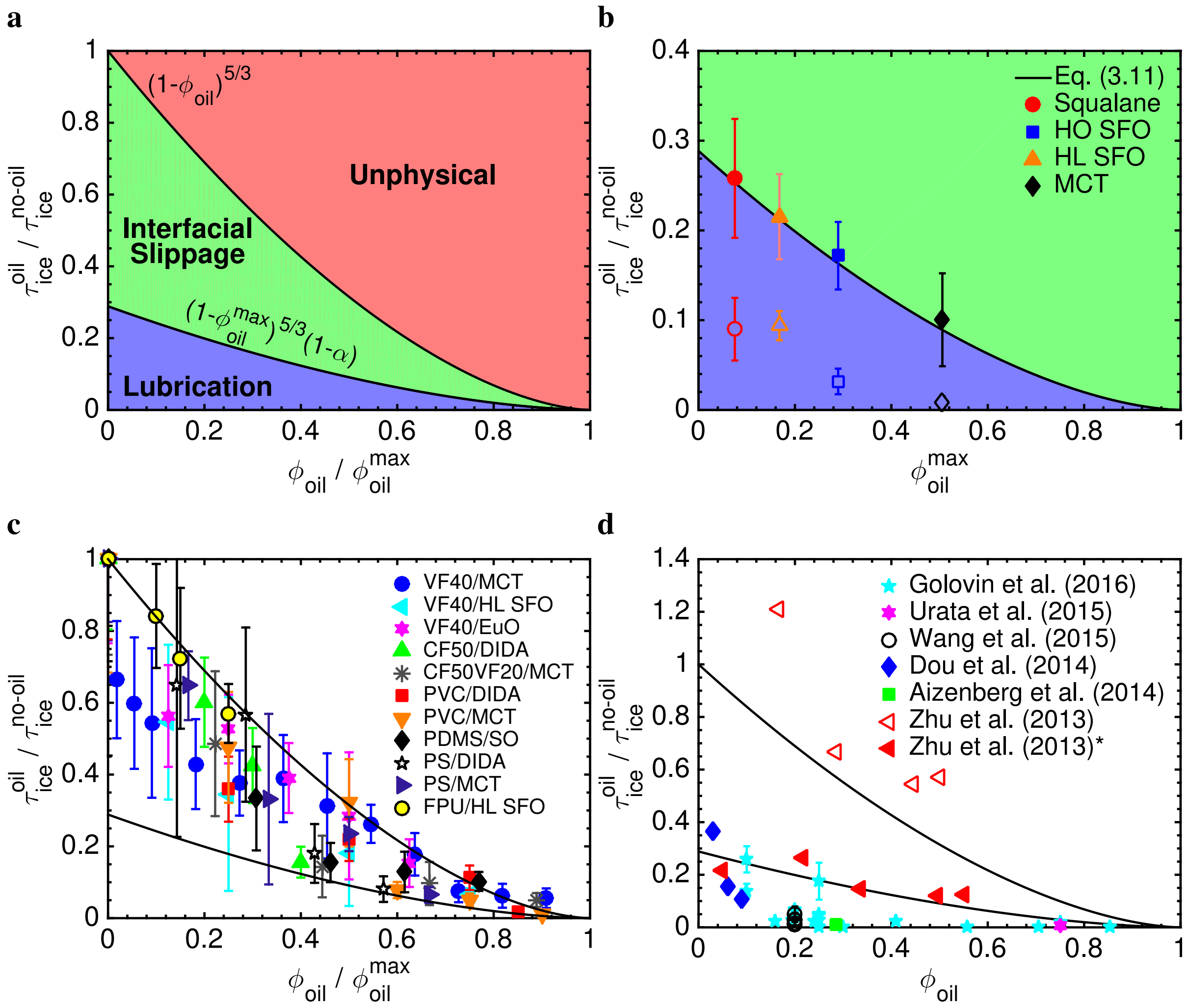

Figure 3.6: Designing icephobic surfaces. a, a phase diagram for oil-filled materials. The regime of possible durability, the green region containing surfaces utilizing interfacial slippage, is bounded by Eq. (3.10) and Eq. (3.11). b, when Vytaflex 40 was lubricated with four oils of differing solubility, the initial τ_{ice} values (open symbols) fell within the lubrication regime. Eq. (3.11) exactly predicted the value that the ice adhesion strength increased to upon wiping away the free oil layer (closed symbols). c, for 10 different elastomer/oil combinations, our measured reductions in τ_{ice} for surfaces that exhibited interfacial slippage were always bounded by Eq. (3.10) and Eq. (3.11). EuO = eucalyptus oil. d, lubricated elastomers from prior studies can initially achieve ultra-low reductions in τ_{ice}, and the reported τ_{ice} values correctly lay in the lubrication region predicted by Eq. (3.11). The data from Zhu *et al.* (2013), re-cast using the literature τ_{ice} value for PDMS, is denoted by an asterisk. For the data of Wang *et al.* (2015), only one ϕ_{oil} value was reported, so all the surfaces have been placed at this value.

Table 3.2: Ten different icephobic systems fabricated in this work.

Base	Oil (ϕ_{oil}^{max})	ϕ_{oil}	τ_{ice} (kPa)
PDMS	Silicone (1.0)	0.5	6.5±1.0
VF40	MCT (0.51)	0.4	4.9±1.8
VF40	HL SFO (0.3)	0.15	4.3±1.0
VF40	Eucalyptus (0.8)	0.5	11±4
CF50	DIDA (0.25)	0.2	50±12
CF50VF20	MCT (0.36)	0.35	9.0±3.0
PVC	DIDA (0.9)*	0.85	5.2±2.7
PVC	MCT (0.86)*	0.75	16±5
PS	DIDA (0.16)*	0.2	27±6
PS	MCT (0.16)*	0.2	24±8

*The ϕ_{oil}^{max} values for plasticized PVC and PS were found using a best fit to Eq. (3.9) and do not represent values obtained by swell tests.

comprised of less than 47% oil will not result in the required ice adhesion strength unless the surface is fully lubricated. No more than 75% oil is necessary, because Eq. (3.10) dictates that an even lower ice adhesion strength will be achieved for $\phi_{oil} \geq 0.75$. Thus, an oil must be selected where $\phi_{oil}^{max} > 0.47$ and the amount of oil added should be $0.47 \leq \phi_{oil} \leq 0.75$. Should this material instead be lubricated, for example with an oil for which $\phi_{oil}^{max} = 0.2$, the ice adhesion strength will increase to $\tau_{ice} \approx 60$ kPa once the oil is depleted, and the coating will become ineffective. PVC, a durable engineering plastic, displayed a non-plasticized ice adhesion strength of $\tau_{ice}^{no-oil} = 312 \pm 70$ kPa. When plasticized with 60 wt% MCT oil, for which $\phi_{oil}^{max} \approx 0.9$, the ice adhesion strength reduced to $\tau_{ice} = 24 \pm 4$ kPa, and did not increase over 10 icing/de-icing cycles. In contrast, CF50 ($\tau_{ice}^{no-oil} = 319 \pm 44$ kPa) lubricated with MCT oil (for which $\phi_{oil}^{max} \approx 0.07$) initially displayed $\tau_{ice} \approx 14$ kPa. When the MCT oil was wiped away, the observed ice adhesion strength increased to $\tau_{ice} \approx 150$ kPa.

The above examples illustrate why engineering surfaces displaying $\tau_{ice} \leq 30$ kPa without lubrication has been challenging in the past. Almost all materials exhibit $\tau_{ice} > 200$ kPa[56], making the choice of oil and oil content necessarily precise. The above examples also illustrate why several lubricated, icephobic systems have been reported[90, 77, 3, 78, 91, 75, 70], whereas we have only recently observed ultra-low ice adhesion strengths without the use of lubrication[54]. In Fig. 3.6d we compile six previous studies on lubricated, icephobic elastomers. Almost all the τ_{ice} values for these lubricated systems fall into the region of lubrication predicted by our phase diagram. Once the lubricants are removed, the ice adhesion strengths should increase to values predicted by Eq. (3.11). Note that the τ_{ice} values for the surfaces created by Zhu *et al.*[70] fall outside the allowable range predicted by our model, even though the surface was a mixture of

PDMS and silicone oil, similar to surfaces in this work (Fig. 3.4c) and in references [77] and [91]. The ice adhesion of the unfilled PDMS in the work of Zhu *et al.* was reported to be $\tau_{ice} = 55$ kPa, much lower than the accepted literature value of $\tau_{ice} = 250 - 300$ kPa[54, 56, 69]. It is likely that unreacted siloxane chains enabled interfacial slippage in their unfilled PDMS, a commonly reported phenomenon[54, 81]. Recasting their data using the literature value for the ice adhesion strength of PDMS placed their measured τ_{ice} values correctly near the lubrication regime.

3.6 Conclusions

In this work we have modeled the mechanism of interfacial slippage that allows oil-filled elastomers to exhibit remarkably low ice adhesion strengths. The addition of oil lowers the ice adhesion in two ways: by lowering the effective crosslink density of the elastomer, and by making only a fraction of the elastomer's surface available to adhere to ice. Excellent agreement was observed between our model, Eq. (3.9), and a wide range of elastomers and linear polymers filled with various oils. Moreover, the use of Eq. (3.11) allows lubricated systems to be fabricated with full knowledge of their expected ice adhesion strength once the lubricant becomes depleted. Overall, our proposed model will allow for a wide range of icephobic materials to be fabricated from essentially any chemistry and base components. Many of the formulations exemplified in this work may find immediate usage for solving the ice accretion problem in a host of different sectors worldwide. One caveat, however, is that lowering the ice adhesion strength of a given material only lowers the required force to remove the accreted ice *per unit area*. Because ice adhesion scales with interfacial area, the total force required to de-bond ice from large structures may be prohibitively high. In the next chapter we address this issue, and develop a new method for repelling ice accretion on large-scale surfaces.

CHAPTER 4

Designing Anti-Icing Surfaces Exhibiting Low Interfacial Toughness with Ice

4.1 Introduction

The goal of this chapter is to understand and develop a new class of anti-icing materials based on surfaces that exhibit low interfacial toughness (LIT) with ice. In contrast to what we have previously termed as icephobic surfaces in Chapters 2 and 3 (*i.e.* surfaces with low ice adhesion *strength*), the force required to detach ice from LIT materials can be independent of the interfacial area. As part of this work, we will first investigate the interfacial toughness between ice and many common engineering materials. We will then modify these materials to lower the toughness of their interfaces with ice. Some of the materials fabricated in this work display an interfacial toughness approaching the theoretical lower limit of 0.1 J/m^2 (purely van der Waals interactions)[99].

The accretion of ice significantly hinders many industrial and residential activities across the globe[63, 100, 101, 102]. Airplane wings, wind turbine blades, automotive windshields, boat hulls, and power lines are just a few examples of technologies that are routinely plagued by the accumulation of unwanted ice[54]. The adhesive strength between ice and a given material, τ_{ice}, is typically defined as the shear force required to remove a unit area of adhered ice[72]. Since the 1950s[103], a single value of τ_{ice} has always been reported for a given material system. Recently, a new class of materials, icephobic surfaces, have shown promise for their ability to significantly lower τ_{ice}, sometimes by several orders of magnitude[98, 100, 54, 56, 67, 77, 104]. However, attempting to minimize τ_{ice} will always run into the same problem: the force required to overcome the adhesive strength of the iced surface increases with the interfacial area[72, 56]. Therefore, large areas will require prohibitively high detachment forces. Part of this work will disprove this commonly held belief, and we will show that certain material systems may achieve virtually any desired ice adhesion strength.

The field of interfacial fracture mechanics, developed outside the ice-adhesion community, has focused on the role of interfacial toughness, rather than adhesive strength, as an important fracture parameter [61, 105]. In this work, we study materials that exhibit low interfacial toughness with ice, such that the loss of adhesion is controlled by crack propagation at the ice interface, resulting in a force to detach the ice that may be independent of the adhesive bond length[106, 61, 105].

Cohesive-zone models bring both the concepts of strength and toughness into models of adhesion [107, 108, 109]. These models allow one to rationalize the behavior of interfaces as a function of scale, to describe both icephobic surfaces, which display a constant τ_{ice}, as well as LIT materials, that display a constant detachment force, regardless of length. It will be noted that, for these latter systems, the apparent ice adhesion strength decreases with the length of accreted ice, to the point where it may become lower than τ_{ice} for icephobic systems. For large-scale applications, the force required to remove an area of accreted ice can then be several orders of magnitude lower. However, LIT materials have never been studied for de-icing applications, and before this work, the interfacial toughness between ice and essentially all materials was unknown.

In Chapters 2 and 3 we fabricated icephobic surfaces with some of the lowest τ_{ice} values ever reported. Our model in Chapter 3 allows one to rationally design τ_{ice} for effectively any polymeric system. However, because icephobic materials are characterized by τ_{ice}, a shear *stress*, an increase in area necessitates a proportional increase in the applied force required to remove the ice. Typically, the shear force experienced on iced materials does not scale with the area that is iced. For example, the centripetal force experienced by a wind turbine blade scales with the length of the blade, whereas the shear stress scales with the blade area[110]. As a further example, the wind shear experienced by an airplane wing during takeoff does not scale with the size of the wing, but instead with the speed of the plane[111]. Therefore, large-scale systems may require a prohibitively high force to remove accreted ice, even from an icephobic surface. The wing of a Boeing 747 has an area of 2,750 m^2 when viewed from above[112]. If this wing were coated with an icephobic system exhibiting $\tau_{ice} = 1$ kPa, the removal of ice would still require a force of approximately 3 MN. Surfaces that require a constant force of ice detachment, irrespective of area, would therefore be highly desirable. However, such surfaces have never been discussed in the ice-adhesion literature. Here we show that such surfaces are a natural result of a full understanding of the interfacial mechanics, and we perform a detailed study of these materials, with a focus on how to design and fabricate surfaces for different applications and length scales.

4.1.1 Fracture mechanics of interfaces

The bonding across an interface is characterized by two physical properties: the strength (N/m^2) (maximum value of the bonding tractions), and the toughness (J/m^2) (area under the traction-displacement curve for an interface)[107, 113, 114]. For the interface between ice and a material, we will refer to its interfacial adhesion strength, τ_{ice}, and its interfacial toughness, Γ_{ice}. It is

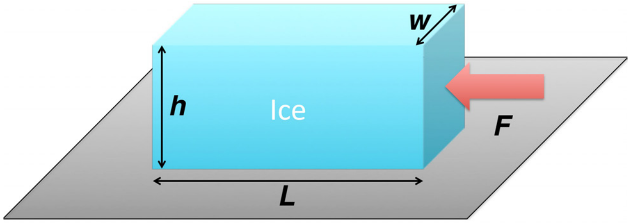

Figure 4.1: A schematic of the situation currently being investigated. In many of our experiments, $L \gg w$.

recognized that adhesion is typically a mixed-mode problem, involving both shear (mode-II) and normal (mode-I) components. For the purposes of the current discussion, this issue will be ignored.

Whether strength or toughness controls the fracture of an interface depends on the scale of the interface compared to what is known as the cohesive-length scale, $\xi = \bar{E}\Gamma_{ice}/\tau_{ice}^2$, where $\bar{E}$ is the effective modulus of the interface[108, 109]. If the bonded length is much bigger than ξ, the toughness of the interface controls fracture. If the bonded length is much smaller than this quantity, then the strength controls fracture. This concept can be illustrated by the following discussion:

Consider the block of ice shown in Fig. 4.1, with an interface that can be fractured. As we have normally assumed in the previous two chapters, the required force (per unit width) to remove the ice is,

$$F/w = \tilde{F}_{ice} = \tau_{ice} L \tag{4.1}$$

where w is the width of ice (normal to the direction of the force), and L is the length of ice (along the axis of the applied load). The interfacial area is given by wL. From now on we shall consider the two dimensional case, and we denote the force per unit width as $\tilde{F}_{ice}$. Eq. 4.1 is a strength-based argument, and assumes any initial de-bond a (such as a crack or cavity) is such that $a \ll L$[105].

In contrast, consider an interface that fails by the propagation of a crack. A crack will advance along an interface if the potential energy of the system decreases by an amount greater than the increase in energy associated with the creation of new surfaces[114]. In this case, the force (per unit width) required to de-bond the ice has been shown to follow[115],

$$\tilde{F}_{ice} = \sqrt{\bar{E}\Gamma_{ice}} L^{3/2} f(h/L) \tag{4.2}$$

where h is the thickness of the ice, and f is a function of geometry. Although the strength and the toughness both control the fracture of an interface, the force required to detach the ice will be given by the smaller value of Equations 4.1 and 4.2. For geometrically similar materials, this leads to a dependence of apparent strength on size given by Fig. 4.2A. The adhesive bond of an interface is controlled by strength for small structures until a critical length, L_c, is reached. Beyond

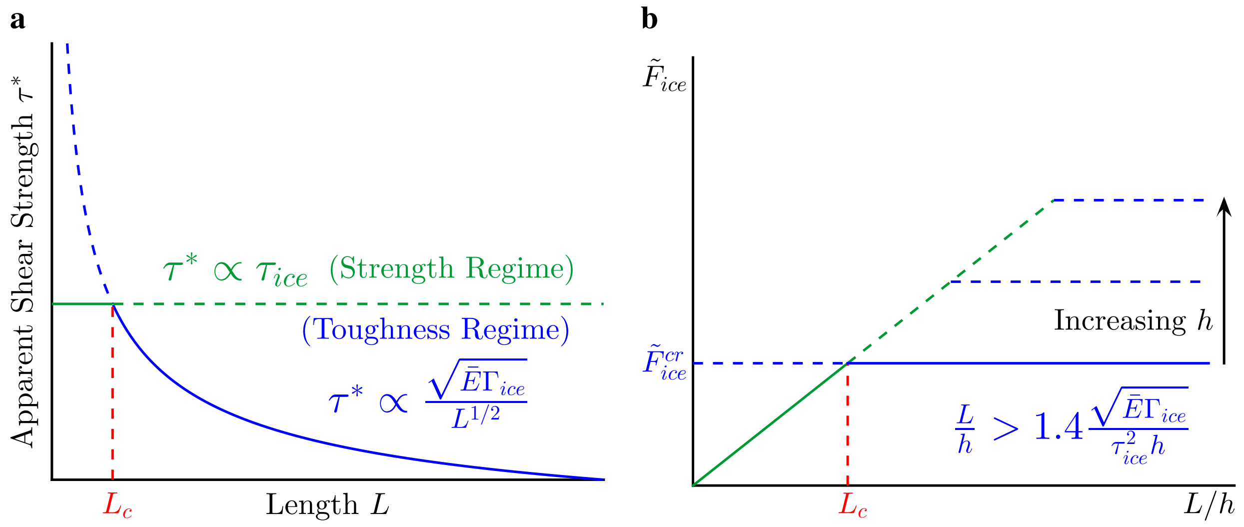

Figure 4.2: a, the apparent shear strength of an interface as a function of its length. Before L_c, the interface is controlled by strength and the apparent shear strength is constant. At lengths exceeding the critical length, the shear stress decreases with an inverse square root dependence[10]. b, the force (per unit width) required to fracture an interface increases linearly with length until L_c. Beyond L_c, the interface fails by crack propagation and the force required to propagate the crack is independent of length. Increasing the height (thickness of ice) causes L_c to increase, but the force still plateaus above some critical length.

L_c, toughness dominates the interfacial fracture and the *apparent* adhesive strength, which we will denote by a superscript asterisk (τ_{ice}^*), will decrease as the length increases. In terms of the applied load, the force required to detach ice at small interfacial lengths is proportional to the length of the interface (Fig. 4.2B). Beyond L_c, fracture occurs solely by crack propagation, and the necessary force of detachment becomes independent of the length of the adhered ice, $\tilde{F}_{ice}^{cr}$.

Assuming the thickness of the adhered ice is small, the problem can be treated as a thin-film geometry. Once the size of the crack grows to more than a few times the ice thickness, Eq. 4.2 may be simplified to[116, 10],

$$\tilde{F}_{ice}^{cr} \approx 1.4\sqrt{\bar{E}\Gamma_{ice}h}. \tag{4.3}$$

Thus, for thin-film geometries, by equating Eq. 4.1 and Eq. 4.3, the critical length may be found by,

$$L_c \approx 1.4\sqrt{\bar{E}\Gamma_{ice}h/\tau_{ice}^2}. \tag{4.4}$$

Below L_c, fracture of the interfacial bond is controlled by τ_{ice}, and beyond L_c, it is controlled by Γ_{ice}. This is consistent with experimental results that have been obtained for how the lap-shear strength of a joint depends on bond length[115]. Whether one needs a low-strength material or a low-toughness material, in order to optimize the de-icing properties of a system, depends on how the bond length compares to L_c.

4.2 Materials and methods

4.2.1 Materials and synthesis

Mold Max STROKE (Smooth-On Inc.) was mixed in a 10:1 base:crosslinker ratio, per manufacturer instructions. 2 mL of toluene was added to 10 g of total material, and the mixture was vortexed until homogeneous. The solution was then poured onto Al metal substrates measuring $6 \times 22 \times 0.08$ cm. To fabricate a more icephobic system, the same procedure as above was followed but with a 40 wt% silicone oil (100 cP, Sigma Aldrich) mixture of the Mold Max STROKE. Both these systems were cured at room temperature over night. For visualization, Oil-Red-O dye (Alfa Aesar) was added to the toluene (10 mg/mL) before mixing with the silicone rubber. To fabricate a much thinner ($t \approx 1$ μm) sample, a solution of Mold Max STROKE and 40 wt% silicone oil was formed in hexane at an overall concentration of 25 mg/mL. Note that the typical thickness of these coatings without dilution is ≈ 1 mm.

Icephobic PDMS was fabricated from Sylgard 184 (Dow Corning) in a 10:1 base:crosslinker ratio, per manufacturer instructions. The mixture was vortexed until homogeneous, degassed to remove bubbles, and poured onto the same size Al substrates as above. The sample was then cured at 150 °C for 1 hour. For icephobic Sylgard 184, 25 wt% silicone oil (100 cP, Sigma Aldrich) was used (similar to coating I from Table 2.1 in Chapter 2).

We also evaluated the interfacial properties between ice and many different engineering plastics. All were purchased from McMaster at a thickness of 1.58 mm and included: ultra-high molecular weight polyethylene (UHMWPE), low density polyethylene (LDPE), polypropylene (PP), polycarbonate (PC), polystyrene (PS), polymethylmethacrylate (PMMA), glycol-modified polyethylene terephthalate (PETG), nylon, acrylonitrile butadiene styrene (ABS), polyvinylchloride (PVC), chlorinated polyvinylchloride (CPVC), and polytetrafluoroethylene (PTFE).

To fabricate plasticized PVC, polyvinyl chloride (M_w = 120,000, Scientific Polymer) was dissolved in a 60/40 vol% mixture of acetone and n-methyl pyrrolidone (Sigma Aldrich) at concentrations of 200 mg/mL, 100 mg/mL, 50 mg/mL, and 25 mg/mL. Once fully dissolved, MCT was added to the solution at 50 wt%, and the system was homogenized using a vortexer at room temperature. The solutions were then poured onto aluminum substrates. The coated Al samples were placed on a 35 °C hotplate for 10 minutes to evaporate the acetone, and then a 70 °C hotplate over night to remove the NMP. This resulted in coatings all exhibiting roughly $\theta_{adv}/\theta_{rec} = 92^\circ/80^\circ$, but with variable thickness, from about 1 μm to about 150 μm.

4.2.2 Ice adhesion measurement

The measurement of τ_{ice} or $\tilde{F}_{ice}$ was conducted similarly to the procedure used in Sec. 2.2.4 of Chapter 2. However, two minor differences are worth noting. First, to observe a critical length during ice adhesion testing, a larger Peltier plate system was required. The new Peltier plate system used in this work measured 22 cm in length and 6 cm in width (Fig. 4.3). Second, to evaluate different lengths of interfacial area in a relatively short amount of time, the entire substrate was used for ice adhesion testing. For example, in Fig. 4.3 we show a typical test, where 11 different pieces of ice are all frozen together. By always placing shorter length samples closer to the force gauge arm, and therefore dislodging them before the longer length samples, we confirmed that the measurements did not affect one another. In all experiments, the height and width of ice were fixed at $h = 0.6$ cm and $w = 1$ cm, respectively.

4.2.3 Surface analysis

Advancing and receding contact angles were measured using a Ramé-Hart 200 F1 contact angle goniometer. Scanning electron microscopy (SEM) was performed using a Phillips XL30 FEG. Surface profilometry was performed using an Olympus LEXT interferometer with a step size of 1.25 μm and an overall scan area of 1.3 × 1.3 mm. Three different locations were averaged. The root mean squared roughness, S_q, was determined from the height-maps generated by the microscope. The data was flattened and noise was removed before calculating S_q. The thickness of the samples was measured using either a micrometer (for samples where the coating could be delaminated), or in cross-section using SEM. An average of six different locations was reported.

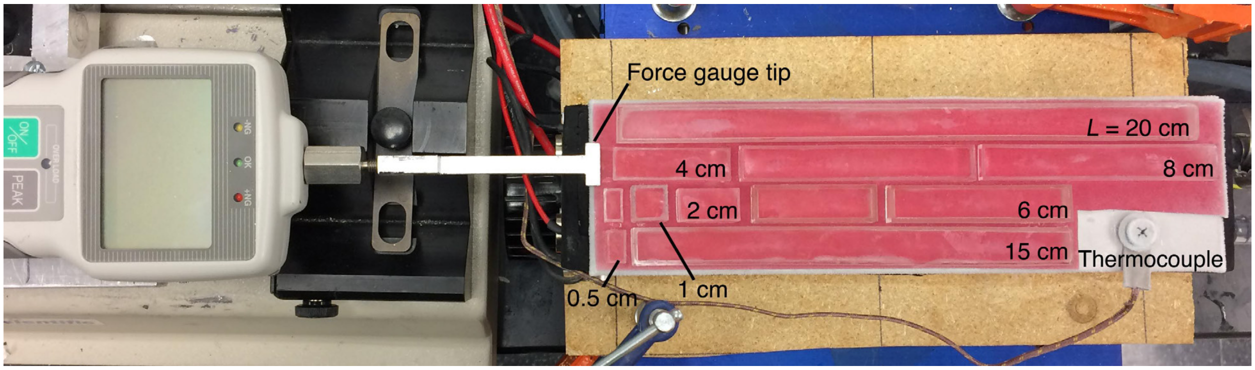

Figure 4.3: The modified setup capable of measuring specimens varying in length. Here 11 pieces of ice (8 different lengths) were frozen to a Mold Max STROKE sample (dyed red for visualization).

4.2.4 Statistical analysis

Error bars were obtained for each length of ice evaluated by testing a minimum of five points per length. Dissimilar to the method used in Chapter 2, τ_{ice} is given by the slope of the $\tilde{F}_{ice}$ vs L curve in the strength regime, *i.e.* Eq. 4.1. Often times it was ambiguous if lengths very close to L_c were within the strength regime (and should therefore be taken into the linear fit). For consistency, lengths were included within the linear fit that minimized the overall error in the measurement of τ_{ice}. The error in the ice adhesion strength, $\sigma_{\tau_{ice}}$, was found using[117],

$$\sigma_{\tau_{ice}} = \sqrt{\frac{1}{\Delta}\sum\frac{1}{\sigma_L^2}} \tag{4.5}$$

where σ_L is the standard deviation in the measurement of the force of detachment recorded at each length of ice, and Δ is given by[117],

$$\Delta = \sum\frac{1}{\sigma_L^2}\sum\frac{F_L^2}{\sigma_L^2} - \Big(\sum\frac{F_L}{\sigma_L}\Big)^2 \tag{4.6}$$

with F_L being the mean force per unit width measured at each length L of ice.

L_c was found from the intersection of the linear fit in the strength regime and the mean value of $\tilde{F}_{ice}^{cr}$ in the toughness regime. Once the best fit for τ_{ice} was found using the method described above, $\tilde{F}_{ice}^{cr}$ was determined by averaging the recorded $\tilde{F}_{ice}$ values for all $L > L_c$. Error in the intercept of the best fit line, σ_{τ_b}, for τ_{ice} was found using[117],

$$\sigma_{\tau_b} = \sqrt{\frac{1}{\Delta}\sum\frac{F_L^2}{\sigma_L^2}}. \tag{4.7}$$

Error in L_c was then found in the following way. We assumed the value of $\tilde{F}_{ice}^{cr}$ to be correct, and perturbed τ_{ice} using $\sigma_{\tau_{ice}}$ and σ_{τ_b}. We computed the maximum and minimum deviations from L_c using $y_{max} = (m - \delta m)x + b - \delta b$ and $y_{min} = (m + \delta m)x + b + \delta b$, where the best fit for τ_{ice} is given by the line $y = mx + b$, and the error in slope and intercept are $\delta m = \sigma_{\tau_{ice}}$ and $\delta b = \sigma_{\tau_b}$, respectively. L_c^{max} and L_c^{min} are found from the intersection of these deviated lines with $\tilde{F}_{ice}^{cr}$. We then set the error in L_c as $\sigma_{L_c} = \frac{1}{2}(L_c^{max} + L_c^{min})$.

4.3 Results and discussion

4.3.1 Ice adhesion of icephobic surfaces as a function of length

We initially measured $\tilde{F}_{ice}$ for various lengths of ice on a number of different icephobic surfaces, like the ones developed in Chapters 2 and 3. Results are presented in Figs. 4.4-4.7. Similar to Fig. 4.2 above, we plot both $\tilde{F}_{ice}$ and τ^*_{ice} against the length of the ice. For all the icephobic systems we evaluated, $\tilde{F}_{ice}$ linearly increased with L up until our maximum experimental length of $L = 20$ cm. Accordingly, τ^*_{ice} remained constant for each icephobic surface over this entire range of lengths. As such, ice be-bonded from all these materials by adhesive *strength* ($\tau^*_{ice} = \tau_{ice}$).

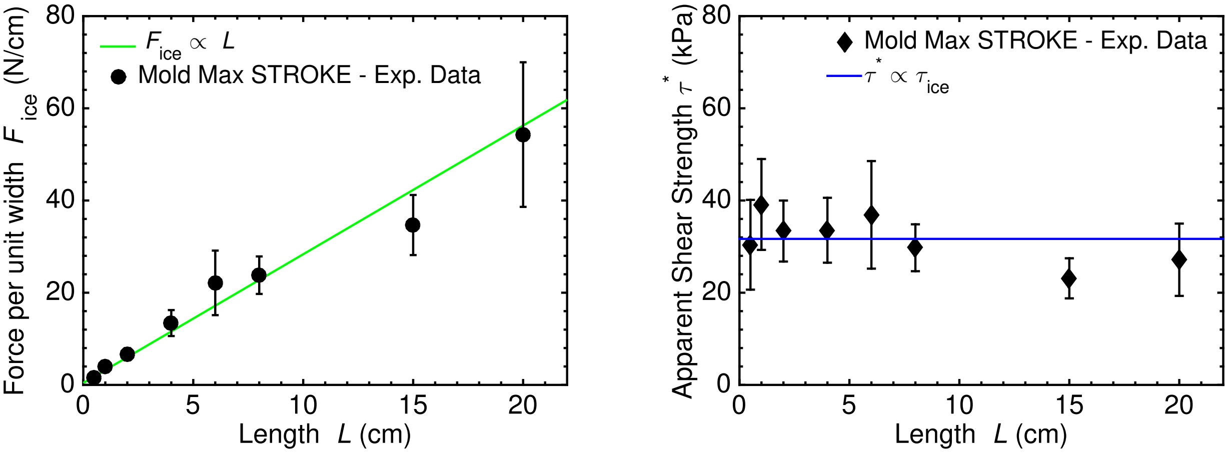

Figure 4.4: (left) The force per unit width to detach ice from a silicone rubber (Mold Max STROKE). (right) The apparent ice adhesion strength of Mold Max STROKE. No critical length was observed, and $\tau^*_{ice} = \tau_{ice} = 28 \pm 3$ kPa.

The issue with icephobic surfaces became apparent in Fig. 4.7 especially. This system displayed $\tau_{ice} = 71 \pm 1$ kPa for $0.5 \leq L \leq 20$ cm. However, the force required to de-bond the ice at $L = 20$ cm was $\tilde{F}_{ice} = 128 \pm 18$ N/cm. This extremely high force will eventually become prohibitively high, either in practice or due to the cohesive failure of ice[118]. Indeed, as shown in Fig. 4.6, the material Sylgard 184 (PDMS) displayed $\tau_{ice} = 117 \pm 23$ kPa for $L \leq 15$ cm. However, when we tried to measure τ_{ice} for $L = 20$ cm, ice failed cohesively for the majority of samples (*i.e.* the fracture surface was along an ice-ice interface, and a sheet of ice remained adhered to the underlying surface after fracture).

The cohesive strength of ice has been measured previously as $\Gamma_{ice} = 1 - 3$ J/m^2[118, 119, 120, 121, 122]. Substituting $\Gamma_{ice} = 3$ J/m^2 into Eq. 4.4 yields $L_c = 14.8$ cm, for the Sylgard 184 material. As such, ice will not un-adhere from this material for lengths $L > 14.8$ cm, even though $\tau_{ice} \approx 100$ kPa. This result clashes with over 60 years of ice adhesion studies, but is well explained by our fracture mechanics analysis.

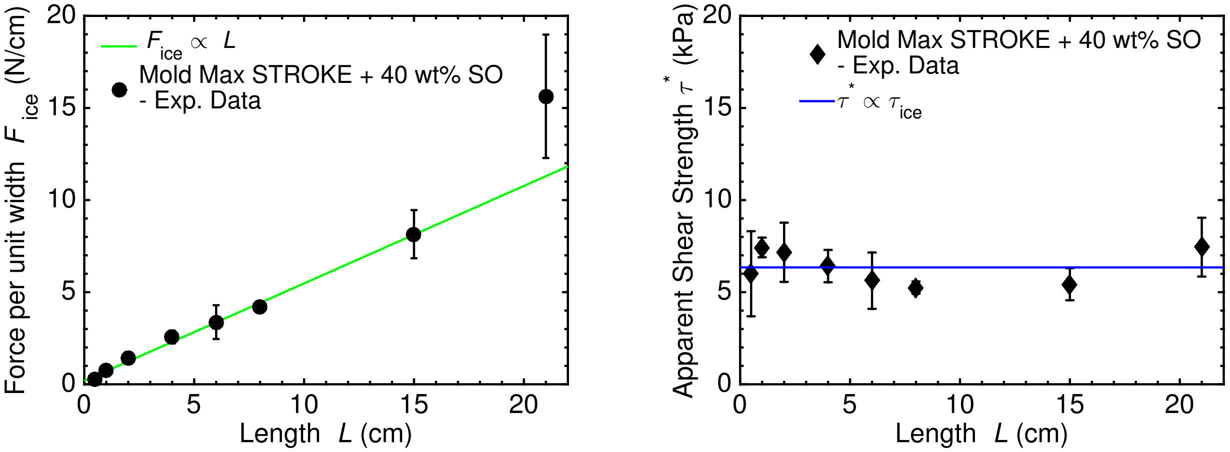

Figure 4.5: (left) The force per unit width to detach ice from an icephobic silicone rubber (Mold Max STROKE filled with 40 wt% silicone oil). (right) The apparent ice adhesion strength of this surface. No critical length was observed, and $\tau^*_{ice} = \tau_{ice} = 5.3 \pm 0.3$ kPa.

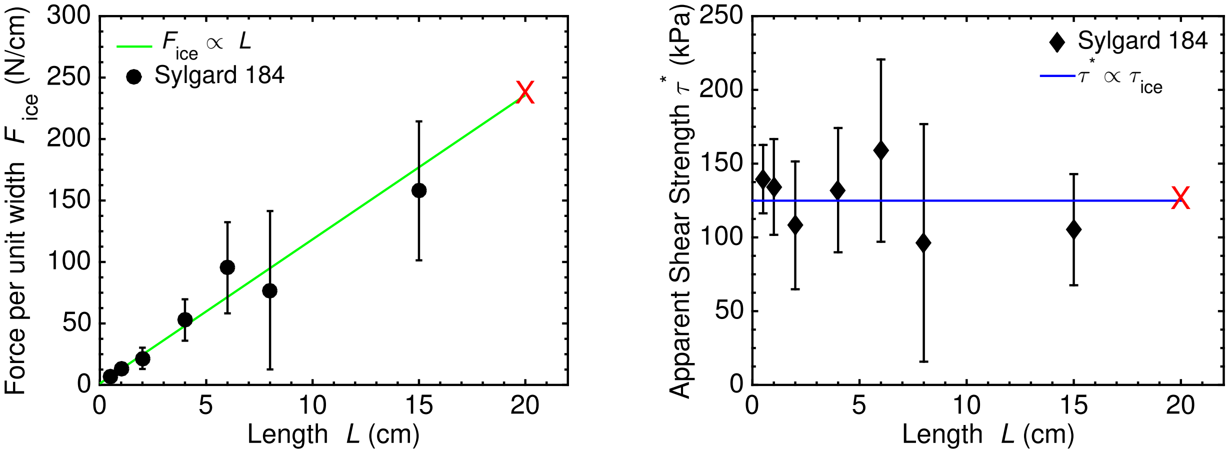

Figure 4.6: (left) The force per unit width to detach ice from PDMS (Sylgard 184). (right) The apparent ice adhesion strength of Sylgard 184. No critical length was observed, and $\tau^*_{ice} = \tau_{ice} = 117 \pm 23$ kPa. Note that after $L = 15$ cm, ice failed cohesively.

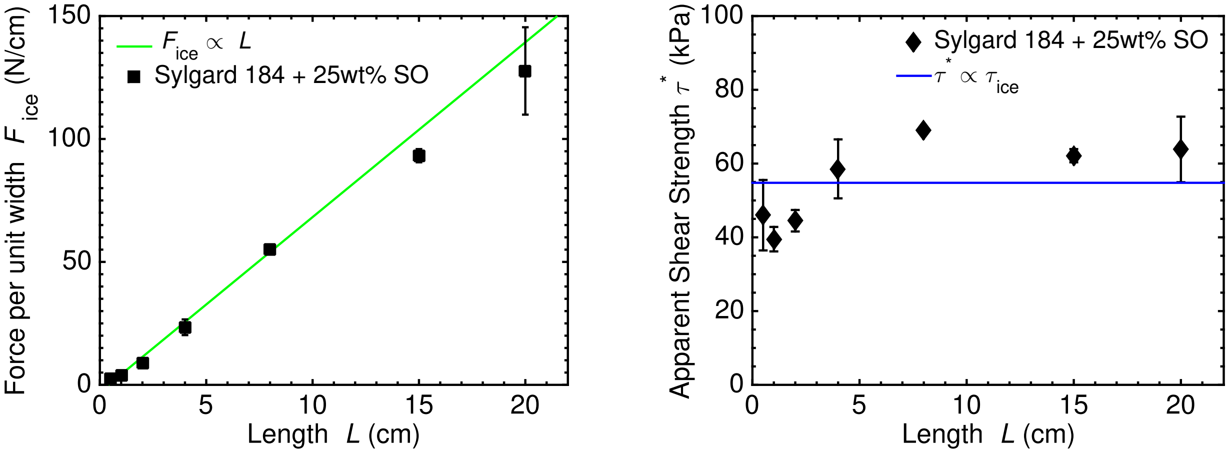

Figure 4.7: (left) The force per unit width to detach ice from icephobic PDMS (Sylgard 184 + 25 wt% silicone oil). (right) The apparent ice adhesion strength of this surface. No critical length was observed, and $\tau^*_{ice} = \tau_{ice} = 71 \pm 7$ kPa.

As a side note, we point out that using the slope of the force (per unit width) versus length plot allows for a very accurate τ_{ice} to be measured. In Figs. 4.4-4.7 above, and especially in Figs. 4.8-4.13 below, the accuracy of τ_{ice} for any single length is typically $25 - 50\%$. Using the best fit for τ_{ice} suggested here greatly reduced this error. Moreover, a greater area of the sample is necessarily sampled, making the result more representative of the entire surface. This is in stark contrast to other ice adhesion setups, including the one used in Chapters 2 and 3[54].

4.3.2 Ice adhesion of engineering plastics

We also measured the adhesion of ice to common engineering plastics like PP, PS, and PE (Sec. 4.2). Dissimilar to icephobic systems, these materials displayed high τ_{ice} values (Figs. 4.8-4.13). For example, for UHMWPE, $\tau_{ice} = 221 \pm 38$ kPa (Fig. 4.8). For 1 cm^2 of ice, τ_{ice} is about 3× greater than the icephobic Sylgard 184 + 25 wt% silicone oil surface (Fig. 4.7). However, for each of these plastics, a critical length was observed (Table 4.1).

The length at which the force became independent of the length varied from $L_c = 2.5$ cm, for ABS, to $L_c = 9.3$ cm, for PVC. From this asymptotic $\tilde{F}^{cr}_{ice}$ value, the interfacial toughness can be calculated by[61],

$$\Gamma_{ice} = \frac{(\tilde{F}^{cr}_{ice})^2}{2E_{ice}h} \tag{4.8}$$

where E_{ice} is the elastic modulus of ice ($\approx$ 8.5 GPa)[118]. Γ_{ice} for the polymers we evaluated ranged from $\Gamma_{ice} = 0.5$ J/m^2, for UHMWPE, to $\Gamma_{ice} = 5.1$ J/m^2, for PVC. However, as we did not observe a critical length for some of our icephobic systems, we note the minimum possible value for Γ_{ice} in Table 4.1 by substituting the force of detachment registered at $L = 20$ cm into Eq. 4.8.

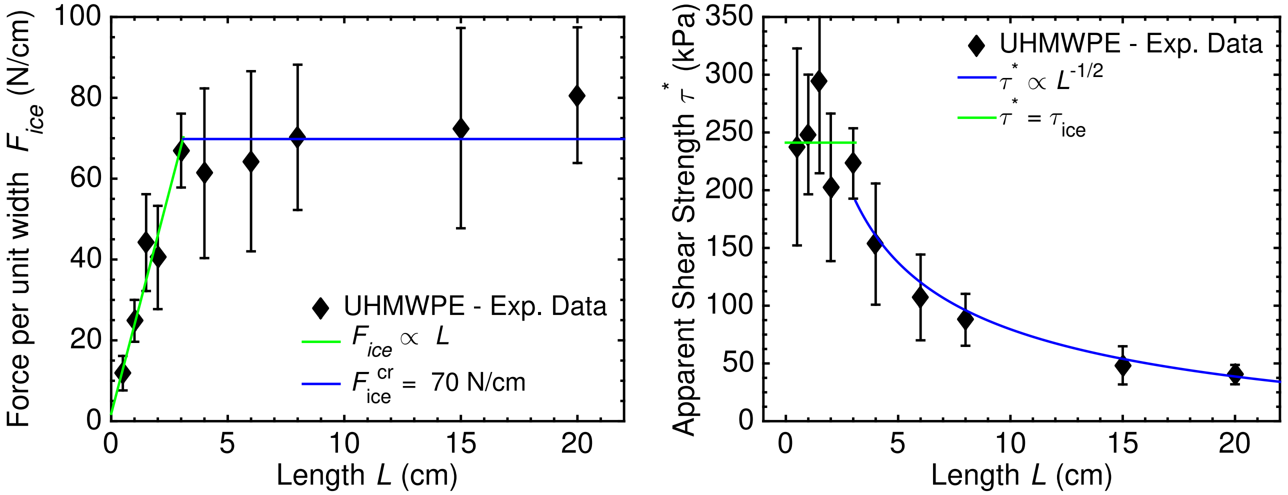

Figure 4.8: (left) The force per unit width required to detach ice from UHMWPE. (right) The apparent ice adhesion strength of UHMWPE. After $L_c = 3.1$ cm, the force becomes constant, and τ^*_{ice} begins to decrease. At $L = 20$ cm, $\tau^*_{ice} = 40 \pm 8$ kPa.

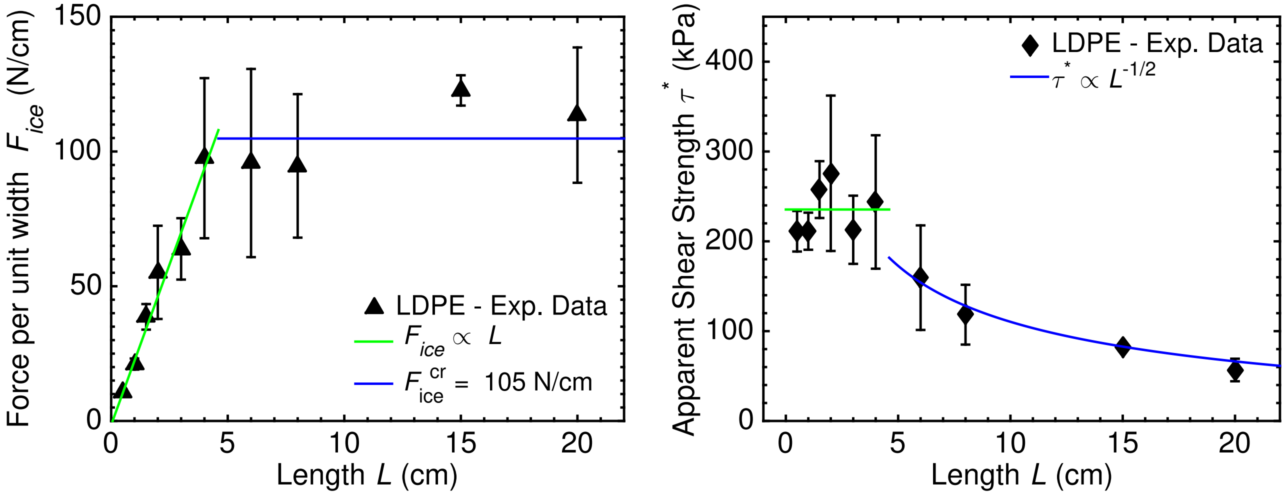

Figure 4.9: (left) The force per unit width required to detach ice from LDPE. (right) The apparent ice adhesion strength of LDPE. After $L_c = 4.6$ cm, the force becomes constant, and τ^*_{ice} begins to decrease. At $L = 20$ cm, $\tau^*_{ice} = 57 \pm 13$ kPa.

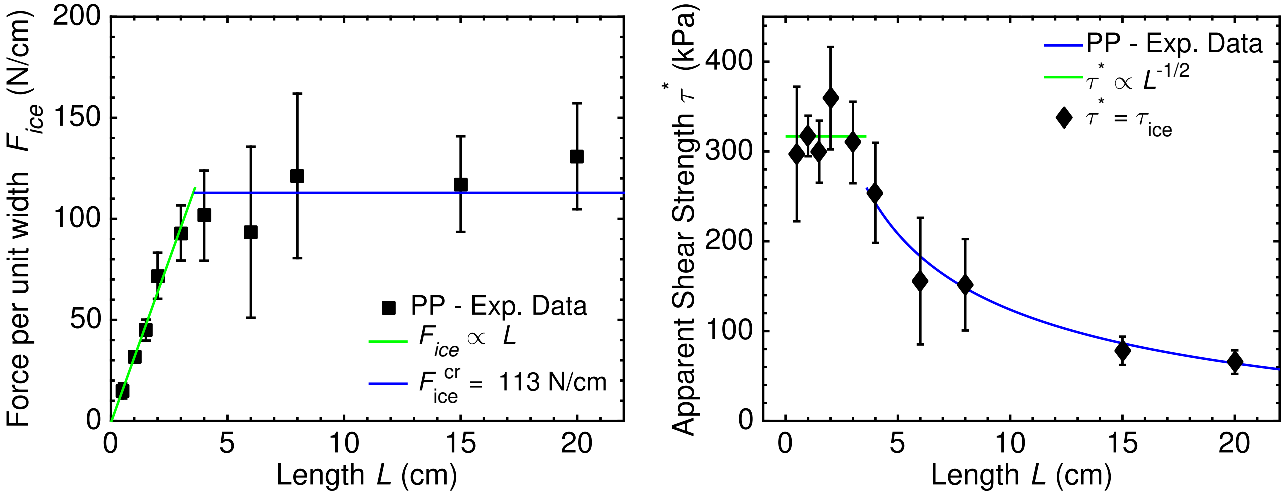

Figure 4.10: (left) The force per unit width required to detach ice from PP. (right) The apparent ice adhesion strength of PP. After $L_c = 3.6$ cm, the force becomes constant, and τ_{ice}^* begins to decrease. At $L = 20$ cm, $\tau_{ice}^* = 65 \pm 13$ kPa.

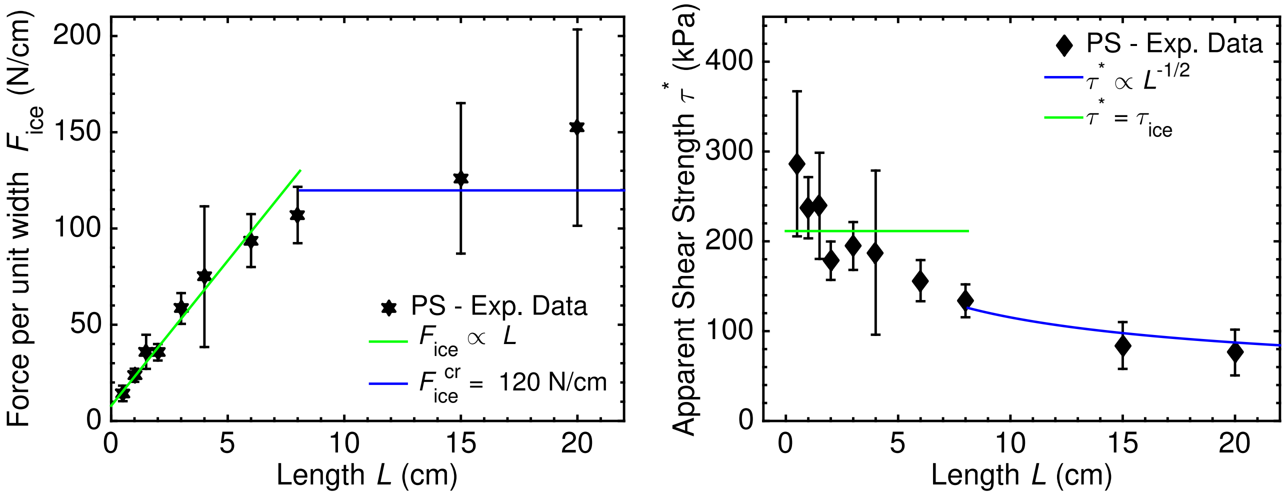

Figure 4.11: (left) The force per unit width required to detach ice from PS. (right) The apparent ice adhesion strength of PS. After $L_c = 8.1$ cm, the force becomes constant, and τ_{ice}^* begins to decrease. At $L = 20$ cm, $\tau_{ice}^* = 76 \pm 25$ kPa.

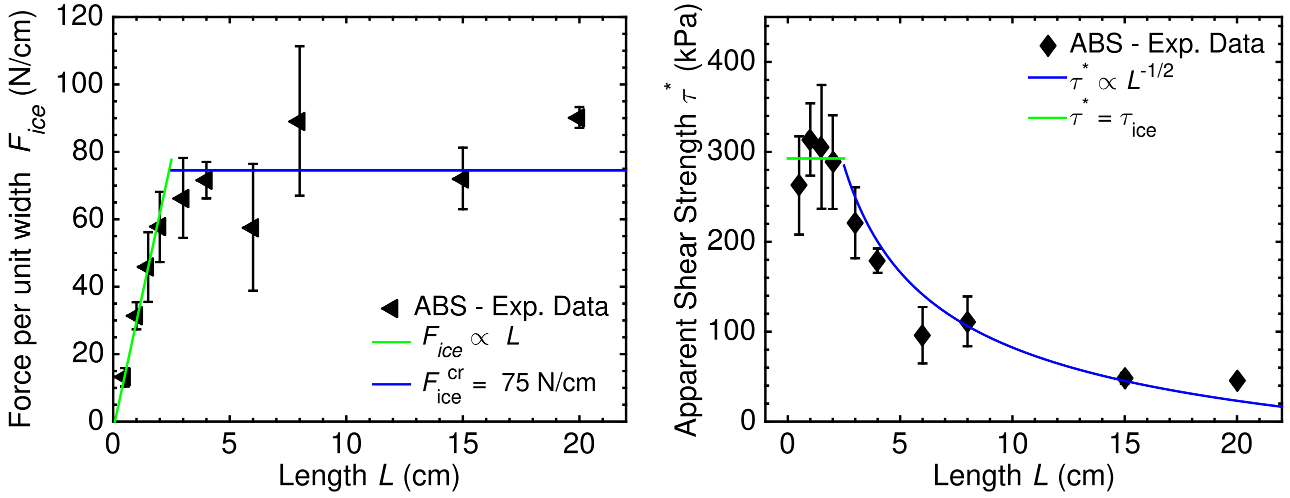

Figure 4.12: (left) The force per unit width required to detach ice from ABS. (right) The apparent ice adhesion strength of ABS. After $L_c = 2.5$ cm, the force becomes constant, and τ^*_{ice} begins to decrease. At $L = 20$ cm, $\tau^*_{ice} = 45 \pm 2$ kPa.

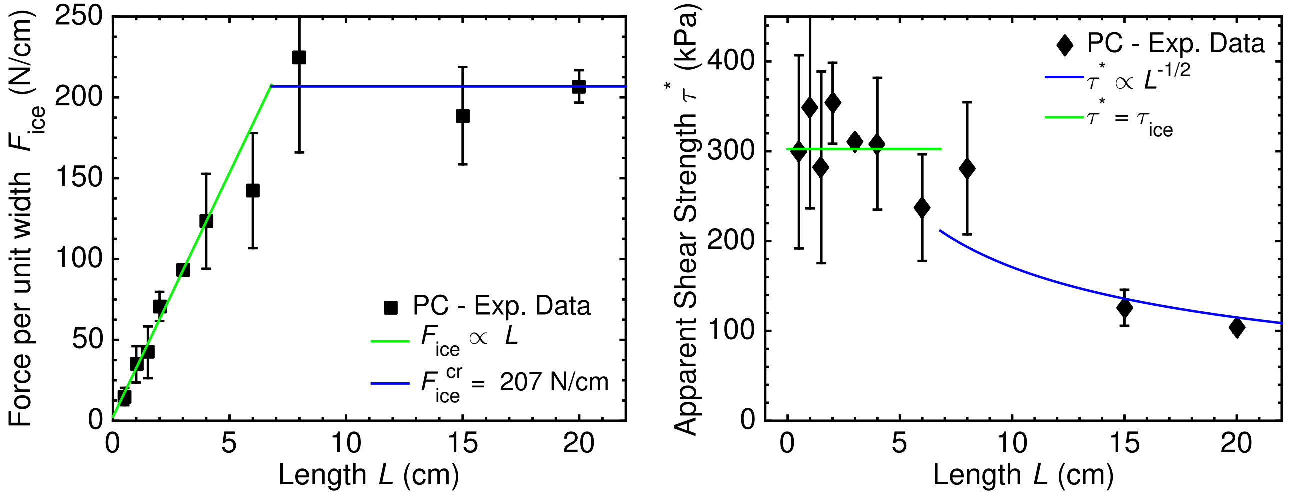

Figure 4.13: (left) The force per unit width required to detach ice from PC. (right) The apparent ice adhesion strength of PC. After $L_c = 6.5$ cm, the force becomes constant, and τ^*_{ice} begins to decrease. At $L = 20$ cm, $\tau^*_{ice} = 103 \pm 5$ kPa.

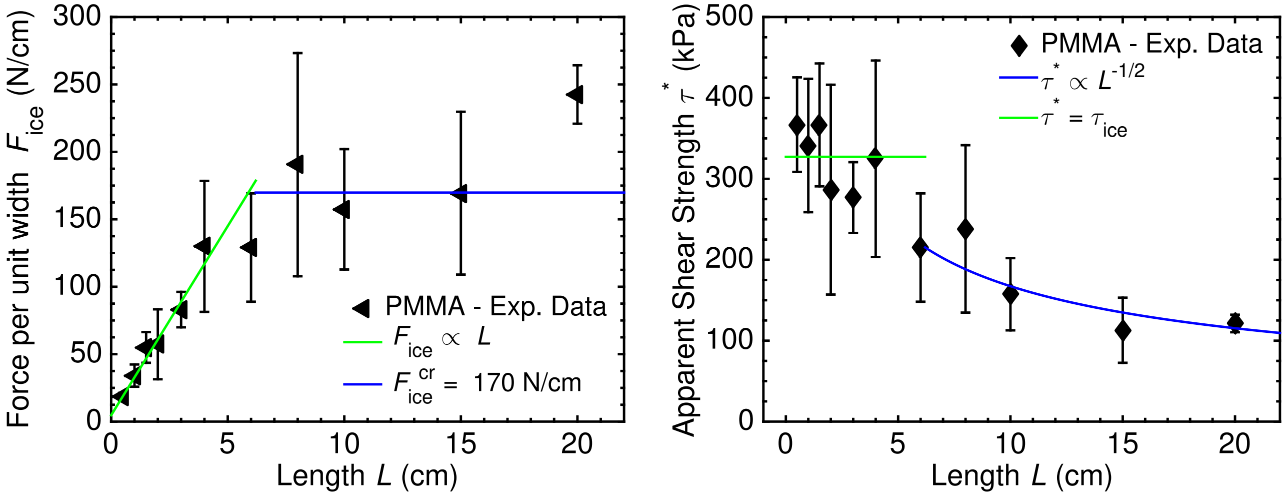

Figure 4.14: (left) The force per unit width required to detach ice from PMMA. (right) The apparent ice adhesion strength of PMMA. After $L_c = 6.2$ cm, the force becomes constant, and τ_{ice}^* begins to decrease. At $L = 20$ cm, $\tau_{ice}^* = 121 \pm 11$ kPa.

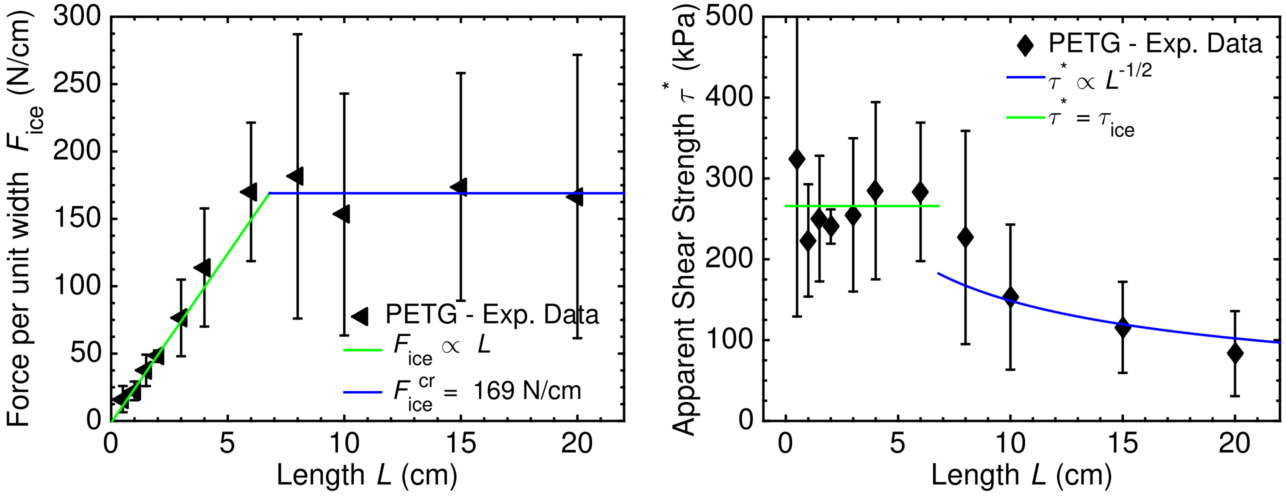

Figure 4.15: (left) The force per unit width required to detach ice from PETG. (right) The apparent ice adhesion strength of PETG. After $L_c = 6.8$ cm, the force becomes constant, and τ_{ice}^* begins to decrease. At $L = 20$ cm, $\tau_{ice}^* = 83 \pm 53$ kPa.

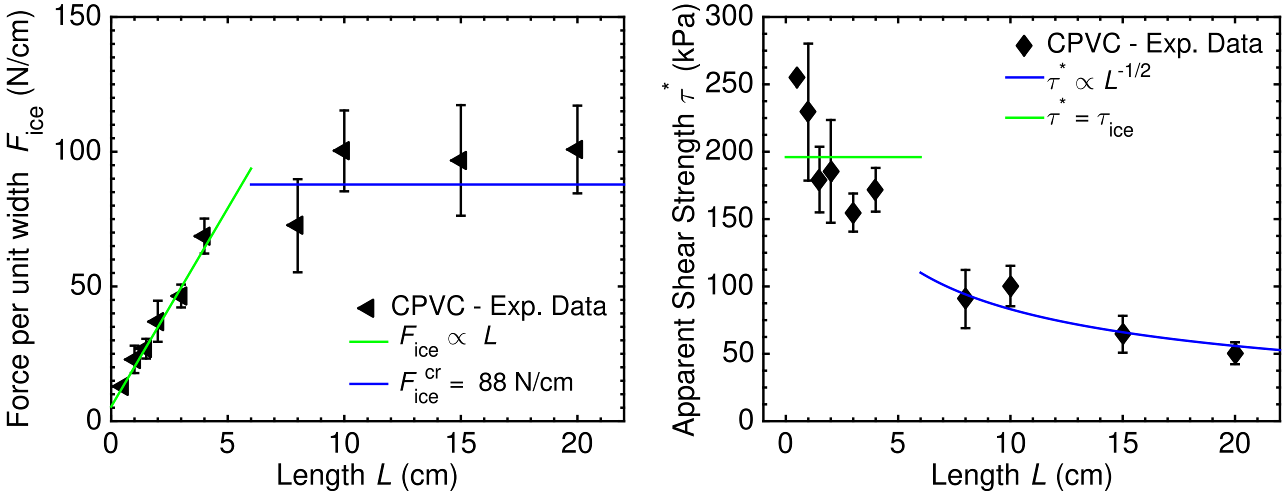

Figure 4.16: (left) The force per unit width required to detach ice from CPVC. (right) The apparent ice adhesion strength of CPVC. After $L_c = 5.6$ cm, the force becomes constant, and τ^*_{ice} begins to decrease. At $L = 20$ cm, $\tau^*_{ice} = 50 \pm 8$ kPa.

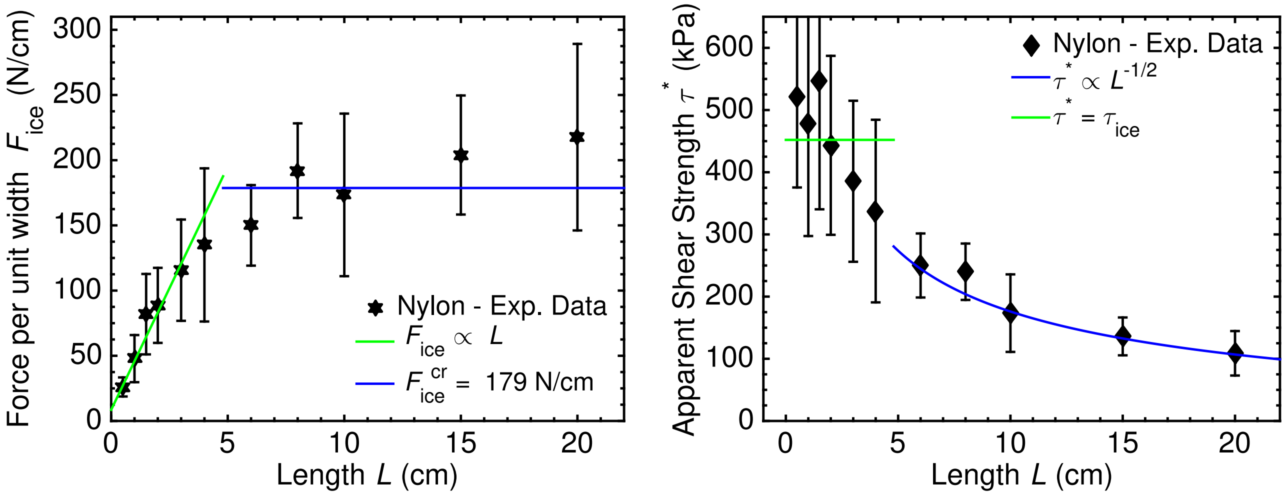

Figure 4.17: (left) The force per unit width required to detach ice from Nylon. (right) The apparent ice adhesion strength of Nylon. After $L_c = 4.8$ cm, the force becomes constant, and τ^*_{ice} begins to decrease. At $L = 20$ cm, $\tau^*_{ice} = 109 \pm 36$ kPa.

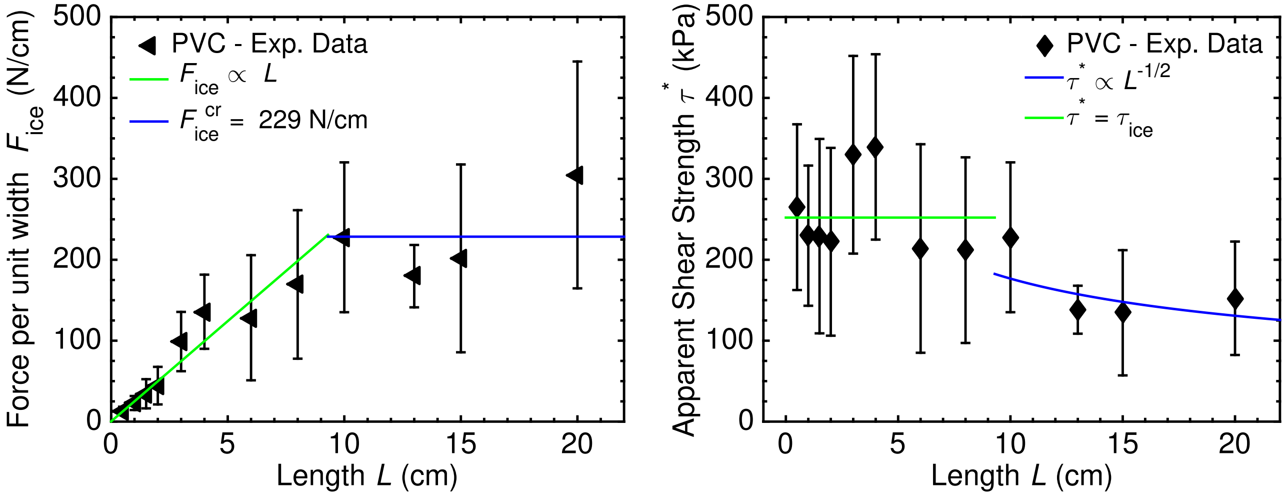

Figure 4.18: (left) The force per unit width required to detach ice from PVC. (right) The apparent ice adhesion strength of PVC. After $L_c = 9.3$ cm, the force becomes constant, and τ_{ice}^* begins to decrease. At $L = 20$ cm, $\tau_{ice}^* = 152 \pm 70$ kPa.

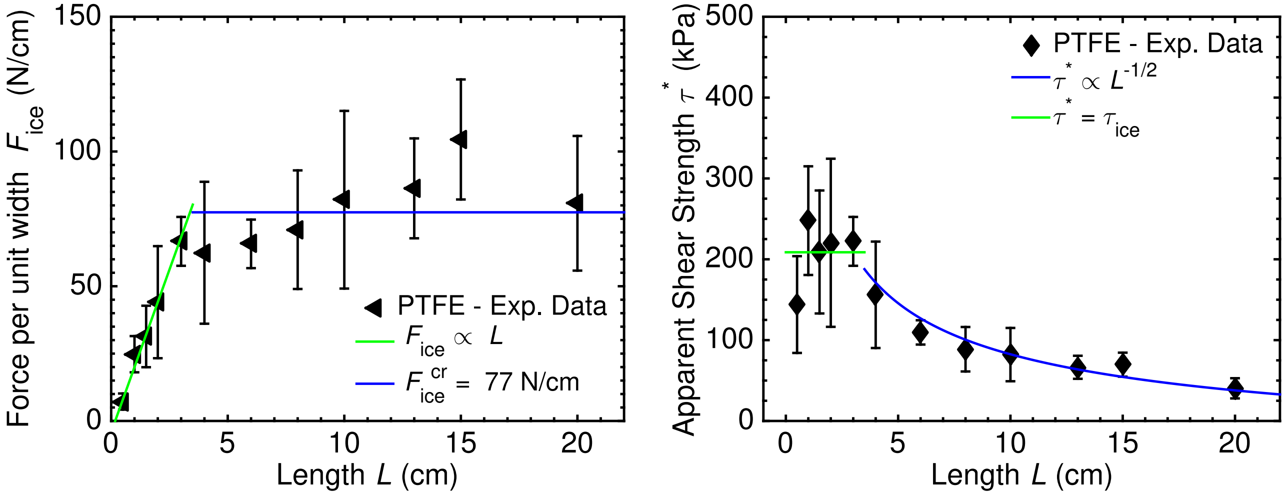

Figure 4.19: (left) The force per unit width required to detach ice from PTFE. (right) The apparent ice adhesion strength of PTFE. After $L_c = 3.5$ cm, the force becomes constant, and τ_{ice}^* begins to decrease. At $L = 20$ cm, $\tau_{ice}^* = 40 \pm 12$ kPa.

Table 4.1: The various interfacial properties measured between ice and 21 different surfaces. SO: silicone oil. PM: PVC plasticized with 50 wt% MCT, drop-cast at differing solution concentrations to control the final film thickness (see methods in Sec. 4.2).

Surface	S_q (μm)	$\theta_{rec}/\theta_{adv}$	τ_{ice} (kPa)	L_c (cm)	$\tilde{F}_{ice}^{cr}$ (N/cm)	Γ_{ice} (J/m^2)
Mold Max STROKE	0.71 ± 0.11	$113°/96°$	28 ± 3	≥ 20	≥ 55	≥ 0.29
↑ + 40 wt% SO	0.59 ± 0.24	$115°/86°$	5.3 ± 0.3	≥ 20	≥ 16	≥ 0.02
↑ ($t \approx 1$ μm)	0.56 ± 0.11	$113°/96°$	54 ± 20	6.7 ± 3.2	35 ± 4	0.12 ± 0.03
Sylgard 184	0.26 ± 0.10	$120°/87°$	117 ± 23	$\times$	≥ 175	≥ 2.44
↑ + 25 wt% SO	0.19 ± 0.15	$112°/102°$	55 ± 11	≥ 20	≥ 128	≥ 1.60
UHMWPE	3.3 ± 0.3	$103°/76°$	221 ± 38	3.1 ± 0.8	70 ± 8	0.48 ± 0.11
ABS	0.33 ± 0.03	$99°/59°$	320 ± 56	2.5 ± 0.6	75 ± 5	0.54 ± 0.07
PTFE	2.4 ± 0.1	$123° \pm 91°$	241 ± 36	3.5 ± 0.7	77 ± 8	0.59 ± 0.12
CPVC	1.2 ± 0.2	$89°/72°$	147 ± 11	5.6 ± 0.5	85 ± 6	0.70 ± 0.10
LDPE	0.73	$108°/83°$	238 ± 27	4.6 ± 0.6	105 ± 12	1.08 ± 0.24
PP	0.29 ± 0.13	$104°/86°$	322 ± 42	3.6 ± 0.7	113 ± 12	1.25 ± 0.27
PS	4.2 ± 0.1	$103°/64°$	151 ± 20	8.1 ± 1.4	120 ± 17	1.41 ± 0.40
PETG	0.15 ± 0.03	$89°/62°$	251 ± 49	6.8 ± 1.8	169 ± 40	2.80 ± 1.33
PMMA	0.16 ± 0.04	$78°/52°$	280 ± 45	6.2 ± 1.2	170 ± 22	2.83 ± 0.72
Nylon	0.35 ± 0.24	$53°/15°$	373 ± 99	4.8 ± 1.7	179 ± 22	3.13 ± 0.76
PC	0.10 ± 0.04	$92°/69°$	302 ± 20	6.5 ± 0.7	207 ± 22	4.19 ± 0.90
PVC	0.13	$92°/63°$	248 ± 52	9.3 ± 2.2	229 ± 52	5.12 ± 2.33
PM ($t = 139$ μm)	0.10 ± 0.02	$92°/83°$	70 ± 4	≥ 20	≥ 150	≥ 2.21
PM ($t = 88$ μm)	0.27 ± 0.07	$95°/75°$	84 ± 10	13.9 ± 1.9	103 ± 11	1.05 ± 0.21
PM ($t = 48$ μm)	0.15 ± 0.02	$93°/82°$	67 ± 7	14.0 ± 1.7	87 ± 12	0.74 ± 0.20
PM ($t = 2.4$ μm)	0.40 ± 0.19	$93°/81°$	99 ± 21	7.1 ± 1.8	72 ± 11	0.51 ± 0.16
PM ($t = 1.5$ μm)	1.5 ± 0.3	$97°/77°$	128 ± 75	3.3 ± 3.9	46 ± 5	0.20 ± 0.05

It is important to note that icephobic surfaces, *i.e.* low τ_{ice} materials, do not necessarily exhibit low Γ_{ice}. As we alluded to in Sec. 4.1.1 above, energy and strength are two independent parameters that both control the fracture of interfaces.

Previously it has been shown that $\tau_{ice} \propto (1+\cos\theta_{rec})$ (Eq. 1.9)[68, 56]. While we too observed this trend for the twelve different plastics evaluated in Table 4.1, no apparent trend was found with Γ_{ice} and the $1 + \cos\theta_{rec}$ parameter (Fig. 4.20). Whereas the solid surface energy correlated to the work of adhesion, and therefore the adhesive strength with ice, it did not serve as a good predictor for the interfacial toughness between a material and ice. Therefore, LIT materials need not be fabricated from low surface energy components (a similar conclusion was reached for our cavitating, icephobic rubbers fabricated in Chapter 2).

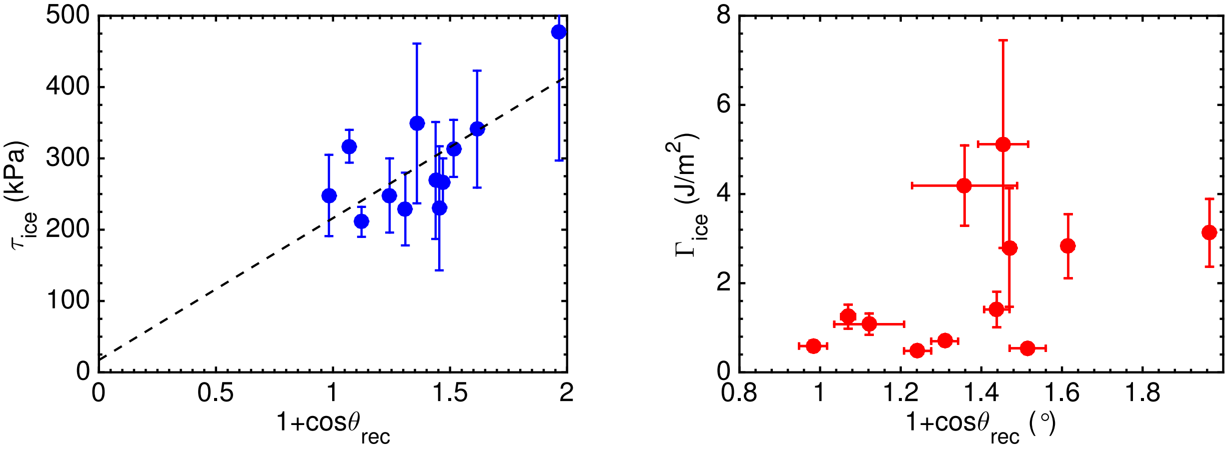

Figure 4.20: (left) The ice adhesion strength of twelve different polymers, plotted against the $1 + \cos\theta_{rec}$ parameter. As has previously been shown, the more hydrophobic a surface, the lower the adhesive strength with ice. (right) The interfacial toughness between ice and the same twelve polymers, plotted against the same parameter. Unlike adhesive strength, interfacial toughness was independent of the work of adhesion.

LIT materials are useful for large interfacial areas in the following way. Consider two of the materials tested above: UHMWPE and Sylgard 184 + 25 wt% silicone oil (Fig. 4.8 and Fig. 4.7, respectively). Although the icephobic PDMS displayed a τ_{ice} about 3× less than the τ_{ice} of UHMWPE, this only holds true until $L = L_c$ for UHWMPE (Fig. 4.21). After the critical length, toughness controlled the fracture of ice from UHMWPE, and accordingly, τ_{ice} began to decrease. At $L = 12$ cm, the force required to detach ice from the icephobic PDMS was actually greater than the force required to detach it from UHMWPE. As the length increased, this effect became more pronounced. At $L = 20$ cm, the apparent ice adhesion strength of UHMWPE, τ^*_{ice}, *i.e.* the measured force of detachment divided by the interfacial area, was almost half that of the icephobic PDMS. This is highly counter intuitive. From the conventional way of thinking ($\tau_{ice} = \tau^*_{ice}$ for all lengths), UHMWPE, and in fact any LIT material, can achieve *any desired ice adhesion strength*, simply by increasing L.

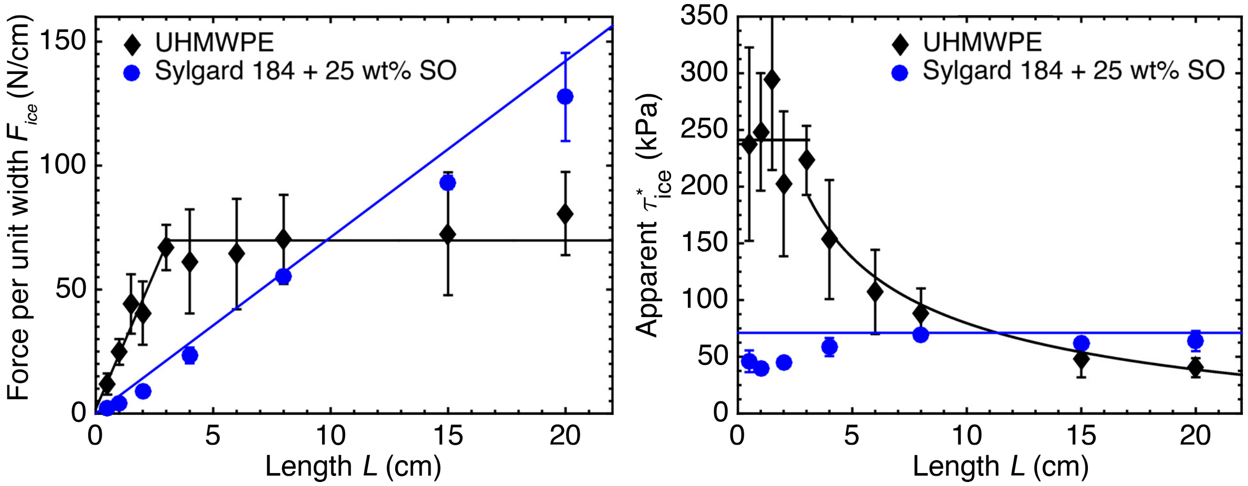

Figure 4.21: The compiled fracture data for two materials, UHMWPE (♦), and icephobic PDMS, Sylgard 184 + 25 wt% silicone oil (●). After $L \approx 12$ cm, less force was required to detach ice from the UHMWPE than the icephobic PDMS.

These results highlight an important distinction for the ice adhesion community. Icephobic surfaces should be defined by τ^*_{ice} and *not* τ_{ice}. For interfacial lengths less than ξ, the proper materials to use are icephobic surfaces that exhibit extremely low $\tau^*_{ice} = \tau_{ice}$. These materials fracture by adhesive strength, leading to low forces of detachment per adhesive area. However, for adhesive lengths greater than ξ, *i.e.* large structures, LIT materials that exhibit low τ^*_{ice} should be used, assuming $L \gg L_c$. LIT materials also have the distinct advantage of being fabricated from common, durable, engineering polymers. Achieving $\tau_{ice} < 10$ kPa is difficult without using fairly soft rubbers, filled with oils (Chapters 2 and 3). Achieving $\tau^*_{ice} < 10$ kPa is relatively easy with LIT materials, assuming a long adhesive length. For example, UHMWPE will exhibit $\tau^*_{ice} < 10$ kPa for any $L > 70$ cm.

4.3.3 Designing LIT materials

Recall Eq. 1.10 from Chapter 1, where $\tau_{ice} \propto t^{-1/2}$, and t is the thickness of the material. This inverse dependence necessitates that τ_{ice} will increase as the thickness of the film decreases. This trend has been verified previously[69]. What, effect, if any, does changing the thickness have on Γ_{ice}?

To understand the effect of thickness on Γ_{ice}, we evaluated our icephobic PVC, plasticized with MCT oil (see Fig. 3.5a), at thicknesses ranging from $t \approx 1$ μm to $t \approx 150$ μm. At a thickness of $t = 139 \pm 22$ μm, the force of detachment linearly increased with the length of interfacial

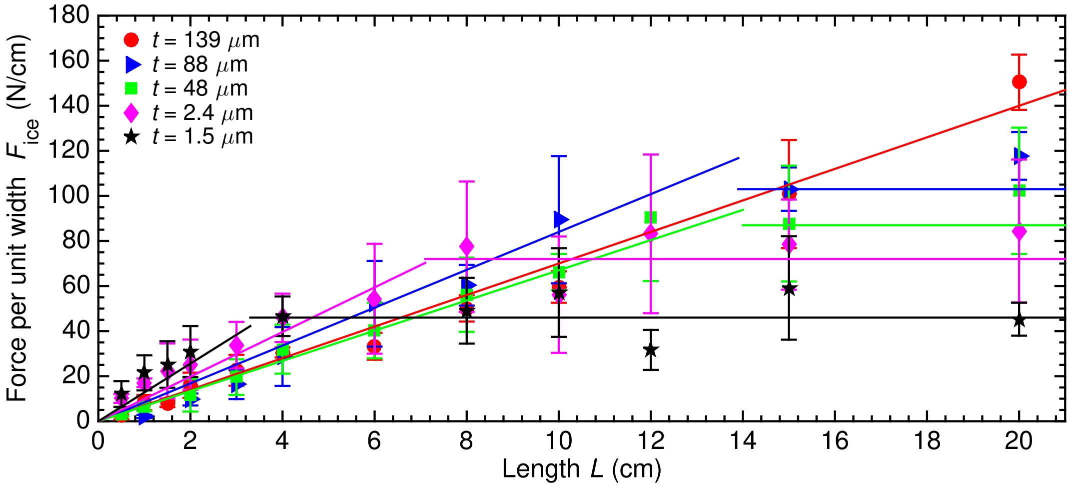

Figure 4.22: For five different thicknesses of PVC plasticized with 50 wt% MCT oil, the force to detach ice versus the length of interfacial area. Note that, for the thickest sample, a critical length was not observed.

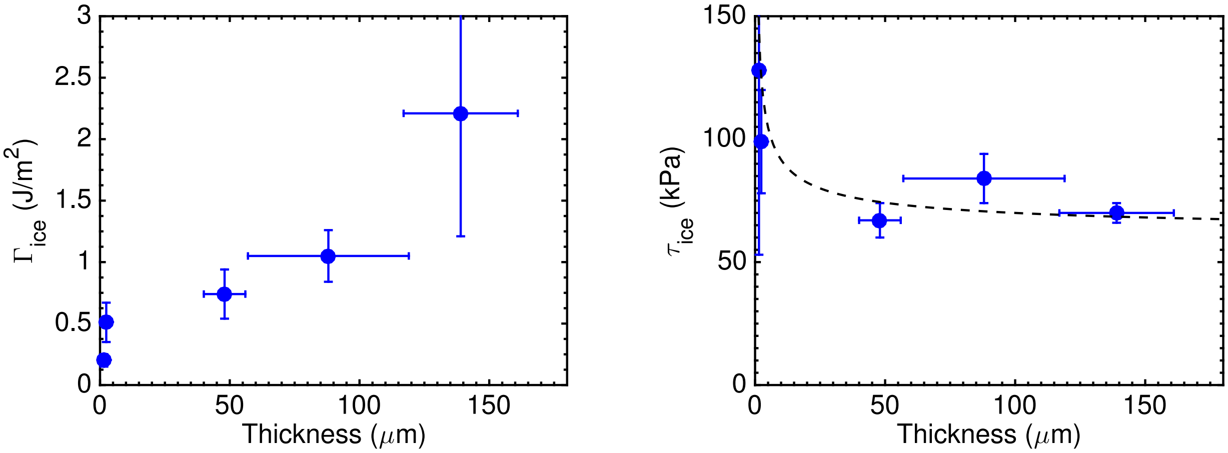

Figure 4.23: (left) Γ_{ice} for five different thicknesses of PVC plasticized with 50 wt% MCT oil. (right) The ice adhesion strength of the same five samples follows the inverse square root dependence predicted for failure by cavitation (Eq. 1.10).

area (*i.e.* fracture was controlled by adhesive strength). However, decreasing the thickness caused $\tilde{F}_{ice}^{cr}$ to also decrease, indicating that Γ_{ice} decreased with decreasing thickness (Fig. 4.22). For the plasticized PVC surface with $t = 1.5 \pm 0.5$ μm, $\Gamma_{ice} = 0.20 \pm 0.05$ J/m^2. After a length of $L \approx 6$ cm, the force necessary to dislodge ice from the thinnest plasticized PVC was less than the force required for the thickest plasticized PVC, even though the ice adhesion *strength* scales as $\tau_{ice} \propto t^{-1/2}$ (Fig. 4.23). A similar trend was observed for the icephobic Mold Max STROKE surface (Table 4.1).

To verify the length-independence of $\tilde{F}_{ice}^{cr}$ for surfaces whose fracture is controlled by tough-

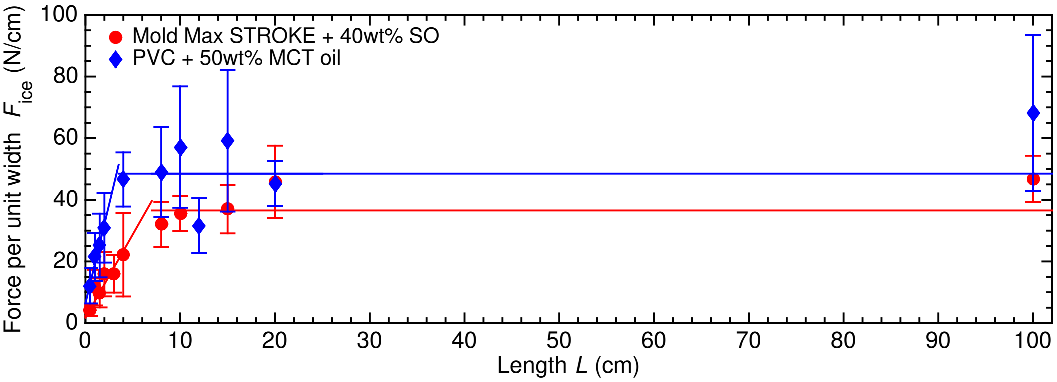

Figure 4.24: The force of detachment versus the interfacial length for two LIT materials. We evaluated the force of detachment at a length of $L = 100$ cm, and observed no increase in the required force of detachment. The apparent ice adhesion strength at this length was $10\times$ lower than τ_{ice} for both the materials.

ness, we fabricated meter-long specimens of our two surfaces with the lowest Γ_{ice} values: thin PVC plasticized with MCT oil, and thin Mold Max STROKE filled with silicone oil (see methods in Sec. 4.2). We then moved our ice adhesion setup into a walk-in freezer held at -20 °C. Even over an adhesive length of $L = 100$ cm, the required force of detachment was not increased (Fig. 4.24). The apparent ice adhesion strength for these two surfaces was $\tau^{*}_{ice} = 7 \pm 3$ kPa, and $\tau^{*}_{ice} = 4.7 \pm 0.8$ kPa, for the plasticized PVC and filled Mold Max STROKE surfaces, respectively. In fact, some of our individual $\tilde{F}_{ice}$ measurements at $L = 100$ cm were lower than values at $L = 2$ cm, for the plasticized PVC surface (*i.e.* on occasion, we observed a greater required force to detach ice from an area $50\times$ smaller). This unambiguously confirmed that the fracture of ice from LIT materials is indeed independent of adhesive length, when the fracture is controlled by interfacial toughness.

4.4 Conclusions

In this chapter we investigated the never-before measured property of interfacial toughness, between ice and a wide variety of different surfaces. Whereas icephobic materials are useful for short interfacial areas, when fracture is controlled by adhesive strength, LIT materials are useful for longer interfacial areas, for which toughness dominates the fracture. We showed that LIT materials can exhibit any desired ice adhesion strength, and that the ice adhesion community should investigate interfacial toughness as a new material property for low ice adhesion applications, especially those where the length scale is significantly larger than ξ.

CHAPTER 5

Hysteresis Free Surfaces: Design and Application

5.1 Introduction

Fouling, in its most general sense, involves a foreign contaminant adsorbing to a surface and mitigating some property[32]. Fouling is a ubiquitous hindrance, including the bio-fouling of marine vessels[123], the staining of teeth[124], the adhesion of dirt to apparel[125], the accretion of ice on power lines[98], and the adsorption of contaminants to water purification membranes[44]. Fouling can be subdivided into two categories: the unwanted adsorption of liquids, or the unwanted adhesion of solids. Many liquid-repellent materials have been fabricated, including superhydrophobic[126, 127, 32, 128, 129], superamphiphobic[130, 131, 26, 132, 133], omniphobic[19, 134, 135, 136, 39] and superomniphobic surfaces[137, 138, 42, 38]. Similarly, several surfaces have been fabricated to resist the adhesion of solids, including lubricated systems[3, 75, 67, 64, 139], soft rubbers[62, 54, 140, 104, 69], omniphobic surfaces[56, 57, 68, 39, 19] and hygroscopic polymers[141, 142, 75, 68, 143]. Some overlap exists[136, 56, 19, 3], but in general there are no reported materials that can universally resist a broad range of both solid and liquid contaminants. In this work we present a facile method for fabricating fluorine-free coatings capable of both drastically lowering the adhesion of solids, including ice, wax, superglue and mud, and perfectly repelling essentially all liquids, from water to oils to alcohols and even ultra-low surface tension liquids like fluorinated solvents.

5.1.1 Imparting low liquid adhesion

As we delineated in Chapter 1, two metrics exist for characterizing the liquid repellency of a given surface: θ^* and $\Delta\theta$. To achieve both high θ^* and low $\Delta\theta$, sufficient texture leading to the Cassie-Baxter state (Fig. 1.2b) is necessary[32, 2]. Such surfaces can ideally exhibit close to $\theta^*_{adv}/\theta^*_{rec} \approx 180^\circ/180^\circ$[144]. However, typically these ultra-high contact angles are not maintained with low surface tension liquids without highly controlled, re-entrant texture[26, 41, 145]. Moreover, the mechanical durability of such texture elements is typically very poor[38, 146]. And once damaged, a superomniphobic surface will exhibit $\Delta\theta \gg 0^\circ$ (and typically $\theta^*_{rec} = 0^\circ$) with low-γ_{LV} liquids.

Even without mechanical damage, low-γ_{LV} liquids easily transition from the Cassie-Baxter state to the Wenzel state on superomniphobic surfaces[38]. For low-γ_{LV} liquids, the Cassie-Baxter state is metastable and the Wenzel state is always energetically preferred[26]. Pressure perturbations[41], droplet impact[137], flow[147], and evaporation[148] can all cause low-γ_{LV} liquids to wet superomniphobic surfaces. As such, their efficacy as a long term solution for repelling all liquids may be limited. Note that many of the above issues also limit the solid repellency of these highly textured surfaces. Once wetted, the high interfacial area from the texture ($r = r_\phi$) may lead to extremely high values of adhesion[73, 66, 149].

One way of overcoming the above issues is to generate smooth surfaces that still maintain $\Delta\theta \approx 0^\circ$, but without the ultra-high θ^* values. Smooth films are necessarily in the Wenzel state, and therefore do not suffer from pressure instability[1]. Moreover, no texture elements exist that can be easily mechanically damaged. In principle, a homogeneous material displays θ_Y without $\Delta\theta$. In practice, fabricating surfaces displaying $\Delta\theta < 10^\circ$ with water is difficult, and low-γ_{LV} liquids wet almost all known materials ($\theta_{rec} = 0^\circ$)[26].

Contact angle hysteresis is a product of many different sources, all arising from solid-liquid-vapor interactions in very close proximity to the three-phase contact line[150]. From a surface design standpoint, the two largest sources of $\Delta\theta$ that can be reduced are physical and chemical heterogeneity[23] (the condition of the vapor phase and the nature of the probe liquid cannot be controlled by interfacial engineering). Physical heterogeneity, or surface roughness, can usually be minimized through mechanical methods like polishing[151]. Chemical homogeneity, in contrast, is much more difficult to achieve[136].

Recall Fig. 2.8 from Chapter 2. There we evaluated the ice adhesion strength of a silicon wafer treated with two different monolayers: a highly perfluorinated system and a PDMS-based system. Whereas the perfluorinated monolayer forms a densely packed, crystalline structure, the PDMS monolayer remains amorphous and liquid-like[39]. Consequently, the PDMS monolayer exhibited interfacial slippage whereas the perfluoinated monolayer did not. The following work further explores the properties of these liquid-like monolayers, in terms of both their low adhesion to solids, and their absence of contact angle hysteresis with essentially all liquids (omniphobicity, see Table 1.3).

5.2 Materials and methods

5.2.1 Materials

Silicon wafers (University Wafers, 500 μm thickness, 1.5 nm native oxidel layer, $< 100 >$ orientation) were used as received. Chlorine terminated PDMS (n =2,3,4,6, and 30-50) was purchased from Gelest. As the silane is bi-functional, we refer to the bidentate attachment of these small molecules as b-PDMS. Heptadecafluoro tetrahydrodecyl dimethyl monochlorosilane (F17 silane) was purchased from Gelest. Ethanol, hexadecane, dodecane, decane, octane, hexane, and perfluorodecalin were purchased from Fisher Scientific and used without further purification. Diidomethane, formamide, methoxyperfluorobutane (Sigma Aldrich), hexafluorobenzene (Syquest), Krytox GPL 100 (Dupont), pentafluorobutane (Alfa Aesar), ortho-fluorotoluene, trimethylchlorosilane, and 4-chlorobenzotrifluoride (Acros Organics) were used as received. SF-100 superglue (3M), calcined gypsum (commonly called plaster of paris, Sheetrock Easy Sand 5), PDMS (Sylgard 184, Dow Corning), and paraffin wax (Sigma Aldrich) were used for solid adhesion studies.

5.2.2 Synthesis

Pieces of Si wafer roughly 1 cm^2 were placed in a 3 cm closed petri dish along with 200 μL of the desired b-PDMS silane. Although various reaction times, temperatures, and pressures were experimented with, the optimized reaction involved a room temperature silanization for 10 minutes. After exposure, the wafers were rinsed in toluene and 2-propanol (Fisher Scientific). The silanization and washing step was then repeated three additional times.

A perfluorinated monolayer was prepared for comparative purposes. First, the Si wafers were cleaned with O_2 plasma using a Harrick Plasma PDC-001 with an RF source power of 30 Watts and a pressure of ≈ 200 mTorr for 15 min. Note that we found plasma cleaning did not help for the b-PDMS silanization, and thus this was not done for any of the PDMS monolayers formed. The plasma-cleaned wafer was then exposed to vapors of the F17 silane at 100 °C in a vacuum oven for 24 hours.

Oxygen plasma is known to turn PDMS into silica[81]. To evaluate the reproducability of our b-PDMS silanization technique on a single surface, a b-PDMS wafer was oxygen plasma treated for 15 minutes following the same procedure as above.

5.2.3 Capping procedure

1,3-dichlorotetramethyldisiloxane, due to steric hindrance, can react with at most $\approx 1/3$ of a completely hydrlized silicon substrate[12]. As such, a procedure was developed to further react the remaining hydroxyls still present on the Si wafer. Note that the above reason was why oxygen plasma was not necessary for the b-PDMS silanization: as only one third of the total surface hydroxyls may be reacted with, a dense monolayer of -OH groups was not necessary. A b-PDMS-treated wafer was placed in a closed container with 200 μL of trimethylchlorosilane for 1 hour. The sample was then washed with toluene and 2-propanol. We refer to this procedure as 'capping'. Capped samples (Cb-PDMS) typically displayed a roughly $5°$ increase in θ_Y with water, and $\Delta\theta$ was either unchanged or slightly improved. A schematic of the proposed mechanism for attachment is shown in Fig. 5.1.

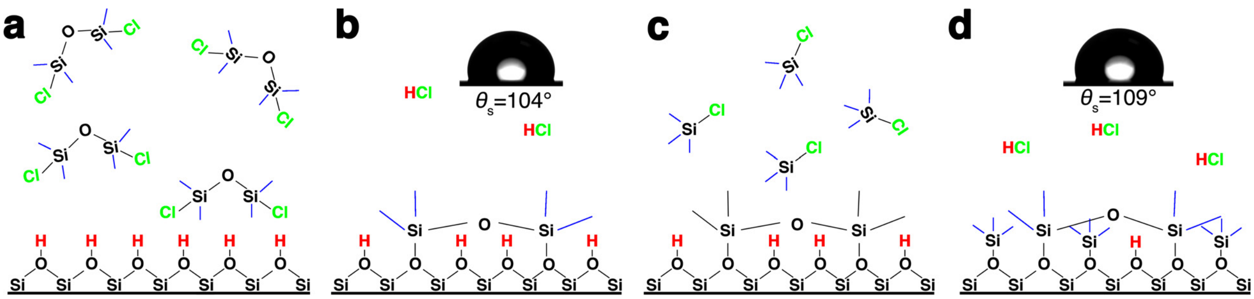

Figure 5.1: The proposed mechanism for the bidentate attachment of 1,3-dichlorotetramethyldisiloxane. a, a Si wafer with surface hydroxyls is exposed to the vapor of the silane. b, the silane reacts with the hydroxls, but with a maximum surface coverage of only $\approx 1/3$. Hydrochloric acid is given off as a reaction product. The final surface can be quite hydrophobic ($\theta_{adv}/\theta_{rec} \approx 104°$), but surface hydroxyls still remain. c, the reacted wafer is subsequently exposed to vapors of trimethylchlorosilane, to react with the remaining surface hydroxyls. d, the capped wafer, where most of the hydroxyls are now converted to fully methylated Si atoms. The cb-PDMS exhibited contact angles approaching the values observed for close-packed monolayers of trimethyl groups ($\theta_Y = 110°$)[11]. Note that we show the likely case where complete reaction is not achieved, due to steric hindrance[12].

5.2.4 Thickness determination

Variable-angle spectroscopic ellipsometry using an M-2000 Ellipsometer (J. A. Woollam Co.) was performed to measure monolayer thickness. The measurements were performed in reflection mode using incidence angles of 55°, 60°, 65°, 70°, and 75°. The data was fit using the CompleteEASE software. The optical constants of the silicon and oxide were taken from values within the program.

5.2.5 Contact angle measurement

Contact angles were measured using a Ramé-Hart 200-F1 goniometer. Measurements were made by advancing and receding a single droplet of liquid ($\approx$6 μL) from a 2 mL micrometer syringe (Gilmont). Averages from at least five independent measurements were reported. When measuring contact angles for Krytox 100 and silicone oil, the droplet is very slowly advanced and receded to minimize viscosity effects.

5.2.6 Solid adhesion measurement

Ice adhesion was measured using the techniques already reported in Chapters 2-4 (Fig. 4.3). To measure the adhesion of SF-100, plaster of paris (PoP), paraffin wax (PW), or PDMS, the same force gauge setup was employed. For PoP, gypsum was mixed in a 1 g/mL DI water solution for 5 minutes and then poured into the 1 cm^3 cuvettes as used previously. The PoP was allowed to harden over night. PW was heated to 100 °C and then poured into the cuvettes and allowed to cool to room temperature. Sylgard 184 was mixed in the normal 10:1 base:crosslinker ratio, and then cured on a 150 °C hotplate for 1 hour. SF-100 adhesion was evaluated by jamming a 1 cm^3 plastic cube into the cuvette so that a recessed area of $\approx$ 1 mm in height was exposed. SF-100 was poured into this area, and then the cuvette was placed atop the surface to be evaluated. This procedure was necessary because, unlike the other solid adherents, SF-100 does not cure into a mechanically rubust solid mass. Using a thin layer of the adhesive allowed us to still evaluate the adhesive properties on our current setup. All reported values are the average of at least five independent measurements.

5.2.7 Micro-hoodoo fabrication and treatment

A 3 μm thick layer of photoresist (SPR 220-3.0, Shipley) was spin-coated on a Si wafer and baked for 90 sec at 115 °C. The lateral dimensions (Diameter : 10 μm, Spacing : 40 μm) were defined by 365 nm UV exposure (Karl Suss MA6 mask aligner) and then developed in AZ300 MIF. Inductively coupled plasma reactive-ion etching (ICP-RIE, STS Pegasus) formed $\approx$ 30 μm height pillars in the exposed regions, and the prepared structure was cleaned in O_2 plasma for 5 min. The prepared structure was further etched with XeF_2 etching (Xactix, 3 mT, 40 sec per cycle, 30 cycles), and the process provided a well defined hoodoo structure all over the patterned surface (Fig. 5.2).

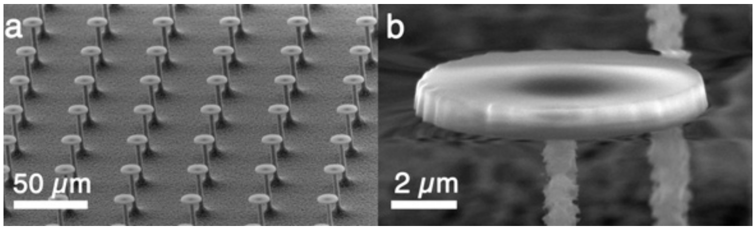

Figure 5.2: a, the micro-hoodoo structures fabricated in this work

5.3 Results and discussion

5.3.1 Low hysteresis surfaces

We found that 1,3-dichlorotetramethyldisiloxane ($n = 2$) was optimal for producing low $\Delta\theta$ surfaces in a very simple manner (Sec. 5.2). By increasing the reaction time (30 seconds to 1 hour), the thickness of the b-PDMS layer increased. Complete surface coverage, indicated by a minimum in $\Delta\theta$, was achieved after 10 minutes of silane vapor exposure, when the monolayer thickness reached ≈ 4 nm (Fig. 5.3a). Monolayers thinner than 4 nm left hydroxyl groups exposed, decreasing θ_{rec}. After the optimal 10 minute exposure, the PDMS-silane can still potentially react with individual surface hydroxyls, but the bidentate attachment is sterically hindered (see reaction scheme in Fig. 5.1b). As such, any additional attachment will either result in a dangling chlorine atom, which can react with water vapor and leave a residual silanol group, or cause the PDMS-silane to self-polymerize, adding nanoscopic roughness. We observed that thicknesses greater than 4 nm exhibited both an increased θ_{adv} and a decreased θ_{rec}, indicating that self-polymerization was indeed taking place (neither thickness, nor θ_{adv}, would increase from residual silanols alone). The optimal reaction time of 10 minutes at room temperature produced b-PDMS surfaces with minimal $\Delta\theta$.

To ensure that the overall thickness of the b-PDMS monolayer was not contributing to the increased $\Delta\theta$, we exposed our optimal b-PDMS surface (thickness: 4 nm, $\Delta\theta = 2°$) to oxygen plasma (Sec. 5.2). After 15 minutes of exposure, the surface was completely wetting to water, as all the methyls had been converted to silanol groups[81]. Exposing this plasma-treated surface to the same optimized silanization procedure described above yielded a new, low-$\Delta\theta$ surface, but now with increased thickness (Fig. 5.3b). Repeating this procedure $10\times$ allowed us to grow a 15 nm thick b-PDMS film still exhibiting $\Delta\theta = 2°$. We therefore conclude that thickness in of itself does not increase $\Delta\theta$, but non-bidentate polymerization of the PDMS silane does increase thickness and $\Delta\theta$.

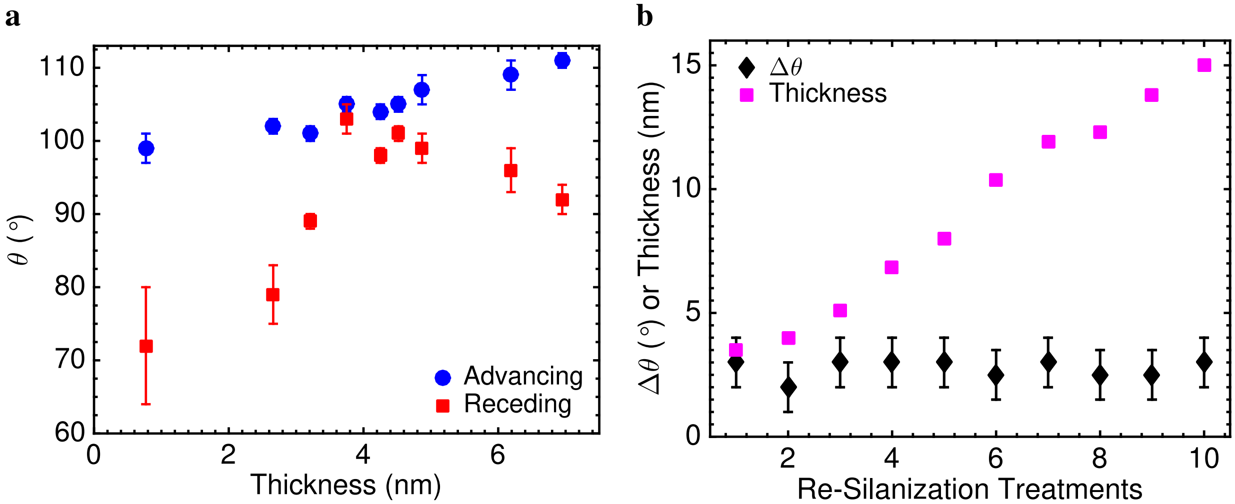

Figure 5.3: a, the advancing and receding water contact angles on the b-PDMS surface as a function of thickness. Here the thickness was controlled by the exposure time to the silane (ranging from 30 seconds to 1 hour). Complete surface coverage was achieved around a thickness of 4 nm. b, exposing the b-PDMS surface to O_2 plasma and subsequently re-silanizing the surface yielded a new surface with identical $\Delta\theta$ as before oxygen plasma treatment. However, the thickness was increased, and this could be repeated for at least ten subsequent exposures.

5.3.2 Capping residual hydroxyls

1,3-dichlorotetramethyldisiloxane can only react with one third of a completely hydrolyzed silicon wafer[12]. Thus, although we stated that our 4 nm thick b-PDMS surface achieved full surface coverage, we do not imply that it has fully reacted with all the available surface hydroxyls. Indeed, this is why an increase in $\Delta\theta$ was observed with increased thickness of the monolayer (Fig. 5.3a). To remove these potential pinning points, we capped the remaining hydroxyl groups with trimethylchlorosilane (Fig. 5.1c,d). We refer to the capped bidentate PDMS silanized surface as cb-PDMS. Whereas the b-PDMS surface exhibited $\theta_Y \approx 104°$ with water, the cb-PDMS exhibited $\theta_Y \approx 109°$ (Table 5.1). This roughly 5° increase in θ_Y approached the intrinsic contact angle of a purely methylated surface, $\theta_Y = 110°$[11].

We measured advancing and receding contact angles for a wide range of probe liquids on both the b-PDMS and cb-PDMS surfaces (Table 5.1). For comparison, we also fabricated a perfluorinated monolayer (F17) that exhibited $\theta_{adv}/\theta_{rec} = 122°/108°$ with water (see Sec. 5.2 for methods). As expected, the perfluorinated film exhibited larger contact angles than the PDMS-based surfaces, as the surface energy of perfluorinated systems ($\gamma_{SV} \approx 10$ mN/m) is lower than PDMS ($\gamma_{SV} \approx 20$ mN/m). However, as the F17 monolayer is highly crystalline, surface defects can act as potential pinning points, even if γ_{SV} is still quite low. For every single probe liquid evaluated, $\Delta\theta$ for the F17 surface was significantly higher than with either the b-PDMS or the cb-PDMS monolayers. Whereas the typical $\Delta\theta$ for the F17 surface was $\Delta\theta \approx 10°$, for the b-PDMS and cb-PDMS,

Table 5.1: $\theta_{adv}/\theta_{rec}$ for the F17 functionalized surface, the b-PDMS surface, and the cb-PDMS surface.

Liquid	γ_{LV} (mN/m)	F17	b-PDMS	cb-PDMS
Water	72	122°/108°	105°/103°	109°/108°
Hexadecane	28	75°/60°	36°/35°	36°/35.5°
Ethanol	22	64°/43°	26°/25°	32°/31.5°
o-fluorotoluene	28	68°/52°	28°/26.5°	27.5°/27°
p-chlorobenzotrifluoride	24	61°/43°	25°/24°	25°/24°
Hexafluorobenzene	21	41°/35°	20°/18.5°	21°/21°
Perfluorodecalin	19	27°/23°	28°/27°	35°/34°
Krytox 100	16	23°/11°	32°/30°	32.5°/31.5°
AK-225	16	27°/17°	11°/10°	13°/12°
Pentafluorobutane	15	17°/0°	10°/10°	14.5°/14°
Vertrel XF	14	8°/0°	9°/9°	12°/12°
Methoxyperfluorobutane	13	12°/0°	10°/10°	14.5°/14°

typical contact angle hysteresis was always $\Delta\theta \leq 1°$.

5.3.3 Fluorophobic surfaces

We also measured contact angles for a large number of fluorinated solvents, ranging in surface tension from $13 \leq \gamma_{LV} \leq 28$ mN/m (Table 5.1). Whereas larger advancing and receding contact angles for high-γ_{LV} liquids were always observed on the F17 surface, this did not hold for the fluorinated liquids. Fluorine-fluorine interactions are known to play a large role in the solvation of fluorinated species[96]. This was most likely the reason why several of the liquids did not recede from the perfluorinated monolayer. Moreover, for perfluorodecaline and Krytox 100 (a short-chain perfluoropolyether[19]), we actually observed higher contact angles with the PDMS-based systems (indicating very strong F-F interactions).

Quite remarkably, we observed both a non-zero θ_{rec} value, and extremely low $\Delta\theta$, for liquids with lower surface tension than the solid surface energy of PDMS[96]. This is highly counter-intuitive, as Zisman has shown[152] that the surface energy of a polymer is roughly equal to the surface tension of a liquid that displays $\theta \approx 0°$ on the surface. From a traditional Zisman analysis (Fig. 5.4), the surface energy of the b-PDMS film was $\gamma_{SV} = 20$ mN/m, using receding contact angle values and not including fluorinated liquids. Adding the fluorinated liquids to the Zisman analysis merely produced large scatter near and below the surface energy of bulk PDMS.

The glass transition temperature of PDMS is 150 Kelvin (-123 °C)[88]. At room temperature, PDMS exists as a liquid and fully dissolves in non-polar liquids like toluene and hexadecane. In its crosslinked state, solid PDMS swells in such liquids (by an amount given by Eq. 3.3), and displays $\theta_{rec} = 0°$[81]. Why, then, does the b-PDMS monolayer repel hexadecane with $\theta_Y = 36°$ and $\Delta\theta < 1°$ (Table 5.1)? Two theories have been put forward. Cheng *et al.* have suggested that

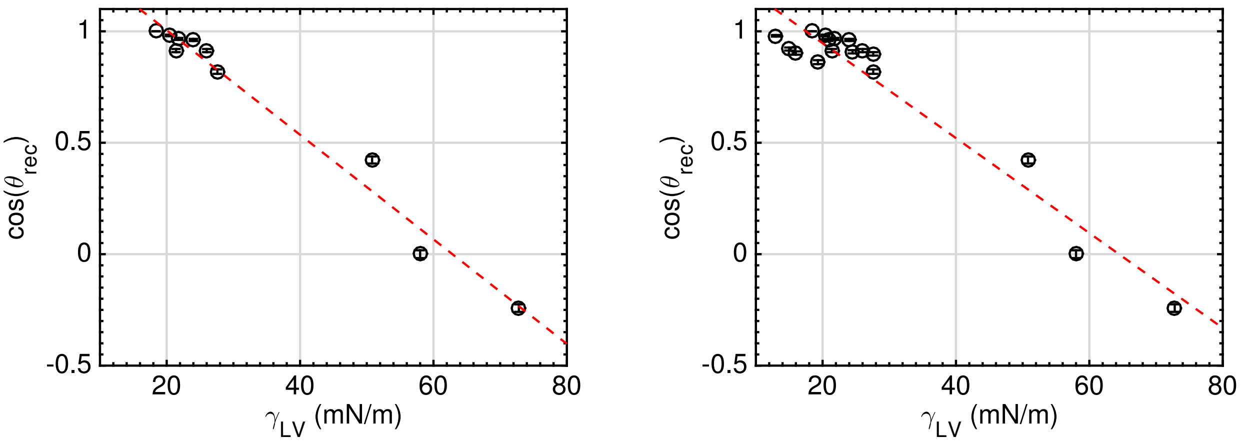

Figure 5.4: (left) A traditional Zisman plot for the b-PDMS surface. Fluorinated liquids are not included in the analysis. The critical surface tension is $\gamma_{LV} = 20$ mN/m. (right) the Zisman plot with fluorinated liquids included. Contrary to a typical Zisman analysis, liquids with surface tension less than the critical surface tension do not exhibit $\theta = 0°$.

the monolayers do swell in such compatible liquids, and observed decreasing $\Delta\theta$ with increasing solvation of the PDMS chains[153]. They suggest that the effect only works with liquids that dissolve PDMS chains. However, in Table 5.1, only hexadecane and AK-225 dissolve bulk PDMS. All the other liquids are immiscible with PDMS, but still display $\Delta\theta \approx 1°$. Thus, the swelling of the PDMS monolayers seems unlikely. Ellipsometry measurements of the b-PDMS film, after soaking in 5 cSt silicone oil (which perfectly wets the monolayer), did not yield a thickness change (*i.e.* even with a non-evaporating liquid that perfects wets the b-PDMS, swelling was not observed).

Contrary to the theory put forth by Cheng *et al.*, Wang and McCarthy[39] have suggested that the liquid-like nature of PDMS simply reduces solid/liquid interactions, and therefore receding events, near the contact line. McCarthy has previously shown that even molecular topography can contribute to contact angle hysteresis[154]. By creating a mobile interface, the liquid can effortlessly dewet the solid surface. And if the surface is molecularly smooth, very low $\Delta\theta$ can be achieved.

One recently proposed system for achieving low $\Delta\theta$ is to imbibe a lubricant into a highly textured surface[19]. If the lubricant is perfluorinated, a wide range of liquids, both of high and moderately low surface tension, can be repelled with $\Delta\theta \approx 2°$. However, such systems cannot repel fluorinated liquids, as the lubricant easily dissolves in these solvents. Moreover, as the fluorinated liquid can remove the lubricant, the liquid repellency of the lubricated systems will be lost, even for high-γ_{LV} liquids like water. The b-PDMS and cb-PDMS surfaces can become fully wetted by a small number of liquids (silicone oil, hexane, and pentane). However, dissimilar to lubricated systems, exposure to such wetting liquids does not remove the liquid repellency of the surface. The bidentate attachment formed strong, covalent bonds between the PDMS chains and the surface, and the low $\Delta\theta$ was always fully recovered upon drying.

To highlight the significant advantage of the cb-PDMS surfaces over a lubricated system, we placed 10 μL droplets of Krytox 100 on our cb-PDMS surface at a tilt angle of $0.5°$ (Fig. 5.5). This is the same lubricant employed by omniphobic, lubricated systems[19]. Rather than being completely wet by such a liquid, the cb-PDMS surfaces repelled the lubricant with relatively high contact angle ($\theta_Y \approx 32°$) and $\Delta\theta = 1°$. The lubricant easily dewet and slid from the cb-PDMS surface without leaving a residual trail.

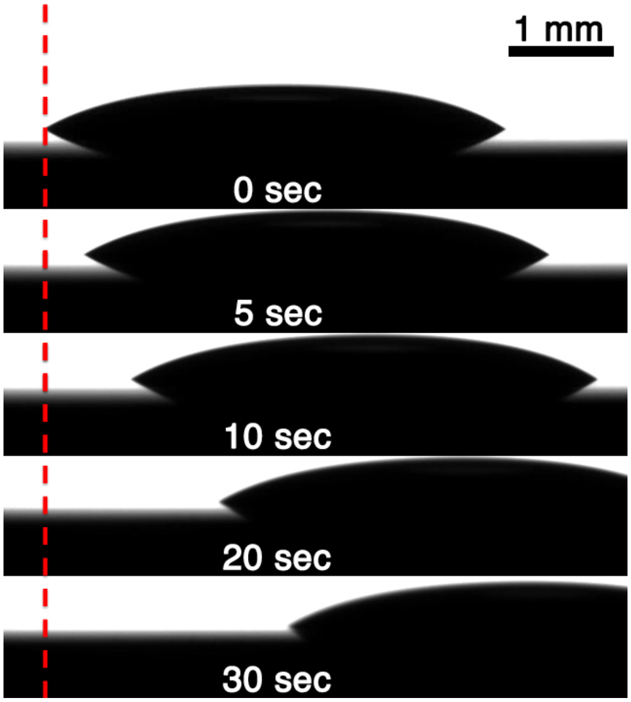

Figure 5.5: A droplet of Krytox 100 (a perfluoropolyether lubricant, γ_{LV} = 16 mN/m) was placed on the cb-PDMS surface at a tilt angle of $0.5°$. The droplet easily slid from the surface, displaying negligible hysteresis, and did not leave a wetting trail.

5.3.4 Durability characterization

To ensure that the monolayer was not easily damaged, we subjected the cb-PDMS coating to 5,000 cycles of linear Taber abrasion using the CS-5 wheel-set (resilient felt) and a 250 g load. The advancing and receding contact angles after abrasion, for both water and hexadecane, are shown in Fig. 5.6. The contact angles deviated from their initial values by at most $1°$. Dissimilar to our durable icephobic surfaces from Chapter 2, the coating did not lose mass during the abrasion process. As the thickness was only 4 nm, any surface degradation would result in a catastrophic contact angle decrease, especially for the receding angle of hexadecane. This was not observed, indicating that this level of abrasion did not damage the coating at all.

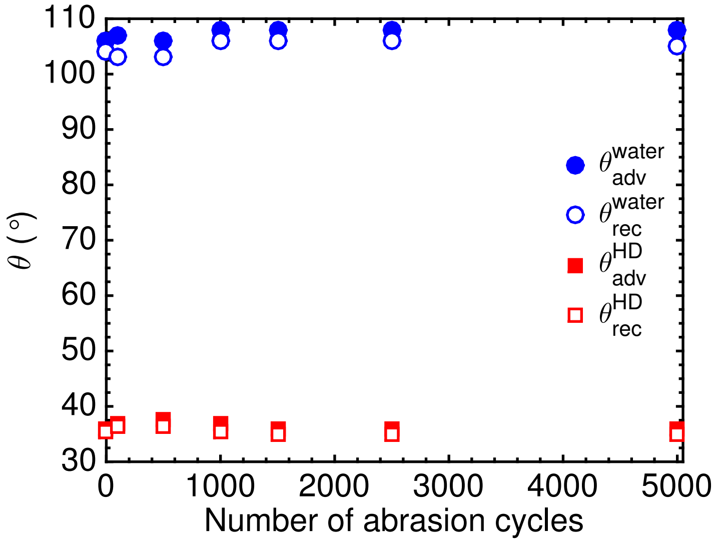

Figure 5.6: Advancing and receding contact angles for both water and hexadecane on the cb-PDMS surface, as a function of the number of linear Taber abrasion cycles. No degradation of either θ or $\Delta\theta$ was observed.

5.3.5 Fluorine-free superomniphobic surfaces

The only other reported method for repelling fluorinated liquids is by using so-called doubly-re-entrant texture[155]. This texture can be thought of as having a negative texture angle (ψ), and was predicted to show increased robustness to low-γ_{LV} liquids about a decade ago[26]. However, such texture can only be micro-fabricated in a clean room, and these surface still suffer from all the problems of maintaining the Cassie-Baxter state, as discussed in Chapter 1. Still, to further show the utility of the b-PDMS and cb-PDMS films, we fabricated micro-hoodoos using traditional lithography techniques (Fig. 5.2). After treating such a texture with our cb-PDMS monolayer, the resultant surface was superomniphobic and could also repel fluorinated liquids, even without the doubly-re-entrant geometry (Fig. 5.7). For example, droplets of perfluorodecalin displayed $\theta^*_{adv}/\theta^*_{rec} = 165°/111°$, and rolled from the surface without transitioning to the Wenzel state. Note that $\Delta\theta^*$ on these hoodoos was much greater than $\Delta\theta$ on the smooth, chemically identical counterpart. Thus, unless high θ^* is required, smooth omniphobic surfaces may prove advantageous over their high contact angle, superomniphobic counterparts. Note that, on F17-treated hoodoos, $\theta^*_{adv}/\theta^*_{rec} = 163°/141°$ with water, and $\theta^*_{adv}/\theta^*_{rec} = 166°/123°$ with hexadecane. However, both Krytox 100 and perfluorodecalin completely wet the texture, *i.e.* $\theta^*_{adv}/\theta^*_{rec} = 0°/0°$.

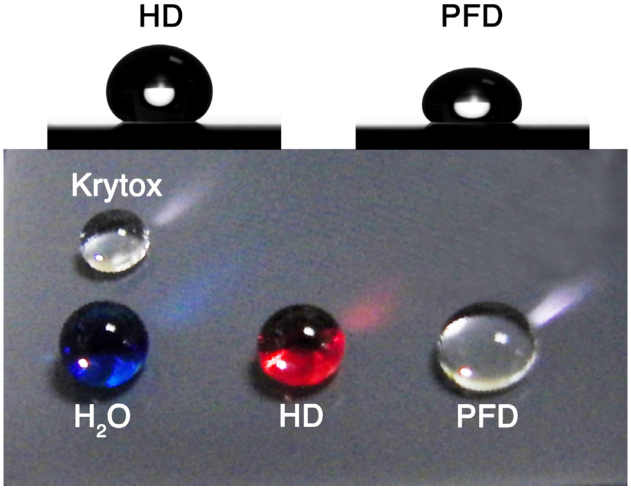

Figure 5.7: Droplets of four different liquids (water; HD: hexadecane; Krytox 103; PFD: perfluorodecalin) atop our cb-PDMS-treated micro-hoodoos. Static droplets from goniometric analysis are shown in the top of the figure, and an optical image of the droplets in shown in the bottom. The water and hexadecane were dyed for visualization. For water, $\theta^*_{adv}/\theta^*_{rec} = 163°/134°$. For hexadecane, $\theta^*_{adv}/\theta^*_{rec} = 168°/115°$. For PFD, $\theta^*_{adv}/\theta^*_{rec} = 165°/111°$. Viscous effects prevented accurate dynamic contact angle measurements of Krytox 103.

5.3.6 Liquid-like characterization of monolayers

To better characterize the liquid-like nature of our b-PDMS monolayers, we evaluated ice adhesion strengths using the same setup and methodology as Chapters 2-4. However, we explored the viscous nature of our b-PDMS monolayers by stepping through four orders of magnitude in shear rate. Typical ice adhesion testing in all previous chapters was conducted at a force gauge speed of 74 μm/s. Here we measured ice adhesion using speeds between 4 μm/s and 2 mm/s (Fig. 5.8a). Because of the large viscous component of our b-PDMS monolayers, a strong dependence on the shear rate, $\dot{\gamma}$, was observed. We convert from speed to $\dot{\gamma}$ using $\dot{\gamma} = v/h$, where v is the speed and we assume a monolayer thickness of $h = 4$ nm[45].

PDMS, as a bulk polymer, is a shear thinning liquid at room temperature[88]. Shear thinning liquids are known to follow a power-law dependence over a certain range of shear rates, leading to,

$$\tau = K\dot{\gamma}^n \tag{5.1}$$

where τ is the shear stress, K is the consistency index, and n is the power law index[156]. A Newtonian fluid exhibits $n = 1$ and shear thinning fluids exhibit $0 \leq n \leq 1$. K and n may be found by re-plotting τ against $\dot{\gamma}$ in logarithmic space (Fig. 5.8b). We found $K = 186$ Pa and $n = 0.58$ for the b-PDMS monolayer, and $K = 187$ Pa and $n = 0.51$ for the cb-PDMS monolayer.

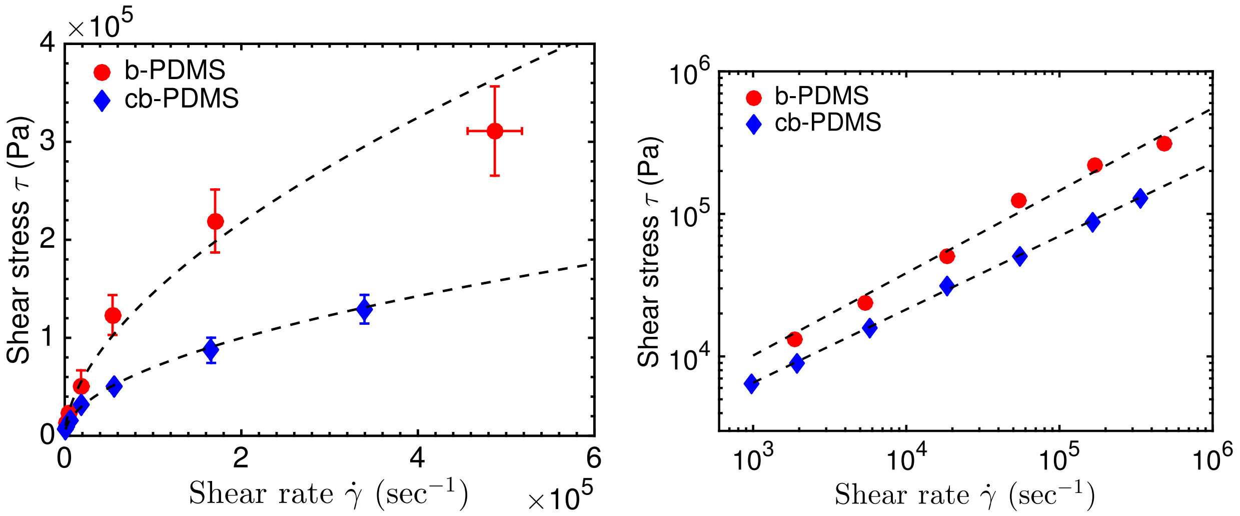

Figure 5.8: (left) The measured ice adhesion shear strength as a function of shear rate, for the b-PDMS and cb-PDMS surfaces. (right) When plotted in logarithmic space, a straight line was observed, indicating the power law regime of the viscous fluid.

If the power-law regime were to be extended to infinitely slow shear rates, K would effectively represent the minimum possible ice adhesion strength observable on these two monolayers. It is recognized that there is typically an onset shear rate for the shear thinning behavior of PDMS[157]. However, the extremely thin layer (4 nm) makes all practical velocities well above the onset of at least 1 Hz. For example, even at a speed of 10 nm/s, $\dot{\gamma} = 2.5$ Hz. It is then likely that K represents the minimum possible ice adhesion strength observable on PDMS monolayers. Note that coating Q from Chapter 2, a soft PDMS highly filled with silicone oil, initially displayed $\tau_{ice} = 150$ Pa. Because coating Q was spin-cast, the thickness was around 100 μm, making $\dot{\gamma} < 1$ Hz . Good consistency was therefore observed between the measured shear stress of bulk PDMS (coating Q) and our measured value of K.

5.3.7 Anti-solid adhesion

Ice adhesion is chemically dependent on a material's ability to hydrogen bond with water molecules[56]. Materials like metals, glass, ceramics, and hydrophilic polymers all display such a high affinity for water (and therefore ice) that the ice typically fails cohesively at all reasonable lengths (recall from Chapter 4 that even icephobic surfaces can cause ice to fail cohesively at large L). However, other solid contaminants are not as strongly dependent on hydrogen bonding. We evaluated the solid adhesion to our b-PDMS monolayers using cyanoacrylate superglue (covalent bonds), plaster of paris (a mud substitute, polar interactions), and paraffin wax (van der Waals bonding) (Fig. 5.9a). We additionally adhered crosslinkable PDMS as a negative control, because the PDMS monolayer was completely wet by the uncured PDMS pre-polymer and should therefore interact strongly with

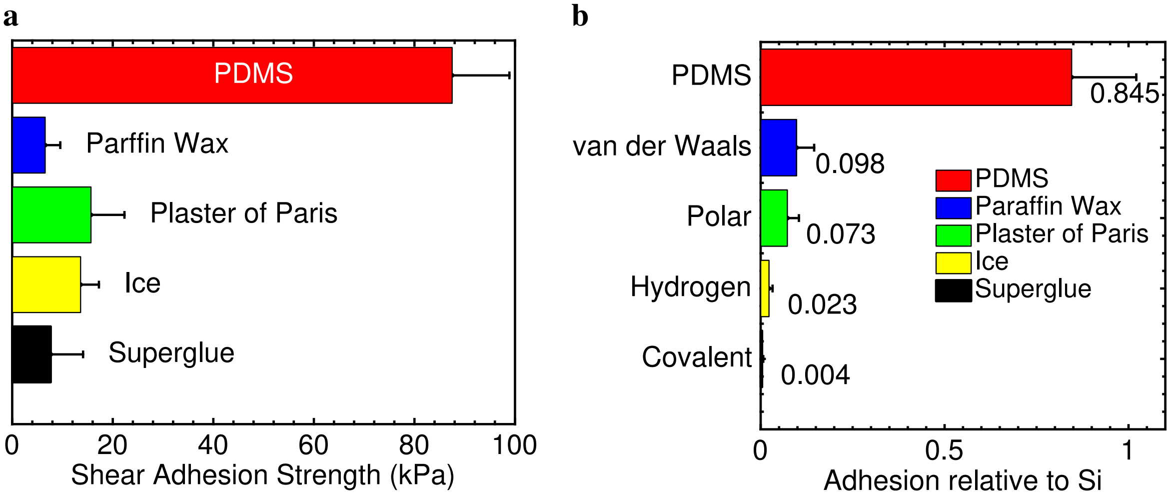

Figure 5.9: a, the adhesion shear strength between five different solid adherents and the b-PDMS monolayer. b, the relative adhesion strength, normalized by the adhesion strength of the adherents to bare silicon. The five adherents are classified by their primary bonding type.

the bulk PDMS after crosslinking.

As expected, the b-PDMS monolayer reduced the solid adhesion significantly for the covalent, polar, and van der Waals bonding solids. Compared to an untreated silicon wafer, covalent bond strength was reduced by 99.6%, hydrogen bond strength by 98%, polar bond strength by 93%, and van der Waals bond strength by 90% (Fig. 5.9b). Note that, in the case of the cyanoacrylate superglue, about half the samples never crosslinked, and remained liquid the following day (and the data was discarded). However, crosslinkable PDMS bond strength was barely altered, and several b-PDMS adhesion tests displayed values greater than the adhesion of PDMS to bare silicon. This control supports the conclusion that the b-PDMS monolayer reduces adhesion through interfacial slippage, but only when the PDMS chains can slip. The PDMS pre-polymer completely wet the b-PDMS monolayer, and once cured, prevented such slippage from occurring. Note that in all cases, the solid adherent started in a liquid state (methods, Sec. 5.2), and therefore perfect solid/solid contact can be assumed.

5.4 Conclusions

Surfaces lacking contact angle hysteresis due to interfacial slippage show promise in a wide range of fields, from liquid repellent coatings to surfaces minimizing solid adhesion. Here we explored the bidentate attachment of PDMS monolayers. The fabricated surfaces are the first to repel fluorinated solvents with low contact angle hysteresis, and may find usage in boiling and condensation heat transfer applications, due to their low hysteresis and non-zero contact angles with refrigerants. For this application, the high interfacial area between the solid and the liquid promotes heat transfer. However, one potential drawback of the high interfacial area with the liquid is the phenomenon of pearling. Pearling involves sliding droplets pinching off and leaving smaller, satellite droplets on the surface. It occurs when $U\eta = 2A\gamma_{LV}(\theta^*_{rec})^3$, where U is the droplet speed, η is the viscosity, and A is a constant. Pearling is therefore highly dependent on the receding contact angle[158]. Although the b-PDMS and cb-PDMS monolayers exhibit extremely low contact angle hysteresis, their contact angles are low. In the following Chapter, we discuss the fabrication of superomniphobic surfaces that display $\theta^* > 150^\circ$ and $\Delta\theta^* < 3^\circ$, even with low-γ_{LV} liquids like ethanol.

CHAPTER 6

Transparent, Flexible Superomniphobic Surfaces with Ultra-Low Contact Angle Hysteresis

6.1 Introduction

Engineered surfaces that repel low-surface-tension liquids, such as various oils and alcohols, have a wide array of applications, including stain-proof apparel, fuel transport, chemical shielding, and self cleaning[137, 159, 32, 160, 38]. Superomniphobic surfaces display $\theta^* > 150°$, and exhibit low contact angle hysteresis, with essentially all liquids[38]. Previous work has shown how re-entrant curvature is necessary for repelling low-surface-tension liquids[137, 159, 161, 42, 162, 26, 41, 163]. However, it is generally difficult to obtain ultra-low contact angle hysteresis ($\Delta\theta^* < 5°$) with such low-surface-tension liquids. In previous work, we discussed the critical role of hierarchical texture in developing superomniphobic surfaces with ultra-low $\Delta\theta^*$ values[137, 42]. Unfortunately, such hierarchical, superomniphobic surfaces are usually opaque[137, 42, 34, 164, 165, 166, 167, 168]. The development of *transparent* superomniphobic surfaces is essential for a range of applications, such as coatings for windows, phones, tablets, and computer screens. In this chapter, we discuss a facile method for the development of flexible and highly transparent (optical transmission $> 90\%$) superomniphobic surfaces that can repel a wide range of liquids with both low or high surface tension.

At the time of writing, only a handful of transparent and superomniphobic surfaces had been fabricated[169, 170, 171, 130]. None of these surfaces possesses hierarchical texture, which may yield ultra-low $\Delta\theta^*$ values. In most of the previous studies, transparency was only achieved at the expense of lower θ^* and/or higher $\Delta\theta^*$ values, for low-γ_{LV} liquids. In this work, using previously developed design parameters[26], we were able to tune the texture of our surfaces to develop one of the first transparent superomniphobic surfaces with ultra-low contact angle hysteresis.

6.1.1 Estimation of the contact angle

When a liquid droplet comes in contact with a solid surface, the droplet can either adopt the wetted, Wenzel state[1] or the non-wetted, Cassie-Baxter state[2] (see Fig. 1.2). A robust Cassie-Baxter state is required for superomniphobicity because surfaces in the Wenzel state cannot achieve $\theta^* > 90°$. As discussed in Chapter 1, roughness enhances the intrinsic wettability of surfaces in the Wenzel state, and no known material exhibits $\theta_Y > 90°$ for low-γ_{LV} liquids. Accordingly, the rational design of superomniphobic surfaces that repel low-γ_{LV} liquids should focus on keeping the metastable Cassie-Baxter state as robust as possible.

Surfaces that are textured on multiple length scales are beneficial for ultra-low $\Delta\theta^*$, because $\Delta\theta^*$ strongly depends on the solid-liquid contact area[137, 38, 42]. Two dimensionless parameters have previously been developed that may be useful in the design of superomniphobic surfaces[26]. The first parameter, D^*, is a measure of the solid-liquid interfacial area. For the square lattice of cylindrical pillars discussed in this work,

$$D^*_{pillar} = \frac{4(R_{pillar} + D_{pillar})^2}{\pi R^2_{pillar}} \tag{6.1}$$

where $2R_{pillar}$ is the diameter of the pillars, and $2D_{pillar}$ is the spacing between pillars (Fig. 6.1).

As D^* increases, the liquid comes in contact with less of the solid surface, which leads to an increase in the apparent contact angle. In this work, we fabricate hierarchical surfaces comprised of micro-pillars that are subsequently spray-coated with a second layer of texture that decorates only the tops of the pillars. The apparent contact angle for a hierarchical structure can be found recursively, by examining the texture on each length scale[159, 42, 137, 172]. Using our definition for the porosity of the surface, the Cassie-Baxter equation[2] can be written as,

$$\cos\theta^*_{pillar} = -1 + \frac{1 + \cos\theta_Y}{D^*_{pillar}}. \tag{6.2}$$

where the tops of the pillars are assumed to be flat, *i.e.* $r_\phi = 1.0$. For a hierarchical structure, the correct contact angle to use is not θ_Y, but rather the apparent contact angle on the smaller (nano) length scale, $\theta^*_{particle}$[159, 42]. Thus, under the assumption that the pillars are completely covered with particles, the apparent contact angle of our hierarchical surface is given by,

$$\cos\theta^*_{hierarchical} = -1 + \frac{1 + \cos\theta^*_{particle}}{D^*_{pillar}}. \tag{6.3}$$

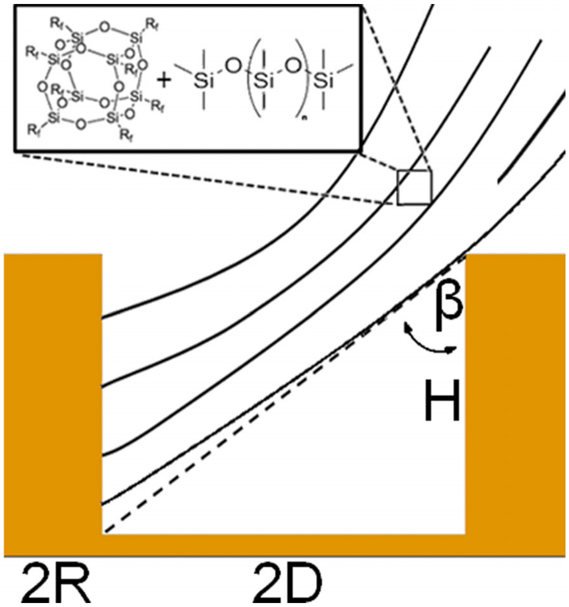

Figure 6.1: The geometric configuration of micro-pillars discussed here. The value of β shown is for an ideal case where particles reach the bottom of the pillars, but not the region in between the pillars ($\beta = \beta_{cr}$). The pillars alone lack re-entrant curvature and cannot support a composite interface with low-γ_{LV} liquids. These points are discussed below. Within the streamlines are the two chemical components used in this work, PDMS and F-POSS (see Sec. 6.2).

6.1.2 Robustness factor

The robustness factor, A^*, was previously developed to characterize a surface's resistance to wetting[38]. Textures yielding $A^* < 1.0$ cannot support a composite interface, and surfaces exhibiting $A^* \gg 1.0$ have a highly stable Cassie-Baxter state. To predict if surfaces in this work, of known D^*, will support a composite interface, a modified expression for the robustness factor was derived. Particles forming an overhang on micro-pillars generate a hoodoo-like structure[26, 41]. In this case, the robustness factor is given by the harmonic mean between a droplet's dimensionless sagging height (characterized by H^*), and its dimensionless sagging angle (characterized by T^*). For the hoodoo-like surfaces discussed here,

$$H^* = \frac{2R\ell_{cap}\Big[(1 - \cos\theta_Y) + H/R\Big]}{D^2(1 + \sqrt{D^*})} \tag{6.4}$$

and

$$T^* = \frac{\ell_{cap}\sin\theta^*_{particle}}{D(1 + \sqrt{D^*})} \tag{6.5}$$

where ℓ_{cap} is the capillary length ($\ell_{cap} = (\gamma_{LV}/\rho g)^{1/2}$, ρ being the fluid density and g the gravi-

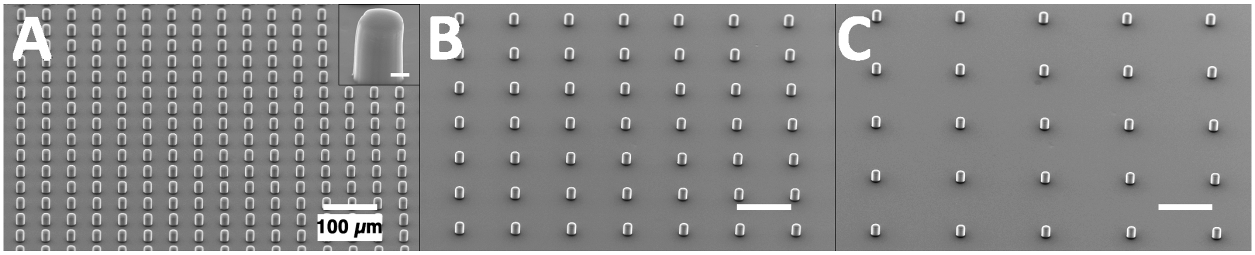

Figure 6.2: A-C) SEM micrographs of 20 μm high PDMS pillars with D^* values of 10, 42, and 100, respectively, without any spray coating. Images are taken at 45 °from the horizontal. Scale bars are 100 μm. The inset in A shows a single pillar; scale bar is 5 μm.

tational constant). Typically there exists some minimal texture angle such that θ_Y can be adopted, ψ_{min}[26, 41], but for hoodoos we assume $\psi_{min} = 0°$. The robustness factor for our surfaces is approximately given by,

$$\frac{1}{A^*} \approx \frac{1}{H^*} + \frac{1}{T^*}. \tag{6.6}$$

We designed the surfaces in this work such that both $D^* \gg 1$ and $A^* \gg 1$.

6.2 Materials and methods

6.2.1 Master mold fabrication

A 3 μm thick layer of photoresist (SPR 220-3.0, Shipley) was spin-coated on a silicon wafer and baked for 90 sec at 115 °C. The lateral layouts of the micropattern were defined by 365 nm UV exposure (Karl Suss MA6 mask aligner) and developed in AZ300 MIF. Inductively coupled plasma reactive-ion etching (ICP-RIE, STS Pegasus) formed $\approx$20 μm and 40 μm deep micropore arrays in the exposed regions, and the photoresist was stripped (Baker PRS 2000). The master molds were then exposed to vapors of (heptadecafluoro-1,1,2,2-tetrahydrodecyl)trichlorosilane at 120 °C for 1 hour. This rendered the master molds hydrophobic.

6.2.2 Synthesis of micro-pillars

Polydimethylsiloxane (PDMS, Sylgard 184 Kit, Dow-Corning) was mixed in a 10:1 (w/w) ratio as received, and poured over the Si master molds at room temperature. The mixture was degassed and subsequently cured for 3h at 80 °C. The PDMS was removed from the mask, leaving a square array of pillars (Fig. 6.2).

20 mg/mL solutions of 25 wt% 1H,1H,2H,2H-heptadecafluorodecyl polyhedral oligomeric silsesquioxane (F-POSS) + PDMS were prepared in Asahiklin 225 (AK225, Asahi Glass Co.).

The pillars were sprayed using an airbrush (Paasche Airbrush Co., product code 02661400031-1) at a distance of 10 cm with an N_2 pressure of 58 psi. Sprayed pillars were subsequently cured again at 80 °C for 3 h.

6.2.3 Contact angle evaluation

Contact angles were measured using a Ramé-Hart 200-F1 goniometer. Measurements were made by advancing and receding a single droplet of liquid ($\approx$6 μL) from a 2 mL micrometer syringe (Gilmont). Averages from at least five independent measurements were reported. The surface tension of probe liquids was evaluated using the pendant drop method and all values fell within ± 5 % of literature values.

6.2.4 Electron microscopy

Surfaces were imaged using a Phillips XL30 scanning electron microscope (SEM) at 15 kV. A thin layer (≈ 50 nm) of gold was sputtered onto the surfaces to reduce charging. Spraying movies were obtained using a VistaVision VWR optical microscope with a $5\times$ objective. At 15 second intervals the substrates were transferred from the spraying apparatus to the microscope stage.

6.2.5 Transparency and flexibility analysis

A Varian Cary 50 Bio UV-Vis Spectrometer was used to obtain transmittance data in the 200-800 nm range at a scanning speed of 600 nm/s. Surfaces with small D^* exhibited significantly reduced optical transmission (Fig. 6.3).

Averages of three independent measurements are reported. An image of the sprayed pillar substrate atop an iPhone 3GS backlit by a repeated image of 'M's was taken. To highlight the flexibility of the surfaces, a single droplet ($\approx$ 2 μL) of liquid was placed on the sprayed pillar surface, which had been bent inside a scintillation vial (diameter = 2 cm). Videos were obtained with a Casio EX-F1 camera, analyzed using Windows Movie Maker, and time-lapse photos were constructed using Adobe Photoshop CS5.1.

6.3 Results and discussion

Transparent, flexible, superomniphobic surfaces were created using a facile spray method on master-molded polydimethyl siloxane (PDMS) pillars. Briefly, silicon master molds with a uniform square array of holes ($2R = 15 \pm 0.2$ μm) were fabricated as described above. We prepared

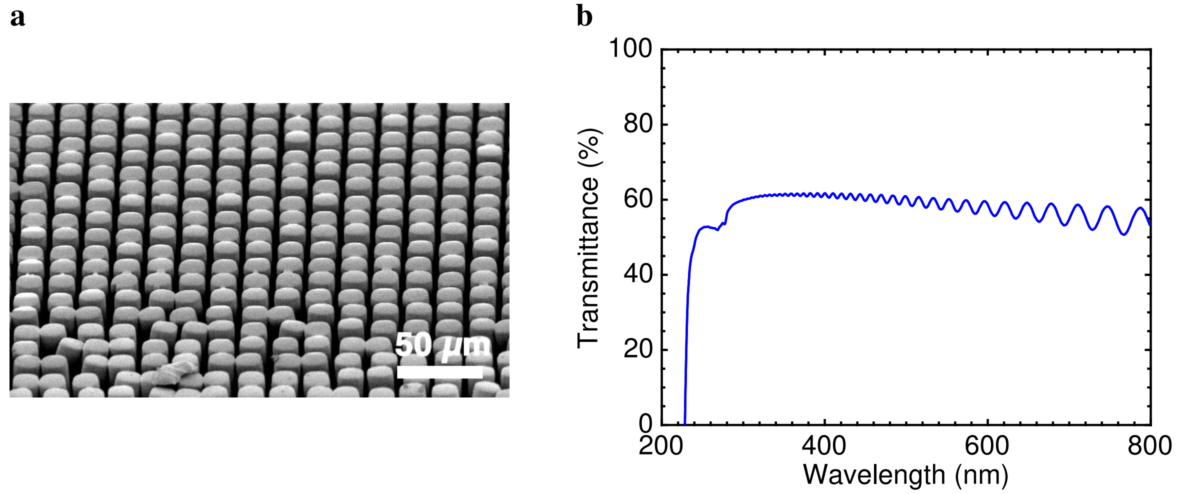

Figure 6.3: Although a smooth PDMS film was roughly 96% transparent in the visible range, PDMS micropillars can cause significant light scattering. a, SEM micrograph of 30 μm high pillars with $D^* \approx 1$ seen from a 65°angle from the horizontal. b, Transmittance as a function of wavelength for the structure shown in (A).

molds with several D^* values ranging from 10-100 (corresponding A^* values from 27 to 0.8 with water, see Table 6.1).

Table 6.1: Robustness factor A^* for three different probe liquids for spray times of 30, 60, and 120 seconds, on surfaces with D^* values of 10, 42, and 100.

	A^*_{water}			$A^*_{hexadecane}$		$A^*_{ethanol}$		
D^*	30 s	60 s	120 s	30 s	60 s	30 s	60 s	120 s
10	27.8	31.1	33.9	2.91	14.9	0.39	5.27	5.72
42	4.89	5.69	6.3	2.35	2.74	0.95	1.1	1.66
100	1.94	3.31	3.78	0.94	1.85	0.42	0.92	1.04

PDMS was chosen as the pillar material because it is highly transparent, flexible, and possesses a low surface energy[169]. Pillar heights of 20 and 40 μm were chosen for this work. Pillars were subsequently sprayed with solutions of 1H,1H,2H,2H-heptadecafluorodecyl polyhedral oligomeric silsesquioxane (F-POSS)[26, 134], along with additional PDMS to serve as a binder. The high degree of fluorination makes F-POSS one of the lowest-surface-energy molecules available ($\gamma_{SV} \approx 10$ mN/m). Spraying low-surface-energy polymers can lead to a controllable re-entrant texture with oleophobic properties, as explained previously[34]. A schematic of the synthesis methodology is shown in Fig. 6.4. Note that the photolithography necessary to create the master mold only needs to be performed once (see Sec. 6.2 above).

SEM micrographs of two representative surfaces with $D^* = 10$ and $D^* = 100$ that were sprayed with the PDMS/FPOSS system for various spray times are shown in Fig. 6.5. Without any sprayed solution (Fig. 6.2), only the surface with $D^* = 10$ is robustly superhydrophobic, and

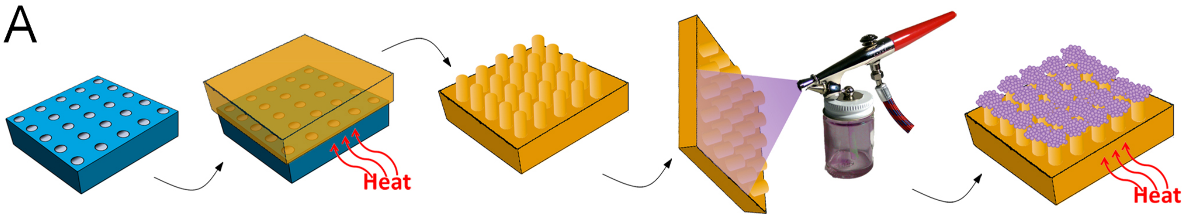

Figure 6.4: Fabrication method. First, the desired pattern is etched into a silicon master mold using photolithography. PDMS is poured into the master mold and cured in an oven. PDMS/F-POSS is sprayed onto the pillars, which are subsequently cured again. See Sec. 6.2 for more details.

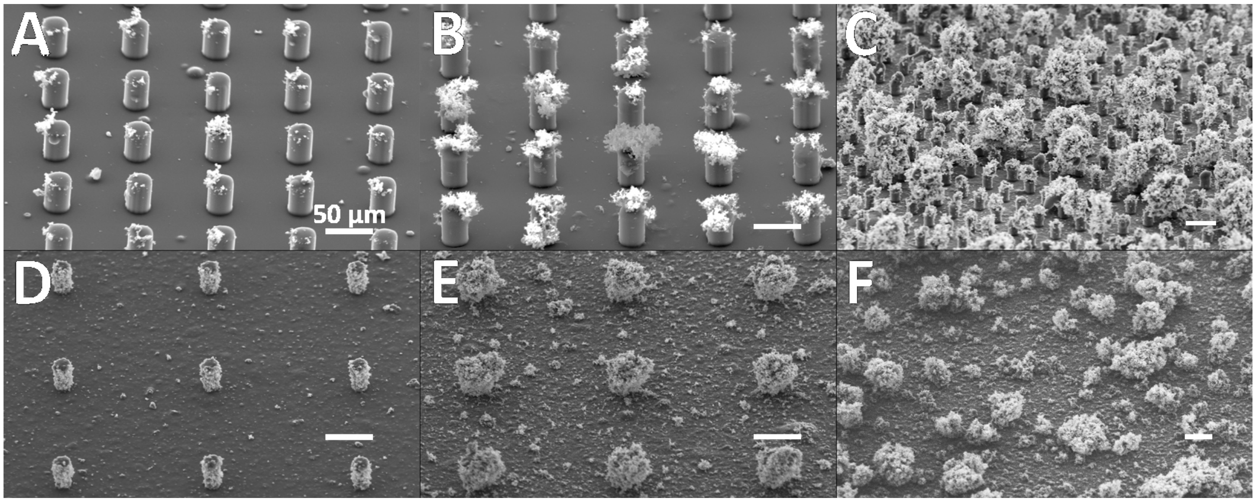

Figure 6.5: A-C) PDMS pillars ($D^* = 10$) spray-coated with PDMS/F-POSS for 30, 120, and 240 seconds. D-F) PDMS Pillars with $D^* = 100$, spray-coated for 30, 120, and 180 seconds.

neither of the surfaces are superomniphobic (as they lack re-entrant curvature). This matches well with the calculated values of A^*_{water} and $A^*_{ethanol}$ tabulated in Table 6.1. In two recent publications, discrete pillars were fabricated with re-entrant curvature on the macroscale[169, 170]. However, without hierarchical texture, these surfaces have relatively high contact angle hysteresis ($\Delta\theta^* > 5°$) for low surface tension liquids. The spray-coating-based method described herein introduces both re-entrant curvature (overhang of the sprayed aggregates atop the pillars), and a hierarchical texture, which leads to ultra-low $\Delta\theta^*$.

6.3.1 Axisymmetric stagnation-point flow

The spray method was chosen because it creates a unique flow field that can localize particle deposition, which enables the fabrication of hierarchically textured surfaces. When the spray gun was pointed parallel to the pillar axes (Fig. 6.6), an axisymmetric stagnation-point flow field was

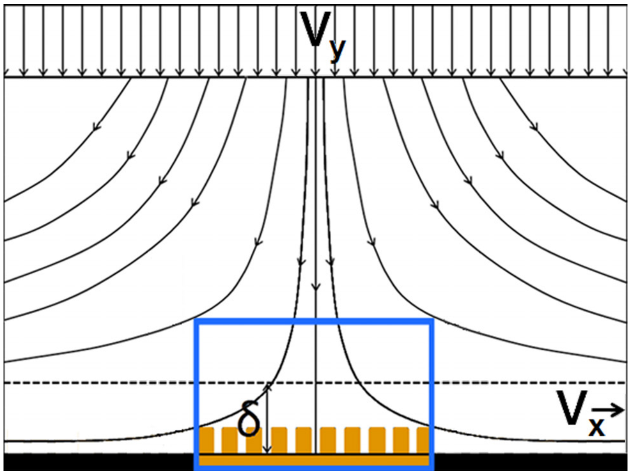

Figure 6.6: The stagnation point flow created by our spray setup (δ is the boundary layer thickness). The corresponding streamlines are also shown. The blue box denotes the applicable region for our setup, where substrates are directly beneath the axis of the spray gun.

created.

This type of flow field is well-characterized and has a boundary layer thickness δ, which may be described by[173],

$$\delta = 2.4\sqrt{\frac{\nu}{a}}. \tag{6.7}$$

Here, ν is the kinematic viscosity, and a is a constant arising from non-dimensionalizing the velocity profile ($V_y = -ay$). For a hydrodynamically smooth surface, the correct velocity scale (for V_y) is $\sqrt{\nu a}$, which leads to,

$$a = V_y^2/\nu. \tag{6.8}$$

The boundary layer thickness may then be rearranged to,

$$\delta = 2.4\nu/V_y \tag{6.9}$$

By measuring the mass flow rate Q (22 mg/s at an N_2 pressure of 58 psi), and nozzle diameter $d = 790\ \mu$m), the boundary layer thickness can be found using,

$$\delta = 2.4\frac{\pi d^2 \mu}{4Q} \tag{6.10}$$

where μ is the viscosity of the sprayed mixture (N_2 and polymer solution). Therefore, by measuring the diameter of the spray gun and mass flow rate of the spray feed, the boundary layer thickness can be readily evaluated.

Our flow field yielded a boundary layer thickness of $\delta = 94 \pm 5\ \mu$m. Physically, a boundary

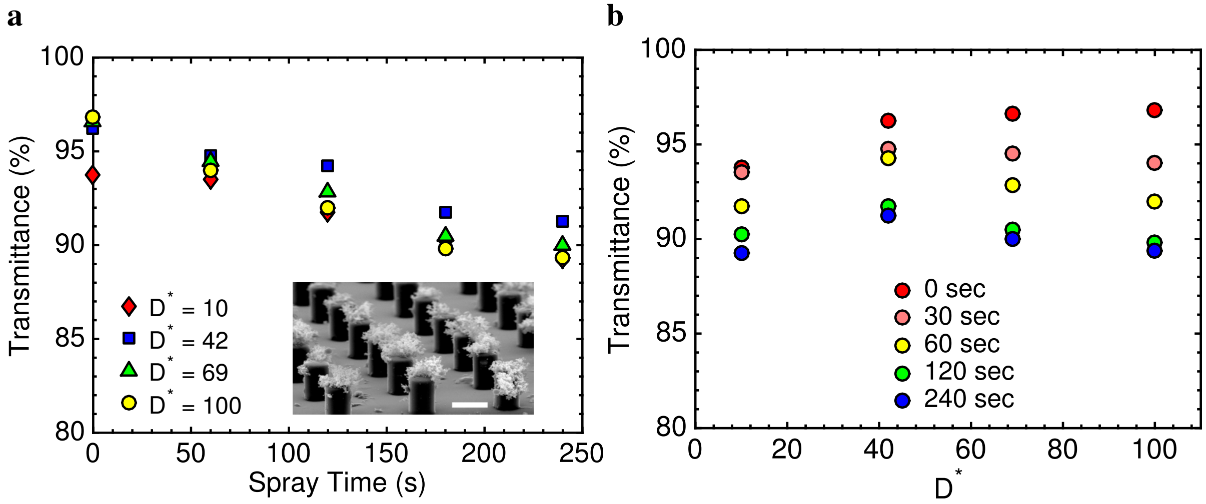

Figure 6.7: Transparency of the surfaces sprayed with the PDMS/F-POSS for different spray times and D^* values. For all spray times greater than 0 seconds, a maximum in transparency persisted at $D^* = 42$. The inset in (a) shows the pillars with ($D^* = 10$). Scale bar: 25 μm.

layer thickness of this scale implies that any height up to approximately 100 μm from the surface will have a significant velocity component that is perpendicular to the pillar axis (V_x), even though the spray setup is pointed along the pillar axis. Beyond δ, 99% of the velocity profile matches the mainstream flow (along the pillar axis). A two-dimensional model elucidated how the horizontal velocity component (V_x) lead to controllable and localized particle deposition (Fig. 6.1).

6.3.2 Design parameters for pillar geometry

Particles within the streamlines of the flow approach the pillar tops at an angle β. Considering a pillar height H and an inter-feature spacing $2D$, the critical angle required for a streamline to intersect the bottom of a pillar is given by,

$$\beta_{cr} = tan^{-1}\left(\frac{2D}{H}\right) \tag{6.11}$$

Typically, β is fixed for a set of given spray conditions. However, in our experiments the pillar spacing was varied over a wide range. For a given pillar height and spacing, values of $\beta < \beta_{cr}$ will cause streamlines to intersect the substrate in between the pillars rather than to hit the pillar sidewalls. The effects of varying both spray time and D^* on the transparency of the fabricated surfaces are illustrated in Fig. 6.7.

As the fraction of pillars per unit area decreases (increasing D^*), the transmittance increases, as expected. The deviations in transmission from a smooth PDMS film originate from the slight scattering that is caused by the pillar edges, and this effect was amplified with increasing pillar

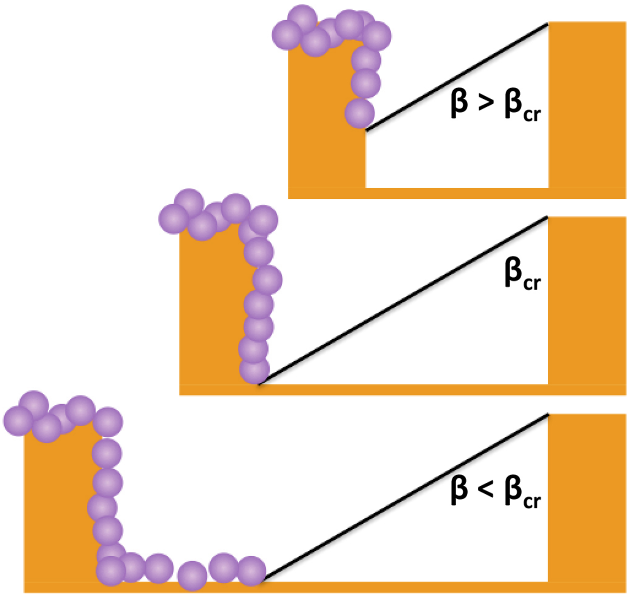

Figure 6.8: A schematic illustrating the various possible cases when β is either less than, equal to, or greater than β_{cr}. The effects of varying β on controllable particle deposition is also shown.

density. For a sample with $D^* \approx 1$ (Fig. 6.3), the transparency was lower than 60%.

As the spray time increases, the transparency decreases because a higher fraction of the surface is covered with the opaque PDMS/F-POSS particles. For our spray conditions, the highest transparency was always observed for $D^* = 42$ ($R = 15$, $2D = 82$; Fig. 6.7B). Because of the axisymmetric stagnation point flow field, a maximum in transparency can be expected. Increasing D^* reduced the scattering caused by the pillar edges, but also increased the probability of particles aggregating in between the pillars.

Assuming that $\beta = \beta_{cr}$ for pillars with $D^* = 42$, for a pillar height of 20 μm, we estimated $\beta = 76°$. Physically this means that, for all pillar spacings such that $D^* < 42$, all incoming particles will aggregate on a pillar wall, rather than land in between the pillars. For $D^* > 42$ (or $\beta < \beta_{cr}$), particles will aggregate on the pillar walls as well as in between the pillars. For the geometry (D^*) with optimal transparency, all particles with a velocity component that is perpendicular to the pillar axis will stick to a pillar wall rather than land in the regions between the pillars.

Other geometries can then be divided into two regimes: $\beta < \beta_{cr}$ and $\beta > \beta_{cr}$. For our surface with $D^* = 10$, we calculated $\beta_{cr} = 58°$. Although the spacing between the pillars ($2D$) has changed, the spray conditions are equivalent to the $D^* = 42$ case, and thus $\beta = 76°$ still. Back-solving for the height of the pillars at minimum incidence yields a value of 8 μm (Fig. 6.8), which implies that, as our pillars are 20 μm in height, only the top 12 μm will collect particles, which leads to controllable particle deposition.

This model is supported by the SEM micrographs in Fig. 6.5a-c and Fig. 6.7a (inset). The

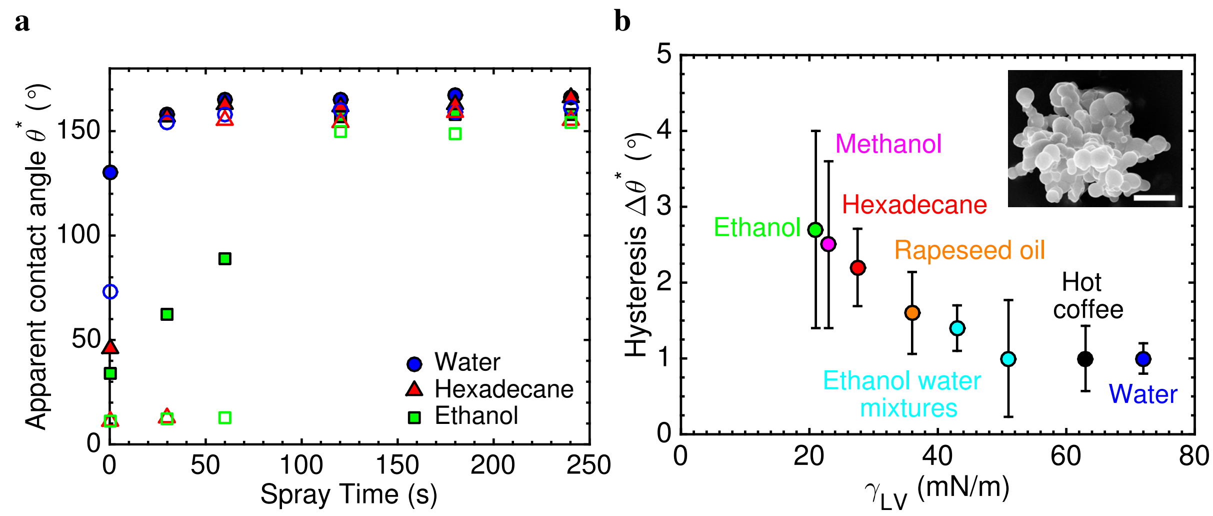

Figure 6.9: A, Contact angle measurements with water, hexadecane, and ethanol for pillars with $D^* = 100$. The filled and open symbols represent advancing and receding contact angles, respectively. B, Contact angle hysteresis as a function of γ_{LV} for pillars with $D^* = 100$, sprayed for 120 seconds. The inset shows the re-entrant PDMS/F-POSS structure; scale bar: 5 μm.

majority of the PDMS/F-POSS aggregates lay atop the PDMS pillars. A similar analysis can be performed for a geometry with $D^* = 100$. In this case, $\beta_{cr} = 82°$, which allowed particles to not only stick to the pillar walls, but also to the space in between the pillars (Fig. 6.5d-f). The re-entrant curvature produced by particles sitting atop the pillars and on the pillar side walls was necessary to repel liquids exhibiting $\theta_Y < 90°$ *i.e.* low-γ_{LV} liquids. For example, spraying the same solution onto a flat PDMS substrate yielded oleophilic surfaces, with $\theta^* = 22°$ and $\theta^* = 28°$, for ethanol and hexadecane, respectively.

6.3.3 Wettability of resultant surfaces

Once high transparency had been achieved through localized particle deposition, we evaluated the liquid repellency of our surfaces. For our experiments, we chose hexadecane (non-polar liquid) and ethanol (polar) as representative low-γ_{LV} liquids ($\gamma_{LV} = 27.5$ mN/m and $\gamma_{LV} = 22.1$ mN/m, respectively)[18]. The advancing and receding contact angles were measured versus spray time for a pattern with $D^* = 100$ (Fig. 6.9A).

As stated earlier, without spraying the surface, $A^*_{water} = 0.84$ (Table 6.1). After spraying with the PDMS/F-POSS solution for 30 seconds, the composite interface can be supported for water, but not for hexadecane ($A^*_{water} = 1.94$, but $A^*_{hexadecane} = 0.94$). After a spray time of 60 sec, hexadecane can exist in the Cassie-Baxter state ($A^*_{hexadecane} = 1.85$; $A^*_{ethanol} = 0.92$), and after 120 seconds, ethanol is also repelled by the surface ($A^*_{ethanol} = 1.04$). For patterns with $D^* = 10$, water is stable in the Cassie-Baxter state without any spray deposition, exhibiting $A^*_{water} = 26.8$,

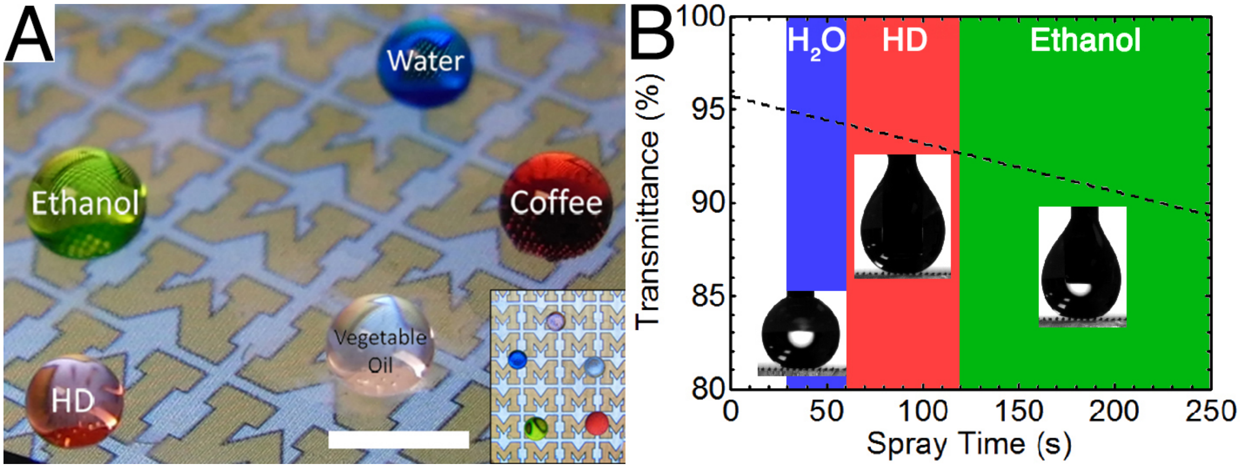

Figure 6.10: A) Droplets of varying surface tension beading up on an Apple iPhone 3GS screen coated with 20 μm pillars with $D^* = 42$, and spray coated with PDMS/ F-POSS for 120 seconds. The inset shows the top view of the same droplets to highlight the transparency of the coating. Scale bar: 500 μm. B) A design diagram for pillars with $D^* = 100$ combining transparency and liquid repellency characteristics. The insets are optical images of droplets of water, hexadecane (HD), and ethanol sitting atop the spray-coated pillars. The composite interface was clearly visible underneath the liquid droplets.

whereas ethanol is repelled after a spray time of approximately 45 seconds (Table 6.1). For lower D^* values, low-γ_{LV} liquids exhibited larger $\Delta\theta^*$ for all tested spray times ($\Delta\theta^* > 10°$), owing to the increased solid fraction. $\Delta\theta^*$ for pillars with $D^* = 100$ that were sprayed for 120 seconds is shown as a function of liquid surface tension in Fig. 6.9B. Even for liquids with very low surface tension, such as ethanol, we observed $\Delta\theta^* < 3°$.

An iPhone 3GS screen that was coated with one of our surfaces ($D^* = 42$, spray time of 120 s) repelled different liquids with a range of surface tensions (Fig. 6.10A). The inset is a top view of the screen. It is evident that our surfaces are not only mathematically transparent (*i.e.*, there is a small percentage of sparsely located opaque pillars), but also visually transparent, because the pillars are invisible to the naked eye.

With our control over D^*, re-entrant curvature, and hierarchical texture, a design diagram was constructed for coated micro-pillars with $D^* = 100$ (Fig. 6.10B). This diagram combines aspects of liquid repellency, transparency, and spray time into a single plot. It is then trivial to select the desired surface tension liquid that is to be to repelled and to predict the final transparency of the substrate. Similar design diagrams could be constructed for other D^* values.

6.3.4 Localized deposition analysis

We also evaluated the effects of varying the pillar height on the transparency of the fabricated surfaces. With increasing pillar height, the PDMS/F-POSS particles were found to agglomerate more

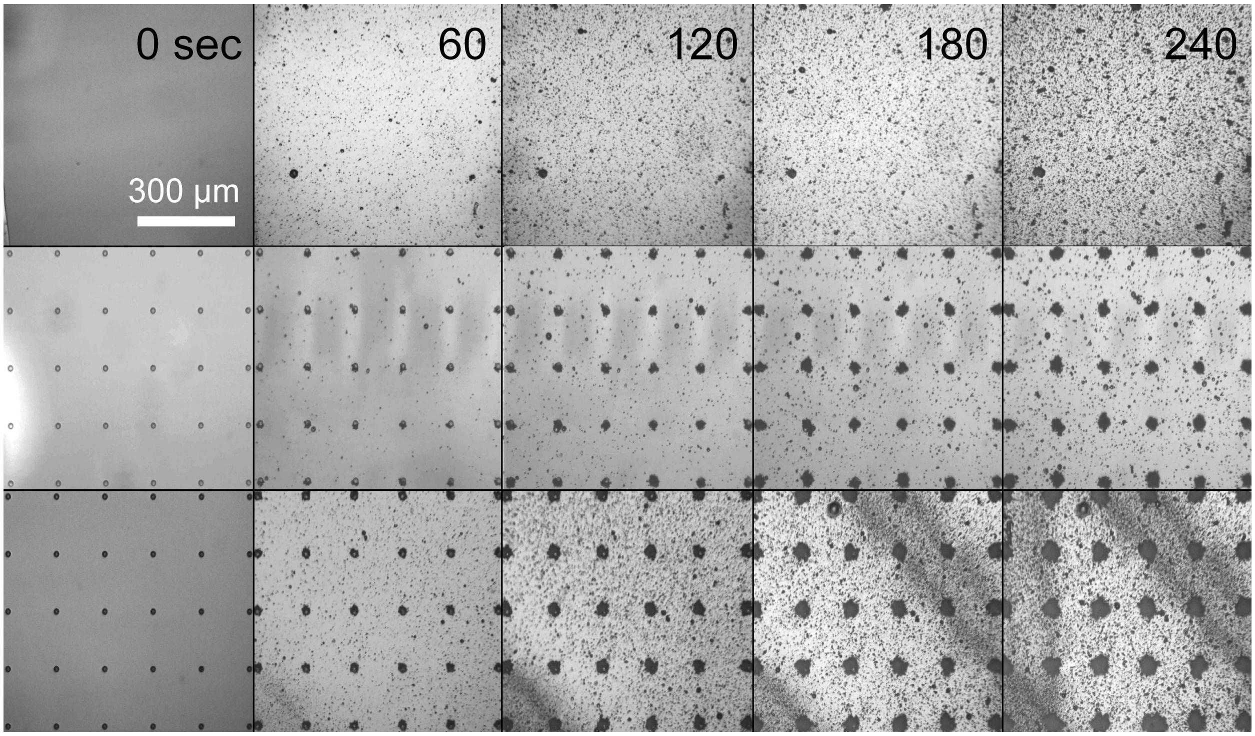

Figure 6.11: Time-lapsed movie frames corresponding to flat PDMS (top), 20 μm high pillars with $D^* = 100$ (middle), and 40 μm high pillars with $D^* = 100$ (bottom). The frames support the proposed model, as fewer particles accumulate between the 20 μm high pillars than between the 40 μm high pillars.

quickly around the pillars because of the increase in surface area (and decreasing β_{cr}). To better understand this phenomenon, spray coating was combined with time-lapsed optical microscopy for different pillar heights and D^* values over a spray time of 240 seconds, in intervals of 15 seconds. In Fig. 6.11, still frames are shown that correspond to flat PDMS, pillars with $D^* = 100$ and $H = 20$ μm, and pillars with $D^* = 100$ and $H = 40$ μm, respectively.

It should be emphasized that all surfaces were sprayed together within 5 mm of one another, so that the observed effects were purely due to geometry. It was evident that a greater pillar height lead to faster lateral growth of the PDMS/F-POSS aggregates, which in turn lowered the overall transparency. However, because of the small pillar size ($2R = 15$ μm) and sparse pillar density ($2D = 140$ μm), the optimally sprayed surfaces were visually still close to a transparency of 100%.

The low $\Delta\theta^*$ and the flexibility of our fabricated surfaces are highlighted in Fig. 6.12. The fabricated surfaces with $D^* = 100$ (sprayed for 120 seconds) were curved into arcs, and various droplets of liquids with high or low surface tension were deposited on them. The droplets rolled back and forth along the length of the surface until the edge was reached. The trajectories of both water and ethanol molecules are shown in the superimposed frames, spaced every 10 ms.

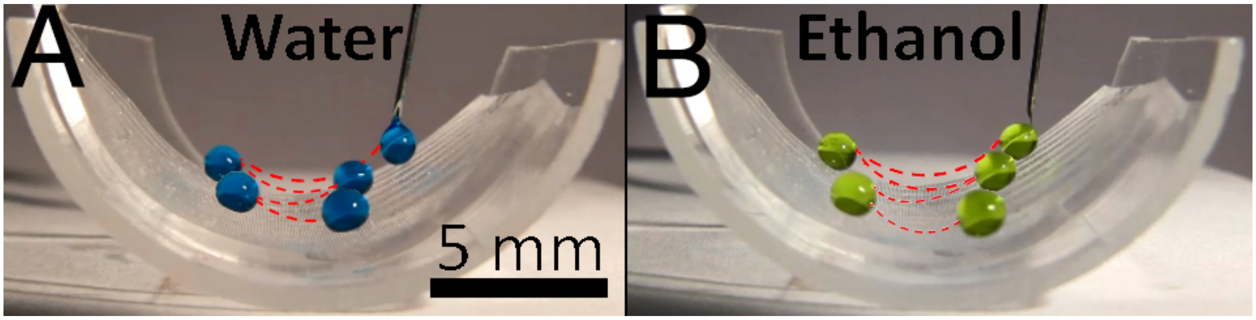

Figure 6.12: Movie frames taken with 10 ms intervals were superimposed for droplets of water and ethanol, respectively. The droplets rolled back and forth several times before reaching the edge of the substrate, which highlights the ultra-low $\Delta\theta^*$.

6.3.5 Conclusions

To the best of our knowledge, this is one of the first flexible and transparent surfaces that displays ultra-low contact angle hysteresis with low surface tension liquids, such as ethanol. Furthermore, the simple mold and spray fabrication method may be well-suited to scale-up to functionalize significantly larger areas. However, one shortcoming of these systems is their mechanical durability. PDMS as a base material is mechanically poor, and thus even relatively mild mechanical abrasion renders these surface wetting to both high and low surface tension liquids. In the next chapter I discuss a new method for fabricating extremely mechanically robust superhydrophobic surfaces (note, *not* superomniphobic).

CHAPTER 7

Designing Self-Healing Superhydrophobic Surfaces with Exceptional Mechanical Durability

7.1 Introduction

Superhydrophobic surfaces have garnered much attention over the last few decades for their ability to be self-cleaning[32], drag-reducing[126], stain-resisting[174] and anti-fouling[127]. By trapping pockets of air in their porous texture, SHSs display water contact angles $\theta^* > 150^\circ$ and low roll-off angles[145]. The design and optimization of such surfaces have been well studied[32, 126, 174, 127, 145, 175, 176, 128, 129, 26, 41, 146, 177, 178, 179, 14, 180]. However, most natural and artificial SHSs suffer from poor mechanical durability, as their fragile and porous surface texture can be easily removed even by the swipe of a finger[146]. Only a few SHSs have been reported to exhibit mechanical durability, as characterized by sand impact[181, 182, 130, 183, 184], rubbing with a soft cloth[174, 185, 186, 187], tape peel tests[176, 182, 188, 133, 189], or sandpaper abrasion[129, 146, 178, 179, 14, 182, 186, 190, 191, 192, 193, 194, 195, 141, 196, 197, 198, 199, 200]. However, all such reports present single material systems. The development of design criteria to aid in the systematic fabrication of durable SHSs, generalizable to multiple chemistries or fillers, is expected to be extremely useful to the field. In the first part of this work, we develop such criteria.

Even the most durable SHSs will eventually become damaged by extreme or repeated mechanical abrasion, which damages a SHS's low surface energy and/or texture. SHSs that can regenerate both their surface texture and chemistry[201, 185, 11], akin to the lotus leaf's ability to regenerate its nano-structured wax[32], would be highly desirable. Herein we also report mechanically durable SHSs that exhibit physical and chemical self-healing. The developed surfaces can fully recover their water-repellency even after being abraded, scratched, burned, plasma cleaned, flattened, sonicated and chemically attacked. These surfaces, and the design parameters used to develop them, may find immediate usage in a wide range of academic and industrial sectors across the globe.

7.2 Materials and methods

7.2.1 Materials and synthesis

All solvents, pre-polymers, and crosslinking agents were used as-received. Fluorinated solvents HCFC-225ca/cb (Asahiklin-225, Asahi Glass Co.) and HFC-43-10mee (Vertrel XF, DuPont) were purchased from Techspray and TMC Industries, Inc. respectively. Poly(methyl methacrylate) (PMMA), polystyrene (PS, 45 kDa or 1.2 kDa) and polyisobutylene (PIB) were purchased from Scientific Polymer. Luxecolor 4FVBA fluorinated polyol resin (FPU, 55% solids in n-butyl acetate) was purchased from Helicity Technologies, Inc. Desmophen 670BA polyol was provided by Bayer MaterialScience, A.G. Isocyanate crosslinkers Desmodur N3200 and Wannate HMDI (4,4-Diisocyanato-methylenedicyclohexane) were provided by Bayer MaterialScience, A.G. and Wanhua Chemical Group Co., Ltd. respectively. Crosslinker ratios were 9.7 and 3.4 wt% respectively with FPU, and 28.5 wt% N3200 with 670BA. Propylene glycol, a chain-extending agent that increases the modulus of the final cross-linked polyurethane network, was obtained from MP Biomedicals, LLC. A polyurethane elastomer (Vytaflex 40) was purchased from Smooth-On, Inc., and was prepared according to manufacturer directions. CNR (chlorinated polyisoprene) was provided by Covestro. Polydimethylsiloxane elastomer (Dow Corning Sylgard 184) was obtained from Krayden, Inc. and a 10:1 base:crosslinker ratio was used according to manufacturer directions. Acrylate-terminated perfluoropolyether resin (CN4001, purchased from Sartomer USA, LLC) was mixed with 5 wt% radical photoinitiator (Irgacure 2022, provided by BASF Corporation) to yield a UV-curable fluorinated polymer matrix. Cyanoacrylate adhesive (3M Scotch-Weld SF-100) was purchased from Pack-n-Tape, Inc. Two-part epoxy adhesive (Selleys Araldite 90 seconds) was used in an approximate 1:1 volume ratio of the components, per manufacturer instructions.

Fluorodecyl and fluorooctyl polyhedral oligomeric silsesquioxanes (F-POSS, FO-POSS) were prepared by condensing perfluorinated triethoxysilanes as previously reported[134]. Octaisobutyl polyhedral oligomeric silsesquioxane (IB-POSS) was purchased from Hybrid Plastics, Inc. Eicosane was purchased from Acros Organics.

7.2.2 Coating sample fabrication

Spray coating solutions were prepared by solubilizing the filler, polymer or pre-polymer, and crosslinker or photoinitiator (if applicable) at an overall solution concentration of 100 mg/mL. The fraction of filler in the total solution was varied from 0 to 50 wt%. The solvents used for F-POSS and FO-POSS blends were: pure Vertrel XF (for FPU and PFPE), pure AK-225 (for SF100, 670BA, PMMA, chain extended FPU and PDMS), 50:50 Chloroform:Vertrel XF (for Vytaflex 40, PS and Araldite epoxy) and 50:50 AK-225:Hexane for PIB. Pure chloroform was used for

IB-POSS blends with 670BA and FPU. Pure toluene was used for blends of eicosane and CNR.

No significant effect on spray coating morphology was observed between these solvents, as they have similar volatility and surface tension. The solutions were applied to 10 cm × 10 cm 6061 aluminum sheets with an ATD Tools 6903 high-volume-low-pressure spray gun. 20 mL of coating solution was applied to each plate, which resulted in coatings that were approximately 100 μm thick. However, because the surfaces are both porous and extremely rough, the thickness cannot be well-defined, and during abrasion tests the percent mass loss was tracked instead. Spray coated samples were held at room temperature for at least one day and then cured as necessary prior to further testing (polyurethanes: 80 °C two days; PDMS: 150 °C 1 h; epoxy and cyanoacrylate: room temperature at least 2 h; PFPE acrylate resin: 15 min simultaneous exposure to 254 and 365 nm UV mercury lamp irradiation under N_2 atmosphere).

7.2.3 Hansen solubility parameter determination

Hydrophobic filler miscibility within the polymeric binders was analyzed with the aid of the HSPiP software package and associated database of Hansen solubility parameters. All solvents were used without further purification, including acetone, THF, chloroform, ethylene glycol, toluene, cyclohexane, hexane, dodecane, DMSO, ethanol, n-butyl acetate, MEK and o-fluorotoluene (Fisher), as well as 1-hexanol, chlorobenzene, perfluorodecalin, hexafluorobenzene, p-chlorobenzotrifluoride, diisopropylamine, and pentafluorobutane (Sigma-Aldrich). Additionally, DI water, AK-225, and Vertrel XF were used.

Crosslinked polymers and elastomers were swollen in a selected number of solvents until a consistent mass was achieved. Samples were weighed and then the solvent was extracted using a vacuum oven at 100 °C. The goodness of a solvent was determined by ranking the swelling ratio (divided by the mass of the solvent) from 1 to 6, with 1 being solvents that swell the polymer the most. These were then input into the HSPiP software in order to determine the center and radius of the given system, or to determine other solvents necessary to better define the radius of the Hansen sphere. The results of the Hansen sphere determination are tabulated in Table 7.1 (fillers), Table 7.2 (binders from this work), and Table 7.3 (binders from the HSPiP database).

7.2.4 The Hansen miscibility sphere for F-POSS

To determine the Hansen sphere for F-POSS, we found solubility maxima in a wide variety of fluorinated solvents. We only used fluorinated solvents so as to not confound results with the additional variable of percent fluorination. F-POSS is completely immiscible in all alkanes, whereas it dissolves in fluorinated alkanes to an extent, in agreement with the Hansen theory[96]. We evaluated

Table 7.1: Hansen Solubility parameters for the three previously unreported fillers determined in this chapter. Hansen parameters for IB-POSS (18.0 ± 0.1,2.1 ± 0.2,2.7 ± 0.3, 4.3) were sourced from the literature[20].

	F-POSS	FO-POSS	Eicosane
Water	×	×	×
Ethanol	×	×	×
Ethylene Glycol	×	×	×
Hexanol	×	×	-
Acetone	×	×	×
Chlorobenzene	×	×	-
Chloroform	×	×	✓
THF	×	×	-
MEK	×	×	×
MIBK	×	×	✓
nBA	×	×	✓
Toluene	×	×	✓
Cyclohexane	×	×	✓
Hexane	×	×	✓
Dodecane	×	×	✓
Diisopropylamine	×	×	✓
Asahiklin-225	✓	✓	-
Vertrel XF	✓	✓	-
Perfluorodecalin	✓	×	-
DMF	×	×	×
DMSO	×	×	×
Acetic acid	×	×	-
Hexafluorobenzene	✓	✓	-
o-fluorotoluene	×	×	-
p-chlorobenzotrifluoride	×	×	-
Pentafluorobutane	×	✓	-
PGMEA	-	-	×
δ_D (MPa$^{1/2}$)	14.7 ± 0.1	13.6 ± 0.1	15.9 ± 0.3
δ_P (MPa$^{1/2}$)	0.0 ± 0.8	1.9 ± 0.6	3.0 ± 0.6
δ_H (MPa$^{1/2}$)	0.0 ± 1.2	0.0 ± 0.5	3.9 ± 0.4
R_o (MPa$^{1/2}$)	3.2	5.1	6.0

Table 7.2: Hansen parameters for the five previously unreported binders evaluated in this work.

	FPU	FPU-PG	PFPE	SF-100	Vytaflex 40	Desmophen 670BA
Water	×	×	×	×	×	×
Ethanol	×	×	×	×	×	×
Ethylene Glycol	×	×	×	×	×	×
Hexanol	×	-	×	×	×	×
Acetone	✓	✓	×	✓	✓	✓
Chlorobenzene	✓	✓	×	✓	✓	✓
Chloroform	✓	✓	×	✓	✓	✓
THF	✓	✓	×	✓	✓	✓
MEK	✓	✓	×	✓	✓	✓
nBA	✓	✓	×	✓	✓	✓
Toluene	✓	✓	×	✓	✓	✓
Cyclohexane	×	×	×	×	×	×
Hexane	×	×	×	×	×	×
Dodecane	×	×	×	×	×	×
Diisopropylamine	×	×	×	✓	×	-
Asahiklin-225	✓	✓	✓	✓	×	✓
Vertrel XF	×	×	✓	×	×	×
Perfluorodecalin	×	×	✓	×	×	×
DMF	×	-	×	✓	×	✓
DMSO	×	-	×	✓	×	✓
Acetic acid	✓	-	-	-	✓	-
δ_D (MPa$^{1/2}$)	16.0 ± 0.2	17.3 ± 0.4	12.6 ± 0.2	17.1 ± 0.3	18.0 ± 0.5	18.0 ± 0.7
δ_P (MPa$^{1/2}$)	9.5 ± 0.5	7.0 ± 0.7	4.4 ± 0.8	7.2 ± 0.3	4.9 ± 0.6	8.7 ± 0.6
δ_H (MPa$^{1/2}$)	3.6 ± 0.5	4.6 ± 1.2	0.1 ± 1.2	6.4 ± 0.4	9.9 ± 1.0	5.9 ± 0.8
R_o (MPa$^{1/2}$)	9.3	5.2	5.1	8.4	4.4	8.4

Table 7.3: Hansen solubility parameters for binders present in the HSPiP database.

	PMMA	PS	PIB	PDMS	Araldite (epoxy)	Pergut (CNR)
δ_D (MPa$^{1/2}$)	18.6	18.9	16.9	17	14	17.4
δ_P(MPa$^{1/2}$)	10.5	8.1	2.5	2.9	7.4	9.5
δ_H(MPa$^{1/2}$)	5.1	4.6	4.0	2.6	9.4	3.8
R_o (MPa$^{1/2}$)	8	10.3	7.2	5.7	13.7	10

seven pure fluorinated solvents (Table 7.1) and 27 mixtures of those solvents to get the F-POSS Hansen sphere (Fig. 7.1a).

As stated in Sec. 7.2.2, we sprayed our coatings at a concentration of 100 mg/mL, and the highest percentage of F-POSS in any coating was 50 wt%. Thus, our method for ranking F-POSS solubility was as follows: Any solvent that dissolved at least 50 mg/mL F-POSS is ranked a 1 (in the HSPiP program), and any solvent with less than 1 mg/mL solubility is ranked a 6. Solvents with F-POSS solubility in between these limits were graded from values of 2 - 5 based on interpolation. Because F-POSS has essentially no polar or H-bonding components, trends between concentration, radius and dispersive components became apparent (Fig. 7.1b). We also modified our rankings for different concentrations, which effectively shrank the sphere and shifted it towards better solvents as the concentration was increased (Fig. 7.1c).

The highly perfluorinated arms of the POSS cage make both the polar and hydrogen bonding solubility parameters of F-POSS effectively zero. However, for consistency, we always chose the Hansen sphere that maximized the fit and minimized the residuals, for both F-POSS and all binders evaluated. This is why we report values of 0.03 MPa$^{1/2}$ for both polar and hydrogen bonding components of F-POSS (Table 7.1). Careful mixtures of solvents with identical dispersive components, but slightly differing polar and hydrogen bonding components, confirmed that F-POSS is only dispersive in nature. Moreover, although the dispersive component of F-POSS was found to be $\delta_D = 14.26 \pm 0.1$ MPa$^{1/2}$, by far the best solvent for F-POSS is hexafluorobenzene. Hexafluorobenzene appears close to the edge of the F-POSS Hansen sphere due to the approximation of the hydrogen bonding parameter. In 3-parameter Hansen space, $\delta_H^2 = 2\delta_a\delta_b$, where δ_a is the proton acceptor component, and δ_b is the proton donor component[202]. Thus, although many fluorinated solvents are known to have large proton donor components[203], most have a zero proton acceptor component, resulting in a net zero hydrogen bonding parameter.

7.2.5 Wettability analysis

Advancing and receding contact angle measurements were obtained via the sessile drop method using a Ramé-Hart 200 F1 contact angle goniometer. A water droplet suspended from a vertical dispensing needle was brought into contact with the substrate, and its volume increased and decreased to obtain the advancing and receding contact angles. A circular drop profile on the live video feed in the DROPImage Advanced software was used to obtain contact angle data. At least three points were measured for each surface at each abrasion condition. Droplet roll-off angles, $\theta_{Roll-off}$, were obtained by placing at least five 25 μL water droplets distributed across the surface with a micropipette, and using the manual tilting stage of the goniometer to gradually increase the angle. The tilt angle was recorded when each droplet rolled off, and the average across the droplets

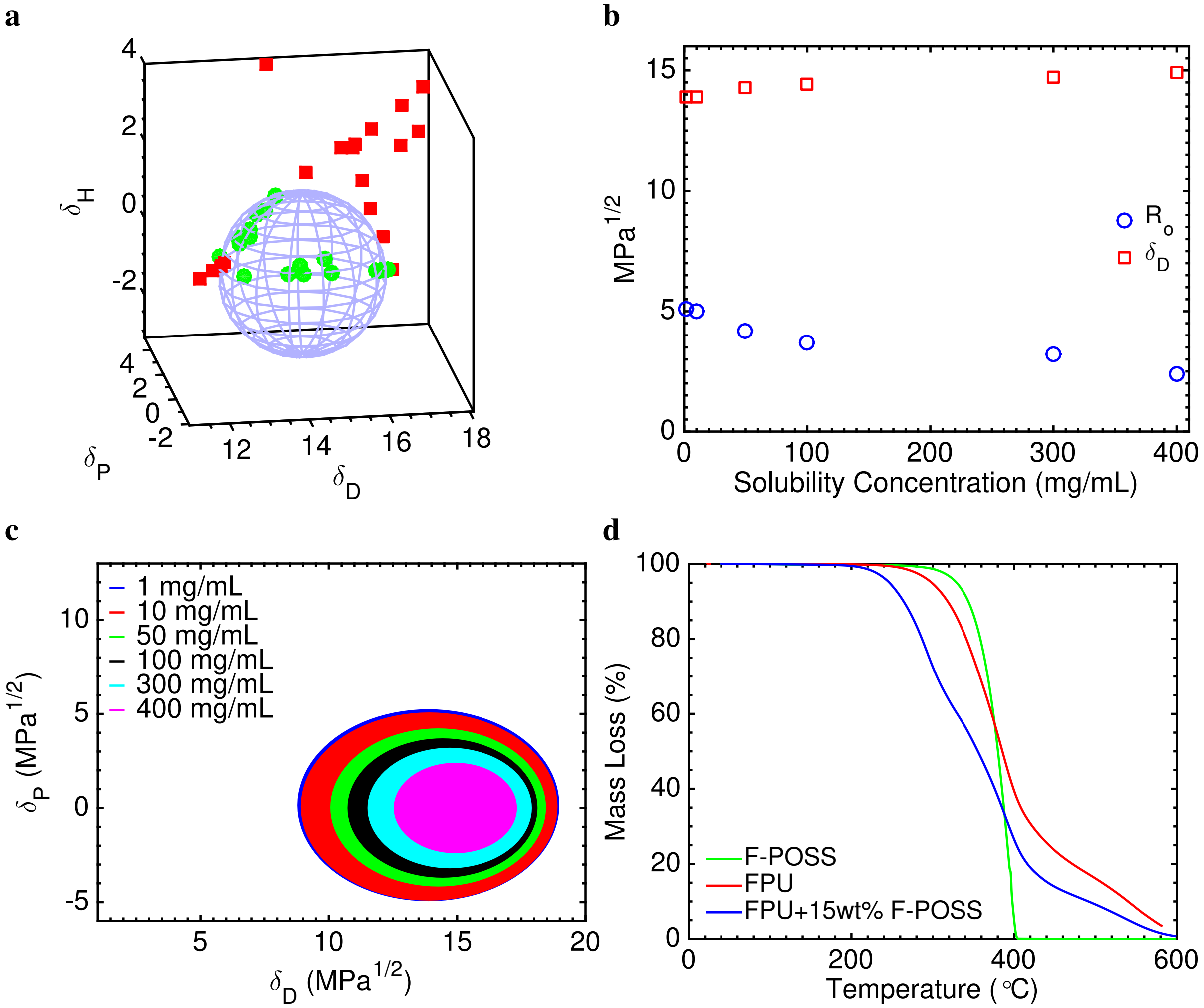

Figure 7.1: Data for F-POSS. a, The Hansen sphere for F-POSS, constructed using seven pure fluorinated solvents and 27 mixtures. See Table 7.1 for the coordinates of the sphere. b, The Hansen radius and dispersive component as a function of F-POSS solubility concentration. As expected, forcing higher concentrations of F-POSS to be solubilized decreased the radius of the sphere, and shifted the center closer to the best solvent, hexafluorobenzene. c, The change in F-POSS radius and dispersive component as a function of concentration. Other than the 1 mg/mL concentration, all other spheres had essentially no polar or H-bonding components. The 1 mg/mL sphere was centered at ($\delta_D = 13.88 \pm 0.05$, $\delta_P = 0.15 \pm 0.55$, $\delta_H = 0.60 \pm 1.10$ MPa$^{1/2}$). The radius was $R_o = 5.1$ MPa$^{1/2}$. d, TGA (10 °C/min) for pure F-POSS, pure FPU and the blend of FPU + 15 wt% F-POSS.

was calculated. Droplets that did not roll off were recorded as $\theta_{Roll-off} = 90^\circ$ for averaging purposes. Large error bars were observed for some abraded samples, which arose from averaging areas that wet with areas that remained superhydrophobic.

7.2.6 Abrasion testing

Abrasion testing based on ASTM standard D4060 was performed with a Taber Model 5135 Rotary Abraser with CS-10 resilient abrasive wheels. 250 g weights were placed on the rear of the wheel arms such that the applied normal load was 60 g, and the sample was then rotated relative to the freely spinning abrasion wheels such that a shearing abrasion action occurred. Excess debris was removed continuously with a vacuum nozzle. The result was a circular region on the sample that was consistently mechanically damaged.

The manual sandpaper abrasion test performed in [14] was automated using a Taber Model 5750 Linear Abraser. A 2.5 × 2.5 cm spray coated sample was mounted facing downwards on the reciprocating head, and brought in contact with 240 grit sandpaper, with an applied load of 250 g. The sample was then moved under load on the static sandpaper, and the test was continued until water droplets were pinned. Water roll-off angles were measured periodically to confirm the retention of superhydrophobicity (Fig. 7.2b).

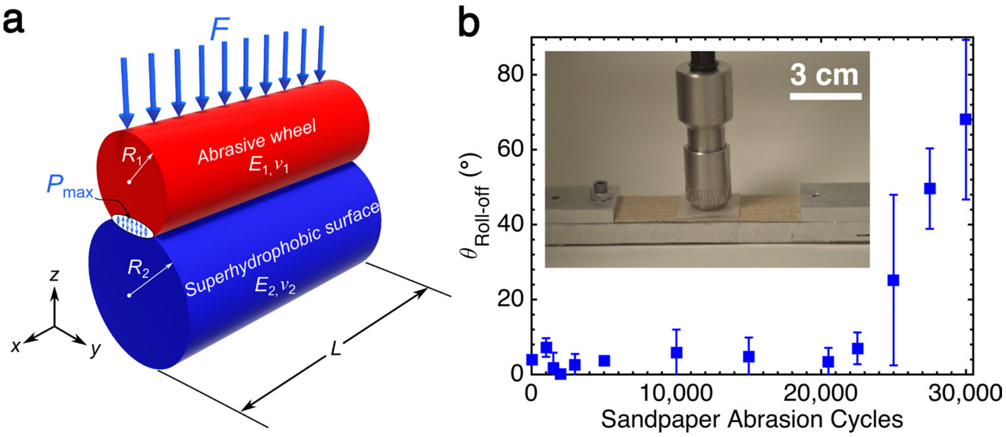

Figure 7.2: The forces experienced during Taber abrasion, found using Hertzian contact mechanics, assuming a cylinder/cylinder configuration[13]. b, The 25 μL water roll-off angle for the FPU/F-POSS coating versus the number of sandpaper abrasion cycles, mimicking a previously reported durability characterization[14]. The inset shows the linear Taber abrasion machine, modified to perform sandpaper abrasion.

7.2.7 Hertzian contact mechanics of Taber abrasion

Although it is an industrial standard for measuring the mechanical durability of coatings, Taber abrasion has rarely been used to evaluate superhydrophobic surfaces. Here we briefly show the relevant contact stresses involved in Taber abrasion. During the abrasion process, two wheels are constantly rubbed against the coated surface. According to Hertzian contact mechanics, this situation can be modeled by cylinder/cylinder contact (Fig. 7.2a), in which the lower surface is given an infinite radius of curvature[13]. In such a case, the area of contact between the abrading wheel and the coated surface is an ellipse, with half-width b given as,

$$b = \sqrt{\frac{4RF[E_2(1-\upsilon_1^2) + E_1(1-\upsilon_2^2)]}{\pi L E_1 E_2}}. \tag{7.1}$$

Here R is the radius of the wheel (49 mm), F is the normal load (60 g), L is the length of abrasion (10 mm), and E_1, υ_1, E_2, and υ_2 are the elastic moduli and Poisson ratios of the wheel and coating, respectively. The maximum pressure exerted on the coating is given as,

$$P_{max} = 2F/\pi bL. \tag{7.2}$$

Although this pressure can compress the surface, the main degradation occurs because of the shear stresses generated. If we define x as the direction tangential to the rotation during Taber abrasion, and z along the thickness of the coating, the principle stresses are given as,

$$\sigma_x = -2\upsilon_2 P_{max}\left[\sqrt{\frac{z^2}{b^2}+1} - |z/b|\right] \tag{7.3}$$

and

$$\sigma_z = -P_{max}(z^2/b^2+1)^{-1/2}. \tag{7.4}$$

And finally the shear stress in the xz-direction (the direction of abrasion) is,

$$\tau_{xz} = \frac{1}{2}|\sigma_x - \sigma_z| \tag{7.5}$$

For our FPU-based coatings we measured the elastic modulus using standard tensile testing[83]. Using this modulus value resulted in a maximum shear stress experienced of $\tau_{xz} \approx 120$ kPa. Solving for the solid fraction using the contact angles of water on our surfaces gives a local shear stress of a few MPa at the texture elements during abrasion.

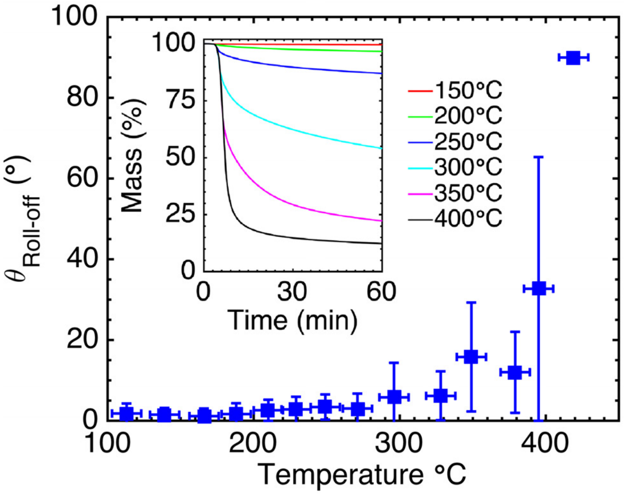

Figure 7.3: The roll-off angle of the FPU + 15 wt% F-POSS coating versus temperature held for 1 hour. The inset shows TGA of the same coating, at different temperature points.

7.2.8 Imaging and metrology

Scanning electron micrographs were obtained with a Philips XL30 SEM after sputter coating the samples with gold to reduce charging effects. Two-dimensional height-maps (2.4 mm × 2.4 mm) of the surfaces were obtained with an Olympus LEXT OLS4000 3D Laser Measuring Microscope with a $10\times$ objective, and at least five height maps were collected for each sample at each abrasion condition. This data was subsequently analyzed to yield statistical topographical parameters using MATLAB (see Sec. 7.3.2 below). The root-mean-squared roughness, S_q, was found using,

$$S_q = \sqrt{\frac{1}{xy}\sum_x \sum_y h_{x,y}^2} \tag{7.6}$$

where $h_{x,y}$ is the height of the surface at point (x,y), after the mean height has been set to zero.

7.2.9 Thermal degradation analysis

A sample of FPU+15 wt% F-POSS was placed on a hot plate at temperatures from 150 - 425 °C in increments of 25 °C, 1 hour per temperature point. After each baking step, the advancing, receding, and roll-off angles were measured (Fig. 7.3). To correlate the onset of degradation of the Cassie-Baxter state with chemical degradation of the sample, thermogravimetric analysis was performed with a TA Instruments Discovery Series TGA using a 6 mg sample scraped from the same spray-coated surface. This sample was heated from 25 - 600 °C at 10 °C/min in a 10 mL/min N_2 gas purge flow while continually monitoring its mass (inset, Fig. 7.3).

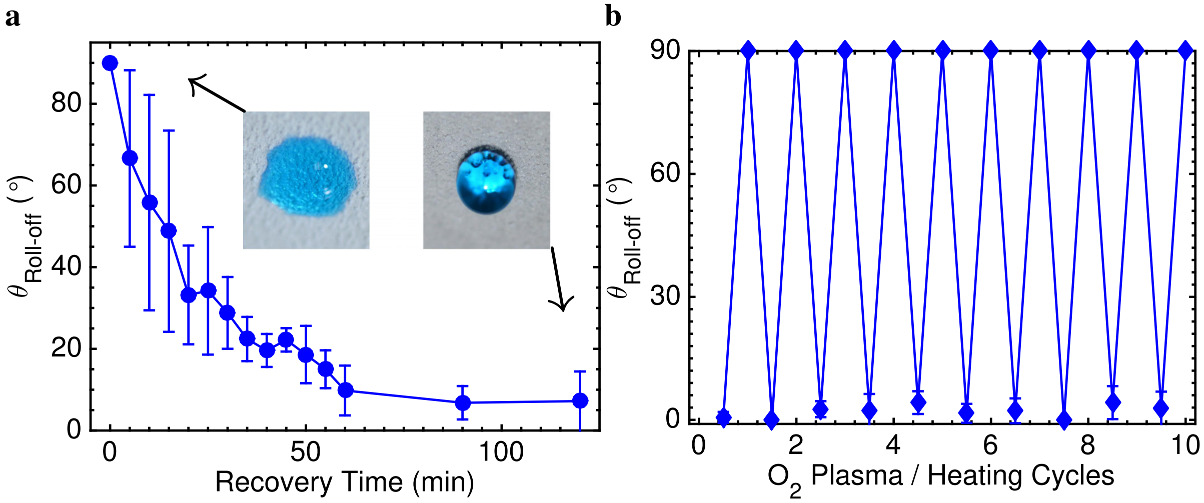

Figure 7.4: a, The roll-off angle of the FPU + 15 wt% F-POSS coating after O_2 plasma treatment, as a function of recovery time at 80 °C. As the fully fluorinated chains bloomed to the surface, the surface energy decreased, and water was more easily repelled. The insets show water droplets (dyed blue) after O_2 plasma treatment, and after thermal recovery. b, Ten successive O_2 plasma/recovery cycles, highlighting that the self-healing nature of the FPU/F-POSS coating was quite robust.

7.2.10 UV and oxygen plasma exposure

A sample of FPU+15 wt% F-POSS was placed under 254 nm UVC at a distance of 5 cm. The contact angles were measured after five hours of continuous exposure. For oxygen plasma exposure, a sample of FPU+15 wt% F-POSS was exposed to O_2 plasma (Harrick Plasma PDC-001) using an RF source power of 30 Watts and a pressure of $\approx$ 200 mTorr for 20 min. Contact angles were measured to verify the complete wetting of the surface. To recover the water repellency, the coated surface was placed on a hotplate at either 80 °C or 150 °C). For the time-dependent recovery, the substrate was removed from the hotplate after temporal increments and the contact angles were measured. For the O_2 plasma cycling, the substrate was placed on a 150 °C hotplate for 20 min before measuring contact angles. The O_2 plasma exposure followed by the 150 °C recovery is denoted as one cycle in the inset of Fig. 7.4b.

7.2.11 Corrosion

Corrosion testing was done in accordance to ASTM B117[84]. Briefly, steel tabs measuring 25 mm × 75 mm were spray-coated at with the FPU+15 wt% F-POSS coating. The coated pieces were hung in a salt-spray fog chamber (Bemco Inc.) kept at 35 °C for 200 hours. A 25 mm scratch was made along the length of the coating so that the steel underneath was exposed. After the accelerated corrosion, the contact angles were measured.

7.2.12 Compression

Compression testing was done using a Carver 4350 compression molder with a 30 ton capacity. Samples of known dimensions were placed between aluminum plates and a certain force was applied and held for 60 seconds. The contact angles were then measured immediately following compression. Following compression, the sample was self-healed on a 100 °C hotplate for 5 minutes, and contact angles were recorded again.

7.2.13 Breakthrough pressure

Pressure stability was measured both statically and dynamically. Static pressure testing was done using a pressure tank (TCP Global) with a 7 cm head of DI water. The pressure was regulated using compressed air. Samples were submerged and the pressure was raised to the set level for 60 seconds at a ramp rate of no more than 5 psi/s. After the pressure was released, samples were removed to determine if they remained dry. Due to the inhomogeneity of the surfaces, breakthrough was considered to have occurred when the sample was fully wetted upon removal from the water tank.

Dynamic pressure testing was done using impacting water droplets and a high-speed camera (Fastec Imaging HiSpec 1) at 2,000 frames per second. The breakthrough pressure was considered when the droplet became pinned on the surface upon impact. As the maximum droplet height for our experimental setup was 1.7 m, corresponding to an impact velocity of 5.7 m/s, many surfaces exhibited breakthrough pressures too high to measure using droplet impact.

7.3 Design criteria

7.3.1 The miscibility parameter

The lowest possible surface energy, $\gamma_{SV} \approx 6$ mN/m, is achieved with a monolayer of -CF_3 groups[11]. Chemically grafting such monolayers requires specific substrate chemistry. Moreover, the thin monolayer only renders the uppermost surface hydrophobic, and any surface degradation will expose the higher surface energy material underneath. In contrast, the incorporation of highly perfluorinated compounds within a coating allows one to achieve equally low surface energies without the need for chemical grafting[134, 96]. Moreover, these unbound species can diffuse to the surface, restoring the low surface energy after mechanical or chemical attack, thereby reducing the formation of hydrophilic defects upon damage[146]. Such coatings can be universally applied to any substrate, and impart low surface energy throughout the entire thickness of the coating. In this work, we fabricated a library of SHSs using sprayed blends of polymeric binders and hydrophobic fillers. Due to its low surface energy, $\gamma_{SV} \approx 10$ mN/m, we primarily focus on systems incorporating 1H,1H,2H,2H-heptadecafluorodecyl polyhedral oligomeric silsesquioxane (F-POSS)[134], although the developed design parameters are generalizable to other material systems, as we show. Spray coating was chosen as the primary methodology for the application of the superhydrophobic coatings because it is inexpensive, scalable, and allows control over the surface energy and texture of our coatings via simple changes in experimental parameters.

The cohesive energy of any material species can be broken into its dispersive, polar, and hydrogen bonding Hansen solubility parameters, (δ_D,δ_P,δ_H)[96]. A miscibility sphere can be experimentally constructed for any compound, with its center at some point in a 3D space defined by these three solubility parameters, and its volume encompassing all good solvents and excluding all non-solvents. We first determined the miscibility spheres for several hydrophobic fillers and a wide variety of binders (Fig. 7.5), by screening their solubility in a large number of solvents (Tables 7.1-7.3).

The overlap between the Hansen spheres of the binder and filler is indicative of their chemical compatibility, and the extent to which they phase separate and form texture during the spray-coating process. In order to quantify a polymer's miscibility with the filler, we developed the miscibility parameter S^*, which is given as,

$$S^* = \frac{\Delta R - R_{binder} + R_{filler}}{2R_{filler}} \tag{7.7}$$

Here ΔR is the distance in 3D solubility space between the centers of the filler's sphere and the binder's sphere, with their radii denoted by R_{filler} and R_{binder}, respectively.

Similar to Hansen's Relative Energy Difference value[96], S^* is defined such that the filler is completely immiscible with a binder when the two spheres do not overlap ($S^* > 1.0$, also see schematic in Fig. 7.5). Alternately, binders with $S^* < 0$ have solubility spheres that completely encompass the filler's sphere, and are hence fully miscible (at a given concentration, see Fig. 7.1). In between these two extremes is the regime of partial miscibility, which we will show greatly affects a SHS's ability to maintain water repellency after mechanical abrasion.

The S^* parameter allows one to predict if the filler will phase separate from the binder during spray coating. This phase separation manifests in the sprayed surface's root-mean-squared roughness, S_q. For example, we determined the solubility spheres for a polyurethane and an epoxy, which are both commonly used hydrophilic adhesives (Tables 7.2 and 7.3). For the epoxy, $S^* \approx 0.2$ with F-POSS, and an epoxy + 5 wt% F-POSS blend, when sprayed, resulted in a smooth surface with $S_q = 0.8$ μm. Conversely, for the polyurethane, $S^* \approx 1.6$, and a polyurethane + 5 wt% F-POSS blend, when sprayed in the exact same manner, resulted in a very rough surface ($S_q = 41$ μm). Thus, immiscibility alone can induce roughness during the spray coating process. However,

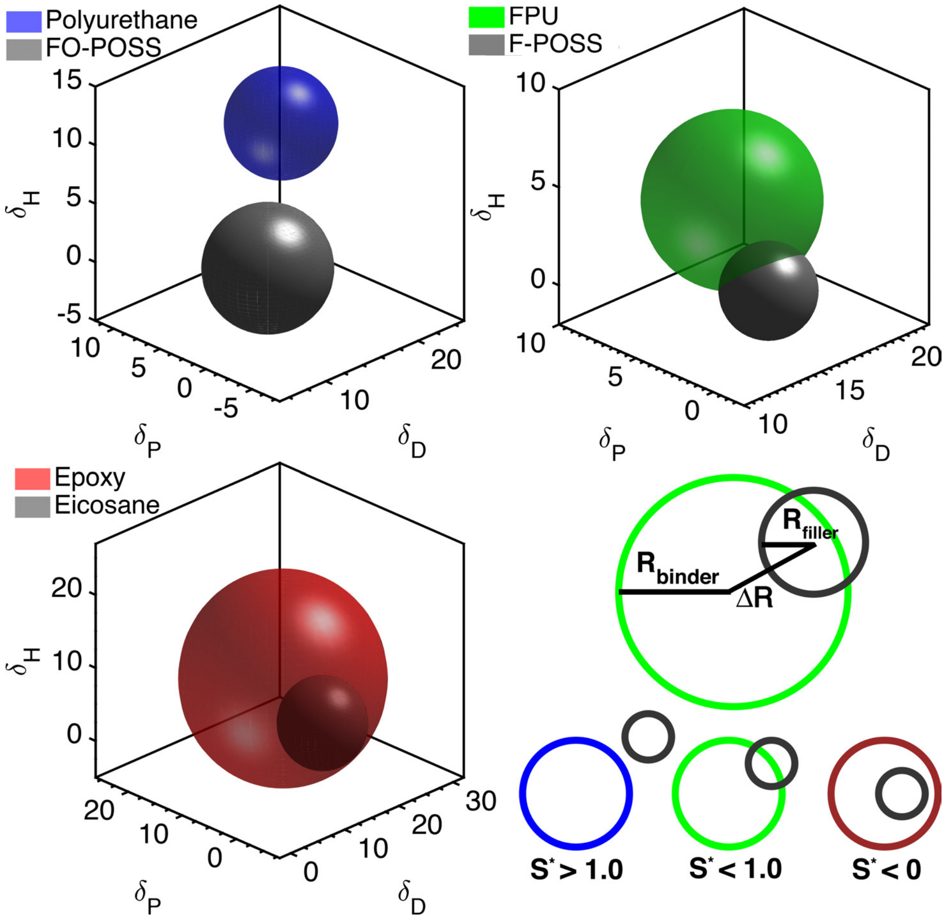

Figure 7.5: Visualization of the S^* parameter for three binders in 3D Hansen space. FO-POSS: fluorooctyl polyhedral oligomeric silsesquioxane. FPU: fluorinated polyurethane. F-POSS: fluorodecyl polyhedral oligomeric silsesquioxane.

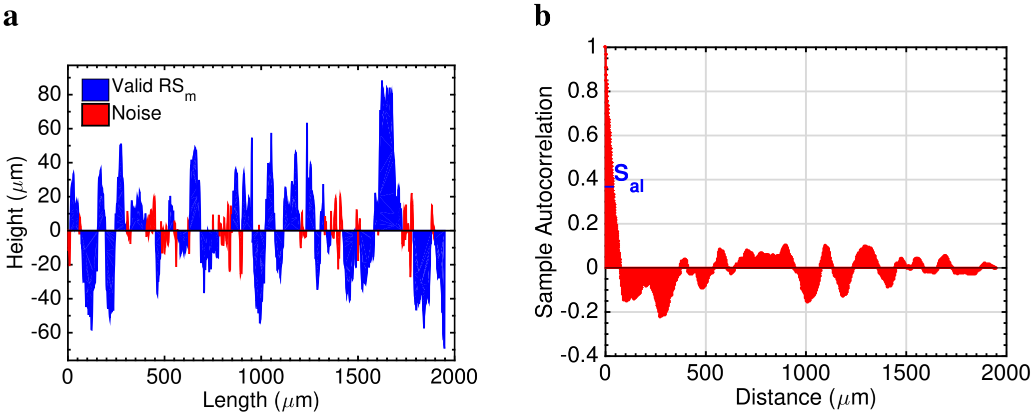

Figure 7.6: a, The parameter RS_m is shown by filling in each periodic 'element'. b, The autocorrelation function of a surface versus the distance along the surface examined. In this work, a value of e^{-1} was used as a cutoff.

a large S_q does not guarantee superhydrophobicity[204].

7.3.2 The superhydrophobic potential

Water on SHSs can exist in the Cassie-Baxter state, in which air pockets are trapped in the surface's porous texture[2]. However, water can displace these air pockets, leaving the surface in a wetted, Wenzel state[1]. SHSs should ideally be designed such that the Cassie-Baxter state is energetically preferred[32]. We developed a method to predict when the Cassie-Baxter state would be energetically favorable over the Wenzel state using only the topographical statistics of a given surface. Because each binder/filler combination exhibited a distinct, characteristic surface morphology, we wished to develop universal metrics that characterize surfaces with widely varying topographies. To do so, we measured three statistical surface properties: peak periodicity, RS_m, auto-correlation length, S_{al}, and the Wenzel roughness, r[1].

RS_m represents the length along the surface between large surface features, and can be thought of as the center-to-center distance between texture elements[205]. RS_m is defined as,

$$RS_m = \frac{1}{m}\sum_{i=1}^{m} X_i \tag{7.8}$$

where X_i is the length of a peak (Fig. 7.6a)[151]. A peak is defined such that its height is $> 10\%$ of the maximum height, and its length is $> 1\%$ of the total sampling length. This allows one to separate genuine texture features from noise. In Fig. 7.6a the noise and valid X_i are labeled.

The second statistical parameter, S_{al}, is the shortest autocorrelation length. An autocorrelation function can be constructed for any surface by evaluating the self-similarity of heights when small perturbations in distance are made[204]. In effect, S_{al} represents the distance at which a peak becomes a valley or vice versa. In this work we use the popular cutoff in the autocorrelation function of e^{-1} (Fig. 7.6b).

Before defining the porosity of random surfaces using the above statistical parameters, we first briefly make the connection to the canonical surface of micro-pillars. Such surfaces are often studied for their simple geometry but relatively good water repellency. Square pillars can be defined by their width $2R$ and the spacing in between pillars $2D$ (see Fig. 6.1 in Chapter 6). If water is placed on such a surface (with $\theta \geq 90°$, it may be able to support a composite solid-liquid-air interface, which will be contingent upon the dimensions of R and D. Should the composite interface be stable, the fraction of solid in contact with the air is given by $\phi_s = 2R/(2R + 2D)$ in the one dimensional case (Fig. 6.1). Converting to two dimensions simply involves squaring ϕ_s.

For a randomly rough surface we must resort back to the statistical lengths of RS_m and S_{al}. The one-dimensional solid fraction may be defined as $\phi_s = S_{al}/RS_m$. In our previous work[26], we found it instructional to define the porosity of a surface as the inverse of ϕ_s,

$$D^*_{stat} = (RS_m/S_{al})^2 \tag{7.9}$$

where the second power is added to convert from properties measured along one-dimensional height profiles to the porosity of a two-dimensional surface[145]. Larger values of D^*_{stat} indicate surfaces with higher porosity. Note that we use the two dimensional form, and that we average the measured RS_m and S_{al} values over the entire two-dimensional surface.

For the Cassie-Baxter state to be favored over the wetted, Wenzel state, it must be the global energy minimum[33]. For a given surface topography, the free energies of the two states can be balanced (*i.e.* equating Eq. 1.5 with Eq. 1.6). The non-wetted state is energetically preferred only if the intrinsic contact angle, θ_Y, exceeds a critical value, θ_c. This critical intrinsic contact angle is given by[33],

$$\cos\theta_c = (\phi_s - 1)/(r - \phi_s) \tag{7.10}$$

where ϕ_s is the fraction of solid in contact with water (note $D^*_{stat} \approx \phi_s^{-1}$, and we assume $r_\phi = 1.0$). Stated differently, and recalling that intrinsic water contact angles cannot exceed 120°[26], there exists some minimal texture that any surface, regardless of chemistry, must exhibit in order to achieve an energetically favorable Cassie-Baxter state. Substituting this maximum contact angle as θ_c yields,

$$\cos\theta_c = \cos 120° = (1/D^*_{stat} - 1)/(r - 1/D^*_{stat}) \tag{7.11}$$

or

$$-0.5 = (1 - D^*_{stat})/(rD^*_{stat} - 1). \tag{7.12}$$

We can then define a surface's superhydrophobic potential, P^*, such that only for values of $P^* < 1.0$ is the Cassie-Baxter state the global energy minimum. Doing so yields,

$$P^* = 2(D^*_{stat} - 1)(rD^*_{stat} - 1). \tag{7.13}$$

For any surface that exhibits $P^* > 1.0$, the wetted state is energetically preferred, regardless of surface chemistry. Note that water can exist in a metastable Cassie-Baxter state through the addition of re-entrant texture[26], and hence a value of $P^* > 1.0$ does not necessarily indicate wetting. P^* is useful because surfaces are often created with a given topography, and then subsequently rendered superhydrophobic by applying a low surface energy layer on top[32]. As such, measuring P^* allows one to determine *a priori* if such a surface will become superhydrophobic before applying such a (often expensive) low surface energy monolayer. Moreover, if a surface is superhydrophobic in spite of a $P^* > 1.0$ value, one can say with certainty that water will exist in a metastable state, and such a surface should be used with caution. By measuring the dynamic contact angles on many surfaces, both wetted and non-wetted, we probed the effectiveness of P^*.

When water initially advances on a SHS, it displays θ^*_{adv}[206]. If any texture elements become wetted, the apparent angle at which water recedes, θ^*_{rec}, will be much lower than θ^*_{adv}. Thus, θ^*_{adv} can be thought of as a measure of the SHS's inherent porosity (*i.e.* fraction of air pockets), ignoring how stable the air pockets may be, and θ^*_{rec} gives an indication of their stability[23]. We measured θ^*_{rec} for more than fifty combinations of F-POSS and various polymeric binders, as a function of P^* (Fig. 7.7a). These binders included both crosslinked networks, such as different urethanes, acrylates, epoxies, and cyanoacrylates, as well as linear polymers such as polystyrene, polymethylmethacrylate and polyisobutylene (Sec. 7.2, Table 7.4). We observed a high θ^*_{rec} only for systems with a stable Cassie-Baxter state, *i.e.* $P^* < 1.0$. This was confirmed by the sharp jump in θ^*_{rec} at a value of $P^* = 1.0$. The specific value of $P^* = 1.0$, corresponding to an intrinsic contact angle $\theta_Y \approx 120°$, indicated that all the surfaces had a high percentage of F-POSS at the solid-liquid interface, although there were vast differences in topography. Thus, we were able to predict if an F-POSS-containing surface could be superhydrophobic solely by measuring P^*. Without measuring P^*, there is no easy way to determine if a randomly textured surface has the potential to become superhydrophobic, *a priori*.

Moreover, for surfaces with $P^* < 1.0$, recasting the Cassie-Baxter relation (Eq. 1.6)[2] in terms of D^*_{stat} effectively predicted θ^*_{adv} (Fig. 7.7b). We observed that the predictive power of D^*_{stat} and P^* extended to other SHSs not containing F-POSS. These SHSs included polymer blends with other hydrophobic fillers like eicosane, octa-isobutyl POSS (IB-POSS) and fluoro-octyl POSS (FO-POSS), as well as other SHSs such as three commercially available superhydrophobic formulations (Sec. 7.2, Tables 7.1-7.3), lithographically fabricated microstructures[138], textured

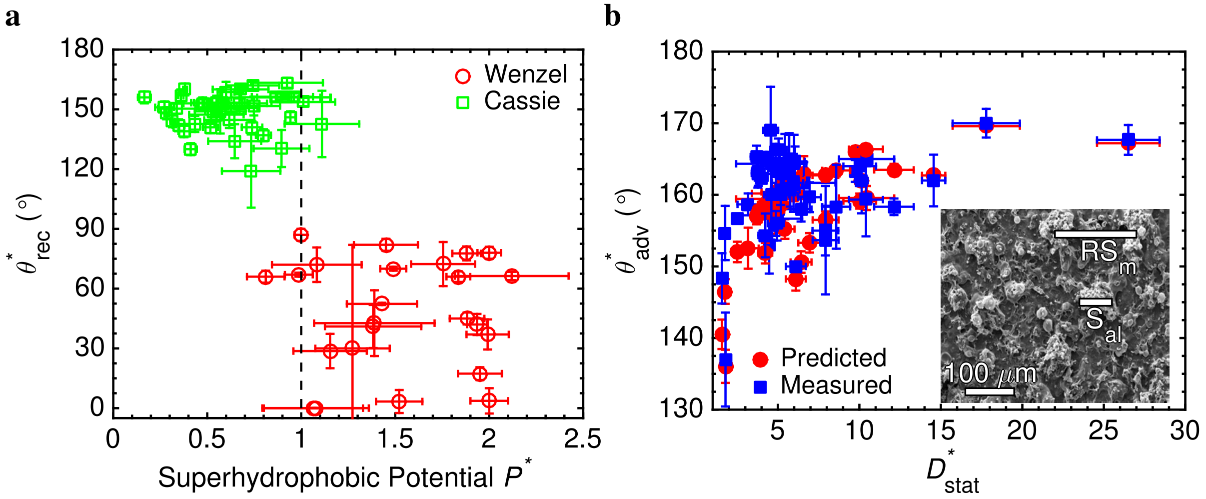

Figure 7.7: a, The apparent receding contact angle versus the P^* parameter. The sharp transition at $P^* = 1.0$ denoted an intrinsic contact angle of $\theta_Y = 120°$. b, Measured and predicted apparent advancing contact angles versus the developed statistical porosity parameter, D^*_{stat}. This plot includes all the different systems from Table 7.4. The inset shows an SEM micrograph of the FPU + 15 wt% F-POSS sprayed surface, with representative RS_m and S_{al} values indicated.

metals treated with self-assembled monolayers[207, 165], and binders filled with hydrophobic particles[208]. As such, the design parameters developed in this work are applicable to SHSs produced using a wide range of binders, fillers, and fabrication techniques.

For each binder (fixed S^*), we varied P^* by adjusting the amount of hydrophobic filler in the blend. Combining the S^* and P^* parameters allowed us to construct a phase diagram for the different possible surfaces created when spraying the binder/filler blends (Fig. 7.8). Here we denote surfaces with a (×) when the water roll-off angle was $\theta_{Rolloff} > 15°$ (not superhydrophobic), and surfaces that exhibited $\theta_{Rolloff} < 15°$ (superhydrophobic) as (■). These two regions were demarcated by a line at $P^* = 1.0$, *i.e.* we never observed a SHS for which $P^* > 1.0$.

Low surface energy species are known to preferentially migrate to the solid-air interface[44]. For binders with $S^* > 1.0$, the final surface was always very mechanically weak, with a powdery consistency, because the filler was completely immiscible with such binders. Surfaces that remained superhydrophobic after mechanical abrasion (discussed below) are denoted with (●) in Fig. 7.8. These mechanically durable SHSs were only observed when a binder exhibited partially miscibility with the filler ($S^* < 1.0$), *i.e.* we never observed a durable SHS with $S^* > 1.0$. Finally, we note that increasing the amount of filler within a sprayed blend was not always efficacious. As the binder can be much more mechanically resilient than the filler molecules, any excess filler within the blend, beyond what is required to achieve superhydrophobicity ($P^* < 1.0$), can lower the overall durability. For example, a perfluorinated polyether, PFPE, with 25 wt% F-POSS remained superhydrophobic after abrasion, but PFPE with 35 wt% F-POSS did not, although the S^*

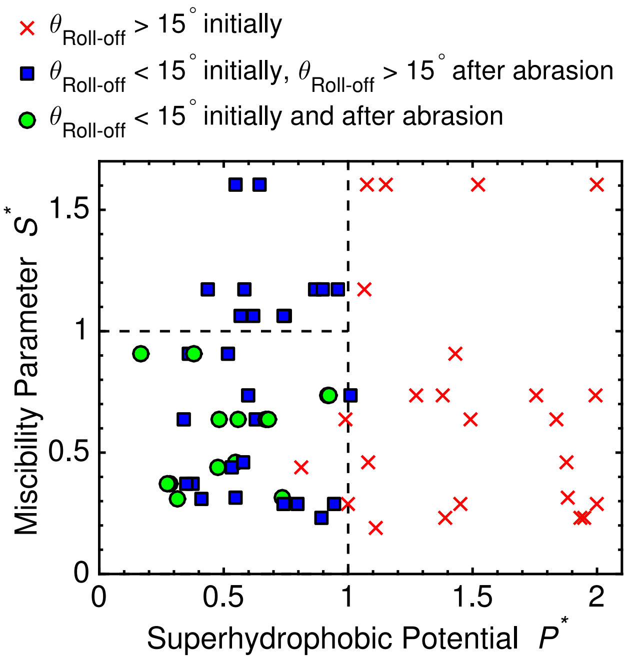

Figure 7.8: A Phase diagram for all the surfaces developed in this work (see Table 7.4). Only surfaces with $P^* < 1.0$ can be superhydrophobic ($\theta_{Roll-off} < 15°$), and additionally only surfaces with $S^* < 1.0$ can be mechanically durable ($\theta_{Roll-off} < 15°$ after 100 abrasion cycles). The non-SHS that exhibited $P^* < 1.0$ was a blend of FPU/FO-POSS. For this blend, $\theta_Y = 91°$, although the sprayed texture required $\theta_c = 114°$. This exemplifies when the texture is sufficient to produce a SHS, but the chemistry does not exhibit low enough surface energy.

and P^* values were equivalent. Overall, choosing components that satisfy $S^* < 1.0$ helps ensure that the final surface will be durable, and choosing a sufficient filler content such that $P^* < 1.0$ assures that the surface will exhibit a robust Cassie-Baxter state.

7.4 Durability of superhydrophobic surfaces

7.4.1 Mechanical abrasion

We utilized the industry standard of rotary Taber abrasion to evaluate the mechanical durability of our sprayed binder/filler blends. The stresses generated by Taber abrasion can be found using a cylinder-cylinder Hertzian contact mechanics analysis (Fig. 7.2a, Sec. 7.2.7 above)[13]. Depending on the elastic modulus of the coating, the exerted shear stress ranged from tens to hundreds of kPa (Fig. 7.9a). Considering the porosity of the surface, the texture elements experienced shear stresses on the order of a few MPa. This is similar or greater than the less systematic durability characterization techniques employed in the literature[129, 146, 178, 179, 14, 182, 186, 190, 191,

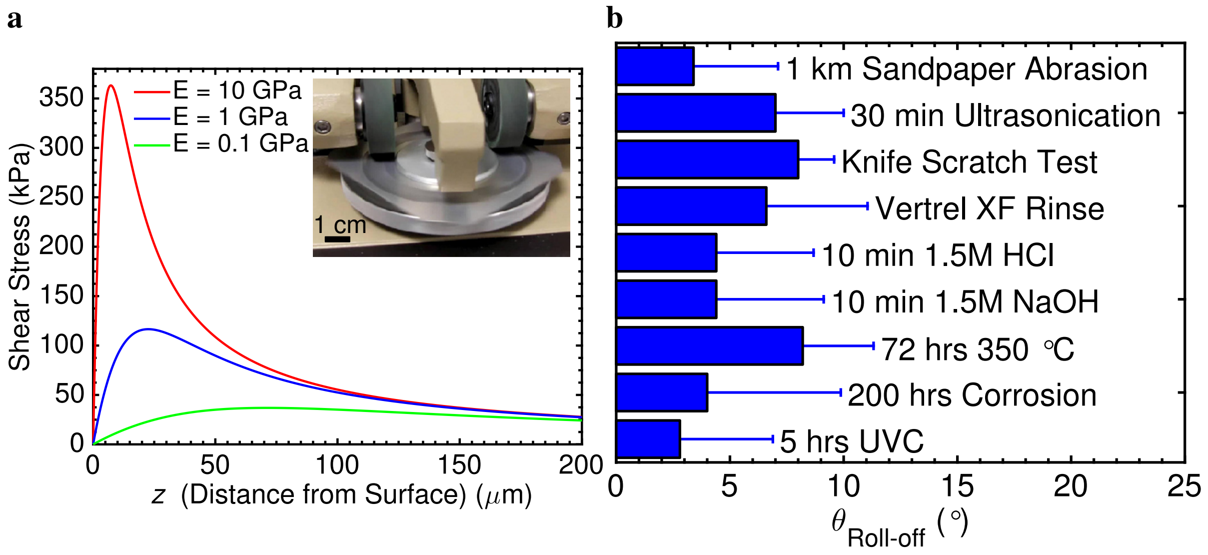

Figure 7.9: a, The shear stress experience during Taber abrasion as a function of depth into the coating. The values were found using Hertzian contact mechanics (see Sec. 7.2.7). The inset shows the Taber abrasion machine. b, Additional durability characterizations that the FPU + 15 wt% F-POSS coating could withstand without self-healing.

192, 193, 194, 195, 141, 196, 197, 198, 199, 200]. For example, in a recent report[14], a durable SHS was abraded with sandpaper along a total length of 800 cm, without degradation of high contact angle. We reproduced such an evaluation for our FPU/F-POSS blend, which maintained high contact angles, as well as low roll-off angles, even after 1 kilometer (100,000 cm) of abrasion using the same sandpaper and applied load (Fig. 7.9b, 7.2b). Thus, we are confident that the surfaces created in this work can also withstand other metrics of mechanical durability reported elsewhere.

One hundred Taber abrasion cycles sufficiently differentiated durable and non-durable SHSs, *i.e.* non-durable surfaces were either completely removed, or water wet the remaining coating, after 100 abrasion cycles. Only surfaces that exhibited $\theta_{Roll-off} < 15^{\circ}$ after 100 abrasion cycles are shown as green circles in Fig. 7.8. All such surfaces exhibited partial miscibility with the hydrophobic fillers ($0 \leq S^{*} \leq 1.0$). We then continued Taber abrasion of our partially miscible blends (Table 7.4).

Table 7.4: Surface properties of the coatings developed in this work, before and after 100 rotary Taber abrasion cycles.

Base	F-POSS (%)	P^{*}	D^{*}_{stat}	Initial θ^{*}_{adv} (°)	Initial θ^{*}_{rec} (°)	Initial $\theta^{*}_{Roll-off}$ (°)	100 cycle θ^{*}_{adv} (°)	100 cycle θ^{*}_{rec} (°)	100 cycle $\theta^{*}_{Roll-off}$ (°)	100 cycle mass loss (%)
NeverWet	-	1.79	7.4	165	162	1	132	32	54	17
Ultra Ever Dry	-	1.36	4.	161	152	1	155	0	90	14
Cytonix WX 2100	-	1.04	1.4	164	156	18	122	77	90	6
FPU ($S^{*} = 0.64$)	0	1.84	7.2	115	66	55	-	-	-	-
FPU	1	0.99	14.3	106	67	90	106	63	90	1
FPU	3	1.49	25.5	121	66	90	122	78	76	3
FPU	5	0.31	1.5	148	112	62	151	102	75	8

Base	FO-POSS (%)	P^*	D^*_{stat}	Initial θ^*_{adv} (°)	Initial θ^*_{rec} (°)	Initial $\theta^*_{Roll-off}$ (°)	100 cycle θ^*_{adv} (°)	100 cycle θ^*_{rec} (°)	100 cycle $\theta^*_{Roll-off}$ (°)	100 cycle mass loss (%)
FPU	10	0.34	2.5	162	150	10	159	124	22	20
FPU	15	0.48	3.9	165	159	2	161	154	2	32
FPU	20	0.56	3.5	163	153	5	161	144	10	40
FPU	25	0.67	6.4	166	153	2	164	152	2	86
FPU	30	0.68	4.8	165	160	2	163	144	3	81
FPU	35	0.63	4.4	160	151	1	146	113	24	56
FPU-PG ($S^* = 1.06$)	5	0.62	5.3	163	145	8	153	98	81	44
FPU-PG	10	0.57	8.2	161	152	7	158	116	57	40
FPU-PG	15	0.75	4.7	162	148	7	161	113	90	27
FPU-PG	20	0.74	5.6	164	151	3	159	123	40	26
PMMA ($S^* = 1.17$)	0	1.06	5.1	155	0	90	-	-	-	-
PMMA	2	0.76	5.5	160	83	14	135	0	90	109
PMMA	5	0.43	4.0	160	143	11	149	123	35	99
PMMA	10	0.58	3.4	163	153	7	159	128	24	104
PMMA	35	0.90	5.9	166	156	2	162	127	26	129
PMMA	50	0.86	4.2	164	156	0	127	84	63	100
SF-100 ($S^* = 0.74$)	0	1.99	2.9	93	37	64	-	-	-	-
SF-100	5	1.38	3	129	41	90	-	-	-	-
SF-100	10	1.75	2.9	140	72	83	-	-	-	-
SF-100	15	1.27	4.5	158	123	13	167	113	37	22
SF-100	20	1.01	3.8	163	157	1	165	164	1	55
SF-100	25	0.92	3.5	169	163	0	166	164	1	55
SF-100	35	0.60	7.0	167	159	2	145	107	34	38
PDMS ($S^* = 0.32$)	0	1.88	3.8	123	45	90	-	-	-	-
PDMS	15	0.73	5.4	154	119	47	158	137	10	20
PDMS	30	0.55	5.4	160	153	4	157	0	66	46
PFPE ($S^* = 0.46$)	0	1.88	18.6	113	78	53	-	-	-	-
PFPE	5	2.12	0.5	127	66	66	-	-	-	-
PFPE	15	1.08	7.0	155	72	47	163	20	90	45
PFPE	25	0.55	3.7	156	147	7	163	142	8	33
PFPE	35	0.58	4.1	165	153	2	164	0	90	100
Vytaflex ($S^* = 1.60$)	0	2.00	1.0	74	4	90	-	-	-	-
Vytaflex	1	1.52	9.6	149	0	90	-	-	-	-
Vytaflex	5	1.08	4.5	150	0	90	-	-	-	-
Vytaflex	10	1.15	3.1	135	29	90	-	-	-	-
Vytaflex	15	0.65	4.5	158	134	11	159	55	39	28
Vytaflex	35	0.55	5.2	160	150	2	161	130	17	-
PS 45 ($S^* = 48$)	0	1.15	29.6	157	123	14	-	-	-	-
PS 45	15	0.60	1.9	157	131	14	156	114	37	26
PS 45	25	0.58	1.4	155	142	15	152	111	38	14
PS 1.2 ($S^* = 0.48$)	15	0.94	8.5	159	153	0	-	-	-	-
PIB ($S^*0.19$)	0	1.27	19.3	118	61	90	-	-	-	-
PIB	15	1.18	10.4	164	143	14	161	118	90	48
Araldite ($S^* = 0.23$)	0	1.95	2.9	101	17	90	-	-	-	-
Araldite	5	1.94	12.5	128	43	90	127	62	87	-
Araldite	15	1.39	1.0	137	43	90	132	69	90	3
Araldite	25	0.89	9.0	158	130	14	158	16	90	25
Desmophen ($S^* = 0.91$)	0	1.43	41.9	85	49	90	-	-	-	-
Desmophen	2.5	0.52	8.9	161	141	8	148	94	74	17
Desmophen	5	0.36	7.8	166	157	5	159	125	23	20
Desmophen	10	0.38	8.4	166	160	4	162	129	16	24
Desmophen	15	0.17	2.3	165	156	9	164	162	2	27

FPU ($S^* = 0.44$)	15	0.81	8.9	141	66	90	137	68	90	4
FPU	25	0.53	7.2	163	149	9	161	124	30	12
FPU	35	0.48	7.0	162	153	4	162	146	14	15
Base	IB-POSS (%)	P^*	D^*_{stat}	Initial θ^*_{adv} (°)	Initial θ^*_{rec} (°)	Initial $\theta^*_{Roll-off}$ (°)	100 cycle θ^*_{adv} (°)	100 cycle θ^*_{rec} (°)	100 cycle $\theta^*_{Roll-off}$ (°)	100 cycle mass loss (%)
FPU ($S^* = 0.31$)	25	0.41	5.1	165	130	15	140	75	90	9
FPU	30	0.31	4.9	164	144	5	165	132	15	17
Desmophen ($S^* = 0.37$)	2.5	0.52	5.7	139	57	90	129	46	90	5
Desmophen	5	0.36	8.6	158	96	81	137	46	90	8
Desmophen	10	0.35	6.6	164	142	13	160	66	90	20
Desmophen	15	0.38	7.8	163	139	14	150	91	61	16
Desmophen	25	0.28	5.8	165	148	8	165	136	15	21
Desmophen	30	0.27	5.8	166	151	10	165	155	6	24
Base	Eicosane (%)	P^*	D^*_{stat}	Initial θ^*_{adv} (°)	Initial θ^*_{rec} (°)	Initial $\theta^*_{Roll-off}$ (°)	100 cycle θ^*_{adv} (°)	100 cycle θ^*_{rec} (°)	100 cycle $\theta^*_{Roll-off}$ (°)	100 cycle mass loss (%)
CNR ($S^* = 0.29$)	0	2.00	18.3	93	78	90	-	-	-	-
CNR	25	1.45	11.3	157	82	84	-	-	-	-
CNR	30	1.00	3.5	162	87	71	-	-	-	-
CNR	35	0.74	4.3	153	161	14	162	92	33	2
CNR	40	0.80	3.4	148	137	15	163	113	38	3
CNR	50	0.94	6.5	160	146	11	164	77	90	11

Desmophen: Desmophen 670BA; Vytaflex: Vytaflex 40.

We compared the durability of these systems to three commercially available, and purportedly durable, SHSs (Fig. 7.10a). None of the commercial coatings maintained a low $\theta_{Roll-off}$ after 100 abrasion cycles. We extended the abrasion testing of our binder/filler blends exhibiting $S^* > 1.0$ and found them to be quite resilient to mechanical wear (Fig. 7.10b). Whereas all other evaluated SHSs became wettable within 100 abrasion cycles, the non-wetting properties of our surfaces fabricated from partially miscible, spray-coated blends endured significantly longer.

When blended with F-POSS, coatings incorporating the PFPE, SF-100, and FPU binders remained superhydrophobic for up to about 400, 500, and 800 Taber abrasion cycles, respectively. Combinations of the polyurethane Desmophen 670BA and IB-POSS, or the FPU and FO-POSS, both exhibited $\theta_{Roll-off} < 15°$ for ≈ 800 cycles. In fact, all such systems only became wettable once almost the entire coating was abraded away. For example, a 100 μm-thick FPU/F-POSS coating maintained $\theta_{Roll-off} < 15°$ even when > 90 μm of its thickness was removed. Note that the coating mass loss was not linear with the number of abrasion cycles, as larger, massive aggregates were removed first.

As further proof that partial miscibility is required for mechanically durable SHSs, we chain extended the FPU by incorporating propylene glycol into the crosslinked network (Sec. 7.2). The chain-extended FPU exhibited a three-fold increase in elastic modulus, and a 12% reduction in mass loss during abrasion of the smooth binder (no filler), as compared to unmodified FPU. However, the increased number of urethane linkages altered the Hansen sphere for the crosslinked network, changing the miscibility with F-POSS from $S^* \approx 0.6$ to $S^* \approx 1.1$. As such, whereas

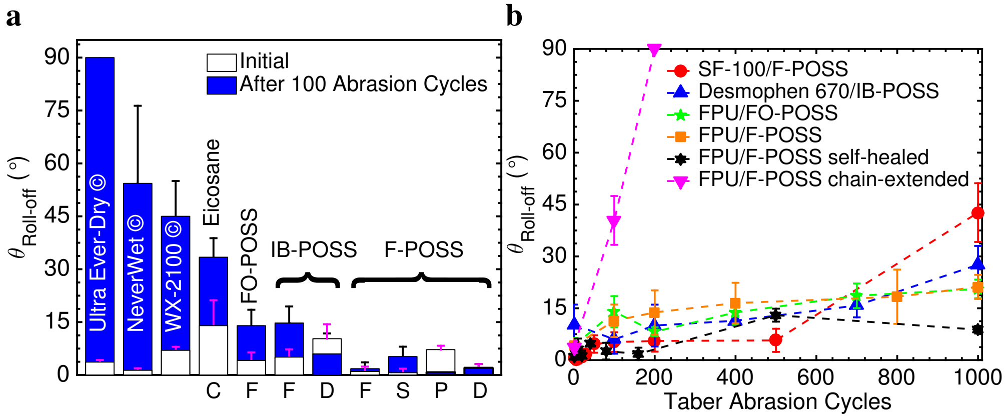

Figure 7.10: a, The roll-off angles for three commercially available SHSs and eight of the SHSs fabricated in this work ($S^* < 1.0$), initially and after 100 abrasion cycles. C: chlorinated rubber, F: FPU, D: Desmophen 670BA, S: SF-100, P: PFPE. b, The droplet roll-off angles for four representative, durable SHSs fabricated in this work. The data for the propylene glycol chain extended FPU/F-POSS, and the self-healed FPU/F-POSS, are also shown.

a sprayed blend of FPU + 15 wt% F-POSS ($P^* = 0.48$) remained superhydrophobic after 800 abrasion cycles, a sprayed blend of the chain extended FPU + 15 wt% F-POSS ($P^* = 0.56$) was no longer superhydrophobic after only 100 abrasion cycles (Fig. 7.10b). This counterintuitive result emphasizes the fact that the binder with the correct miscibility $0 \leq S^* \leq 1.0$, not the most mechanically durable binder, can yield the most mechanically durable SHSs. Moreover, the blend of FPU/F-POSS also withstood a host of other potentially damaging exposures (Sec. 7.2). After ultrasonication, a fluoro-solvent rinse, acid and base submersion, knife scratching, accelerated weathering, ultraviolet exposure, and being held at 350 °C for 3 days, the coating always maintained $\theta_{Roll-off} < 15^\circ$ (Fig. 7.9b).

7.4.2 Abrasion does not induce superhydrophobicity

Although Taber abrasion was employed to remove surface features, we wished to verify that the abrasion process was not itself causing our durable coatings to remain superhydrophobic. To do so, we spin-cast nominally smooth films using the same solution as for the superhydrophobic, spray-coated surfaces. Due to solvent evaporation effects, the surfaces were still somewhat rough (Fig. 7.11a,b).

For comparison, we sprayed pure FPU. We also measured the roughness of the abrasive CS-10 wheel. Over 5,000 abrasion cycles, we tracked the roughness (Fig. 7.11b) and contact angles (Fig. 7.11c) of the smooth coatings. If the abrasion process were imprinting the texture of the wheel into the coating, several distinguishing features would arise. First, the roughness of the coating would

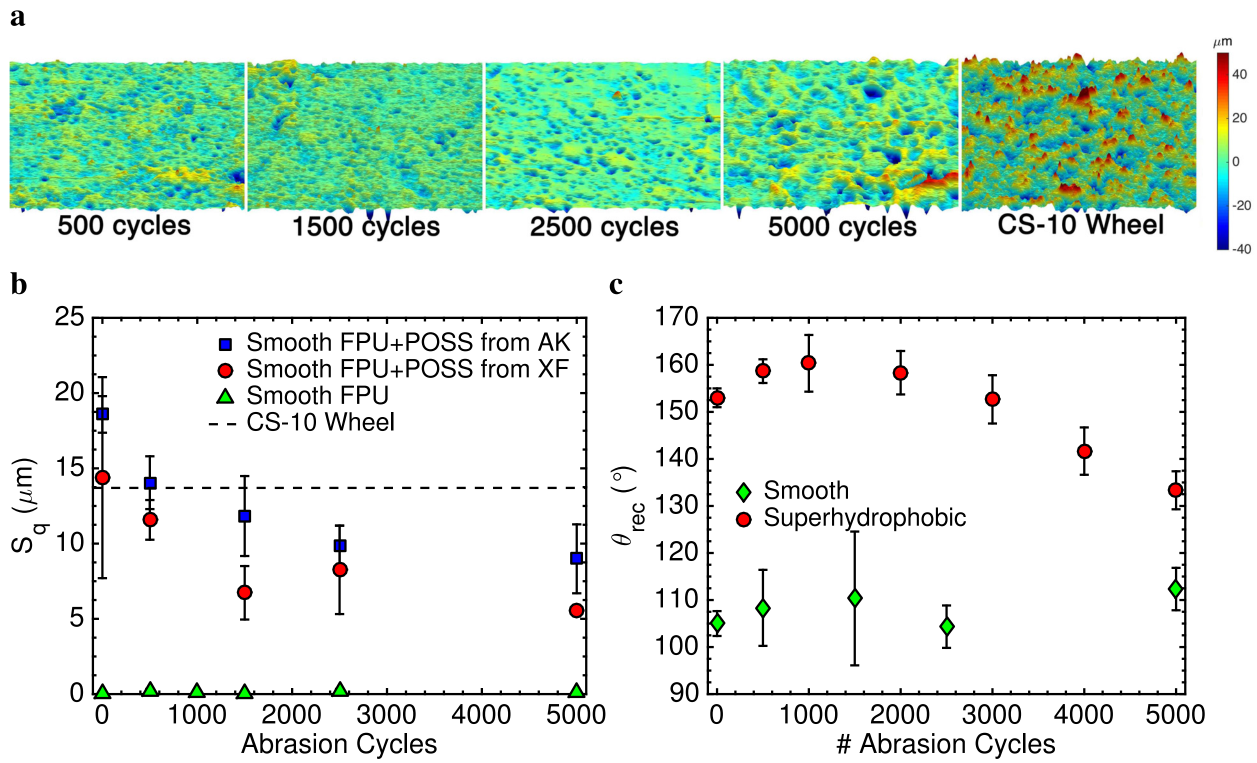

Figure 7.11: a, Heightmaps of a smooth FPU + 15 wt% F-POSS film versus the number of Taber abrasion cycles. b, Root-mean-squared height of smooth FPU + 15 wt% F-POSS, spin-cast from either Asahiklin-225 (AK) or Vertrel XF (XF). Smooth FPU without F-POSS, sprayed from $CHCl_3$, is shown for comparison, along with the CS-10 wheel. c, The receding contact angle of the FPU + 15 wt% F-POSS coating, either smooth or rough, as a function of abrasion. a-c support that the abrasion process was not inducing superhydrophobicity.

eventually reach the roughness of the wheel. This was not the case, and the spin-cast films actually became smoother than the wheel with increasing abrasion. Moreover, the pure FPU, which initially displayed $S_q = 155 \pm 70$ nm, only increased to $S_q = 650 \pm 100$ nm after 1,000 abrasion cycles. Both these experiments support the claim that the roughness of the wheel was not being imprinted onto the coating.

To further prove that the abrasion was not inducing the water repellency, we also measured θ^*_{rec}. Should the smooth coating become superhydrophobic, there would be a drastic jump in θ^*_{rec}. In Fig. 7.11c we show that this did not happen, with only a statistically insignificant increase in θ^*_{rec} after 5,000 abrasion cycles. Thus, we are confident that the Taber abrasion process was not fortuitously causing our FPU/F-POSS coatings to remain superhydrophobic.

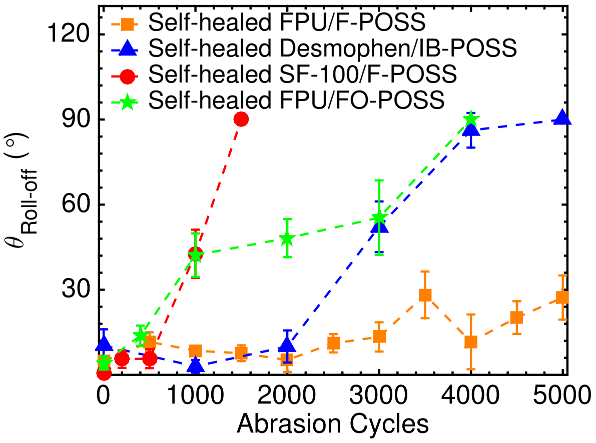

Figure 7.12: The roll-off angle for four binder/filler blends after self-healing, as a function of the number of abrasion cycles.

7.5 Self-healing superhydrophobic surfaces

In the remainder of this work we focus on our most durable coating, the FPU binder blended with 15 wt% F-POSS. Due to the surface migration of F-POSS upon heating, and the elastomeric nature of the FPU ($T_g \ll$ room temperature), the fabricated coating can both chemically and physically self-heal. For example, the as-abraded coating maintained $\theta_{Roll-off} < 15°$ up to about 800 abrasion cycles. Beyond this, $\theta_{Roll-off}$ increased with the number of abrasion cycles. But if the coating was placed on a hotplate for a few minutes, the water repellency was easily restored ($\theta_{Roll-off} < 5°$, Fig. 7.12).

With self-healing, the FPU/F-POSS coating maintained $\theta_{Roll-off} < 15°$ even after 4,000 abrasion cycles. This was expected after measuring the statistical properties of the surface after self-healing, which always yielded $P^* < 1.0$ (Fig. 7.13). Other blends created using different elastomers, such as SF-100/F-POSS, FPU/FO-POSS, or Desmophen 670BA/IB-POSS, also exhibited a self-healing nature. The self-healing and superhydrophobic nature of Desmophen 670BA/IB-POSS system is notable because neither of the components contains any fluorinated species.

7.5.1 Chemical self-healing

The low surface energy of F-POSS causes it to migrate to the solid/air interface[44], imparting different binder/F-POSS blends with a robust, self-healing nature. For example, oxygen plasma, which has the capability of hydrolyzing F-POSS[164], rendered the FPU/F-POSS coating hydrophilic within minutes ($\theta^* = 0°$, although P^* remained unchanged). However, upon heating, the low surface energy was fully restored (Fig. 7.4a). We found that the time required for full

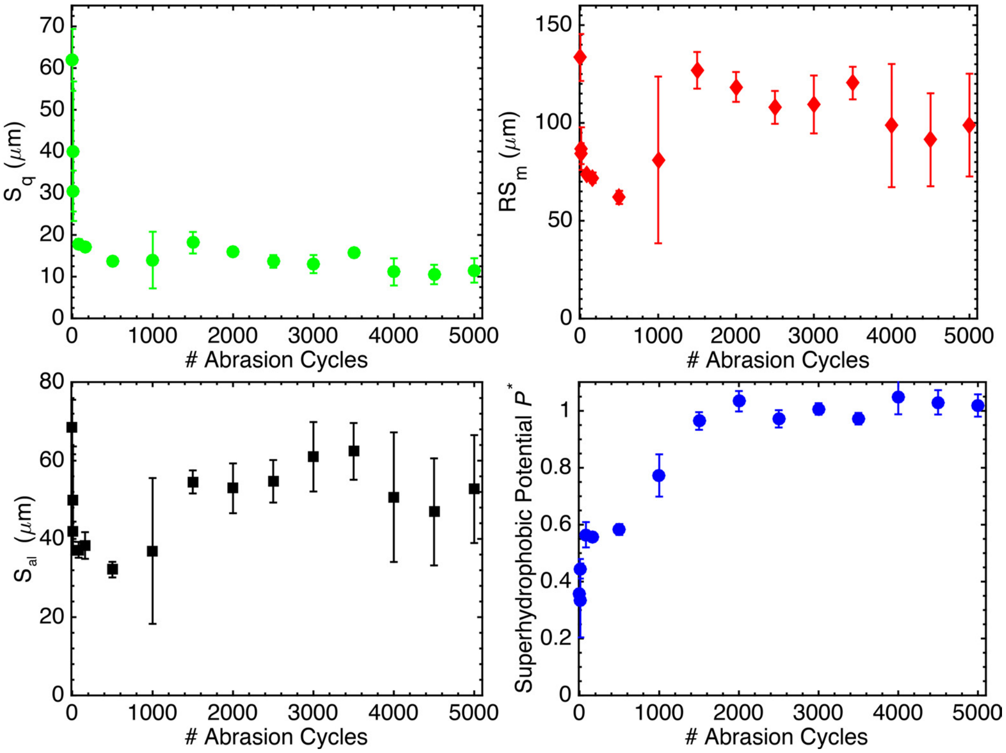

Figure 7.13: The four statistical parameters characterizing the FPU + 15 wt% F-POSS spray-coated blend, as a function of the number of Taber abrasion cycles.

superhydrophobic recovery decreased with increasing temperature, consistent with a diffusion-controlled process. The coating maintained low $\theta_{Roll-off}$ when held at temperatures up to about 400 °C, the point at which F-POSS begins to degrade (Fig. 7.3). However, even when $> 75\%$ of the mass had degraded, the coating maintained $\theta_{Roll-off} < 15°$. We also repeatedly treated the coating with O_2 plasma and found that the water repellency was fully recovered by heating even after 10 successive treatments (Fig. 7.4b).

7.5.2 Pressure resistance

Even after mechanical wear, a robust SHS should also exhibit a large capillary resistance or breakthrough pressure, P_b, defined as the pressure required to force a transition from the Cassie-Baxter to the Wenzel state[26, 145, 33, 209, 210, 204]. Although the FPU/F-POSS coating maintained $P^* < 1.0$ over 5,000 abrasion cycles (Fig. 7.14a), indicating an energetically favorable Cassie-Baxter state, a pressure-induced wetting transition is usually irreversible without some form of energy input[26].

To evaluate the breakthrough pressure, we completely submerged our self-healed FPU/F-POSS coating in a pressurized water tank and observed when wetting occurred. The breakthrough pres-

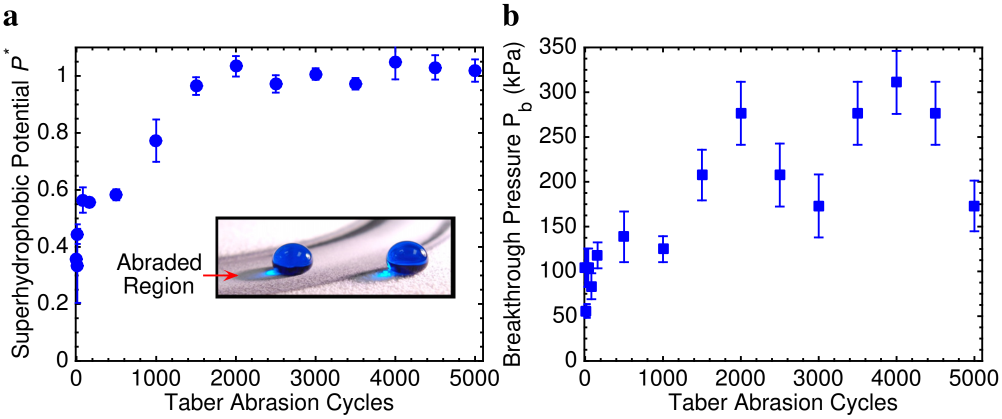

Figure 7.14: Capillary resistance. a, The P^* parameter as a function of the number of abrasion cycles for the FPU/F-POSS coating after self-healing. The inset shows water droplets (dyed blue) displaying high contact angle even after 5,000 abrasion cycles. b, The breakthrough pressure of the FPU/F-POSS coating as a function of abrasion, after self-healing.

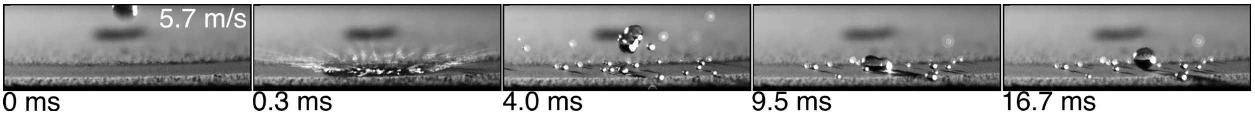

Figure 7.15: A water droplet, dropped from a height of 1.7 m, impacted the abraded region (4,000 abrasion cycles) of the FPU/F-POSS coating at a velocity of 5.7 m/s. After breaking up, the satellite droplet bounced at least four times after impacting the surface. The surface was tilted $1.5°$.

sure of this coating was initially $P_b = 100 \pm 20$ kPa, and never decreased below $P_b = 50$ kPa, even after 5,000 abrasion cycles (Fig. 7.14b). Remarkably, the pressure resistance increased to a maximum of $P_b = 310$ kPa after 4,000 abrasion cycles, due to the decrease in S_q with increasing abrasion. As such, even water droplets impinging the abraded surface at an impact velocity of 5.7 m/s completely rebounded, leaving the surface dry (Fig. 7.15). In fact, the measured breakthrough pressure of 310 kPa corresponds to a droplet impact velocity of $V \approx 25$ m/s ($P_{Bernoulli} = \rho V^2/2$, where ρ is the fluid density), which is higher than the terminal velocity of a millimetric water droplet in air. Whereas often SHSs only maintain high contact angle after mechanical damage, the surfaces reported here preserve all their advantageous, water-repellant properties (high θ^*, $\theta_{Roll-off} < 15°$, high P_b), even after harsh mechanical abrasion.

7.5.3 Physical self-healing

The thermal recovery of low surface energy due to F-POSS migration will only result in a SHS if the texture is also maintained. Although abrasion damages the texture of the FPU/F-POSS coating, we found that the abraded texture was still sufficient for superhydrophobicity (Fig. 7.14a). Further, we also observed that the texture could be partially restored during the thermal treatment. For example, after 1,000 abrasion cycles, the FPU/F-POSS coating exhibited $S_q = 2.6$ μm. Thermal recovery at 100 °C for 120 seconds increased this value to $S_q = 3.3$ μm (measured at identical locations) (Fig. 7.16a). Thus, abrasion also slightly compressed the coating.

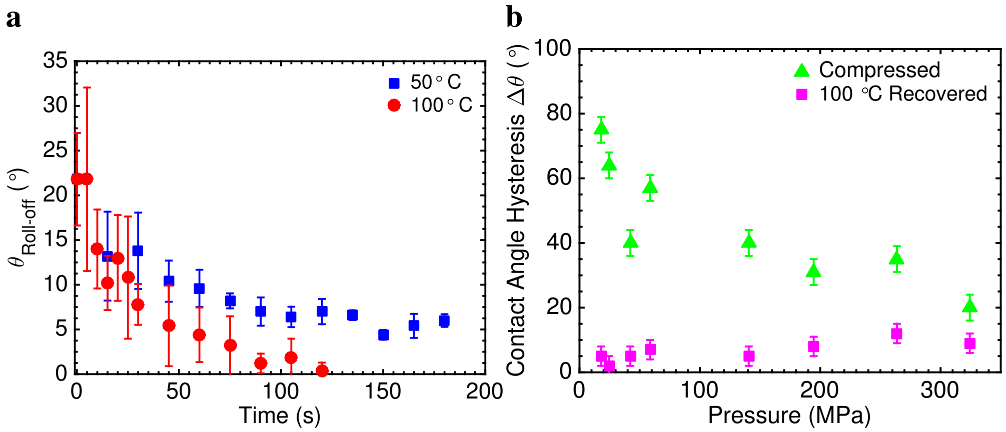

Figure 7.16: Texture recovery. a, The self-healing properties of the FPU/F-POSS coating as a function of time and temperature, after 1,000 Taber abrasion cycles. S_q increased from 2.6 μm to 3.3 μm during self-healing. b, The contact angle hysteresis for the FPU/F-POSS coating before and after thermal recovery from compression, as a function of the compressive load. Note that the compressed coating's $\Delta\theta$ decreased with an increase in applied load because the surface became smoother after compression. All compressed surfaces were fully wetted.

To further explore this, we subjected the coating to compressive stresses up to 350 MPa. Although flattening the texture elements significantly reduced the coating's porosity ($P^* \approx 2.0$, Fig. 7.16b), such damage was reversible, and upon heating, the coating quickly recovered its original porous state ($P^* \approx 0.6$, Fig. 7.16b,7.17). Environmental scanning electron microscopy (ESEM) allowed us to observe this self-healing *in situ* (Fig. 7.17b). As the compression set (percentage of permanent strain after compression) of elastomers is typically non-zero, the use of elastomeric materials in the fabrication of SHSs may be advantageous in terms of their ability to recover from compressive stresses that remove their porous texture.

7.6 Conclusions

In summary, we have explored how miscibility between hydrophobic fillers and polymeric binders allows one to control the formation of surface texture during spray coating, in order to fabricate superhydrophobic surfaces. The S^* parameter quantifies the miscibility between the two sprayable

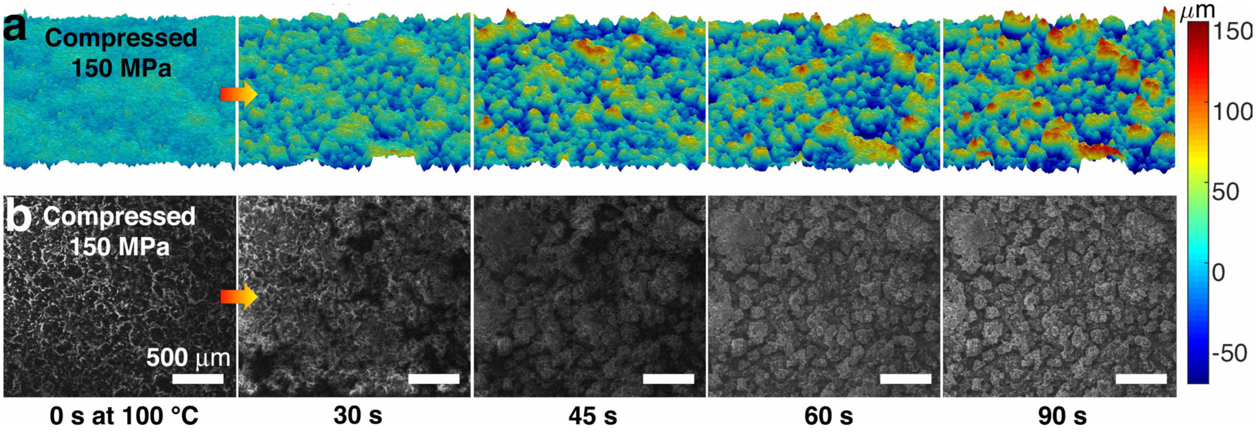

Figure 7.17: a, Height maps of the FPU/F-POSS coating after 150 MPa compression, as a function of recovery time at 100 °C. b, The recovery of the texture was also imaged *in situ* using environmental scanning electron microscopy.

components, and the P^* parameter characterizes the stability of the non-wetted state. Superhydrophobic surfaces should be designed such that $S^* < 1.0$, to afford mechanical durability, and $P^* < 1.0$, to provide a robust non-wetting state. Utilizing these two design criteria, we have fabricated superhydrophobic surfaces with unprecedented mechanical durability. Some of these surfaces also exhibited a self-healing nature, both chemically and physically, and were able to fully recover their superhydrophobicity after a wide variety of extreme chemical and physical exposures. These surfaces, and the design parameters used to develop them, may find immediate usage in a wide range of academic and industrial sectors across the globe. One usage, which had previously been limited by the durability of superhydrophobic surfaces, is drag reduction is turbulent flow. This is the topic of the following chapter.

CHAPTER 8

Design of Superhydrophobic Surfaces for Drag Reduction in Turbulent Flow

8.1 Introduction

The current environmental crisis demands new innovations, capable of reducing our dependence on fossil fuels. In 2012, the U.S. alone used over seven billion gallons of fossil fuels to power marine vessels[211]. Marine fuel consumption is predicted to double between 2010 and 2030[212], and nearly 60% of this fuel will be expended to overcome frictional drag[49]. As such, methods that can effectively reduce the drag on marine vehicles will have an enormous, worldwide impact, both economically and environmentally. Current technologies, such as riblets, polymers, or air-layer drag reduction, have yielded only modest ($5 - 20\%$) reductions of total drag, or require significant mass and/or energy inputs[213, 214, 215]. Therefore, there continues to exist a strong need to develop methods for significantly reducing drag in conditions of naval relevance, *i.e.* high-Reynolds number, turbulent flows.

A large body of work has shown consistently that superhydrophobic surfaces (SHSs) can effectively lower frictional drag in laminar flow[216, 217, 218, 219, 220, 221, 32, 222, 147, 223, 224, 34, 225]. However, the extension of friction drag reduction to wall-bounded turbulent flows, *i.e.* many that are relevant to mechanical, naval, and hydraulic infrastructure, has not been straightforward[213, 216, 217, 218, 226, 227, 228, 229, 230]. Both the efficacy and mechanism of these potentially drag-reducing surfaces have been previously debated[217, 228, 231, 232, 15]. Herein we elucidate the physical properties that enable a SHS to reduce drag in turbulent flow. We then utilize some of the scalable and mechanically robust SHSs fabricated in Chapter 7 to achieve significant friction drag reduction in fully-developed, turbulent channel flow, at the highest Reynolds numbers evaluated to-date.

Recall that SHSs entrap air pockets within their texture elements. When liquid flows over a solid surface, the usual boundary condition assumed is that the velocity of the liquid must match the velocity of the solid[219] (Fig. 8.1).

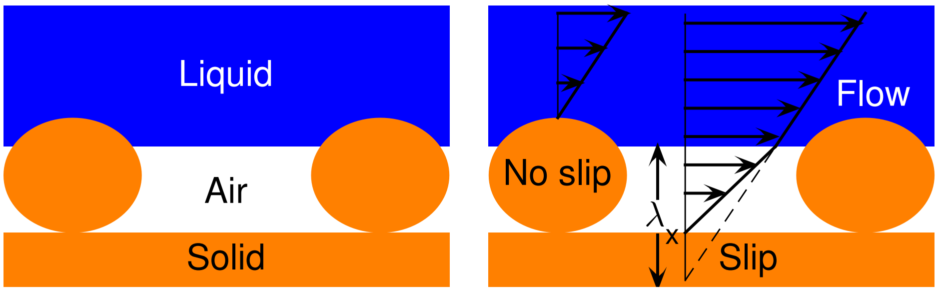

Figure 8.1: Slip on SHSs. a, A schematic of the three phase interface that can form on a superhydrophobic surface. b, Above the solid surface, the velocity of the flow at the wall must go to zero to match the solid. However, over the air pockets, the velocity can be non-zero, creating a slip velocity and a corresponding slip length.

This is typically referred to as the no slip' boundary condition. However, SHSs possess a fraction of air $(1 - \phi_s)$ at the liquid interface (where we recall that ϕ_s is the solid fraction from the Cassie-Baxter equation, Eq. 1.6), which can have a non-zero interfacial velocity. Navier first proposed a slip velocity, u_s, in 1823, where he suggested that the shear rate at the wall was proportional to u_s[45]. For a two-dimensional flow, this can be described by,

$$u_s = \lambda_x \left| \frac{du}{dy} \right|, \qquad v_s = 0, \qquad w_s = \lambda_z \left| \frac{dw}{dy} \right| \tag{8.1}$$

where u, v, and w are the velocity components in the streamwise (x), wall-normal (y), and spanwise (z) directions, and λ_i is the slip length along direction i (see Fig. 8.1b). Thus, SHSs can produce slip at the interface through the incorporation of entrapped air. Because less energy is lost to frictional dissipation, a non-zero u_s indicates a reduction in drag at the solid-liquid interface. For laminar flows, the drag-reducing ability of SHSs has been confirmed experimentally and computationally; see the recent review by Rothstein[219]. Depending on the fraction of air $(1 - \phi_s)$, drag reduction as high as 99% has been previously achieved[233].

However, the ability of SHSs to afford drag reduction in turbulent flow is not well-characterized [213, 216, 217, 218, 226, 227, 228, 229, 230]. Whereas small, micro-fabricated surfaces have shown drag reduction anywhere from 10%[225, 227] to 50%[226, 229], large, scalable SHSs have resulted in drag increase[213, 217, 228], no change[217, 228, 234], or around 10% to 30% drag reduction under certain conditions[213, 228, 234]. In turbulent flow, there is an interaction between the near-wall region and the buffer region. The former is known as the viscous sublayer, which is dominated by viscous shear stresses, while the latter is dominated by turbulent momentum transfer (Fig. 8.2)[15].

This interaction may be modified when micro-features are added to a surface. Additionally, significant momentum transfer is expected in the viscous sublayer due to the presence of the dis-

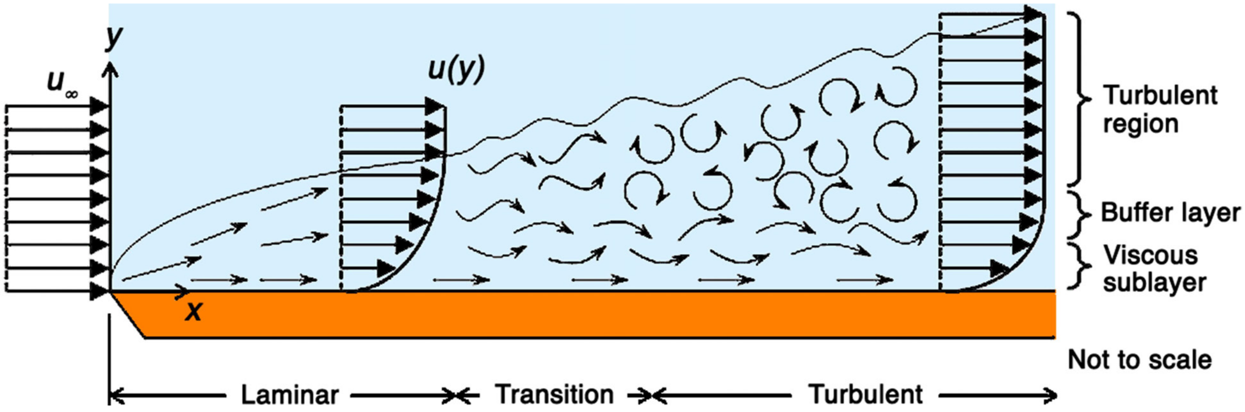

Figure 8.2: A schematic of the turbulent boundary layer that exists very close to the wall of a body in turbulent flow[15]. U_∞ is the mean velocity far away from the surface.

parate liquid-air and liquid-solid interfaces causing mixed slip/no-slip boundary conditions that can exist on textured surfaces. These near-wall flows are complex due to the many turbulent structures, eddies, and vortices that dominate the momentum transfer in the buffer region[173]. Moreover, while slip in the direction of flow $(u_s \neq 0)$ can result in drag reduction, slip in the spanwise direction $(w_s \neq 0)$ can increase the intensity of these turbulent structures, causing a drag increase[227, 235, 236]. As a result, surfaces that reduce drag in laminar flow, where these additional flow features are absent, are not guaranteed to continue reducing drag when exposed to turbulent flow. Table 8.1 summarizes the previous attempts to characterize drag reduction in turbulent flow.

As shown in Table 8.1, many of the previous studies have not reported contact angles, or only reported θ^*, providing no information on $\Delta\theta^*$. From a materials point of view, there are few guidelines regarding how surfaces should be fabricated so as to maximize the drag reducing potential of a SHS in turbulent flow. Typically, reporting θ^*_{adv} and θ^*_{rec} has been considered sufficient to describe a SHS. However, here we show that determination of these angles is necessary, but may not be sufficient, to describe surfaces capable of reducing drag in turbulent flow. Fully-turbulent, high-Reynolds number flows create large pressure fluctuations and high shear stresses. Such large surface pressures can displace the entrapped air pockets of a SHS if its capillary resistance is low *i.e.* only a small pressure is required to transition from the Cassie to the Wenzel state. Similarly, the high shear stresses can mechanically damage and detach any fragile texture elements of the SHS, again removing the entrapped air. Insufficient mechanical durability is one reason SHSs have previously not shown sustainable friction reduction in turbulent flow[213, 217, 228, 34]. Regardless, even if the air remains within the texture elements of a SHS, the surface may still not reduce drag if the texture is not designed correctly[213, 217, 15], as we explain in Sec. 8.1.1 below.

Table 8.1: Previous studies on drag reduction in turbulent flow with corresponding geometry of surfaces, apparent contact angles and contact angle hysteresis reported, lengths of the tested surfaces, and range of friction Reynolds numbers evaluated ($Re_\tau = H/2\delta_\nu = \delta/\delta_\nu$), where H is the channel height, δ_ν is the viscous length scale and δ is the boundary layer thickness. The observed drag reduction (positive) or drag increase (negative) is also tabulated.

Ref.	Geometry	θ^*	$\Delta\theta^*$	Length (cm)	Re_τ	Observed drag reduction
Park *et al.*[230]	Ridges	-	-	2.7	250	0% - +70%
Gogte *et al.*[237]	Random	156°	-	4.3	40 - 288	+3% - +18%
Jung *et al.*[216]	Posts	173°	1°	6	0 - 18	0% - +30%
Woolford *et al.*[227]	Ridges	160°	-	8	3 - 100	-7% - +11%
Bidkar *et al.*[213]	Random	155°	-	15	1,000 - 5,000	-13% - +30%
Henoch *et al.*[229]	Posts, Ridges	-	-	20	150 - 600	0% - +50%
Tian *et al.*[238]	Random	161°	0.9°	20	784	+10%
Lu *et al.*[239]	Random	151°	0.9°	24	0 - 66	0% - +53.3%
Watanabe *et al.*[218]	Random	140°	-	43	-	0% - +15%
Peguero *et al.*[240]	Random, Posts	-	-	43	200	-50% - +40%
Hokmabad *et al.*[234]	Random	165°	-	50	2,530	0% - +15%
Srinivasan *et al.*[225]	Random	161°	0°	60	480 - 3,810	0% - +22%
Zhao *et al.*[217]	Random	-	-	80	1,700 - 3,300	-5% - +9%
Daniello *et al.*[226]	Ridges	-	-	100	100 - 300	0% - +50%
Aljallis *et al.*[228]	Random	164°	5°	122	520 - 5,170	-30% - +30%
This work	Random	Fig. 8.3b	Fig. 8.6	120	215 - 950	-90% - +90%

8.1.1 Form drag on wetted texture elements

As the pressure increases on a SHS, the liquid-vapor interface moves into the air pockets, partially filling the surface texture, thereby increasing ϕ_s and perhaps r_ϕ, depending on the surface geometry. According to Eq. 1.6, θ^* must then decrease (Fig. 8.3a). This has two critical implications. First, the ϕ_s extracted from conventional measurements of θ^*_{adv} or θ^*_{rec} may be significantly different from the ϕ_s in a turbulent flow. Second, the wetted aggregate features that protrude into the flow, *i.e.* $r_\phi\phi_s$, may cause form drag[213, 241, 242, 243, 244], increase turbulent mixing, and/or enhance turbulent structures[173], all which could negate any skin-friction drag reduction, resulting in a net increase in drag. Thus, only contact angles measured at the pressures expected during turbulent flow are relevant to turbulent skin-friction drag reduction (Fig. 8.3b).

The Laplace pressure, P_L, within a water droplet is given by $P_L = 2\gamma_{LV}/R$, where R is the radius of the droplet. By decreasing the size of the droplet used to measure contact angles, the values of r_ϕ and ϕ_s at higher pressures can be determined. Moreover, by measuring the exact surface topography, the size and shape of every wetted texture element can be calculated once the meniscus location under pressure is known. The form drag on each texture element may then be

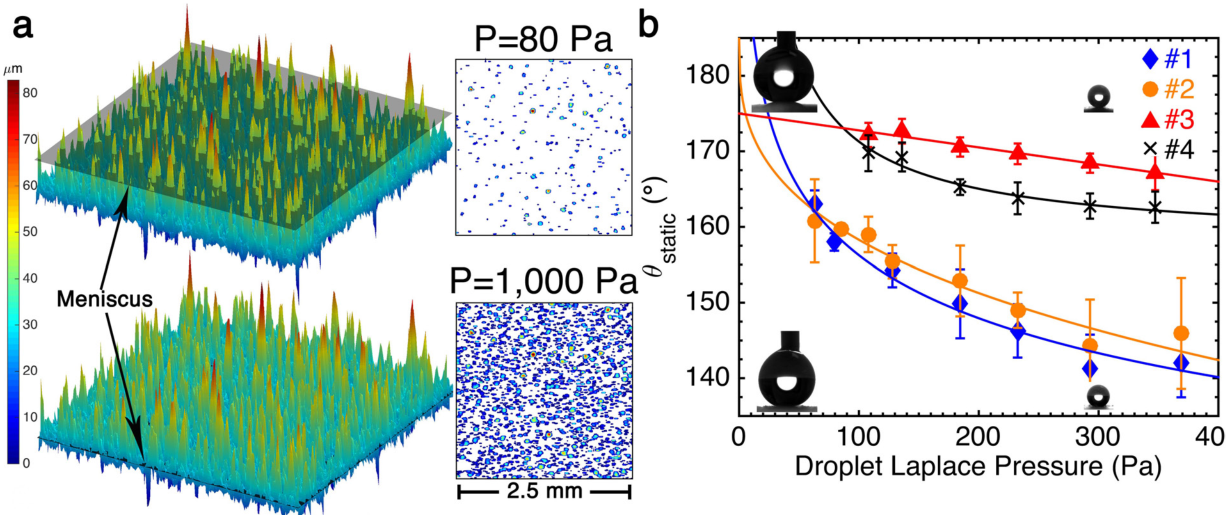

Figure 8.3: a, the location of the meniscus for surface #2 at low pressure (conventionally used to measure contact angles) and at higher pressure. The height maps are 2.5 × 2.5 mm. b, θ^* as a function of pressure for the four surfaces considered in this work. The lines are power law fits to the data. The insets show goniometer images of droplets on surface #1 (below) and #3 (above).

approximated by[173],

$$F_D = \frac{1}{2}\rho U^2 A C_d \tag{8.2}$$

where ρ is the density of water, U is the average flow speed in the vicinity of the texture element, A is the element's projected area in the flow direction, and C_d is the drag coefficient based on the geometry of each element. On a SHS, if the sum of the forces due to form drag on the protruding texture elements exceeds the drag reduction due to the presence of the trapped air pockets, a net drag increase will result. This drag increase is a direct consequence of the meniscus height at pressure, and is independent of the $\theta^*_{adv}/\theta^*_{rec}$ measured at low/atmospheric pressure. Computationally it has been shown that surfaces with $\phi_s \approx 0.1$ exhibit the highest form drag in the fully wetted case[242, 244]. Moreover, the largest texture elements produce disproportionately high form drag[241, 243]. As such, designing SHSs that will not cause significant form drag in turbulent flow is non-trivial and has rarely been investigated[213, 234].

8.2 Materials and methods

8.2.1 Surface fabrication

Surface #1 consisted of an 80/20 wt% blend of a fluorinated polyurethane (Helicity Inc.) and fluorodecyl polyhedral oligomeric silsesquioxane (F-POSS). F-POSS was prepared by condensing

1H,1H,2H,2H-Heptadecafluorodecyltriethoxysilane (Gelest Inc.) as previously reported[134]. The polyurethane was crosslinked using 3.4 wt% 4,4-Diisocyanato-methylenedicyclohexane (Wanhua Chemical Group Co.) All three above components were dissolved in Vertrel XF (Chemours) at an overall concentration of 200 mg/mL. The mixture was sonicated until it became completely transparent, approximately 30 seconds. 40 mL of the solution was sprayed onto a 1.2 m × 0.1 m stainless steel substrate using an ATD Tools 6903 high volume-low pressure spray gun with compressed air at a pressure of 20 psi. The sample was then cured at 80 °C for 72 hours. SEMs of surfaces #1 - #4 are shown in Fig. 8.4.

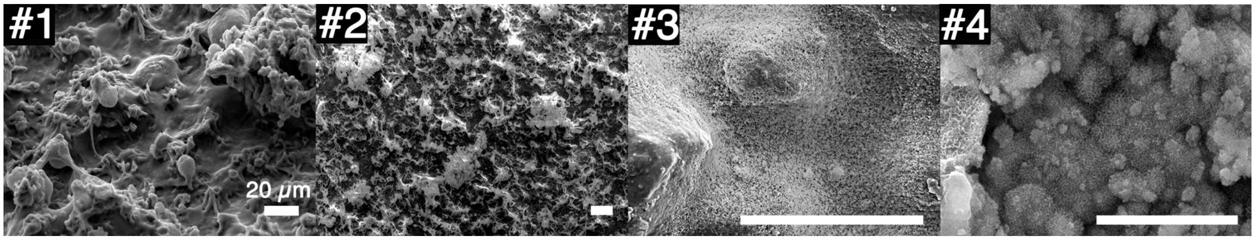

Figure 8.4: SEM micrographs of the four SHSs produced in this work.

Surface #2 consisted of a 50/50 wt% blend of superglue (SF-100, 3M) and F-POSS. The two components were dissolved at a concentration of 50 mg/mL in Asahiklin-225 (Asahi Glass Co.) and sprayed using the same procedure as for surface #1. Surface #2 was cured at 50 °C for 60 minutes. The morphology of this system was altered in the following manner. To increase asperity roughness, a total spray solution of 120 mL was used. To decrease asperity roughness, the spray gun was replaced with a Paasche airbrush, as described previously[138]. SEMs of the three variants of surface #2 and shown in Fig. 8.5.

Surface #3 consisted of a 65/35 wt% blend of the same fluorinated polyurethane as surface #1, along with fluoro-functionalized silica particles, approximately 50 - 100 nm irregular aggregates, the synthesis of which is reported elsewhere[245]. The two components were dispersed at a concentration of 25 mg/mL in Vertrel XF and then 20 mL was sprayed following the same procedures as surfaces #1-2. The surface was then cured at 80 °C for 72 hours.

Surface #4 consisted of aluminum (Al) metal that was etched, boiled and subsequently functionalized with a fluoro-silane. The following procedure was modified from a previously reported technique[246]. Al sheets (McMaster) 8 in × 4 in × 1/8 in were first etched in 2.5 M HCl (Fisher Scientific) for 20 minutes. Following etching, the samples were sonicated to remove residual Al flakes adhered to the surface. The etched Al was then boiled in deionized water for 20 minutes. Finally, the surface was exposed to 1H,1H,2H,2H-Heptadecafluorodecyl triethoxysilane (Gelest Inc.) vapors overnight at 80 °C under vacuum. To span the full channel length, 5 sheets were tiled together.

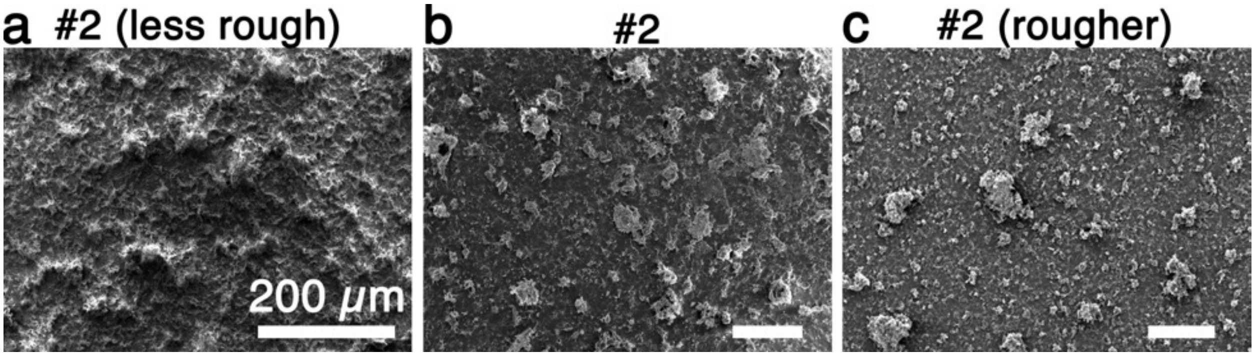

Figure 8.5: Modifying surface #2. In order to change the form drag associated with surface #2 (b), the texture was slightly modified to either decrease (a) or increase (c) surface roughness. Large asperities can be seen for the rougher variant, whereas these were absent in the less rough version of surface #2.

8.2.2 Wettability analysis

Static contact angles were measured using a Ramé-Hart 200 F1 contact angle goniometer with water droplets of decreasing volume (25 μL to 0.25 μL). Contact angle hysteresis was measured by increasing or decreasing the volume of water on the surface for the low pressure measurement. For the higher pressure measurement, small volume (250 nL to 6 μL) droplets were deposited onto the SHS using a low-volume pipette. The surface was then tilted until the droplet rolled off the surface. Here we assume $\theta^*_{max} = \theta^*_{adv}$ and $\theta^*_{min} = \theta^*_{rec}$. The advancing and receding contact angles for four of the surfaces developed in this work are shown in Fig. 8.6.

8.2.3 Surface imaging

Scanning electron microscopy (SEM) was performed using a Phillips XL30 FEG. Samples were first sputtered with a gold-palladium mixture to avoid charging. Surface profilometry was performed using an Olympus LEXT interferometer with a step size of 1.25 μm and an overall scan area of 2.5 × 2.5 mm. A minimum of three locations were averaged. Surface statistics were calculated as outlined in Chapter 7, Sec. 7.3.2. Note that in the fluid mechanics community, the root mean squared roughness is typically denoted as k. We will use this convention, noting that $k = S_q$ from Chapter 7.

8.2.4 Flow facility

8.2.5 Form drag estimation

The form drag was calculated using a custom MATLAB script as follows. The Cassie-Baxter relation was satisfied by taking a contour slice (the meniscus) from height-maps obtained using a

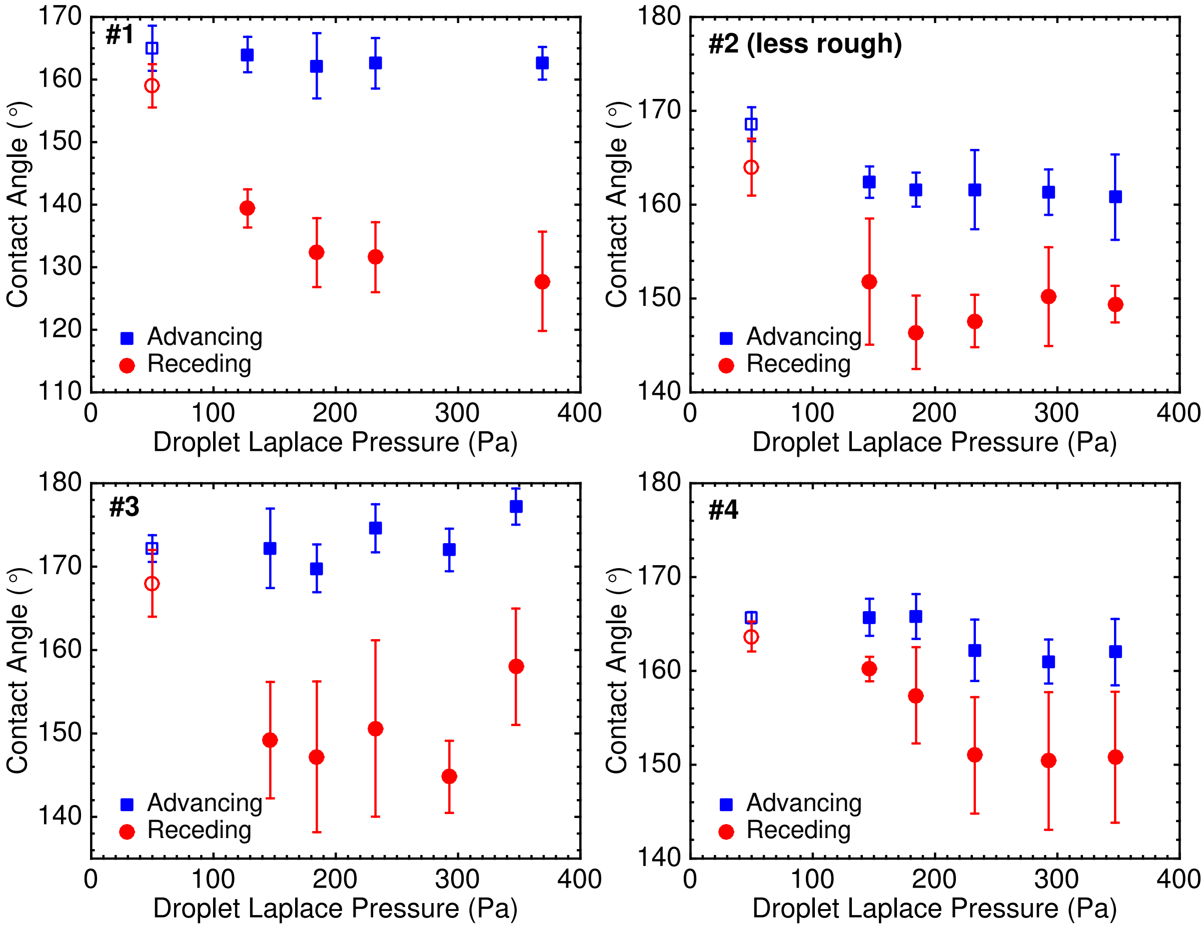

Figure 8.6: Contact angle hysteresis at higher pressure. The advancing and receding contact angles for the four superhydrophobic surfaces reported in this work are shown as a function of droplet Laplace pressure. The closed symbols were obtained using the maximum/minimum contact angle observed before a droplet rolled off the surface. The open symbols were obtained using the conventional goniometric technique. An arbitrary pressure of 50 Pa was chosen for the conventional technique for ease of reading, and is not indicative of the size of the droplets used.

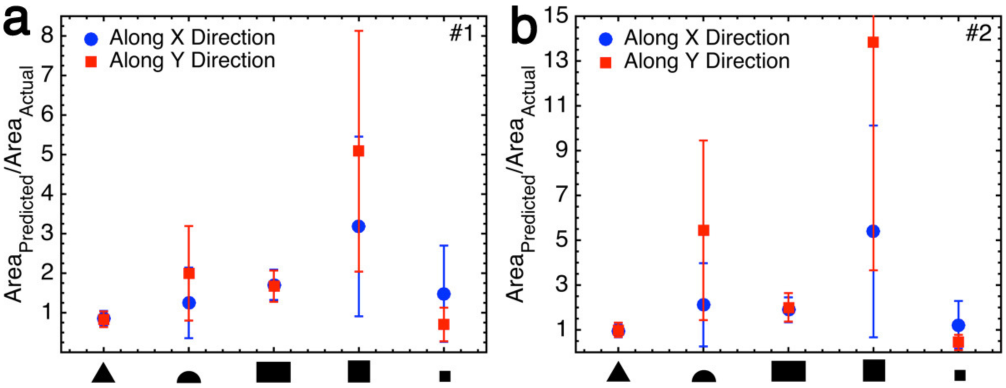

Figure 8.7: Justification for triangular aggregates. The calculated projected area of each aggregate protruding into the flow for surfaces #1 (a) and #2 (b), normalized by its actual area. By using different geometrical area formulae, it was apparent that triangles represented the data quite accurately (as evidenced by a value of unity on the abscissa). Thus, for our form drag calculations on each asperity, $C_D = 0.5$ was used in Eq. 8.2.

LEXT interferometer. When the meniscus height resulted in a value of $r_\phi \phi_s$ that corresponded to the desired contact angle (found to be a function of pressure based on contact angle measurements), each texture element above the meniscus was analyzed. The height and area were recorded and the drag coefficient of the texture elements was determined to most closely match a triangular asperity (Fig. 8.7). The fits from Fig. 8.3b allowed the form drag to be approximated based on pressure and contact angle alone. Other statistical quantities were extracted from the height-maps such as the root-mean-squared roughness, k.

8.2.6 Experimental flow facility

The four SHSs are mechanically durable (Fig. 8.8), easy to fabricate, and were applied over areas of 1.20 m × 0.10 m, an order of magnitude larger than most other SHSs previously tested[213, 216, 226, 229, 230] in fully-developed turbulent flows (Fig. 8.9a). We evaluated the skin-friction of the four SHSs in a fully-developed turbulent channel flow (Fig. 8.9b) at various flow speeds using pressure drop measurements and Particle Image Velocimetry (PIV). PIV data was processed using Lavision from DaVis.

Two noteworthy characteristics of channel flow prove efficacious when compared to zero-pressure gradient flows for the fundamental evaluation of skin-friction in turbulent flow, and particularly, for the development and characterization of SHSs for drag reduction. First, channel flows are internal and have a confined outer length scale (channel height H or boundary layer thickness $\delta = H/2$), which is fixed by the opposing walls. In zero-pressure gradient flows the outer length scale (δ) is unrestricted and grows as a function of distance along the surface. A fixed outer length

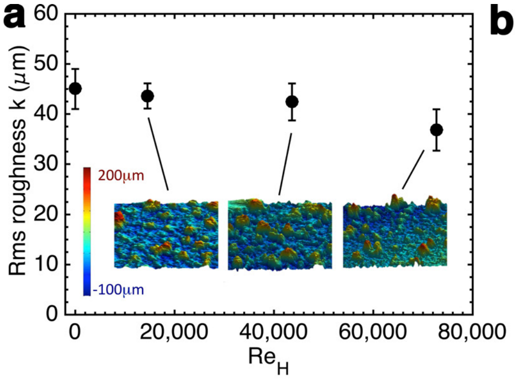

Figure 8.8: a, To evaluate the mechanical durability of our SHSs, we subjected our surfaces to high-speed flow in hour increments, from 2 m/s up to 10 m/s. This corresponded to a height-based Reynolds number of $\mathrm{Re}_\mathrm{H} = 20,000$ up to $\mathrm{Re}_\mathrm{H} = 80,000$. After each speed, the root-mean-squared roughness, k, was measured to ensure that the surface remained intact. The inset height-maps above measured 1.3×1.3 mm. b, The mechanical durability was also assessed by subjecting our most drag-reducing surface, the less rough variant of surface #2, to rotary Taber abrasion. Three commercially available, and purportedly durable, superhydrophobic surfaces were tested for comparison. The contact angle hysteresis, measured conventionally (low pressure measurement), drastically increased only for the commercial coatings, as they became damaged.

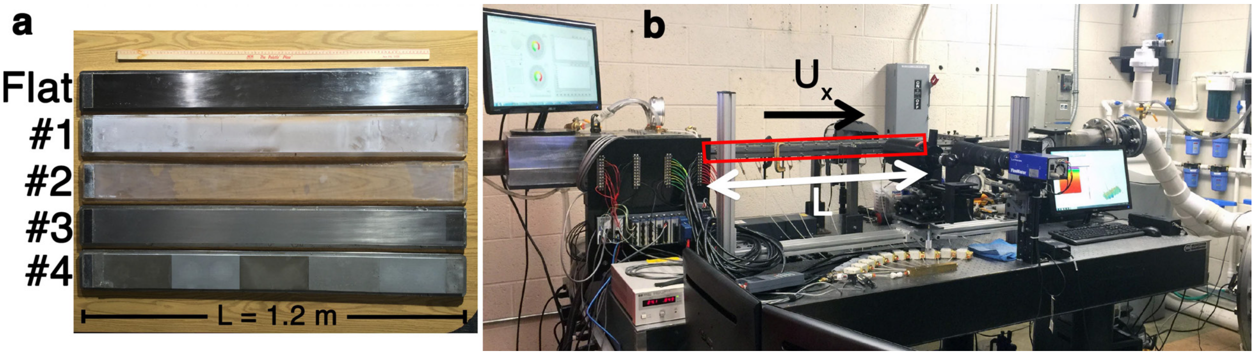

Figure 8.9: a, The four surfaces fabricated in this work, sprayed onto 1.2 m-long substrates. b, The closed-channel flow facility developed for the skin-friction evaluation in this work.

scale eliminates the dependence of the spatial location on scaling, and results in the scaling being primarily dependent on the bulk-flow variables. Second, channel flow facilities simplify the determination of frictional drag by measurement of the pressure drop for a fully-developed turbulent flow. Pressure drop analysis offers the simplest, and perhaps, the most widely utilized method of measuring skin-friction for internal flows. Schultz and Flack[247] provide a thorough discussion of Reynolds-number scaling for turbulent channel flow and ultimately conclude, '*channel flow results show Reynolds-number scaling trends that are consistent with recent experimental results from pipe and boundary layer flows*'. Our channel's height-based Reynolds number ($\mathrm{Re_H}$) ranged from 10,000 to 30,000, and was calculated using,

$$\mathrm{Re_H} = \frac{U_m H}{\nu}. \tag{8.3}$$

Here ν is the kinematic viscosity of water and U_m is the streamwise mean flow speed, determined from the volumetric flow rate, and verified with PIV of the entire flow field. PIV was conducted in the x-y mid-plane of the channel, $95H$ downstream of the channel inlet. As many as 1,200 image pairs were captured, analyzed, and averaged with commercial processing software.

For our system, drag reduction is defined as,

$$DR(\%) = 2 \times 100 \Big[\frac{(C_f)_{baseline} - (C_f)_{SHS}}{(C_f)_{baseline}} \Big] \tag{8.4}$$

where C_f is the skin-friction coefficient. The skin-friction was inferred from the streamwise pressure gradient (dP/dx) along one SHS and one baseline (hydraulically-smooth, $k^+ \ll 1.0$) surface in a fully-developed turbulent flow channel measuring 1.2 m (L) × 0.1 m (W) × 0.0073 m (H). The height of the channel was nominally 0.0073 m. However, the presence of the SHS, in addition to systematic error associated with reassembling the test section for each surface evaluated, caused the height to vary by as much as 0.1 mm. As such, the height of the channel was carefully measured at no less than five locations along the length of the test section using a set of precision gauge blocks. The resulting heights for each test were recorded, averaged, and used to analyze the performance of the SHS. Any anomalies were noted and corrected prior to testing. The error in the height measurement was estimated to be ± 0.05 mm. The pressure drop was measured over a 0.5 m span $(70H)$, starting approximately $50H$ from the channel inlet, and was used to determine the average local wall-shear stress (τ_w) and wall-shear velocity (u_τ) as,

$$\tau_w = -\frac{H}{2}\frac{dP}{dx} \tag{8.5}$$

$$u_\tau = \sqrt{\frac{\tau_w}{\rho}} \tag{8.6}$$

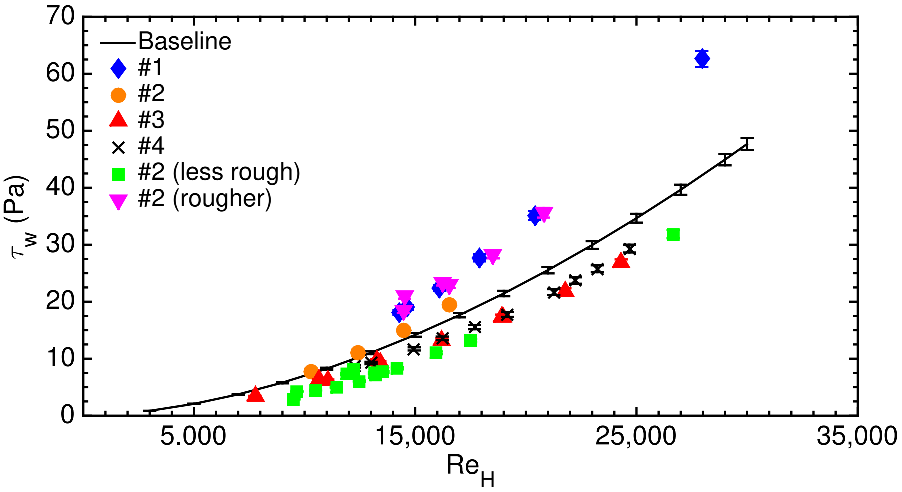

Figure 8.10: Average wall shear stress calculated from the streamwise pressure drop along the fully-developed turbulent channel with one baseline, hydraulically-smooth surface and one SHS. The reduction in shear stress was only observed for some of the SHSs.

The skin-friction coefficient is then given by,

$$C_f = \frac{\tau_w}{2\rho U_m^2}. \tag{8.7}$$

The factor of two in Eq. 8.4 arises as only one of the two channel walls is a SHS. This is equivalently the local skin-friction drag reduction on the SHS, whereas dP/dx is the average pressure drop along the channel with one SHS surface and one hydraulically-smooth surface. A similar scaling was observed by Daniello *et al.* using micro-fabricated, parallel ridges[226]. They observed $\approx 25\%$ drag reduction in their channel using one SHS and one smooth plate, and $\approx 50\%$ drag reduction in their channel using two SHSs. However, we note that the wall shear stresses measured here, for which drag reduction was still observed, are an order of magnitude greater than that of Daniello *et al.* (Fig. 8.10).

The friction on the two sidewalls was neglected due to their small areas and negligible influence on the mean flow properties at the center of the channel[247, 248]. Moreover, local wall shear stress along the top wall of the channel was derived from a simple control volume, constructed along the fully-developed, two-dimensional flow region in the center of the channel. A conservation of momentum analysis of this control volume indicated that shear on the side-walls was negligible. Lastly, although including the side-wall shear would provide a better idea of the overall frictional loss through the duct, this differs from the local shear along the SHS, and would not be pertinent for turbulence scaling arguments.

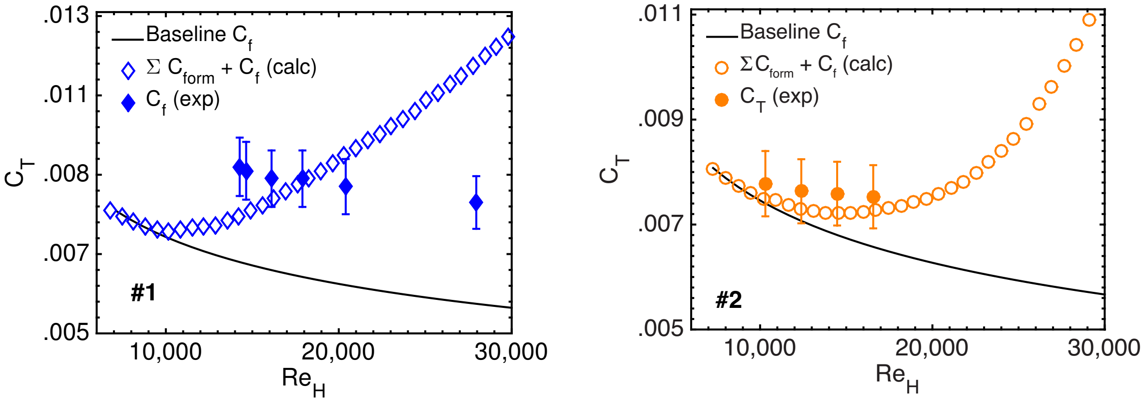

Figure 8.11: Experimental and calculated C_T values for surfaces #1 (left) and #2 (right). The calculated C_T includes the skin-friction expected for a hydraulically smooth flat plate as well as the total form drag due to any asperity roughness. The experimental C_T includes both asperity form drag and the skin-friction drag on the SHS. Therefore, these surfaces may still be producing skin-friction drag reduction locally, but the effect was mitigated by the overall increase in form drag.

8.3 Results and discussion

8.3.1 Friction coefficients

None of our SHSs were wetted following the high-$\mathrm{Re_H}$ flow testing, *i.e.* there was no loss of entrapped air. However, surfaces #1 and #2 increased the overall measured drag coefficient, C_T (Fig. 8.11),

$$C_T = \sum C_{form} + C_f \tag{8.8}$$

where C_{form} is the form drag on an individual texture element protruding into the flow, calculated using Eq. 8.2 as in Sec. 8.1.1. Thus, although the entrapped air pockets of surfaces #1 and #2 provided a shear-free interface, the overall wall shear was increased (Fig. 8.10).

On the other hand, surfaces #3 and #4 showed significant drag reduction, as high as 34% at a Reynolds number of $\mathrm{Re_H} = 19,000$ (Fig. 8.12). For surfaces #3 and #4, the wall shear was significantly lower than that experienced by a hydraulically smooth baseplate. Using our form drag calculations, these results were anticipated. The drag reduction was both sustainable over hours of continuous high-speed flow ($\mathrm{Re_H} \approx 30,000$), and repeatable even after months separating successive runs of the same SHS. To date, in fully-developed turbulence, *i.e.* where the necessary fluid-flow development length ($> 50H$) requires the fabrication of large surfaces, scalable SHSs capable of reducing drag had not been evaluated.

To demonstrate the effect of roughness-induced friction, we slightly modified the fabrication methodology of surface #2 (Fig. 8.5) to either increase or decrease the expected form drag. To increase asperity roughness, the total volume of sprayed solution was doubled. This surface is

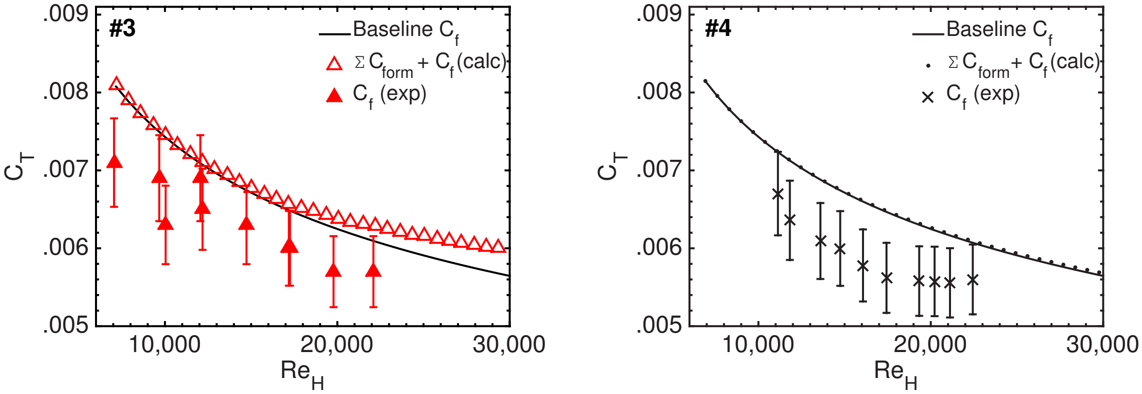

Figure 8.12: Experimental and calculated C_T values for surfaces #3 (left) and #4 (right). The calculated C_T includes the skin-friction expected for a hydraulically smooth flat plate as well as the total form drag due to any asperity roughness. The experimental C_T includes both asperity form drag and the skin-friction drag on the SHS. The local asperity roughness on these surfaces was low enough that significant drag reduction was observed.

denoted surface #2 (rougher). To decrease asperity roughness, the spray gun was replaced with an airbrush with a much finer nozzle[138], resulting in smaller texture elements, and is denoted surface #2 (less rough). All three variants of surface #2 displayed $\theta^* = 165 \pm 3°$ and $\Delta\theta^* < 2°$, at ambient pressure.

The resultant surfaces, with identical surface chemistry, but slightly different texture, were expected to produce drastically different form drag. When exposed to flow, the rougher variant of surface #2 increased the wall shear and form drag significantly (Figs. 8.10, 8.13). Conversely, the less rough variant of surface #2 produced large amounts of drag reduction. The drag savings measured in the channel were in excess of 60% at lower Reynolds number, and spanned 26% to 90% for the investigated Reynolds numbers ranging from 9,500 to 18,000 (decreased savings with increased speeds). Note that, in our channel flow, for $U_m = 1$ m/s, the mean pressure is $P_m \approx 600$ Pa. For $U_m = 5$ m/s, $P_m \approx 9,400$ Pa, highlighting how increasing Re can drastically alter the pressure exerted on the SHS. Regardless, it is clear that even before the surface was exposed to flow, calculating the form drag caused by wetted texture elements could be used to predict the drag-reducing efficacy of each SHS *a priori*.

The calculated C_T values combine the expected drag on a smooth plate[248] plus any additional form drag caused by the wetted roughness elements of the SHS. In contrast, the measured drag coefficients are the summation of any form drag due to surface roughness (C_{form}), plus the frictional drag on the mixed slip/no-slip boundary condition SHS. For SHSs, the latter term could be significantly less than the frictional drag experienced on a smooth, no-slip surface. In this case, our calculated drag coefficients (open symbols, Fig. 8.11-8.13) would be much higher than the measured drag coefficients, as was observed for surface #1 (Fig. 8.11a) and the rougher variant

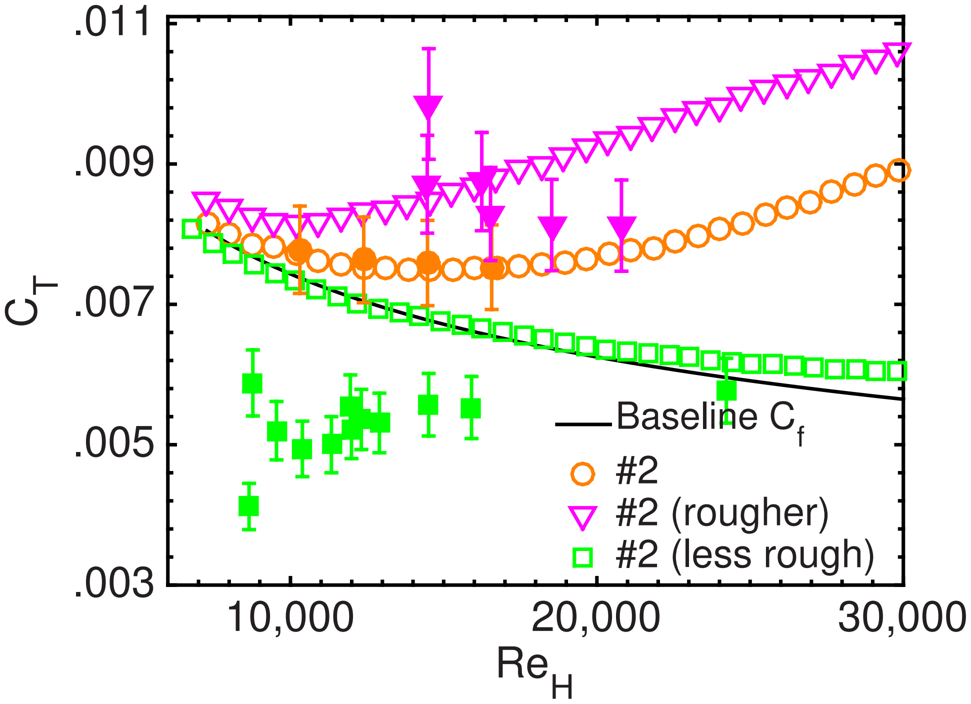

Figure 8.13: Three variations of surface #2, exhibiting either significant form drag, or significant drag reduction. Open symbols are the calculated C_T values and closed symbols are the experimental data. The baseline is for the unmodified surface #2.

of surface #2 (Fig. 8.13). Thus, deviation between measured and calculated *drag increase* most likely indicates surface slip (which decreases drag) that was mitigated by surface roughness (which increases drag). In fact, form drag due to large, sparse ($\phi_s \leq 0.2$) features has been shown to be the major component of total friction for certain texture geometries[241, 242, 243, 244]. When the form drag did not wash out the decrease in frictional drag due to slip, drag reduction was observed (Fig. 8.12,8.13).

8.3.2 Scaling laws

The effect of the roughness was further examined through the results of the mean velocity profile in the fully-developed channel flow (Fig. 8.14). The PIV analysis of the hydraulically-smooth, baseline channel is shown to be in good agreement with the mean velocity profiles from the direct numerical simulations (DNS) of Kim *et al.*[16]. However, significant deviation was observed when reviewing the results from the variations of surface #2. Specifically, the maximum flow speed, which is typically located along the centerline of a symmetric, fully-developed channel, shifted towards the hydraulically-smooth baseline surface ($y = 0$) as the roughness of the SHS

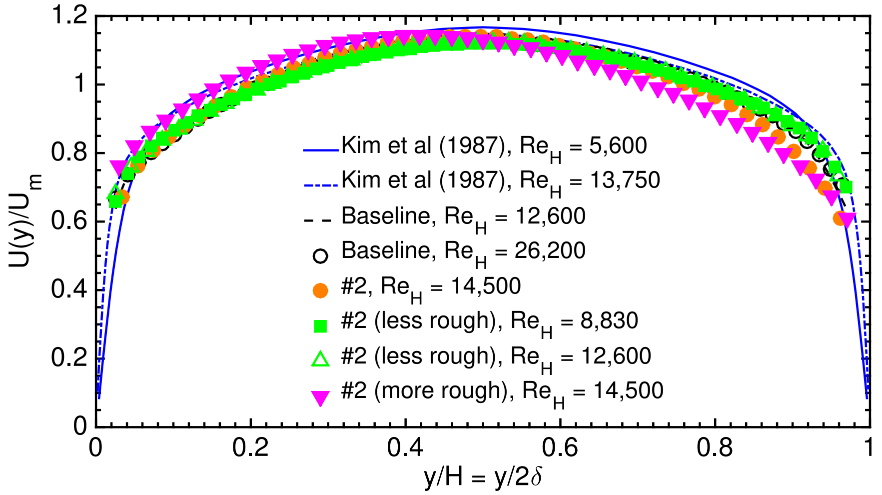

Figure 8.14: Velocity profiles measured over the baseline and the variations of SHS #2. Significant reduction in the velocity occurred in the presence of the roughness elements on the rougher surface variations. DNS data from Kim *et al.* (1987)[16] is included for reference purposes.

increased. From the streamwise conservation of mass and momentum, this necessarily dictated that the fluid speed decreased near the rough' wall, and consequently, the interaction with the roughness elements was increased. Ideally, if the roughness elements are small compared to the purely viscous sublayer, which is typically defined as five times the viscous length scale $\delta_\nu \equiv \nu/u_\tau$, no drag increase is expected. This was observed with the less rough variant of surface #2. However, if the roughness elements are large enough to extend beyond the viscous sublayer, roughness effects will become significant, as seen with surface #2 and its rougher variant.

Several researchers have attempted to limit the allowable root-mean-squared roughness, k, of SHSs that are capable of producing turbulent drag reduction. By non-dimensionalizing with the viscous length scale, δ_ν, values of $k^+ = k/\delta_\nu = 0.1$[232], 0.5[213] and 1.0[249] have been proposed as limits for providing drag reduction. In this work, we observed drag reduction as high as 8% when $k^+ = 0.95$, and a drag increase of 19% even when $k^+ = 0.11$ (Fig. 8.15).

We found that a surface's contact angle hysteresis, measured at higher pressure ($\Delta\theta^{HP}$), explained this unexpected observation (Figs. 8.6, 8.16a). Whereas the conventional measurement of $\Delta\theta^*$ always resulted in $\Delta\theta^* < 3°$ for all our surfaces (open symbols, Fig. 8.6), the higher pressure measurement varied drastically between surfaces that increased or decreased drag (closed symbols, Fig. 8.6). The product of k^+ and $\Delta\theta^{HP}$ collapsed all our drag measurements onto a single curve (Fig. 8.16). A similar collapse of the data was observed with the product of k^+ and the wetted solid surface area, $r_\phi\phi_s$. Note that these are empirical scaling laws, and products of other relevant quantities ($k, \theta^*, \theta^*_{adv}, \theta^*_{rec}, \phi_s$, etc.) did not produce a collapse of the measured drag reduction.

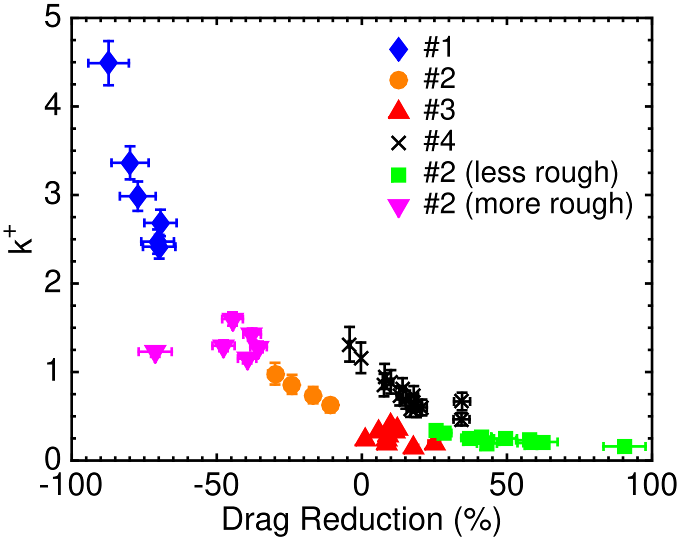

Figure 8.15: The drag reduction or increase (negative means drag increase) provided by all the surfaces considered in this work, as a function of the non-dimensional roughness, k^+. The drag associated with the smooth baseplate has been removed.

It is perhaps unsurprising that the measured drag reduction using SHSs was dependent on both wettability and flow characteristics. $\Delta\theta^{HP}$ gives some indication of the stability of a SHS's entrapped air pockets, but says nothing about how the flow will interact with these air pockets or the texture elements entrapping them. Conversely, k^+ designates if the roughness features will interact with the viscous sublayer, but gives no indication as to how much of the roughness the flow will see (*i.e.* where the meniscus will lie). For example, consider the nanograss evaluated in turbulent flow by Henoch *et al.*, which consisted of nano-posts with diameters of 400 nm and heights of 7 μm[229]. If the height of such posts was arbitrarily increased, k^+ would become extremely large. However, the flat meniscus pinned on the top of these posts ensures that the flow would be oblivious to this additional roughness. Moreover, in laminar flow, in which roughness effects are often negligible, minimizing $\Delta\theta^*$ has been shown previously to maximize drag reduction[250]. We extend this finding to turbulent flow, with two additional stipulations: the pressure, and the surface roughness, must also be considered. Thus, it is clear that to maximize friction drag reduction in turbulent flow, SHSs should be designed such that both k^+ and $\Delta\theta^{HP}$ are minimized. In this work we only observed a reduction in friction when $k^+\Delta\theta^{HP} \leq 5.5 \pm 0.3$.

As a final note, we emphasize that the drag increase caused by SHSs with large k^+ is somewhat unexpected. A surface is considered hydrodynamically smooth when $k^+ \leq 5.0$[111]. Only when $k^+ \geq 60$ is the surface considered fully rough[173]. A fully rough surface will exhibit a drag coefficient independent of Reynolds number. Quite remarkably, we observed such a trend for

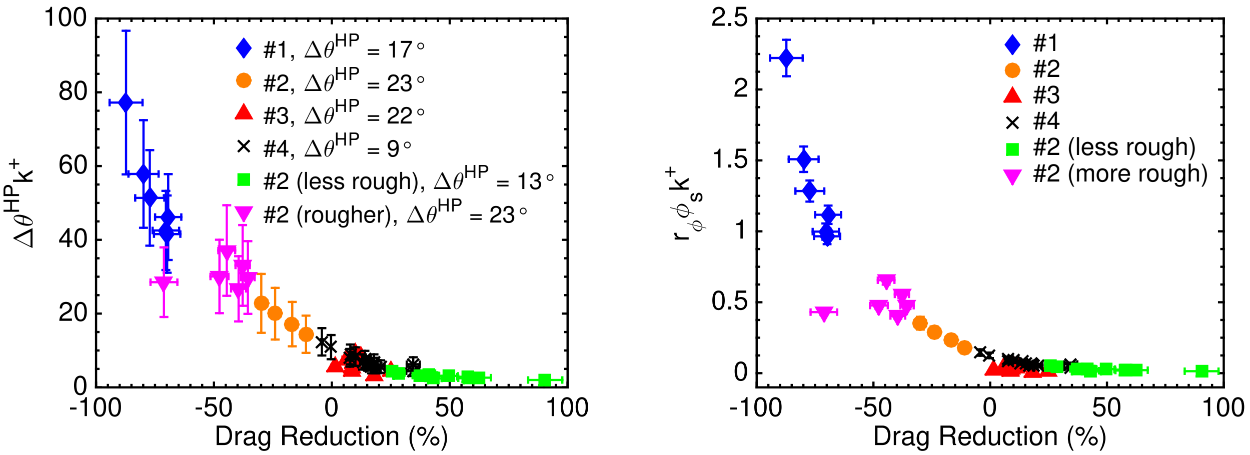

Figure 8.16: New scaling laws. The drag reduction data collapsed onto a single curve when plotted versus the product of the non-dimensional roughness, k^+, and the higher-pressure contact angle hysteresis, $\Delta\theta^{HP}$ (370 Pa for a 250 nL droplet) (left) or $r_\phi \phi_s$ (right).

surfaces #1, #2 and the rougher variant of surface #2, although for all Reynolds numbers tested, $k^+ \leq 4.5$. Some explanation can be found in the computational work of Jelly *et al.*[236]. They found that over 70% of the friction on the regions of no-slip (wetted solid surfaces, $r_\phi \phi_s$) was a direct result of the presence of the slip regions (air pockets, $1-\phi_s$). Thus, the deleterious roughness effects of SHSs with $k^+ \geq 1.0$ may be amplified by the entrapped air pockets. Moreover, as Min and Kim have computed[235], and Woolford *et al.* have experimentally confirmed[227], entrapped air pockets that produce spanwise slip unambiguously increase drag.

8.4 Conclusions

In closing, we have fabricated scalable, mechanically robust, superhydrophobic surfaces that significantly reduced skin-friction, by more than 50%, in high-speed turbulent flows such as those relevant to many naval applications. We did so by fabricating SHSs that minimize the product of the non-dimensional roughness, k^+, and the contact angle hysteresis measured at higher pressure. Only by considering both the wettability and the flow-dependent characteristics of a SHS can turbulent drag reduction be achieved. The conventional characterization techniques for SHSs are lacking, and will not predict if and when a surface can produce turbulent drag reduction. However, when designed correctly, the potential energy and fuel savings achievable with the surfaces described here could have a significant impact on the efficiency of marine vehicles and systems around the world.

CHAPTER 9

Summary and Future Outlook

The purpose of this dissertation was to understand and design surfaces that could repel both solid and liquid foulants. In the first half of this body of work, we discussed several new methods for reducing ice adhesion. We first looked at elastomeric coatings, and how crosslink density affects ice adhesion. We then investigated the surface property of interfacial slippage, and we derived a theoretical model to predict the ice adhesion of surfaces exhibiting interfacial slippage in Chapter 3. We discovered that even high modulus, linear polymers can be rendered icephobic through proper interfacial design. Chapter 4 investigated the ice adhesion of large surfaces, and we uncovered how interfacial toughness can lead to a brand-new type of low-ice-adhesion material.

Although we briefly discussed the repulsion of other solid foulants in Chapter 5, there is much work to still be done using the mechanisms uncovered in the first few chapters of this thesis. Bio-fouling remains a hugely prevalent problem today, and it's likely, but not proven, that the fundamentals delineated in this work can be applied to bio-foulants. Ice, for the most part, is a relatively simple solid adherent in terms of its mechanical properties and homogeneity. Bio-foulants come in all shapes and sizes, adding levels of complexity to an already complex problem. Ice adhesion can be chemically reduced by avoiding hydrogen bond formation, but some bio-foulants are hydrophobic, while others are hydrophilic. Ice adhesion can be physically reduced by allowing for interfacial cavitation through low crosslink density surfaces. Some bio-foulants are stiff like ice, but others are much softer. It is unclear if interfacial cavitation would be advantageous when the solid adherent is also compliant. Interfacial slippage may also fall prey to this complication.

Returning strictly to ice adhesion, the topic of interfacial toughness is still in its infancy. Whereas we showed in Chapter 4 that we could produce surfaces exhibiting low interfacial toughness, much work still remains to be done. Does some closed-form relation, like Eq. 3.9 from Chapter 3, exist for interfacial toughness? Moreover, are icephobic surfaces and low interfacial toughness surfaces forever divorced? We showed that a silicone rubber exhibiting interfacial slippage displayed ultra-low ice adhesion ($\tau_{ice} \approx 5$ kPa) in Fig. 4.5, but in order to achieve low Γ_{ice}, we found it necessary to raise the ice adhesion strength ten-fold. It would be highly desirable to fabricate surfaces exhibiting ultra-low τ_{ice} and Γ_{ice}, but thus far they have remained elusive.

In the second half of this work we discussed liquid repellency, using a number of new surfaces and fabrication techniques. First, in Chapter 5, we discussed PDMS-based monolayers that could repel essentially all solids and liquids through interfacial slippage. However, such monolayers exhibit relatively low contact angles with the probe liquids, and so in Chapter 6 we investigated a new method for fabricating transparent and superomniphobic surfaces. Although highly liquid-repellent, the main drawback of such surfaces is their poor mechanical durability. As such, in Chapter 7, we investigated how to spray extremely mechanically robust superhydrophobic surfaces from a wide range of binder and filler combinations. We designed some of our optimized surfaces to additionally be both chemically and physically self-healing, such that any loss in water repellency could be easily restored. Finally, in Chapter 8, we utilized some of our mechanically durable superhydrophobic surfaces to reduce the frictional drag experienced in turbulent flow. The entrapped air pockets within the porous textures enable interfacial slippage, and we uncovered new scaling laws to predict when the slippage would not be overshadowed by the roughness of the underlying surface.

Superomniphobic surfaces are only just starting to transition outside the laboratory. Whereas many interesting applications exist, such as the drag reduction discussed in Chapter 8, there are few reports of large-scale, successful implementations of these types of surfaces. The main detriment, as we pointed out in Chapter 7, is the mechanically fragile nature of their porous texture. However, now that we've exemplified a new way of fabricating mechanically robust liquid-repellent surfaces, it remains to be seen if these material systems can start finding real, commercial usage.

One additional issue with the textured surfaces discussed in the latter half of this thesis is that solid adhesion is still a concern, especially if the surfaces are only designed to repel liquids. We highlighted in the first few chapters how ice adhesion may not be reduced using superhydrophobic surfaces. Similarly, it's unclear if superhydrophobic drag reduction can still be achieved when solid adherents like barnacles and bio-films attach to the texture elements. If anything, the PDMS monolayers discussed in Chapter 5 show extreme promise because they do repel both solids and liquids simultaneously.

Many questions remain about these monolayers. For example, the capping process always lowered the thickness of the monolayers, regardless of their starting liquid repellency. Why? Whereas PDMS is ideal in terms of interfacial slippage, it is not amenable to surface characterization techniques like XPS. Discerning the exact nature of the monolayers has thus far proven untenable, but understanding exactly how the monolayers react, grow, and cap, will likely be key to their performance. Further, we were able to repeatedly produce surfaces displaying $\Delta\theta \approx 2^\circ$ with water, but never $\Delta\theta = 0^\circ$. Why not? Moreover, we found that liquids with lower surface tension than the critical surface tension of PDMS could be highly repelled, but the exact mechanism remains unclear.

Regardless of these uncertainties, the applications for these surfaces seem endless. One exciting idea is that perfluorinated compounds are no longer necessary to repel oils. Whereas perfluorination has always been assumed to be necessary for oleophobicity, this may not be the case. The contact angle of hexadecane on a perfluorinated monolayer is $< 90°$, and it's not certain what contact angle is necessary to achieve the oleophobic properties that perfluoro-compounds currently offer. Is $\theta_Y > 70°$ required? $\theta_Y > 50°$? Moreover, typical perfluorination processes do not yield perfect perfluorinated monolayers. It remains to be seen if non-fluorinated systems can meet the demands of liquid repellency in, for example, the textile industry.

Another interesting usage of omniphobic surfaces would be in the area of condensation and heat transfer. One parameter that has essentially always been overlook in this field is the contact angle hysteresis. If the droplets are continually shed from the wetted surface, the heat flux can perhaps be enhanced simply by providing more dry surface where liquid can continually condense. Omniphobicity will also come into play when dealing with low surface tension liquids like refrigerants. The effects of the interface on condensation and heat transfer have been extensively studied with water, but less so with low surface tension liquids. Here the low contact angles and contact angle hysteresis of the PDMS monolayers might prove highly efficacious.

Overall, the future of designer surfaces, such as the many examples explored in this thesis, is bright. Interfaces connect materials to all the engineering applications they are used in. Tailoring these interfaces to exhibit innovative properties represents the next paradigm shift in materials science. Bulk material properties have been studied and designed for hundreds of years. Interfacial properties, on the other hand, are perhaps in their adolescence. Whereas topics like corrosion, wetting, and increasing adhesion have a rich and thorough history, the topics discussed here are still relatively untapped. Chapter 4 presents fundamentals that fly in the face of ice adhesion theory accepted for the last seventy years. This highlights just how cutting-edge this field will be in the years to come.

REFERENCES

[1] Wenzel, R. N., "Resistance of solid surfaces to wetting by water," *Industrial & Engineering Chemistry*, Vol. 28, No. 8, 8 1936, pp. 988–994.

[2] Cassie, A. B. D. and Baxter, S., "Wettability of porous surfaces," *Transactions of the Faraday Society*, Vol. 40, No. 0, 1944, pp. 546.

[3] Kim, P., Wong, T. S., Alvarenga, J., Kreder, M. J., Adorno-Martinez, W. E., and Aizenberg, J., "Liquid-infused nanostructured surfaces with extreme anti-ice and anti-frost performance," *ACS Nano*, Vol. 6, No. 8, 2012, pp. 6569–6577.

[4] Takadoum, J., *Materials and surface engineering in tribology*, ISTE, 2008.

[5] Ciobanu, G., Carja, G., Apostolescu, G., and Apostolescu, N., "The physicochemical properties of polyurethane membranes determined by swelling measurements," *Proc. SPIE 7297, Advanced Topics in Optoelectronics, Microelectronics, and Nanotechnologies IV*, edited by P. Schiopu, C. Panait, G. Caruntu, and A. Manea, International Society for Optics and Photonics, Constanta, 1 2009, p. 72970I.

[6] Vorvolakos, K. and Chaudhury, M. K., "The Effects of Molecular Weight and Temperature on the Kinetic Friction of Silicone Rubbers," *Langmuir*, Vol. 19, No. 17, 2003, pp. 67786787.

[7] York, D., Evensen, N. M., Martnez, M. L., and De Basabe Delgado, J., "Unified equations for the slope, intercept, and standard errors of the best straight line," *American Journal of Physics*, Vol. 72, No. 3, 3 2004, pp. 367–375.

[8] Shin, J. and Bond, T. H., "Surface Roughness Due to Residual Ice in the Use of Low Power Deicing Systems," *31st Aerospace Sciences Meeting & Exhibit, Reno NV*, 1993.

[9] Cole, D. M., "ERDC/CRREL nominal mode I ice adhesion testing," Tech. rep., United States., Engineer Research and Development Center (U.S.), & Cold Regions Research and Engineering Laboratory (U.S.), 2014.

[10] Thouless, M. D., Evans, A. G., Ashby, M. F., and Hutchinson, J. W., "The edge cracking and spalling of brittle plates," *Acta Metallurgica*, Vol. 35, No. 6, 1987, pp. 1333–1341.

[11] Schulman, F. and Zisman, W. A., "The Spreading of Liquids on Low-Energy Surfaces. V. Perfluorodecanoic Acid Monolayers," *Journal of Colloid Science*, Vol. 7, No. 5, 1952, pp. 465–481.

[12] Glajch, J. L. and Kirkland, J. J., "Structures surface modified with bidentate silanes," 1986.

[13] Hertz, H., "On the Contact of Elastic Solids," *Journal für die reine und angewandte Mathematik*, Vol. 92, 1882, pp. 156–171.

[14] Lu, Y., Sathasivam, S., Song, J., Crick, C., Carmalt, C., and Parkin, I., "Robust Self-Cleaning Surfaces that Function when Exposed to Either Air or Oil," *Science*, Vol. 347, No. 6226, 2015, pp. 1132–1135.

[15] Golovin, K. B., Gose, J. W., Perlin, M., Ceccio, S. L., and Tuteja, A., "Bioinspired surfaces for turbulent drag reduction," *Philos. Trans. R. Soc., A*, Vol. 374, No. 2073, 2016.

[16] Kim, J., Moin, P., and Moser, R., "Turbulence statistics in fully developed channel flow at low Reynolds number," *Journal of Fluid Mechanics*, Vol. 177, 1987, pp. 133–166.

[17] Callister, W. D. and Rethwisch, D. G., *Materials science and engineering : an introduction*, Wiley, 8th ed., 2009.

[18] Jasper, J. J., "The Surface Tension of Pure Liquid Compounds," *Journal of Physical and Chemical Reference Data*, Vol. 1, No. 4, 10 1972, pp. 841–1010.

[19] Wong, T. S., Kang, S. H., Tang, S. K., Smythe, E. J., Hatton, B. D., Grinthal, A., and Aizenberg, J., "Bioinspired self-repairing slippery surfaces with pressure-stable omniphobicity," *Nature*, Vol. 477, No. 7365, 2011, pp. 443–447.

[20] Guenthner, A. J., Lamison, K. R., Lubin, L. M., Haddad, T. S., and Mabry, J. M., "Hansen Solubility Parameters for Octahedral Oligomeric Silsesquioxanes," *Industrial & Engineering Chemistry Research*, Vol. 51, No. 38, 2012, pp. 12282–12293.

[21] Mazza, P. P. A., Martini, F., Sala, B., Magi, M., Colombini, M. P., Giachi, G., Landucci, F., Lemorini, C., Modugno, F., and Ribechini, E., "A new Palaeolithic discovery: tar-hafted stone tools in a European Mid-Pleistocene bone-bearing bed," *Journal of Archaeological Science*, Vol. 33, No. 9, 2006, pp. 1310–1318.

[22] Emsley, J., "Very strong hydrogen bonding," *Chemical Society Reviews*, Vol. 9, No. 1, 1980, pp. 91.

[23] de Gennes, P. G., Brochard-Wyart, F., and Quere, D., *Capillarity and Wetting Phenomena: Drops, Bubbles, Pearls, Waves*, Springer, 2004.

[24] Zhang, Q., Qi, Y., Hector, L. G., Cagin, T., and Goddard, W. A., "Origin of static friction and its relationship to adhesion at the atomic scale," *Physical Review B*, Vol. 75, No. 14, 4 2007, pp. 144114.

[25] Young, T., "An Essay on the Cohesion of Fluids," *Philosophical Transactions of the Royal Society of London*, Vol. 95, No. 0, 1 1805, pp. 65–87.

[26] Tuteja, A., Choi, W., Ma, M. L., Mabry, J. M., Mazzella, S. A., Rutledge, G. C., McKinley, G. H., and Cohen, R. E., "Designing superoleophobic surfaces," *Science*, Vol. 318, 2007, pp. 1618–1622.

[27] Marmur, A., "Soft contact: measurement and interpretation of contact angles," *Soft Matter*, Vol. 2, No. 1, 2006, pp. 12–17.

[28] Drelich, J., "Guidelines to measurements of reproducible contact angles using a sessile-drop technique," *Surface Innovations*, Vol. 1, No. 4, 12 2013, pp. 248–254.

[29] Gao, L. and McCarthy, T. J., "Teflon is Hydrophilic. Comments on Definitions of Hydrophobic, Shear versus Tensile Hydrophobicity, and Wettability Characterization," *Langmuir*, Vol. 24, No. 17, 9 2008, pp. 9183–9188.

[30] Jennissen, H. P., "Hyperhydrophilic rough surfaces and imaginary contact angles," *Materialwissenschaft und Werkstofftechnik*, Vol. 43, No. 8, 8 2012, pp. 743–750.

[31] McHale, G., "Cassie and Wenzel: Were They Really So Wrong?" *Langmuir*, Vol. 23, No. 15, 2007, pp. 82008205.

[32] Bhushan, B. and Jung, Y. C., "Natural and biomimetic artificial surfaces for superhydrophobicity, self-cleaning, low adhesion, and drag reduction," *Prog. Mater. Sci.*, Vol. 56, No. 1, 2011, pp. 1–108.

[33] Bico, J., Thiele, U., and Quéré, D., "Wetting of textured surfaces," *Colloid Surface A*, Vol. 206, No. 13, 2002, pp. 41–46.

[34] Srinivasan, S., Choi, W., Park, K.-C., Chhatre, S. S., Cohen, R. E., and McKinley, G. H., "Drag reduction for viscous laminar flow on spray-coated non-wetting surfaces," *Soft Matter*, Vol. 9, No. 24, 2013, pp. 5691.

[35] Schellenberger, F., Encinas, N., Vollmer, D., and Butt, H.-J., "How Water Advances on Superhydrophobic Surfaces," *Physical Review Letters*, Vol. 116, No. 9, 2 2016, pp. 096101.

[36] Srinivasan, S., McKinley, G. H., and Cohen, R. E., "Assessing the Accuracy of Contact Angle Measurements for Sessile Drops on Liquid-Repellent Surfaces," *Langmuir*, Vol. 27, No. 22, 11 2011, pp. 13582–13589.

[37] Bartolo, D., Bouamrirene, F., Verneuil, ., Buguin, A., Silberzan, P., and Moulinet, S., "Bouncing or sticky droplets: Impalement transitions on superhydrophobic micropatterned surfaces," *Europhysics Letters (EPL)*, Vol. 74, No. 2, 4 2006, pp. 299–305.

[38] Kota, A. K., Choi, W., and Tuteja, A., "Superomniphobic surfaces: Design and durability," *MRS Bulletin*, Vol. 38, No. 05, 5 2013, pp. 383–390.

[39] Wang, L. and McCarthy, T. J., "Covalently Attached Liquids: Instant Omniphobic Surfaces with Unprecedented Repellency," *Angewandte Chemie International Edition*, Vol. 55, No. 1, 1 2016, pp. 244–248.

[40] Mockenhaupt, B., Ensikat, H.-J., Spaeth, M., and Barthlott, W., "Superhydrophobicity of Biological and Technical Surfaces under Moisture Condensation: Stability in Relation to Surface Structure," *Langmuir*, Vol. 24, No. 23, 12 2008, pp. 13591–13597.

[41] Tuteja, A., Choi, W., Mabry, J. M., McKinley, G. H., and Cohen, R. E., “Robust omniphobic surfaces,” *Proceedings of the National Academy of Sciences*, Vol. 105, No. 47, 11 2008, pp. 18200–18205.

[42] Kota, A. K., Li, Y., Mabry, J. M., and Tuteja, A., “Hierarchically Structured Superoleophobic Surfaces with Ultralow Contact Angle Hysteresis,” *Advanced Materials*, Vol. 24, No. 43, 11 2012, pp. 5838–5843.

[43] Kwon, G., Kota, A. K., Li, Y., Sohani, A., Mabry, J. M., and Tuteja, A., “On-Demand Separation of Oil-Water Mixtures,” *Advanced Materials*, Vol. 24, No. 27, 7 2012, pp. 3666–3671.

[44] Kota, A. K., Kwon, G., Choi, W., Mabry, J. M., and Tuteja, A., “Hygro responsive membranes for effective oil-water separation,” *Nat Commun*, Vol. 3, 2012, pp. 1025.

[45] Navier, C., “Memoire sur les lois du mouvement des fluides,” *Mem. Acad. R. Sci. Inst. France*, Vol. 6, 1823, pp. 389–440.

[46] Migler, K. B., Hervet, H., and Leger, L., “Slip transition of a polymer melt under shear stress,” *Physical Review Letters*, Vol. 70, No. 3, 1993, pp. 287–290.

[47] Ghatak, A., Vorvolakos, K., She, H., Malotky, D. L., and Chaudhury, M. K., “Interfacial Rate Processes in Adhesion and Friction,” *Journal of Physical Chemistry B*, Vol. 104, No. 17, 2000, pp. 40184030.

[48] Troian, S. M. and Thompson, P. A., “A general boundary condition for liquid flow at solid surfaces,” *Nature*, Vol. 389, No. 6649, 9 1997, pp. 360–362.

[49] Mäkiharju, S. A., Perlin, M., and Ceccio, S. L., “On the energy economics of air lubrication drag reduction,” *Int. J. Nav. Arch. Ocean.*, Vol. 4, No. 4, 2012.

[50] Chernyak, Y. B., “On the Theory of the Adhesive Friction of Elastomers,” *Wear*, Vol. 108, 1986, pp. 105–138.

[51] Chung, D. D. L., “Review Joints obtained by soldering, adhesion, autohesion and fastening, studied by electrical resistance measurement,” *Journal of Materials Science*, Vol. 36, No. 11, 2001, pp. 2591–2596.

[52] Newby, B.-m. Z., Chaudhury, M. K., and Brown, H. R., “Macroscopic Evidence of the Effect of Interfacial Slippage on Adhesion,” *Science*, Vol. 269, No. 5229, 1995.

[53] Stafslien, S. J., Sommer, S., Webster, D. C., Bodkhe, R., Pieper, R., Daniels, J., Vander Wal, L., Callow, M. C., Callow, J. A., Ralston, E., Swain, G., Brewer, L., Wendt, D., Dickinson, G. H., Lim, C.-S., and Teo, S. L.-M., “Comparison of laboratory and field testing performance evaluations of siloxane-polyurethane fouling-release marine coatings,” *Biofouling*, Vol. 32, No. 8, 9 2016, pp. 949–968.

[54] Golovin, K., Kobaku, S. P. R., Lee, D. H., DiLoreto, E. T., Mabry, J. M., and Tuteja, A., “Designing durable icephobic surfaces,” *Science Advances*, Vol. 2, No. 3, 2016.

[55] Sun, S., Li, M., and Liu, A., "A review on mechanical properties of pressure sensitive adhesives," *International Journal of Adhesion and Adhesives*, Vol. 41, 3 2013, pp. 98–106.

[56] Meuler, A. J., Smith, J. D., Varanasi, K. K., Mabry, J. M., McKinley, G. H., and Cohen, R. E., "Relationships between water wettability and ice adhesion," *ACS Appl Mater Interfaces*, Vol. 2, No. 11, 2010, pp. 3100–3110.

[57] Smith, J. D., Meuler, A. J., Bralower, H. L., Venkatesan, R., Subramanian, S., Cohen, R. E., McKinley, G. H., and Varanasi, K. K., "Hydrate-phobic surfaces: fundamental studies in clathrate hydrate adhesion reduction," *Physical Chemistry Chemical Physics*, Vol. 14, No. 17, 2012, pp. 6013.

[58] Yebra, D. M., Kiil, S., and Dam-Johansen, K., "Antifouling technologypast, present and future steps towards efficient and environmentally friendly antifouling coatings," *Progress in Organic Coatings*, Vol. 50, No. 2, 2004, pp. 75–104.

[59] Li, S., Thouless, M., Waas, A., Schroeder, J., and Zavattieri, P., "Use of a cohesive-zone model to analyze the fracture of a fiber-reinforced polymermatrix composite," *Composites Science and Technology*, Vol. 65, No. 3, 2005, pp. 537–549.

[60] Rickerby, D., "A review of the methods for the measurement of coating-substrate adhesion," *Surface and Coatings Technology*, Vol. 36, No. 1, 1988, pp. 541–557.

[61] Thouless, M. D., "Cracking and delamination of coatings," *Journal of Vacuum Science & Technology A: Vacuum, Surfaces, and Films*, Vol. 9, No. 4, 1991, pp. 2510–2515.

[62] Chaudhury, M. K. and Kim, K. H., "Shear-induced adhesive failure of a rigid slab in contact with a thin confined film," *Eur Phys J E Soft Matter*, Vol. 23, No. 2, 2007, pp. 175–183.

[63] Mulherin, N. D. and Haehnel, R. B., *Ice engineering : progress in evaluating surface coatings for icing control at Corps hydraulic structures*, U.S. Army Engineer Research and Development Center, Hanover, N.H., 2003.

[64] Baker, H., Bascom, W. D., and Singleterry, C., "The adhesion of ice to lubricated surfaces," *Journal of Colloid Science*, Vol. 17, No. 5, 1962, pp. 477–491.

[65] Jung, S., Dorrestijn, M., Raps, D., Das, A., Megaridis, C. M., and Poulikakos, D., "Are Superhydrophobic Surfaces Best for Icephobicity?" *Langmuir*, Vol. 27, No. 6, 2011.

[66] Varanasi, K. K., Deng, T., Smith, J. D., Hsu, M., and Bhate, N., "Frost formation and ice adhesion on superhydrophobic surfaces," *Applied Physics Letters*, Vol. 97, No. 23, 2010, pp. 234102.

[67] Subramanyam, S. B., Rykaczewski, K., and Varanasi, K. K., "Ice adhesion on lubricant-impregnated textured surfaces," *Langmuir*, Vol. 29, No. 44, 2013, pp. 13414–13418.

[68] Murase, H. and Nanishi, K., "On the Relationship of Thermodynamic and Physical Properties of Polymers with Ice Adhesion," *Annals of Glaciology*, Vol. 6, 1985, pp. 146–149.

[69] Wang, C., Fuller, T., Zhang, W., and Wynne, K. J., "Thickness dependence of ice removal stress for a polydimethylsiloxane nanocomposite: sylgard 184," *Langmuir*, Vol. 30, No. 43, 2014, pp. 12819–12826.

[70] Zhu, L., Xue, J., Wang, Y., Chen, Q., Ding, J., and Wang, Q., "Ice-phobic coatings based on silicon-oil-infused polydimethylsiloxane," *ACS Appl Mater Interfaces*, Vol. 5, No. 10, 2013, pp. 4053–4062.

[71] Rykaczewski, K., Anand, S., Subramanyam, S. B., and Varanasi, K. K., "Mechanism of Frost Formation on Lubricant-Impregnated Surfaces," *Langmuir*, Vol. 29, No. 17, 4 2013, pp. 5230–5238.

[72] Hejazi, V., Sobolev, K., and Nosonovsky, M., "From superhydrophobicity to icephobicity: forces and interaction analysis," *Sci Rep*, Vol. 3, 2013, pp. 2194.

[73] Chen, J., Liu, J., He, M., Li, K., Cui, D., Zhang, Q., Zeng, X., Zhang, Y., Wang, J., and Song, Y., "Superhydrophobic surfaces cannot reduce ice adhesion," *Applied Physics Letters*, Vol. 101, No. 11, 9 2012, pp. 111603.

[74] Arianpour, F., Farzaneh, M., and Kulinich, S., "Hydrophobic and ice-retarding properties of doped silicone rubber coatings," *Applied Surface Science*, Vol. 265, 2013, pp. 546–552.

[75] Dou, R., Chen, J., Zhang, Y., Wang, X., Cui, D., Song, Y., Jiang, L., and Wang, J., "Anti-icing coating with an aqueous lubricating layer," *ACS Appl Mater Interfaces*, Vol. 6, No. 10, 2014, pp. 6998–7003.

[76] Kulinich, S. A., Farhadi, S., Nose, K., and Du, X. W., "Superhydrophobic Surfaces: Are They Really Ice-Repellent?" *Langmuir*, Vol. 27, No. 1, 1 2011, pp. 25–29.

[77] Urata, C., Dunderdale, G. J., England, M. W., and Hozumi, A., "Self-lubricating organogels (SLUGs) with exceptional syneresis-induced anti-sticking properties against viscous emulsions and ices," *J. Mater. Chem. A*, Vol. 3, No. 24, 2015, pp. 12626–12630.

[78] Wang, Y., Yao, X., Chen, J., He, Z., Liu, J., Li, Q., Wang, J., and Jiang, L., "Organogel as durable anti-icing coatings," *Science China Materials*, Vol. 58, No. 7, 2015, pp. 559–565.

[79] Ghatak, A., L. Mahadevan, and Chaudhury, M. K., "Measuring the Work of Adhesion between a Soft Confined Film and a Flexible Plate," *Langmuir*, Vol. 21, No. 4, 2005, pp. 12771281.

[80] Palchesko, R. N., Zhang, L., Sun, Y., and Feinberg, A. W., "Development of polydimethylsiloxane substrates with tunable elastic modulus to study cell mechanobiology in muscle and nerve," *PLoS One*, Vol. 7, No. 12, 2012, pp. e51499.

[81] Lee, J. N., Park, C., and Whitesides, G. M., "Solvent compatibility of poly(dimethylsiloxane)-based microfluidic devices," *Analytical chemistry*, Vol. 75, No. 23, 2003, pp. 6544–6554.

[82] Chassé, W., Lang, M., Sommer, J.-U., and Saalwächter, K., "Cross-Link Density Estimation of PDMS Networks with Precise Consideration of Networks Defects," *Macromolecules*, Vol. 45, No. 2, 1 2012, pp. 899–912.

[83] ASTM, "D412 Standard Test Methods for Vulcanized Rubber and Thermoplastic Elastomers Tension," 2016.

[84] ASTM, "B117-16 Standard Practice for Operating Salt Spray (Fog) Apparatus," 2016.

[85] ASTM, "D3359 Standard Test Methods for Measuring Adhesion by Tape Test," 2016.

[86] Flory, P. J. and Rehner, J., "Statistical Theory of Chain Configuration and Physical Properties of High Polymers," *Annals New York Academy of Sciences*, Vol. 44, No. 4, 1943, pp. 419–429.

[87] Sombatsompop, N., "Practical use of the Mooney-Rilvin equation for determination of degree of crosslinking of swollen NR vulcanisates," *J. Sci. Soc. Thailand*, Vol. 24, 1998, pp. 199–204.

[88] Mark, J. E., *Polymer data handbook*, Oxford University Press, Oxford ; New York, 2nd ed., 2009.

[89] Galliano, A., Bistac, S., and Schultz, J., "Adhesion and friction of PDMS networks: molecular weight effects," *Journal of Colloid and Interface Science*, Vol. 265, No. 2, 2003, pp. 372–379.

[90] Chen, J., Dou, R., Cui, D., Zhang, Q., Zhang, Y., Xu, F., Zhou, X., Wang, J., Song, Y., and Jiang, L., "Robust prototypical anti-icing coatings with a self-lubricating liquid water layer between ice and substrate," *ACS Appl Mater Interfaces*, Vol. 5, No. 10, 2013, pp. 4026–4030.

[91] Aizenberg, J., Aizenberg, M., Cui, J., Hatton, B., Dunn, S., Howell, C., Kim, P., and Wong T S, "Slippery self-lubricating polymer surfaces," 2014.

[92] Parent, O. and Ilinca, A., "Anti-icing and de-icing techniques for wind turbines: Critical review," *Cold Regions Science and Technology*, Vol. 65, No. 1, 2011, pp. 88–96.

[93] Burton, T., Jenkins, N., Sharpe, D., and Bossanyi, E., *Wind Energy Handbook*, John Wiley & Sons, Ltd, Chichester, UK, 5 2011.

[94] Kraus, G., "Swelling of Filler-Reinforced Vulcanizates," *J App Poly Sci*, Vol. 7, 1963, pp. 861–871.

[95] Krawczyk, J., Croce, S., McLeish, T. C. B., and Chakrabarti, B., "Elasticity Dominated Surface Segregation of Small Molecules in Polymer Mixtures," *Physical Review Letters*, Vol. 116, No. 20, 2016.

[96] Hansen, C. M., *Hansen solubility parameters : a user's handbook*, CRC Press, Boca Raton, 2nd ed., 2007.

[97] Wypych, G., *Handbook of Plasticizers*, ChemTec Publishing, Totonto, 2nd ed., 2012.

[98] Kreder, M. J., Alvarenga, J., Kim, P., and Aizenberg, J., "Design of anti-icing surfaces: smooth, textured or slippery?" *Nature Reviews Materials*, Vol. 1, 2016, pp. 15003.

[99] Severin, J. W., Hokke, R., and de With, G., "Adhesion of electrolessly deposited Ni(P) layers on alumina ceramic. I. Mechanical properties," *Journal of Applied Physics*, Vol. 75, No. 7, 1994, pp. 3402–3413.

[100] Menini, R. and Farzaneh, M., "Advanced Icephobic Coatings," *Journal of Adhesion Science and Technology*, Vol. 25, No. 9, 2011, pp. 971–992.

[101] Ryerson, C. C., "Ice protection of offshore platforms," *Cold Regions Science and Technology*, Vol. 65, No. 1, 2011, pp. 97–110.

[102] United States. Army. Corps of Engineers., *Engineering and design : ice engineering*, U.S. Army Corps of Engineers, Washington, D.C., 2002.

[103] Raraty, L. E. and Tabor, D., "The Adhesion and Strength Properties of Ice," *Proceedings of the Royal Society of London A: Mathematical, Physical and Engineering Sciences*, Vol. 245, No. 1241, 1958.

[104] Beemer, D. L., Wang, W., and Kota, A. K., "Durable gels with ultra-low adhesion to ice," *J. Mater. Chem. A*, Vol. 1, 2016, pp. 15003.

[105] Thouless, M. D., "Fracture mechanics for thin-film adhesion," *IBM Journal of Research and Development*, Vol. 38, No. 4, 7 1994, pp. 367–377.

[106] Thouless, M. and Yang, Q., "Chapter 7 Measurement and analysis of the fracture properties of adhesive joints," *Adhesion Science and Engineering*, chap. 7, Elsevier, 2002, pp. 235–271.

[107] Parmigiani, J. and Thouless, M., "The effects of cohesive strength and toughness on mixed-mode delamination of beam-like geometries," *Engineering Fracture Mechanics*, Vol. 74, No. 17, 2007, pp. 2675–2699.

[108] Sills, R. and Thouless, M., "The effect of cohesive-law parameters on mixed-mode fracture," *Engineering Fracture Mechanics*, Vol. 109, 2013, pp. 353–368.

[109] Sills, R. B. and Thouless, M. D., "Cohesive-length scales for damage and toughening mechanisms," *International Journal of Solids and Structures*, Vol. 55, 2015, pp. 32–43.

[110] Hibbeler, R. C., *Engineering mechanics–statics*, Macmillan, New York, 3rd ed., 1983.

[111] Schlichting, H. and Gersten, K., *Boundary-Layer Theory*, Springer, Berlin, Heidelberg, 2017.

[112] Boeing Commercial, A., *Boeing 747 passenger airplane*, Commercial Airplane Division, Everett Branch, Boeing Co., Renton, Wash., 1969.

[113] Yang, Q., Thouless, M., and Ward, S., "Numerical simulations of adhesively-bonded beams failing with extensive plastic deformation," *Journal of the Mechanics and Physics of Solids*, Vol. 47, No. 6, 1999, pp. 1337–1353.

[114] Bažant, Z. P. and Cedolin, L., *Stability of Structures*, World Scientific, 8 2010.

[115] Kafkalidis, M. and Thouless, M., "The effects of geometry and material properties on the fracture of single lap-shear joints," *International Journal of Solids and Structures*, Vol. 39, No. 17, 2002, pp. 4367–4383.

[116] Hu, M. S., Thouless, M. D., and Evans, A. G., "The decohesion of thin films from brittle substrates," *Acta Metallurgica*, Vol. 36, No. 5, 1988, pp. 1301–1307.

[117] Witte, R. S. and Witte, J. S., *Statistics*, J. Wiley & Sons, 2010.

[118] Andrews, E. H. and Lockington, N. A., "The cohesive and adhesive strength of ice," *Journal of Materials Science*, Vol. 18, No. 5, 5 1983, pp. 1455–1465.

[119] Andrews, E. H., Majid, H. A., and Lockington, N. A., "Adhesion of ice to a flexible substrate," *Journal of Materials Science*, Vol. 19, No. 1, 1984, pp. 73–81.

[120] Terzis, A., Pervier, M.-L., and Hammond, D. W., "Temperature Effect on Fracture Toughness of Atmospheric Ice Accreted on a Typical Fan Blade Material," *20th International Society for Air Breathing Engines*, Gothenburg, Sweden, 2011.

[121] Nixon, W. A. and Schulson, E. M., "The Fracture Toughness of Ice Over a Range of Grain Sizes," *Journal of Offshore Mechanics and Arctic Engineering*, Vol. 110, No. 2, 1988, pp. 192–196.

[122] Matbou Riahi, M., Marceau, D., Laforte, C., and Perron, J., "The experimental/numerical study to predict mechanical behaviour at the ice/aluminium interface," *Cold Regions Science and Technology*, Vol. 65, No. 2, 2011, pp. 191–202.

[123] Schultz, M. P., Walker, J. M., Steppe, C. N., and Flack, K. A., "Impact of diatomaceous biofilms on the frictional drag of fouling-release coatings," *Biofouling*, Vol. 31, No. 9-10, 2015, pp. 759–773.

[124] Watts, A. and Addy, M., "Tooth discolouration and staining: Tooth discolouration and staining: a review of the literature," *British Dental Journal*, Vol. 190, No. 6, 3 2001, pp. 309–316.

[125] ASTM, "D6540 - 12: Standard Test Method for Accelerated Soiling of Pile Yarn Floor Covering 1," 2012.

[126] McHale, G., Newton, M. I., and Shirtcliffe, N. J., "Immersed Superhydrophobic Surfaces: Gas Exchange, Slip and Drag Reduction Properties," *Soft Matter*, Vol. 6, No. 4, 2010, pp. 714.

[127] Genzer, J. and Efimenko, K., "Recent Developments in Superhydrophobic Surfaces and Their Relevance to Marine Fouling: A Review," *Biofouling*, Vol. 22, No. 5, 2006, pp. 339–360.

[128] Rykaczewski, K., Osborn, W. A., Chinn, J., Walker, M. L., Scott, J. H. J., Jones, W., Hao, C., Yao, S., and Wang, Z., "How Nanorough is Rough Enough to Make a Surface Superhydrophobic During Water Condensation?" *Soft Matter*, Vol. 8, No. 33, 2012, pp. 8786.

[129] Shen, L., Qiu, W., Liu, B., and Guo, Q., "Stable Superhydrophobic Surface Based on Silicone Combustion Product," *RSC Advances*, Vol. 4, No. 99, 2014, pp. 56259–56262.

[130] Deng, X., Mammen, L., Butt, H.-J., and Vollmer, D., "Candle Soot as a Template for a Transparent Robust Superamphiphobic Coating," *Science*, Vol. 335, No. 6064, 1 2012, pp. 67–70.

[131] Chu, Z. and Seeger, S., "Superamphiphobic surfaces," *Chemical Society Reviews*, Vol. 43, No. 8, 2014, pp. 2784.

[132] Brown, P. S. and Bhushan, B., "Durable, superoleophobic polymernanoparticle composite surfaces with re-entrant geometry via solvent-induced phase transformation," *Scientific Reports*, Vol. 6, 2 2016, pp. 21048.

[133] Barthwal, S., Kim, Y. S., and Lim, S. H., "Mechanically Robust Superamphiphobic Aluminum Surface with Nanopore-Embedded Microtexture," *Langmuir*, Vol. 29, No. 38, 2013, pp. 11966–11974.

[134] Mabry, J., Vij, A., Iacono, S., and Viers, B., "Fluorinated Polyhedral Oligomeric Silsesquioxanes (F-POSS)," *Angewandte Chemie*, Vol. 120, No. 22, 5 2008, pp. 4205–4208.

[135] Rykaczewski, K., Paxson, A. T., Staymates, M., Walker, M. L., Sun, X., Anand, S., Srinivasan, S., McKinley, G. H., Chinn, J., Scott, J. H. J., and Varanasi, K. K., "Dropwise Condensation of Low Surface Tension Fluids on Omniphobic Surfaces," *Scientific Reports*, Vol. 4, 3 2014, pp. 661–667.

[136] Meuler, A. J., Chhatre, S. S., Nieves, A. R., Mabry, J. M., Cohen, R. E., and McKinley, G. H., "Examination of wettability and surface energy in fluorodecyl POSS/polymer blends," *Soft Matter*, Vol. 7, No. 21, 2011, pp. 10122.

[137] Pan, S., Kota, A. K., Mabry, J. M., and Tuteja, A., "Superomniphobic Surfaces for Effective Chemical Shielding," *Journal of the American Chemical Society*, Vol. 135, No. 2, 1 2013, pp. 578–581.

[138] Golovin, K., Lee, D. H., Mabry, J. M., and Tuteja, A., "Transparent, Flexible, Superomniphobic Surfaces with Ultra-Low Contact Angle Hysteresis," *Angew. Chem.*, Vol. 52, No. 49, 2013, pp. 13007–13011.

[139] Irajizad, P., Hasnain, M., Farokhnia, N., Sajadi, S. M., and Ghasemi, H., "Magnetic slippery extreme icephobic surfaces," *Nature Communications*, Vol. 7, 11 2016, pp. 13395.

[140] Kendall, K., "The adhesion and surface energy of elastic solids," *Journal of Physics D: Applied Physics*, Vol. 4, No. 8, 8 1971, pp. 320.

[141] Chen, B., Qiu, J., Sakai, E., Kanazawa, N., Liang, R., and Feng, H., "Robust and Superhydrophobic Surface Modification by a "Paint + Adhesive" Method: Applications in Self-Cleaning after Oil Contamination and Oil-Water Separation," *ACS Applied Materials & Interfaces*, Vol. 8, No. 27, 2016, pp. 17659–17667.

[142] Chernyy, S., Järn, M., Shimizu, K., Swerin, A., Pedersen, S. U., Daasbjerg, K., Makkonen, L., Claesson, P., and Iruthayaraj, J., "Superhydrophilic Polyelectrolyte Brush Layers with Imparted Anti-Icing Properties: Effect of Counter ions," *ACS Applied Materials & Interfaces*, Vol. 6, No. 9, 5 2014, pp. 6487–6496.

[143] Ozbay, S., Yuceel, C., and Erbil, H. Y., "Improved Icephobic Properties on Surfaces with a Hydrophilic Lubricating Liquid," *ACS Applied Materials & Interfaces*, Vol. 7, No. 39, 10 2015, pp. 22067–22077.

[144] Gao, L. and McCarthy, T. J., "A Perfectly Hydrophobic Surface (θA/θR = 180°/180°)," *Journal of the American Chemical Society*, Vol. 128, No. 28, 2006, pp. 90529053.

[145] Tuteja, A., Choi, W., McKinley, G. H., Cohen, R. E., and Rubner, M. F., "Design Parameters for Superhydrophobicity and Superoleophobicity," *MRS Bulletin*, Vol. 33, No. 8, 2008, pp. 752.

[146] Verho, T., Bower, C., Andrew, P., Franssila, S., Ikkala, O., and Ras, R. H., "Mechanically Durable Superhydrophobic Surfaces," *Advanced Materials*, Vol. 23, No. 5, 2011, pp. 673–678.

[147] Bixler, G. D. and Bhushan, B., "Bioinspired micro/nanostructured surfaces for oil drag reduction in closed channel flow," *Soft Matter*, Vol. 9, No. 5, 2013, pp. 1620–1635.

[148] Chen, X., Weibel, J. A., and Garimella, S. V., "Water and Ethanol Droplet Wetting Transition during Evaporation on Omniphobic Surfaces," *Scientific Reports*, Vol. 5, 11 2015, pp. 17110.

[149] Nosonovsky, M. and Hejazi, V., "Why Superhydrophobic Surfaces Are Not Always Icephobic," *ACS Nano*, Vol. 6, No. 10, 10 2012, pp. 8488–8491.

[150] Gao, L. and McCarthy, T. J., "Wetting 101°," *Langmuir*, Vol. 25, No. 24, 12 2009, pp. 14105–14115.

[151] Whitehouse, D. J., *Surfaces and their Measurement*, Butterworth-Heinemann, Jordan Hill, GBR, 2002.

[152] Zisman, W. A., "Relation of the Equilibrium Contact Angle to Liquid and Solid Constitution," *Contact Angle, Wettability, and Adhesion*, chap. 1, American Chemical Society, 1 1964, pp. 1–51.

[153] Cheng, D. F., Urata, C., Yagihashi, M., and Hozumi, A., "A Statically Oleophilic but Dynamically Oleophobic Smooth Nonperfluorinated Surface," *Angewandte Chemie International Edition*, Vol. 51, No. 12, 3 2012, pp. 2956–2959.

[154] Fadeev, A. Y. and McCarthy, T. J., “Trialkylsilane Monolayers Covalently Attached to Silicon Surfaces: Wettability Studies Indicating that Molecular Topography Contributes to Contact Angle Hysteresis,” *Langmuir*, Vol. 15, No. 11, 1999, pp. 37593766.

[155] Liu, T. . and Kim, C.-J. ., “Turning a surface superrepellent even to completely wetting liquids,” *Science*, Vol. 346, No. 6213, 2014.

[156] Ostwald, W., “Ueber die rechnerische Darstellung des Strukturgebietes der Viskosität,” *Kolloid-Zeitschrift*, Vol. 47, No. 2, 2 1929, pp. 176–187.

[157] Hadjistamov, D., “Determination of the onset of shear thinning of polydimethylsiloxane,” *Journal of Applied Polymer Science*, Vol. 108, No. 4, 5 2008, pp. 2356–2364.

[158] Podgorski, T., Flesselles, J.-M., and Limat, L., “Corners, Cusps, and Pearls in Running Drops,” *Physical Review Letters*, Vol. 87, No. 3, 6 2001, pp. 036102.

[159] Choi, W., Tuteja, A., Chhatre, S., Mabry, J. M., Cohen, R. E., and McKinley, G. H., “Fabrics with Tunable Oleophobicity,” *Advanced Materials*, Vol. 21, No. 21, 6 2009, pp. 2190–2195.

[160] Jin, H., Kettunen, M., Laiho, A., Pynnonen, H., Paltakari, J., Marmur, A., Ikkala, O., and Ras, R. H. A., “Superhydrophobic and Superoleophobic Nanocellulose Aerogel Membranes as Bioinspired Cargo Carriers on Water and Oil,” *Langmuir*, Vol. 27, No. 5, 3 2011, pp. 1930–1934.

[161] Ahuja, A., Taylor, J. A., Lifton, V., Sidorenko, A. A., Salamon, T. R., Lobaton, E. J., Kolodner, P., and Krupenkin, T. N., “Nanonails: A Simple Geometrical Approach to Electrically Tunable Superlyophobic Surfaces,” *Langmuir*, Vol. 24, No. 1, 1 2008, pp. 9–14.

[162] Marmur, A., “From Hygrophilic to Superhygrophobic: Theoretical Conditions for Making High-Contact-Angle Surfaces from Low-Contact-Angle Materials,” *Langmuir*, Vol. 24, No. 14, 7 2008, pp. 7573–7579.

[163] Cao, L., Price, T. P., Weiss, M., and Gao, D., “Super Water- and Oil-Repellent Surfaces on Intrinsically Hydrophilic and Oleophilic Porous Silicon Films,” *Langmuir*, Vol. 24, No. 5, 3 2008, pp. 1640–1643.

[164] Kobaku, S. P., Kota, A. K., Lee, D. H., Mabry, J. M., and Tuteja, A., “Patterned Superomniphobic-Superomniphilic Surfaces: Templates for Site-Selective Self-Assembly,” *Angewandte Chemie International Edition*, Vol. 51, No. 40, 2012, pp. 10109–10113.

[165] Yang, J., Zhang, Z., Xu, X., Men, X., Zhu, X., and Zhou, X., “Superoleophobic textured aluminum surfaces,” *New Journal of Chemistry*, Vol. 35, No. 11, 2011, pp. 2422.

[166] Nhung Nguyen, T. P., Brunet, P., Coffinier, Y., and Boukherroub, R., “Quantitative Testing of Robustness on Superomniphobic Surfaces by Drop Impact,” *Langmuir*, Vol. 26, No. 23, 12 2010, pp. 18369–18373.

[167] Xue, C.-H., Zhang, P., Ma, J.-Z., Ji, P.-T., Li, Y.-R., and Jia, S.-T., “Long-lived superhydrophobic colorful surfaces,” *Chemical Communications*, Vol. 49, No. 34, 2013, pp. 3588.

[168] Chhatre, S. S., Tuteja, A., Choi, W., Revaux, A., Smith, D., Mabry, J. M., McKinley, G. H., and Cohen, R. E., "Thermal Annealing Treatment to Achieve Switchable and Reversible Oleophobicity on Fabrics," *Langmuir*, Vol. 25, No. 23, 12 2009, pp. 13625–13632.

[169] Kang, S. M., Kim, S. M., Kim, H. N., Kwak, M. K., Tahk, D. H., and Suh, K. Y., "Robust superomniphobic surfaces with mushroom-like micropillar arrays," *Soft Matter*, Vol. 8, No. 33, 2012, pp. 8563.

[170] Lee, S. E., Kim, H.-J., Lee, S.-H., and Choi, D.-G., "Superamphiphobic Surface by Nanotransfer Molding and Isotropic Etching," *Langmuir*, Vol. 29, No. 25, 6 2013, pp. 8070–8075.

[171] Zhang, J. and Seeger, S., "Superoleophobe Silicon-Beschichtungen mit ultrakleinen Abrollwinkeln," *Angewandte Chemie*, Vol. 123, No. 29, 7 2011, pp. 6782–6786.

[172] Herminghaus, S., "Roughness-induced non-wetting," *Europhysics Letters (EPL)*, Vol. 52, No. 2, 10 2000, pp. 165–170.

[173] White, F. M., *Viscous fluid flow*, McGraw-Hill Higher Education, New York, NY, 3rd ed., 2006.

[174] Liu, Y., Liu, Z., Liu, Y., Hu, H., Li, Y., Yan, P., Yu, B., and Zhou, F., "One-Step Modification of Fabrics with Bioinspired Polydopamine@Octadecylamine Nanocapsules for Robust and Healable Self-Cleaning Performance," *Small*, Vol. 11, No. 4, 2014, pp. 426–431.

[175] Im, M., Im, H., Lee, J.-H., Yoon, J.-B., and Choi, Y.-K., "A Robust Superhydrophobic and Superoleophobic Surface with Inverse-Trapezoidal Microstructures on a Large Transparent Flexible Substrate," *Soft Matter*, Vol. 6, No. 7, 2010, pp. 1401.

[176] Maitra, T., Antonini, C., Auf der Mauer, M., Stamatopoulos, C., Tiwari, M. K., and Poulikakos, D., "Hierarchically Nanotextured Surfaces Maintaining Superhydrophobicity Under Severely Adverse Conditions," *Nanoscale*, Vol. 6, No. 15, 2014, pp. 8710–8719.

[177] Wang, F., Yu, S., Ou, J., Xue, M., and Li, W., "Mechanically Durable Superhydrophobic Surfaces Prepared by Abrading," *Journal of Applied Physics*, Vol. 114, No. 12, 2013, pp. 124902.

[178] Wu, L., Zhang, J., Li, B., Fan, L., Li, L., and Wang, A., "Facile Preparation of Super Durable Superhydrophobic Materials," *Journal of Colloid and Interface Science*, Vol. 432, 2014, pp. 31–42.

[179] Zhu, X., Zhang, Z., Men, X., Yang, J., Wang, K., Xu, X., Zhou, X., and Xue, Q., "Robust Superhydrophobic Surfaces with Mechanical Durability and Easy Repairability," *Journal of Materials Chemistry*, Vol. 21, No. 39, 2011, pp. 15793.

[180] Tian, X., Verho, T., and Ras, R. H., "Moving Superhydrophobic Surfaces Toward Real-World Applications," *Science*, Vol. 352, No. 6282, 2016, pp. 142–143.

[181] Jiang, W., Liu, H., Wang, L., Zhu, S., Yin, L., Shi, Y., Chen, B., Ding, Y., and An, N., "An Effective Route for Transparent and Superhydrophobic Coating with High Mechanical Stability," *Thin Solid Films*, Vol. 562, 2014, pp. 383–388.

[182] Zhang, Y., Ge, D., and Yang, S., "Spray-Coating of Superhydrophobic Aluminum Alloys with Enhanced Mechanical Robustness," *Journal of Colloid and Interface Science*, Vol. 423, 2014, pp. 101–107.

[183] Tolga, A., John, T. S., Andrew, R. L., Rosa, M. T., Gerald, E. J., Ilia, N. I., Stephen, J. P., Daniel, A. H., Kyle, O. W., David, K. C., Scott, R. H., and Haynes, J. A., "Optically Transparent, Mechanically Durable, Nanostructured Superhydrophobic Surfaces Enabled by Spinodally Phase-Separated Glass Thin Films," *Nanotechnology*, Vol. 24, No. 31, 2013, pp. 315602.

[184] Li, Y., Chen, S., Wu, M., and Sun, J., "All Spraying Processes for the Fabrication of Robust, Self-Healing, Superhydrophobic Coatings," *Advanced Materials*, Vol. 26, No. 20, 2014, pp. 3344–3348.

[185] Wang, H., Xue, Y., Ding, J., Feng, L., Wang, X., and Lin, T., "Durable, Self-Healing Superhydrophobic and Superoleophobic Surfaces From Fluorinated-Decyl Polyhedral Oligomeric Silsesquioxane and Hydrolyzed Fluorinated Alkyl Silane," *Angewandte Chemie International Edition*, Vol. 50, No. 48, 2011, pp. 11433–11436.

[186] Chen, L., Sun, X., Hang, J., Jin, L., Shang, D., and Shi, L., "Large-Scale Fabrication of Robust Superhydrophobic Coatings with High Rigidity and Good Flexibility," *Advanced Materials Interfaces*, Vol. 3, No. 6, 2016, pp. 1500718.

[187] Infante, D., Koch, K. W., Mazumder, P., Tian, L., Carrilero, A., Tulli, D., Baker, D., and Pruneri, V., "Durable, Superhydrophobic, Antireflection, and Low Haze Glass Surfaces Using Scalable Metal Dewetting Nanostructuring," *Nano Research*, Vol. 6, No. 6, 2013, pp. 429–440.

[188] Li, J.-H., Weng, R., Di, X.-Q., and Yao, Z.-W., "Gradient and Weather Resistant Hybrid Super-Hydrophobic Coating Based on Fluorinated Epoxy Resin," *Journal of Applied Polymer Science*, Vol. 131, No. 20, 2014, pp. 40955–40962.

[189] Lee, E. J., Kim, J. J., and Cho, S. O., "Fabrication of Porous Hierarchical Polymer/Ceramic Composites by Electron Irradiation of Organic/Inorganic Polymers: Route to a Highly Durable, Large-Area Superhydrophobic Coating," *Langmuir*, Vol. 26, No. 5, 2010, pp. 3024–3030.

[190] Su, F. and Yao, K., "Facile Fabrication of Superhydrophobic Surface with Excellent Mechanical Abrasion and Corrosion Resistance on Copper Substrate by a Novel Method," *ACS Applied Materials & Interfaces*, Vol. 6, No. 11, 2014, pp. 8762–8770.

[191] Yin, L., Yang, J., Tang, Y., Chen, L., Liu, C., Tang, H., and Li, C., "Mechanical Durability of Superhydrophobic and Oleophobic Copper Meshes," *Applied Surface Science*, Vol. 316, 2014, pp. 259–263.

[192] Dyett, B. P., Wu, A. H., and Lamb, R. N., "Mechanical Stability of Surface Architecture-Consequences for Superhydrophobicity," *ACS Applied Materials & Interfaces*, Vol. 6, No. 21, 2014, pp. 18380–18394.

[193] Esteves, A. C. C., Luo, Y., van de Put, M. W. P., Carcouët, C. C. M., and de With, G., "Self-Replenishing Dual Structured Superhydrophobic Coatings Prepared by Drop-Casting of an All-In-One Dispersion," *Advanced Functional Materials*, Vol. 24, No. 7, 2014, pp. 986–992.

[194] Ma, J., Zhang, X. Y., Wang, D. P., Zhao, D. Q., Ding, D. W., Liu, K., and Wang, W. H., "Superhydrophobic Metallic Glass Surface with Superior Mechanical Stability and Corrosion Resistance," *Applied Physics Letters*, Vol. 104, No. 17, 2014, pp. 173701.

[195] Nine, M. J., Cole, M. A., Johnson, L., Tran, D. N., and Losic, D., "Robust Superhydrophobic Graphene-Based Composite Coatings with Self-Cleaning and Corrosion Barrier Properties," *ACS Applied Materials & Interfaces*, Vol. 7, No. 51, 2015, pp. 28482–28493.

[196] Wong, W. S., Stachurski, Z. H., Nisbet, D. R., and Tricoli, A., "Ultra-Durable and Transparent Self-Cleaning Surfaces by Large-Scale Self-Assembly of Hierarchical Interpenetrated Polymer Networks," *ACS Applied Materials & Interfaces*, Vol. 8, No. 21, 2016, pp. 13615–13623.

[197] Yuan, R., Wu, S., Yu, P., Wang, B., Mu, L., Zhang, X., Zhu, Y., Wang, B., Wang, H., and Zhu, J., "Superamphiphobic and Electroactive Nanocomposite toward Self-Cleaning, Antiwear, and Anticorrosion Coatings," *ACS Applied Materials & Interfaces*, Vol. 8, No. 19, 2016, pp. 12481–12493.

[198] Gong, D., Long, J., Jiang, D., Fan, P., Zhang, H., Li, L., and Zhong, M., "Robust and Stable Transparent Superhydrophobic Polydimethylsiloxane Films by Duplicating via a Femtosecond Laser-Ablated Template," *ACS Applied Materials & Interfaces*, Vol. 8, No. 27, 2016, pp. 17511–17518.

[199] Steele, A., Nayak, B. K., Davis, A., Gupta, M. C., and Loth, E., "Linear Abrasion of a Titanium Superhydrophobic Surface Prepared by Ultrafast Laser Microtexturing," *Journal of Micromechanics and Microengineering*, Vol. 23, No. 11, 2013, pp. 115012.

[200] Tian, X., Shaw, S., Lind, K. R., and Cademartiri, L., "Thermal Processing of Silicones for Green, Scalable, and Healable Superhydrophobic Coatings," *Advanced Materials*, Vol. 28, No. 19, 2016, pp. 3677–3682.

[201] Lv, T., Cheng, Z., Zhang, E., Kang, H., Liu, Y., and Jiang, L., "Self-Restoration of Superhydrophobicity on Shape Memory Polymer Arrays with Both Crushed Microstructure and Damaged Surface Chemistry," *Small*, Vol. 13, No. 4, 2016.

[202] Thimmasetty, J., Subrahmanyam, C. V. S., SatheshBabu, P. R., Maulik, M. A., and Viswanath, B. A., "Solubility Behavior of Pimozide in Polar and Nonpolar Solvents: Partial Solubility Parameters Approach," *Journal of Solution Chemistry*, Vol. 37, No. 10, 2008, pp. 1365–1378.

[203] Karger, B. L., Snyder, L. R., and Eon, C., "Expanded Solubility Parameter Treatment for Classification and Use of Chromatographic Solvents and Adsorbents," *Analytical Chemistry*, Vol. 50, No. 14, 1978, pp. 2126–2136.

[204] Bottiglione, F. and Carbone, G., "Role of Statistical Properties of Randomly Rough Surfaces in Controlling Superhydrophobicity," *Langmuir*, Vol. 29, No. 2, 2013, pp. 599–609.

[205] Davim, J. P., editor, *Surface Integrity in Machining*, Springer, London, 2010.

[206] Tadmor, R., "Line Energy and the Relation between Advancing, Receding, and Young Contact Angles," *Langmuir*, Vol. 20, 2004, pp. 7659–7664.

[207] Guo, F., Su, X., Hou, G., and Li, P., "Bioinspired Fabrication of Stable and Robust Superhydrophobic Steel Surface with Hierarchical Flowerlike Structure," *Colloids and Surfaces A: Physicochemical and Engineering Aspects*, Vol. 401, 2012, pp. 61–67.

[208] Campos, R., Guenthner, A. J., Meuler, A. J., Tuteja, A., Cohen, R. E., McKinley, G. H., Haddad, T. S., and Mabry, J. M., "Superoleophobic Surfaces through Control of Sprayed-On Stochastic Topography," *Langmuir*, Vol. 28, No. 25, 2012, pp. 9834–9841.

[209] Reyssat, M., Pépin, A., Marty, F., Chen, Y., and Quéré, D., "Bouncing Transitions on Microtextured Materials," *Europhysics Letters*, Vol. 74, No. 2, 2006, pp. 306–312.

[210] Di Mundo, R., Bottiglione, F., and Carbone, G., "Cassie State Robustness of Plasma Generated Randomly Nano-Rough Surfaces," *Applied Surface Science*, Vol. 316, 2014, pp. 324–332.

[211] "Table 4-5: Fuel Consumption by Mode of Transportation in Physical Units," 2012.

[212] Streeter, B., "Global Marine Fuel Trends 2030," *Mari-Tech 2014 Conference Proceedings*, Niagra Falls, ON, CA, 2014, pp. 1 – 17.

[213] Bidkar, R. A., Leblanc, L., Kulkarni, A. J., Bahadur, V., Ceccio, S. L., and Perlin, M., "Skin-friction drag reduction in the turbulent regime using random-textured hydrophobic surfaces," *Physics of Fluids*, Vol. 26, No. 8, 2014, pp. 85108.

[214] Bushnell, D. M. and Moore, K. J., "Drag Reduction in Nature," *Annual Review of Fluid Mechanics*, Vol. 23, 1991, pp. 65–79.

[215] Garcia-Mayoral, R. and Jimenez, J., "Drag reduction by riblets," *Philos. Trans. A Math Phys. Eng. Sci.*, Vol. 369, No. 1940, 2011, pp. 1412–1427.

[216] Jung, Y. C. and Bhushan, B., "Biomimetic structures for fluid drag reduction in laminar and turbulent flows," *J Phys Condens Matter*, Vol. 22, No. 3, 2010, pp. 35104.

[217] Zhao, J.-p., Du, X.-d., and Shi, X.-h., "Experimental research on friction-reduction with super-hydrophobic surfaces," *Journal of Marine Science and Application*, Vol. 6, No. 3, 9 2007, pp. 58–61.

[218] Watanabe, K. and Udagawa, H., “Drag reduction of non-newtonian fluids in a circular pipe with a highly water-repellent wall,” *AIChE Journal*, Vol. 47, No. 2, 2001, pp. 256–262.

[219] Rothstein, J. P., “Slip on Superhydrophobic Surfaces,” *Annual Review of Fluid Mechanics*, Vol. 42, No. 1, 2010, pp. 89–109.

[220] Gruncell, B. R. K., Sandham, N. D., and McHale, G., “Simulations of laminar flow past a superhydrophobic sphere with drag reduction and separation delay,” *Physics of Fluids*, Vol. 25, No. 4, 2013, pp. 43601.

[221] Busse, A., Sandham, N. D., McHale, G., and Newton, M. I., “Change in drag, apparent slip and optimum air layer thickness for laminar flow over an idealised superhydrophobic surface,” *Journal of Fluid Mechanics*, Vol. 727, No. 5, 7 2013, pp. 488–508.

[222] Bixler, G. D. and Bhushan, B., “Fluid Drag Reduction with Shark-Skin Riblet Inspired Microstructured Surfaces,” *Advanced Functional Materials*, Vol. 23, No. 36, 2013, pp. 4507–4528.

[223] Bixler, G. D. and Bhushan, B., “Shark skin inspired low-drag microstructured surfaces in closed channel flow,” *J Colloid Interface Sci*, Vol. 393, 2013, pp. 384–396.

[224] Jing, D. and Bhushan, B., “Boundary slip of superoleophilic, oleophobic, and superoleophobic surfaces immersed in deionized water, hexadecane, and ethylene glycol,” *Langmuir*, Vol. 29, No. 47, 2013, pp. 14691–14700.

[225] Srinivasan, S., Kleingartner, J. A., Gilbert, J. B., Cohen, R. E., Milne, A. J. ., and McKinley, G. H., “Sustainable Drag Reduction in Turbulent Taylor-Couette Flows by Depositing Sprayable Superhydrophobic Surfaces,” *Physical Review Letters*, Vol. 114, No. 1, 2015, pp. 14501.

[226] Daniello, R. J., Waterhouse, N. E., and Rothstein, J. P., “Drag reduction in turbulent flows over superhydrophobic surfaces,” *Physics of Fluids*, Vol. 21, No. 8, 2009, pp. 85103.

[227] Woolford, B., Prince, J., Maynes, D., and Webb, B. W., “Particle image velocimetry characterization of turbulent channel flow with rib patterned superhydrophobic walls,” *Physics of Fluids*, Vol. 21, No. 8, 2009, pp. 85106.

[228] Aljallis, E., Sarshar, M. A., Datla, R., Sikka, V., Jones, A., and Choi, C.-H., “Experimental study of skin friction drag reduction on superhydrophobic flat plates in high Reynolds number boundary layer flow,” *Physics of Fluids*, Vol. 25, No. 2, 2013, pp. 25103.

[229] Henoch, C., Krupenkin, T., Kolodner, P., Taylor, J., Hodes, M., Lyons, A., Charles, P., and Breuer, K., “Turbulent Drag Reduction Using Superhydrophobic Surfaces,” *3rd AIAA Flow Control Conference*, American Institute of Aeronautics and Astronautics, 2006, pp. 1–5.

[230] Park, H., Sun, G., and Kim, C.-J. ., “Superhydrophobic turbulent drag reduction as a function of surface grating parameters,” *Journal of Fluid Mechanics*, Vol. 747, 2014, pp. 722–734.

[231] Schultz, M. P. and Flack, K. A., "The rough-wall turbulent boundary layer from the hydraulically smooth to the fully rough regime," *Journal of Fluid Mechanics*, Vol. 580, 2007, pp. 381–405.

[232] Ünal, U. O., Ünal, B., and Atlar, M., "Turbulent boundary layer measurements over flat surfaces coated by nanostructured marine antifoulings," *Experiments in Fluids*, Vol. 52, No. 6, 6 2012, pp. 1431–1448.

[233] Joonwon, K. and Chang-Jin, K., "Nanostructured surfaces for dramatic reduction of flow resistance in droplet-based microfluidics," *Micro Electro Mechanical Systems, 2002. The Fifteenth IEEE International Conference on*, 2002, pp. 479–482.

[234] Vajdi Hokmabad, B. and Ghaemi, S., "Turbulent flow over wetted and non-wetted superhydrophobic counterparts with random structure," *Physics of Fluids*, Vol. 28, No. 1, 2016, pp. 15112.

[235] Min, T. and Kim, J., "Effects of hydrophobic surface on skin-friction drag," *Physics of Fluids*, Vol. 16, No. 7, 2004, pp. L55–L58.

[236] Jelly, T. O., Jung, S. Y., and Zaki, T. A., "Turbulence and skin friction modification in channel flow with streamwise-aligned superhydrophobic surface texture," *Physics of Fluids*, Vol. 26, No. 9, 2014, pp. 95102.

[237] Gogte, S., Vorobieff, P., Truesdell, R., Mammoli, A., van Swol, F., Shah, P., and Brinker, C. J., "Effective slip on textured superhydrophobic surfaces," *Physics of Fluids*, Vol. 17, No. 5, 2005, pp. 51701.

[238] Tian, H., Zhang, J., Wang, E., Yao, Z., and Jiang, N., "Experimental investigation on drag reduction in turbulent boundary layer over superhydrophobic surface by TRPIV," *Theoretical and Applied Mechanics Letters*, Vol. 5, No. 1, 2015, pp. 45–49.

[239] Lu, S., Yao, Z. H., Hao, P. F., and Fu, C. S., "Drag Reduction in Turbulent Flows over Superhydrophobic Surfaces with Micro-Nano Textures," *Mechanics in Engineering*, Vol. 35, No. 4, 2013, pp. 20–24.

[240] Peguero, C. and Breuer, K., "On Drag Reduction in Turbulent Channel Flow over Superhydrophobic Surfaces," *Advances in Turbulence XII*, Springer, Berlin, Heidelberg, 2009, pp. 233–236.

[241] Leonardi, S., Orlandi, P., and Antonia, R. A., "Properties of d- and k-type roughness in a turbulent channel flow," *Physics of Fluids*, Vol. 19, No. 12, 2007, pp. 125101.

[242] Leonardi, S. and Castro, I. P., "Channel flow over large cube roughness: a direct numerical simulation study," *Journal of Fluid Mechanics*, Vol. 651, 2010, pp. 519–539.

[243] Xie, Z.-T., Coceal, O., and Castro, I. P., "Large-Eddy Simulation of Flows over Random Urban-like Obstacles," *Boundary-Layer Meteorology*, Vol. 129, No. 1, 2008, pp. 1–23.

[244] Kanda, M., Moriwaki, R., and Kasamatsu, F., "Large-Eddy Simulation of Turbulent Organized Structures within and above Explicitly Resolved Cube Arrays," *Boundary-Layer Meteorology*, Vol. 112, No. 2, 2004, pp. 343–368.

[245] Campos, R., Guenthner, A. J., Haddad, T. S., and Mabry, J. M., "Fluoroalkyl-Functionalized Silica Particles: Synthesis, Characterization, and Wetting Characteristics," *Langmuir*, Vol. 27, No. 16, 2011, pp. 10206–10215.

[246] Yang, J., Zhang, Z., Xu, X., Men, X., Zhu, X., and Zhou, X., "Superoleophobic textured aluminum surfaces," *New Journal of Chemistry*, Vol. 35, No. 11, 2011, pp. 2422.

[247] Schultz, M. P. and Flack, K. A., "Reynolds-number scaling of turbulent channel flow," *Physics of Fluids*, Vol. 25, No. 2, 2 2013, pp. 025104.

[248] Zanoun, E. S., Nagib, H., and Durst, F., "Refined c f relation for turbulent channels and consequences for high- Re experiments," *Fluid Dynamics Research*, Vol. 41, No. 2, 2009, pp. 21405.

[249] Ling, H., Srinivasan, S., Golovin, K., Mckinley, G. H., Tuteja, A., and Katz, J., "High-resolution velocity measurement in the inner part of turbulent boundary layers over super-hydrophobic surfaces," *J. Fluid Mech*, Vol. 801, 2016, pp. 670–703.

[250] Song, D., Daniello, R. J., and Rothstein, J. P., "Drag reduction using superhydrophobic sanded Teflon surfaces," *Experiments in Fluids*, Vol. 55, No. 8, 2014.